SYNTHESIS AND GAS SENSING PROPERTIES OF INORGANIC SEMICONDUCTING, p-n HETEROJUNCTION NANOMATERIALS

Èric Navarrete Gatell

DOCTORAL THESIS

SYNTHESIS AND GAS SENSING PROPERTIES OF INORGANIC SEMICONDUCTING, *p-n* HETEROJUNCTION NANOMATERIALS

Ph. D. Thesis

Èric Navarrete Gatell

Supervised by:

Prof. Eduard Llobet Valero

UNIVERSITAT ROVIRA i VIRGILI

Tarragona 2021

UNIVERSITAT ROVIRA i VIRGILI

FAIG CONSTAR que aquest treball, titulat "SYNTHESIS AND GAS SENSING PROPERTIES OF INORGANIC SEMICONDUCTING, p-n HETEROJUNCTION NANOMATERIALS", que presenta Èric Navarrete Gatell per a l'obtenció del títol de Doctor, ha estat realitzat sota la meva direcció al Departament d'Enginyeria Electrònica, Elèctrica i Automàtica d'aquesta universitat.

HAGO CONSTAR que el presente trabajo, titulado "SYNTHESIS AND GAS SENSING PROPERTIES OF INORGANIC SEMICONDUCTING, p-n HETEROJUNCTION NANOMATERIALS", que presenta Èric Navarrete Gatell para la obtención del título de Doctor, ha sido realizado bajo mi dirección en el Departamento de Ingeniería Electrónica, Eléctrica i Automática de esta universidad.

I STATE that the present study, entitled "SYNTHESIS AND GAS SENSING PROPERTIES OF INORGANIC SEMICONDUCTING, p-n HETEROJUNCTION NANOMATERIALS", presented by Èric Navarrete Gatell for the award of the degree of Doctor, has been carried out under my supervision at the Department Electronic, Electric and Automation Engineering of this university.

Tarragona, 15th May, 2020

El/s director/s de la tesi doctoral

El/los director/es de la tesis doctoral

Doctoral Thesis Supervisor/s

Eduard Llobet Valero

Acknowledgements

M'agradaria dedicar aquest treball a la meva família així com als meus amics i amigues ja que durant aquesta etapa de la meva vida heu estat un pilar fonamental. El suport que m'heu transmès, les moltes històries que em viscut i les que ens queden per viure m'han ajudat a seguir endavant i aconseguir poc a poc els objectius que m'he anat proposant.

Vull agrair al meu director de tesis Eduard Llobet, que m'hagis guiat al llarg de tota la tesis doctoral, la paciència que has tingut amb mi i sobretot la llibertat i la confiança que sempre he sentit que estava dipositada en mi per a poder desenvolupar aquesta tesis. Sota la teva direcció he pogut aprendre tota mena de coneixements nous així com seguir creixent tant professionalment com personalment ja que m'has transmès els teus coneixements, la teva dedicació i compromís.

També vull agrair a l'equip del SCRiT de URV que dona suport als diferents grups de recerca per la seva ajuda i feina , vull agrair al grup de tècnics de microscòpia, i en especial a la Rita, Mariana, Lukas, Mercè l'ajuda, els coneixements i els bons moments que he pogut compartir amb ells durant les llargues hores d'anàlisis.

Also, I would like to dedicate this doctoral thesis to Alexandra and Milena. Because hard working must be always accompanied with hard party, I feel it wouldn't have been the same experience if I hadn't meet you and even our final destinations are far from each other, you will always find my house open for you.

Per últim però no per això menys important, vull fer una menció especial als meus companys els quals m'han ajudat sempre que ho he necessitat i dels que m'emporto un record de per vida, Aanchal, Àngel, Badi, Ernesto, Fàtima, Juan, Maria, Milena, Miriam, Oriol, Pineda, Raúl, Sara, Serena, Sergio, Stella, Tesfalem, Xavi així com tants d'altres amb els que he compartit temps i coneixements durant tota aquesta etapa.

List of Acronyms

AACVD	Aerosol Assisted Chemical Vapor Deposition
BaP	Benzo-a-pyrene
CVD	Chemical Vapor Deposition
EEA	European Environmental Agency
HR-TEM	High Resolution Transmission Electron Microscope
MBE	Molecular Beam Epitaxy
MOx	Metal Oxide
NMVOCs	Non-Methane Volatile Organic Compounds
PL	Photoluminescence
REDOX	Reduction-Oxidation Reaction
SEM	Scanning Electron Microscope
ToF-SIMS	Time of Flying Secondary Ion Mass Spectroscopy
SMOx	Semiconductor Metal Oxide
VOC	Volatile Organic Compound
VPD	Vapor Phase Deposition
VPS	Vapor Phase Synthesis
WHO	World Health Organization
XPS	X-Ray Photoelectron Spectroscopy
XRD	X-Ray Diffraction

TABLE OF CONTENTS

1. Background……..…..1
2. Metal oxide gas sensors……..……...4
   2.1. Solid state sensors, MOXs WO_3……....4
      2.1.1. Nanomaterials for the Selective Detection of Hydrogen at Trace Levels in the Ambient…….....8
      2.1.2. Gas Sensing Mechanisms Study for 1-D WO_3 Nanowires and 2-D Lamellar WO_3 Nanoparticles …….....37
      2.1.3. Using a Second Order Sigma-Delta Control to Improve the Performance of Metal-Oxide Gas Sensors…….....60
   2.2. Synthesis Routes, introduction to AACVD an easy methodology……....74
      2.2.1. Flexible Gas Sensors Employing Octahedral Indium Oxide Films....76
      2.2.2. Gas sensing properties of ZnO nanostructures (flowers/rods) synthesized by hydrothermal method……...90
   2.3. Heterojunction gas sensors……...100
      2.3.1. AACVD and gas sensing properties of nickel oxide nanoparticle decorated tungsten oxide nanowires……...104
      2.3.2. WO_3 nanowires loaded with cobalt oxide nanoparticles, deposited by a two-step AACVD for gas sensing applications……...117
      2.3.3. Tungsten trioxide nanowires decorated with iridium oxide nanoparticles as gas sensing material……...127
      2.3.4. A tungsten oxide–lutetium bisphthalocyanine n–p–n heterojunction: from nanomaterials to a new transducer for chemo-sensing……...138
3. Conclusions…….147
4. Further work……...150
5. Bibliography……151
6. Annex 1 Supporting information…….157
7. Annex 2 Publication List……200
8. Annex 3 Contributions to Conferences……...204

1. Background

Since the industrial revolution back in the XVIII century, human society and technology have been developing exponentially. So far, the higher the development degree of a society, the higher are the consumption and demand of products and services. This development is directly linked to the sustained increase of production in all areas from food supplies, textile and garments to high-end tech such as smartphones, computers [1] [2] [3] [4] as well as new materials with enhanced performance and durability like plastics and electronics for building, clothing, gadgets manufacturing and so. In addition, the production of chemicals as precursors or as finished products themselves are also a high source of pollution due to all the manufacturing by-products [5] [6].

Consequently, such ever-increasing demand could be seen as a source of ever-increasing environmental pollution. Even though usually related, we could classify the types of pollution depending on which media is being affected [7], for instance; we have soil pollution due to introduction of chemicals or destabilizing the natural chemical soil concentrations of metallic ions due to the extended intensive-production of crops (i.e. soil poisoning by metal traces of cadmium (Cd), lead (Pb), arsenic (As), chromium (Cr) among others [8][9]) and intensive livestock farming also promotes soil poisoning due to manure and urine, sources of ammonia and methane, nitrates and phosphates [10] [11]; water pollution due to dumping waste-waters to rivers and the sea [12] [13] and finally air pollution due to the release of dangerous and hazardous gases and its uncontrolled emission to the atmosphere. This is mainly caused by the transportation of goods globally, but also by private transport, which are the focus of pollution generation, especially in cities [14][15][16]. Despite all sources of pollution and polluted medias are utterly concerning, air pollution is the most affected media by far, figure 1. shows major pollution sources.

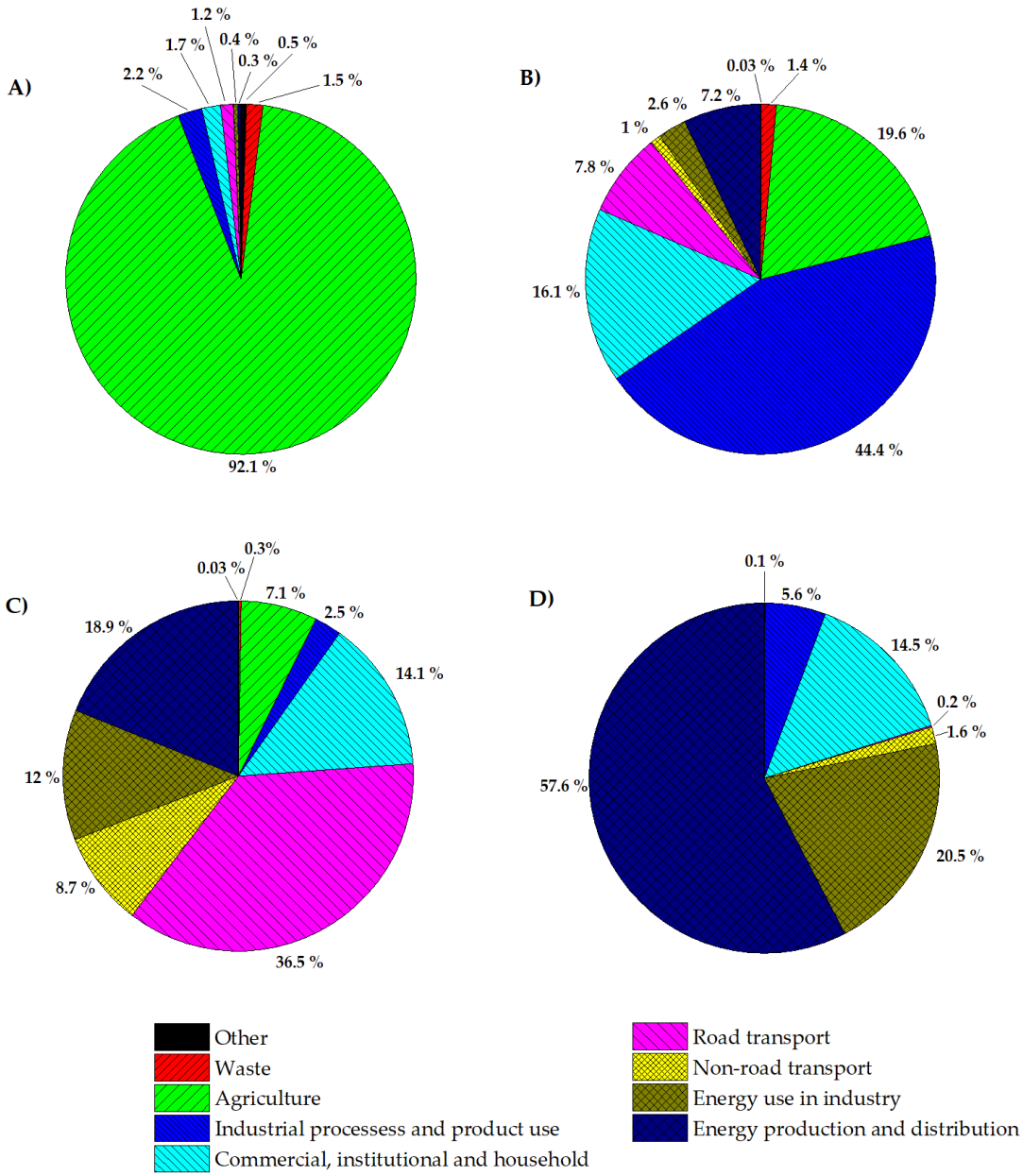

Figure 1. Pollution share contribution in percentage from different emitting sources. A) NH_3 sources; B) NMVOC sources; C) NO_x sources; D) SO_x Sources. Data extracted from European Environmental Agency (EEA): Emissions of the main air pollutants by sector group in the EEA-33.

Anthropologic sources are the ones with higher impact and largely contributing to the decrease in the air quality globally but specially in big cities and high-density inhabitants' clusters [17] [18]. The impact of air pollution in human health

has been investigated and tracked by the EEA which consist on 39 members; 33 members countries plus 6 cooperating countries, during the last years. Such studies reflect the burden caused by air pollution, which has been correlated to premature deaths (Table 1.), life-spawn shortening, increasing medical costs and a global impact to a country economy.

Table 1. Premature death directly attributed by EEA to air pollution. Data is relative to the European Union Member Countries (EU-28).

Year	$PM_{2.5}$	O_3	NO_2
2012	403000	16000	72000
2015	391000	16400	76000
2016	374000	14000	68000

The World Health Organization (WHO) classifies gas pollutants as primary and secondary. Namely, primary pollutants are those which are emitted to the atmosphere and remain as pollutants or are inclined to react with the environment and release secondary pollutants. The primary pollutants described by WHO are ammonia (NH_3), carbon monoxide (CO), nitrogen oxides (NO_x), non-methane volatile organic compounds (NMVOCs), Ozone (O_3) and sulfur dioxide (SO_2), Benzo(a)pyrene (BaP) as indicator of polycyclic aromatic hydrocarbons as well as particle matter PM2.5 and PM10. There are both anthropologic and natural emitting sources for the above listed gases [19] [20][21][22][23][24][25], being the anthropologic sources, the ones having the major impact on the environment and human health. The European Union establishes limit threshold values (Table 2) for human exposure and calculates and assesses the impact of air pollution through the exposure of populations, especially those living in urban areas, to the different primary pollutants [26] [27].

Table 2. Threshold values stablished by European Union and population percentage exposed to values higher than the limits through years.

Pollutant	**EU reference value (1)**	**2014 to 2016 (%)**	**2015 to 2017 (%)**
$PM_{2.5}$	Year (25)	6-8	6-8
PM_{10}	Day (50)	13-19	13-19
O_3	8-hour (120)	7-30	12-29
NO_2	Year (40)	7-8	7-8
BaP	Year (1)	20-24	17-20
SO_2	Day (125)	< 1	< 1

(1) Values in μg/m^3 expect for BaP in ng/m^3.

Despite that the number of deaths attributed to air pollution is slightly decreasing through the years (Table 1.), a huge percentage of population it is still exposed to pollutant concentrations higher than the limit values established as safe values (Table 2) and, therefore, new actions should be taken to prevent both the emission to the atmosphere of and exposure to such pollutants.

In this thesis the focus is placed in the fabrication, development and understanding of gas sensors in order to cope with the air pollution burden, through the fabrication of sensors capable to be employed as air quality monitoring and air quality measurement systems. Therefore, nanostructured sensing layers are developed as new sensors with enhanced properties towards the detection of specific gases in order to achieve the best selectivity and sensitivity towards such targets at trace or low concentration levels.

2. Metal Oxide Gas Sensors

2.1. Solid State Sensors

Solid state sensors can be found integrated in electronic circuits in a wide range of applications from safety in industrial environments (i.e. H_2S monitoring, explosion limit alarms) to health care applications (i.e. Oxygen measurements, glucose in blood). The commercially available sensors could be classified by means of their working principle or the physicochemical property being

measured. For instance, there are sensors based on electrochemical signals produced by chemical reactions such as electrochemical cells or chemo-resistive sensors in which the responses typically are read as a voltage o current change (case of electrochemical) or resistance change (case of chemo-resistive) and then correlated with the concentration of a target gas. On the other hand, catalytic sensors, gravimetric sensors and optical sensors are based on measuring physical properties such as thermal differences, weight or optical properties (adsorption, fluorescence, plasmon resonance, only to cite a few). Currently, the most successful commercially available, low cost sensors for air quality monitoring are those based on electrochemical cells (electrochemical) and metal oxide gas sensors (chemoresistive). Additionally, pellistors (catalytic) are employed to tackle safety issues related to flammable gases (such as hydrocarbons in the petrochemical industry). As they represent in most of the cases a simple and inexpensive solution to meet the safety requirements. In addition, the growing concerns towards air quality and air quality monitoring have increased the amount of research and development put in solid state sensors, especially into metal oxide gas sensors, the most versatile and promising.

Electrochemical cell gas sensors consist of a cylinder were the electrodes; counter, working and reference, are placed inside together with an electrolyte solution (or a solid electrolyte). The solution is in contact with the air through a permeable membrane which enables by diffusion the interaction of the gas with the electrolyte. The operational procedure is the following, the target gas diffuses from the atmosphere to the electrolyte and reaches the working electrode were an oxidation-reduction chemical reaction occurs. When a REDOX reaction is taking place, a flow of electrons is released either for oxidation or reduction, the main difference would be found in the circulation of the electron flow, for instance, depending on which type of target gas is being measured, the reaction taking place will be an oxidation (CO oxidizing to CO_2) and the electrons will be

flowing from the working electrode towards the counter electrode or a reduction (Oxygen reducing to H_2O) in which case the electrons will flow from the counter electrode to the working electrode. Finally, the electron current can be measured and correlated with the concentration of gas measured. Those type of sensors are present in environmental monitoring for measuring a wide spectrum of pollutant gases but also in healthcare applications such as oxygen measuring or the indirect glycaemia analysis via breath analysis, as they can be fairly precise, inexpensive and easy to manage. The main drawback for such sensors is the lifetime span, which is dictated by the stability and evaporation of the electrolyte. Furthermore, another important drawback and maybe the most important is the size of such sensors as a further miniaturization is almost impossible due to the need of the electrolyte as well as the electrode architecture.

Pellistors find their use as alarm sensors to assess the total amount of flammable compounds present in a given atmosphere. The structure of a pellistor consists of two main parts: a platinum string wire coated with a porous material, typically alumina, with catalyst spread among the shell. Pellistors are placed in pairs and used as a comparator meanwhile one is the active sensor the other remains as a reference at a fixed temperature (flammable gases cannot reach the surface of the reference pellistor). The flammable compounds present in the atmosphere are burnt next to the active pellistor and the increment on its temperature in comparison to the reference is indicative of the concentration of flammables. Such sensors are suitable for detecting flammables under their lower explosive levels, i.e. at concentrations of near under 1 %. The main drawback for pellistor based sensors is their lack of ability to distinguish among a mixture of gases nor the possibility to quantify each gas in a mixture as all gases are burnt and therefore the contribution of each gas to the temperature increase is added up. The main use for such sensors is in industrial areas were the prevention of the occurrence of an explosion is the main concern.

Semiconductor metal oxide (SMOx) gas sensors are by far the most promising materials for gas sensing at low costs. Back in 1970s Taguchi patented the first metal oxide sensor [28] and from then and on, the research and efforts to develop new sensors have grown exponentially. Figure 2 shows the publication trend related to SMOx gas sensors, which increases year by year. Metal oxides are suitable to perform gas sensing measurements due to their exceptional properties. The most common metal oxide used and extensively researched is by far tin oxide (SnO_2), although tungsten trioxide (WO_3), zinc oxide (ZnO) and indium oxide (In_2O_3) are also being studied in order to develop new sensors based on different metal oxides. Among their properties, semiconductor metal oxides usually have great chemical resistance, thermal resistance, long-term stability in terms of structure and morphology, and above all properties mentioned, the possibility to shape them into nanostructures is the most attractive characteristic as it implies the development of new characteristics and the capability to tailor their sensing properties.

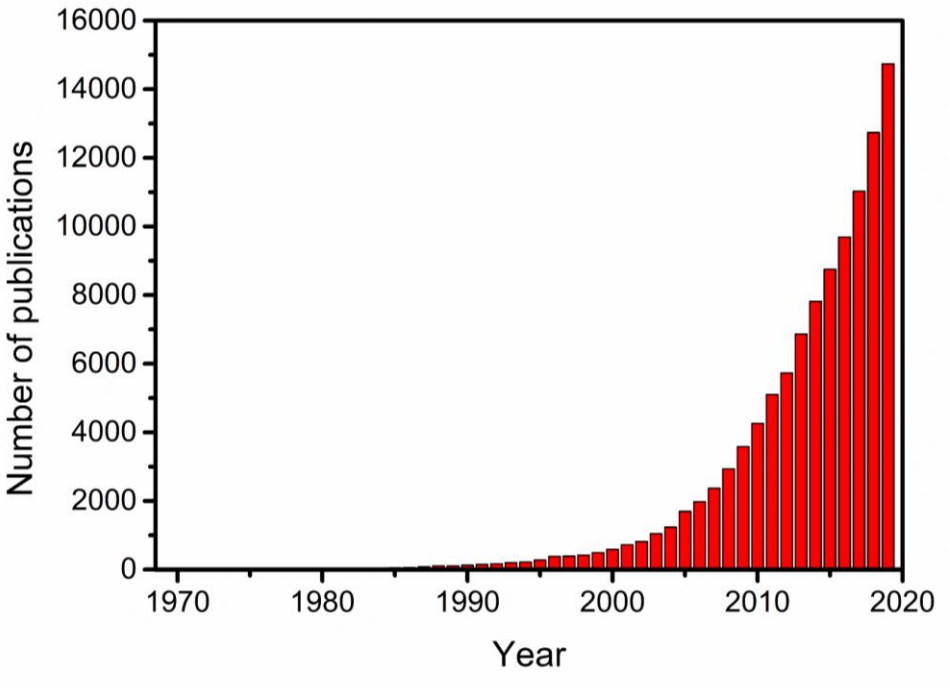

Figure 2. Yearly publications in the field of metal oxide gas sensors. Data extracted from Scopus key words "Metal oxide gas sensor".

2.1.1. Nanomaterials for the Selective Detection of Hydrogen at Trace Levels in the Ambient

Nanomaterials for the Selective Detection of Hydrogen at Trace Levels in the Ambient

50

Eduard Llobet and Eric Navarrete

Contents

Electrochemical Sensors for Detecting Hydrogen 1225
Catalytic Hydrogen Sensors 1226
Resistive Gas Sensors 1226
Metal Oxide Gas Sensors 1227
Metallic Chemoresistors 1230
Carbon Nanomaterial Chemoresistors 1230
Metal-Semiconductor or Metal-Insulator-Semiconductor Structures 1235
Gravimetric Hydrogen Sensors 1237
Optical Hydrogen Sensors 1237
Conclusions and Outlook 1240
References 1241

Abstract

Energy demand has been systematically increasing and the trends indicate that this pattern will not change in the next decade. The use of fossil fuels is responsible for the emission of gases related to global warming together with air pollutants such as toxic species and particulate matter. The realization of a green economy requires the safe use of clean and virtually inexhaustible energy sources. In that sense, hydrogen obtained via solar water splitting has potential for becoming an alternative fuel. The safe production, transport and use of hydrogen as a fuel source requires the improvement of currently existing hydrogen sensors. This chapter critically reviews the current technologies and the main research trends in hydrogen sensing.

E. Llobet (✉) · E. Navarrete
MINOS-EMaS, Universitat Rovira i Virgili, Tarragona, Spain
e-mail: eduard.llobet@urv.cat

L. M. T. Martínez et al. (eds.), *Handbook of Ecomaterials*,
https://doi.org/10.1007/978-3-319-68255-6_12

The demand on energy is systematically increasing and the trends indicate that this demand will keep increasing in the years to come. Nowadays, fossil fuels such as petroleum and natural gas are the main energy sources. However, these are non-renewable and responsible for the emissions of both green-house gases (e.g., carbon dioxide), leading to global warming, and air pollutants (e.g., nitrous, sulfur compounds, and particulate matter), causing respiratory and cardiovascular diseases. The World Health Organization estimates that air pollution is responsible for about 5.4% of all deaths, worldwide, namely some 7 million deaths yearly [1]. Therefore, it is not surprising that the last years have seen important efforts for identifying and developing new energy sources. Renewable sources of energy such as solar, wind, geothermal, hydroelectric, or tidal energy present some limitations in capturing, storing, and transporting this energy. Batteries are in constant evolution for ameliorating performance; however, the range of standard vehicles still compares favorably to the one achieved by electric vehicles and, the production of such batteries, also has an impact in the environment.

An ideal fuel should be energy-efficient, clean, safe to produce, store and use, and virtually inexhaustible. The fact that hydrogen possesses most of these qualities explains why it is being evaluated as a serious option for the replacement of fossil fuels and natural gas in industrial and transport applications [2]. Hydrogen is a very efficient energy carrier, namely, its energy density in MJ/kg nearly triples the one of natural gas, gasoline, diesel, or LPGs. In addition, its combustion (oxidation) produces water, and results in a virtually-zero emission fuel [3]. Pure hydrogen has been manufactured for more than a century and used safely in many petrochemical applications and in rocket propulsion [4]. However, a few severe accidents with important impact have prevented hydrogen to become largely accepted as other fuels in vehicles or for in-home use [5]. Hydrogen is 14 times lighter than air, so it diffuses swiftly. Its absorption on metals causes a loss in ductility (embrittlement), which may eventually result in the failure of the container employed for storage, transport, or delivery. A hydrogen leak may become a serious incident, since hydrogen shows a very wide range of flammability (from 4% to 75% in air), very low ignition energy, and high flame velocity. In [6], a valuable discussion on the risks associated to hydrogen and the safety measures to be implemented is given. Therefore, the realization of a hydrogen economy demands high degrees of safety to be achieved and, in particular, this demands the development of reliable, inexpensive, highly responsive, and selective hydrogen sensors. Such sensors should be able to detect and raise an early warning in case of a hydrogen leak. Hydrogen sensors would be of use along the whole chain of hydrogen production, storage, transport, and end-point application.

According to the US Department of Energy, hydrogen safety sensors research and development activities should target at meeting the specifications as follows [7]:

- A measurement range spanning from 0.1% to 10%
- Operating temperature range from −30 °C to 80 °C
- Response time lower than 1 s
- Ambient humidity range from 10% to 98%

- Lifetime: 10 years
- Selectivity: Not affected by carbon monoxide, hydrocarbons, etc.

Here, we review the state of the art for the detection of hydrogen employing gas sensors, discuss strengths and weaknesses of the different options available, and identify the most promising approaches. In addition, recent developments of nanomaterials with potential for the realization of inexpensive and highly sensitive hydrogen sensors are presented and critically discussed.

Electrochemical Sensors for Detecting Hydrogen

Electrochemical sensors are among the most successfully commercialized sensors for hydrogen safety applications [8]. Amperometric and potentiometric electrochemical sensors are the two main configurations employed for detecting hydrogen. In electrochemical sensors, a working electrode (Pd or Pt) is separated from a counter electrode by an electrolyte (most hydrogen sensors utilize H_2SO_4 electrolytes). In the amperometric configuration, hydrogen molecules diffuse through a hydrophobic porous membrane (generally in Teflon or in polytetrafluoroethylene) to reach the working electrode surface where they oxidize to hydrogen ions, giving two electrons to the electrode per hydrogen molecule. The membrane also prevents the liquid electrolyte to leak out of the sensor. This results in a current that is proportional to H_2 concentration [9]. In potentiometric sensors, the potential difference that develops between the working and counter electrodes at zero current (i.e., when the membrane is at thermodynamic equilibrium and there is not net flux of ions) is measured and the concentration of hydrogen is then derived from the Nernst equation [9]. Electrochemical sensors have good hydrogen sensitivity since some especially sensitive devices show detection limits of about 100 ppm (i.e., 0.01%). Their response time is about 1 min and their lifetime is up to 2 years. The use of liquid electrolytes is often a burden for achieving the miniaturization of the devices and their operability below freezing conditions is at the cost of including a heating element. While ambient humidity does not cause a problem (thanks to the hydrophobic gas diffusion membrane employed), electrochemical hydrogen sensors often suffer from significant cross-sensitivity to other gases such as carbon monoxide.

Miniaturization of electrochemical sensors and cost-reduction via use of solution processing or standard MEMS fabrication technologies can be achieved by replacing the liquid electrolyte by a polymer electrolyte or a solid electrolyte. The most employed polymer electrolyte for detecting hydrogen is NAFION, which shows good chemical stability and great ion conductivity [10]. However, sensor response is affected by ambient humidity. Solid electrolytes (these are crystalline or polycrystalline proton conductors [9]) require in general significantly higher operating temperatures for achieving good ion conductivities and this reduces their lifetime by triggering electrode-poisoning mechanisms. The cost for an individual electrochemical sensor is in the few tens of dollars range.

Catalytic Hydrogen Sensors

Under this approach, we can find pellistors, thermoelectric, and thermal conductivity sensors.

In pellistors, the exothermic catalyzed oxidation of hydrogen in a Pt-loaded porous bead rises its temperature and this is detected by a Pt wire within the bead, which serves both as heating element and thermometer. Pellistors work at significantly high temperatures, are prone to poisoning (i.e., deactivation of the catalyst by silicones or phosphorous compounds), and are not selective to hydrogen. Some selectivity can be achieved, however, by employing porous over layer coatings acting as filters or molecular sieves. Pellistors are commercially available and sold by millions a year, but are employed for unspecifically detecting flammable species (e.g., total hydrocarbons) [11].

Thermoelectric hydrogen sensors employ a film of a thermoelectric material (e.g., alkali-doped NiO [12] or SiGe [13]) deposited as a thin or thick film on an insulating substrate (e.g., glass or alumina). Part of the thermoelectric film is coated with a suitable catalyst (e.g., Pt) and the remaining film is left unmodified. Upon exposure to hydrogen, the Pt-loaded part will increase its temperature due to the exothermic oxidation reaction and this generates a temperature gradient along the thermoelectric material. This temperature gradient results in a voltage signal generated by the Seebeck effect, which is related to hydrogen concentration. In comparison to pellistors, thermoelectric sensors are operated at a significantly lower temperature, which helps reducing their cross-sensitivity to other flammable gases. The response times for both pellistors and thermoelectric sensors are in the few tens of seconds range.

Thermal conductivity sensors can be employed for measuring hydrogen, since this gas shows a significantly higher thermal conductivity than air. In this approach, two deactivated pellistor beads (i.e., not loaded with Pt catalyst) are kept with a fixed temperature difference between them and heat transfers from the hot to the cold bead by thermal conduction via the gas under analysis. The power needed to keep the hot element at known and fixed temperature above the one of the cold element depends on the thermal conductivity of the gas analyzed. If this gas is assumed to be hydrogen, then this power can be translated into hydrogen concentration. Thermal conductivity sensors are interesting because they can operate without oxygen, they are not prone to poisoning (since no catalyst is used), and show response times in the range of few ten seconds. However, these sensors cannot detect low hydrogen concentrations (only higher than 1%), are affected by changes in ambient temperature, and high thermal conductivity gases such as methane or carbon monoxide would generate important cross-sensitivity [14].

Resistive Gas Sensors

Resistive gas sensors include metal oxide, metallic, and carbon nanomaterial chemoresistors for the detection of hydrogen.

Metal Oxide Gas Sensors

Metal oxide gas sensors have been extensively researched and used for the detection of both reducing and oxidizing species in air. Metal oxide gas sensors are sold by millions every year and most of these employ tin oxide, an *n*-type semiconductor material, as gas-sensitive material. When devised for detecting hydrogen, commercially available metal oxide gas sensors can detect this gas from about 10 ppm up to half its lower explosive limit (LEL) in air (i.e., 2%), with response times of about few tens of seconds. The response mechanism involves the hydrogen molecule being adsorbed on the sensor surface and reacting with surface ionosorbed oxygen species, which results in the formation of water that is eventually desorbed from the metal oxide surface. The presence of hydrogen decreases the amount of oxygen adsorbates in which electronic charge is trapped. This increases the amount of free electrons in the conduction band of the metal oxide semiconductor, which translates in a decrease in sensor resistance (for *n*-type metal oxides such as SnO_2). In general, high operating temperatures (e.g., well above 150 °C and typically of 300 °C and even higher) are needed for these sensors to be sensitive and fast enough. Valuable reviews on metal oxide materials for detecting hydrogen can be found in [15, 16]. Hydrogen response of metal oxide gas sensors is affected by ambient moisture and shows significant cross-sensitivity to many toxic species. A way to improve hydrogen selectivity consists of loading metal oxides with small amounts of noble metals. Pd or PdO nanoparticles have been widely used for increasing the sensitivity of metal oxides to hydrogen [17–19]. Pd-based nanoparticles dissociate hydrogen molecules to hydrogen atoms, enhancing electrochemical reactions at the surface of metal oxides. High hydrogen sensitivity has been reported employing Pd-loaded metal oxides such as SnO_2 [20], ZnO [21], or WO_3 [22], operated at temperatures near to 300 °C. In the last few years, the use of low-dimensional metal oxide nanostructures (e.g., nanoparticle, nanowires, nanorods) has been studied for hydrogen sensing, because these offer higher specific surface area and interesting charge transport characteristics [23]. Pd-loaded WO_3 nanoclusters have been found to be sensitive and stable enough for detecting hydrogen in real applications [24]. Recently, Annanouch and coworkers [25] reported the direct growth, via a chemical vapor deposition process, of PdO-loaded WO_3 single crystalline nanowires onto MEMS resistive transducers. Figure 1 illustrates the sensor and the morphology of the nanomaterial.

These sensors show a high response to hydrogen (>500 for 100 ppm of H_2), extremely low cross-sensitivity to ammonia, benzene, or carbon monoxide (the response for these species is more than 250 times lower than for hydrogen at equal concentration), and are largely insensitive to ambient moisture. The optimal operating temperature for detecting hydrogen is 150 °C, at which sensors respond in a few ten seconds. However, sensors retain high hydrogen response (>20 for 500 ppm of H_2) at a low operating temperature of 50 °C.

At 150 °C, both electronic and chemical sensitization explains the hydrogen sensing mechanism of PdO-loaded WO_3 nanowires. In electronic sensitization, PdO nanoparticles behave as p-type semiconductors, which accept electrons from

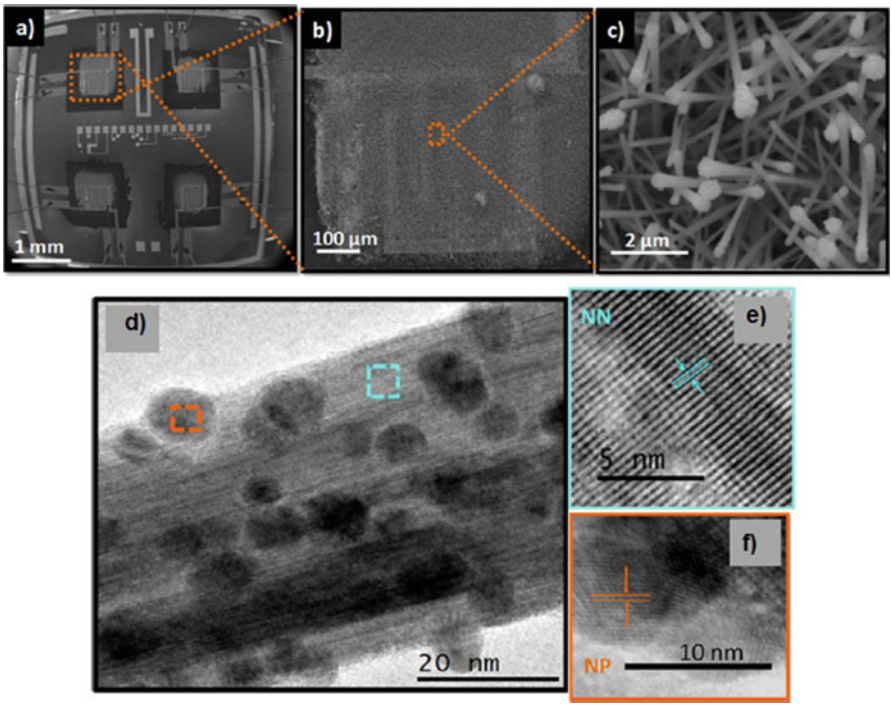

Fig. 1 Film morphology observed by SEM images at (**a** and **b**) low and (**c**) high magnification. The MEMS substrate comprises four membranes with independent heating resistor and electrodes. (**d**) TEM image of a Pd nanoparticle-decorated WO_3 nanowire. HRTEM images of (**e**) WO_3 nanowires and (**f**) Pd nanoparticles. The color code of the insets corresponds to the areas indicated in the TEM image from which the HRTEM images were taken (Adapted from [25], with permission ©The American Chemical Society, 2016)

the n-type WO_3 nanowires and develop electron depletion layers at the PdO-WO_3 interfaces. When hydrogen interacts with PdO nanoparticles, the molecule dissociates into positively charged hydrogen ions, electronic charge is transferred from PdO toward WO_3, and the electron depletion layers are relaxed. In consequence, the electrical resistance of the film decreases in the presence of hydrogen [26]. In chemical sensitization, PdO nanoparticles increase the concentration of oxygen adsorbed species on the surface of WO_3 nanowires and favor that hydrogen ions spill over WO_3 where they react with oxygen surface species [26, 27]. Once more, this leads to a decrease in sensor resistance in the presence of hydrogen. It is well-known that Pd and PdO nanoparticles are very reactive in the dissociation of the hydrogen molecule and generation of hydrogen ions, and this explains the extremely high response to hydrogen in comparison to the low response observed for ammonia, benzene, or carbon monoxide [28]. This response mechanism is illustrated in Fig. 2a.

At low operating temperatures (e.g., at 50 °C), Annanouch and coworkers [25] showed that the sensing mechanism was related to the dissolution of atomic

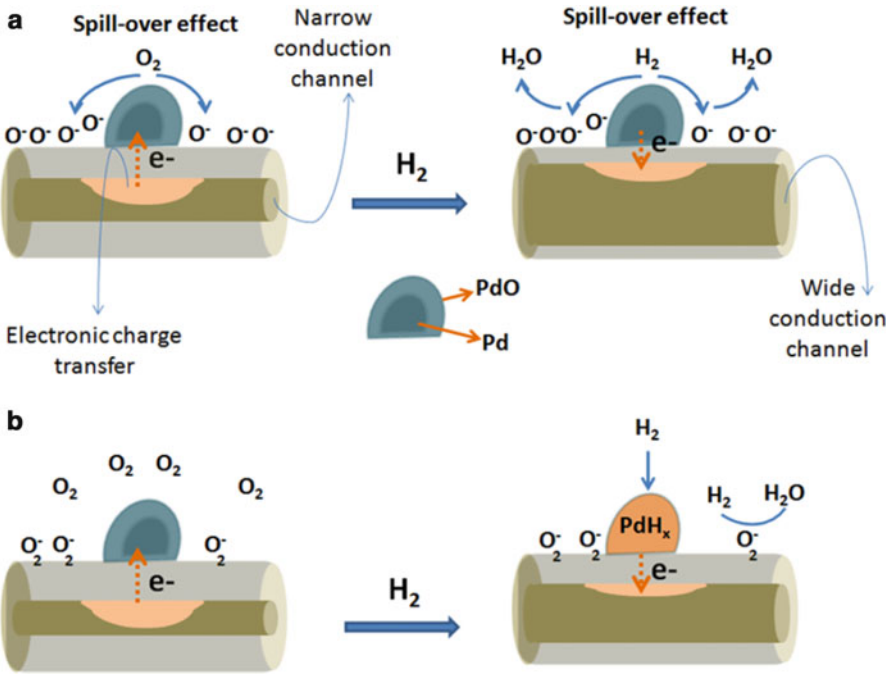

Fig. 2 Mechanism of WO_3 sensitization by PdO nanoparticles toward H_2 (**a**) at an operating temperature clearly exceeding that of the ambient temperature and (**b**) at an operating temperature equal or lower than 50 °C (Reproduced from [25], with permission ©The American Chemical Society, 2016)

hydrogen in PdO nanoparticles forming a palladium hydride (PdH_x). Palladium hydride has a lower work function compared to PdO, facilitating the transfer of electrons from nanoparticles to the WO_3 nanowires [29]. This results in the decrease in sensor resistance upon exposure to hydrogen. The formation of palladium hydride can be seen as the initial part of the mechanism described for higher temperatures, in which the spillover of hydrogen ions is arrested due to the low operating temperature. When hydrogen is removed from the ambient, PdO nanoparticles are regenerated and sensor resistance is raised back to its baseline value. This explains why a remarkable hydrogen response is retained, even when the operating temperature is significantly reduced. This response mechanism is illustrated in Fig. 2b.

As observed in PdO/WO_3 nanowires, the loading with Pd or PdO nanoparticles helps suppressing cross-sensitivity to water vapor. Existing studies on Pd or PdO nanoparticles supported on n-type metal oxides indicate that adsorbed oxygen species are not influenced by the presence of water vapor and that the electron depletion layers resulting from the p-n heterojunctions impede the adsorption of hydroxyls [30]. Furthermore, well dispersed Pd nanoparticles provide initial adsorption sites for oxygen species, minimizing the effect of ambient moisture on the Pd/metal oxide surface [31].

Metallic Chemoresistors

This approach exploits the fact that many metal and metal alloys increase their resistance upon the absorption of hydrogen. In line with what is discussed above, palladium is a good choice since hydrogen is highly soluble in this metal and the H_2/Pd interaction is quite selective. Palladium hydride shows higher electrical resistance than metallic palladium and, thus, a palladium resistor can be employed as a hydrogen sensor [32, 33]. Pure Pd hydrogen sensors are prone to poisoning by hydrogen sulfide, sulfur oxide, and, to a lesser extent, by carbon monoxide [34]. Resilience to poisoning and long-term stability heavily depends on the morphology and microstructure of Pd films [35]. For example, the use of Pd alloys with Ni or Ni-Mg seems to suppress the phase transition occurring in pure Pd exposed to hydrogen, enhancing sensor stability [36, 37]. In a different approach, the fact that Pd nanoparticles and nanowires swell upon hydrogen absorption and formation of palladium hydride has been exploited for developing resistive hydrogen sensors consisting of sparsely distributed Pd nanostructures deposited over interdigitated electrodes [38, 39]. The resistance of these films drops when hydrogen is present (due to new conductive paths appearing, upon nanostructure swelling). Limits of detection of about 10 ppm H_2 with millisecond response times have been reported.

A few commercially available hydrogen sensors employ metallic Pd resistors for measuring hydrogen, typically in the 0.5–30% concentration range at temperatures varying from room temperature to 200 °C. Response time is about a few seconds.

Carbon Nanomaterial Chemoresistors

Carbon nanotubes in the form of mats deposited by drop casting, air-brushing, or inkjet printing over substrates comprising a pair of interdigitated electrodes have been explored as gas sensitive nanomaterials [40, 41]. Carbon nanotubes produced either by arc discharge or chemical vapor deposition are chemically treated (e.g., by wet chemistry processes or by reactive cold plasmas) to graft functional groups to their external wall and/or generate controlled defects [42, 43]. These treatments allow carbon nanotubes to de-bundle, giving better suspensions in standard solvents and enabling the coating of substrates with quite homogeneous films. In addition, defects can be used to graft metal or metal oxide nanoparticles to carbon nanotube sidewalls in a quite homogeneous and stable manner, which tailors, to some extent, the reactivity of the resulting hybrid nanomaterials to different target gases [43–45].

Given the fact that the catalytic properties of Pd or Pt nanoparticles in the decomposition of hydrogen were well known, and these had been already exploited in the context of metal oxide hydrogen sensors, different research groups have reported promising results in the detection of hydrogen employing Pd [46, 47] or Pt [48] nanoparticle-decorated carbon nanotube films. The mechanism of detection is attributed to the chemisorption of hydrogen via adsorption at catalytic particles, dissociation, and spill-over onto carbon nanotubes. Upon hydrogen adsorption, electronic charge is transferred toward carbon nanotubes. In addition, an electronic

sensitization effect caused by the dissolution of hydrogen at Pd or Pt interstitials with electronic charge transferred from nanoparticles to carbon nanotubes has been considered too [48]. Hydrogen exposure results in an increase in sensor resistance, indicating that Pd- or Pt-decorated carbon nanotubes mats behave as *p*-type semiconductors. The intensity of this resistance increase correlates well to hydrogen concentration in the ambient. This response is reversible and the baseline resistance of the sensor is regained when hydrogen is removed from the ambient. Reaction of ambient oxygen with chemisorbed hydrogen at carbon nanotubes and with dissolved hydrogen at Pd or Pt interstitials with the formation of water molecules, which subsequently desorb from the hybrid nanomaterial, is considered to be the mechanism for such reversibility. Even though hydrogen response for sensors operated at room temperature has been widely reported [46–48], heating to some 100 °C helps ameliorating baseline stability and speeding up response and recovery dynamics. However, carbon nanotube hydrogen sensors still suffer from long-term stability issues, baseline recovery is still a matter of minutes rather than of seconds, and their sensitivity and selectivity appear to be lower than those of the previously discussed materials. Important cross-sensitivity to nitrogen dioxide, methane, ammonia, and ambient moisture has been reported [48]. These unsolved issues may explain why there are no commercially available hydrogen sensors employing carbon nanotube materials. Despite these difficulties, current research is addressing them and fast response and recovery (few seconds) hydrogen sensors have been reported employing a carpet of vertically-aligned carbon nanotube film covered by a 6-nm-thin film of Pt [49]. These results are illustrated in Fig. 3.

In an attempt to enhance hydrogen sensitivity, the use of Pt supported on TiO_2 nanoparticles dispersed on a carbon nanotube mat has been studied very recently [50]. The role of TiO_2 would be to enhance the injection of electron charge onto the carbon nanotubes upon hydrogen adsorption by minimizing the electron-hole recombination at the Pt-carbon nanotube interface. This strategy seems to enhance hydrogen response but, unfortunately, no study on cross-sensitivity to other gases or ambient moisture has been conducted.

The use of other metals such as Co [51] or Au [52] has been reported in metal-loaded carbon nanotubes for achieving hydrogen sensors. In [53], the use of single-walled carbon nanotubes dip-coated onto interdigitated electrodes and loaded with either Au, Cu, or Sn clusters as resistive sensors was evaluated for detecting hydrogen in a nitrogen background. Gold was found to be the most promising metal among the three tested. However, overall performance in all these studies appears to be slightly lower than the one reported for Pt- or Pd-loaded carbon nanotube sensors.

More recently, the use of graphene-like materials for gas sensing has been envisaged. High-quality graphene is a material where all its atoms lie exposed to the environment and, therefore, offers great potential for interacting with its chemical environment. However, similarly to pristine carbon nanotubes, pristine graphene is poorly reactive with the gases present in its environment and its functionalization is necessary for enhancing and tailoring gas response. Considering the results already discussed for carbon nanotube nanomaterials, loading graphene with Pd or Pt nanoparticles should lead to enhanced responses toward hydrogen. Indeed, many

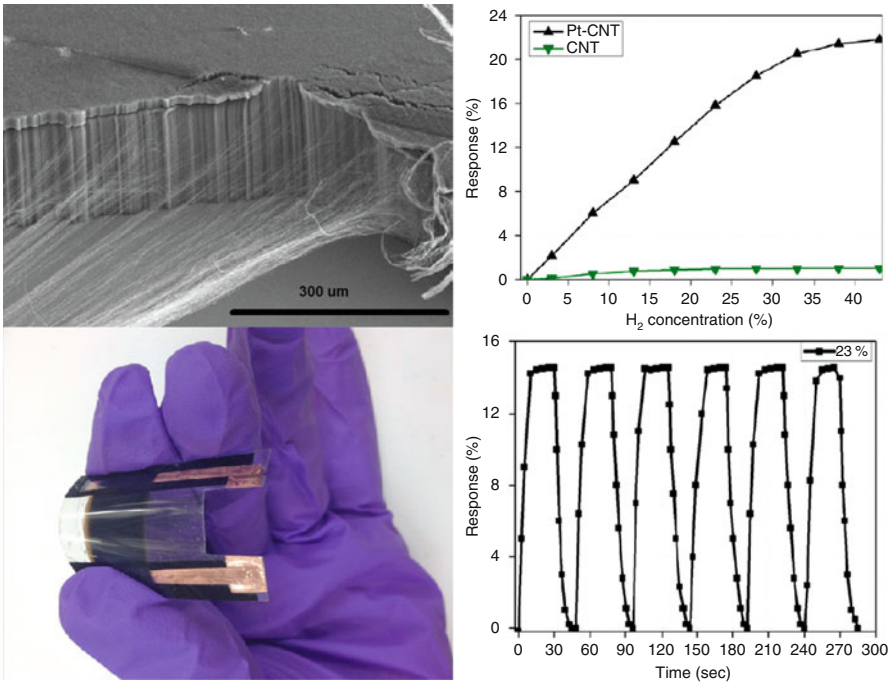

Fig. 3 Forest of vertically aligned carbon nanotubes coated with a thin Pt film on top (upper left). Flexible sensor (lower left). Hydrogen response comparison between a 6-nm Pt film coated and an uncoated carbon nanotube sensor (upper right). Repeated response and recovery cycles to hydrogen for a sensor comprising a 6-nm-thin Pt film coating a forest of vertically aligned carbon nanotubes operated at room temperature (Adapted from [49], with permission © The American Chemical Society, 2015)

authors have reported the hydrogen-sensing properties of Pd- or Pt-loaded graphene [54–60] or reduced graphene oxide [61, 62]. However, it has already been pointed out that these nanomaterials suffer from important cross-sensitivity effects and long recovery times. Besides using metal loaded graphene, metal oxide particles supported on graphene flakes have been reported as well for hydrogen sensing. In [63], graphene was synthesized via a modified Hummer's method and the In_2O_3/graphene hybrids were obtained by mixing graphene with ethanol and indium acetylacetonate under sonication, autoclaving for 24 h at 150 °C in a Teflon vessel and finally calcining at 600 °C for 2 h. The resulting powders are drop casted onto a substrate with interdigitated gold electrodes. Sensors show optimal hydrogen response when operated at 250 °C, which seems rather high. In addition, they suffer from baseline drift and no cross-sensitivity study is reported. Similarly, other metal oxides such as titanium [64] or tungsten oxides [65] have been employed in Pt- or Pd-loaded-metal oxide/graphene hybrids.

In [66], an innovative sensor configuration is presented in order to fight cross-sensitivity issues. A resistive sensor is built employing high-quality graphene loaded

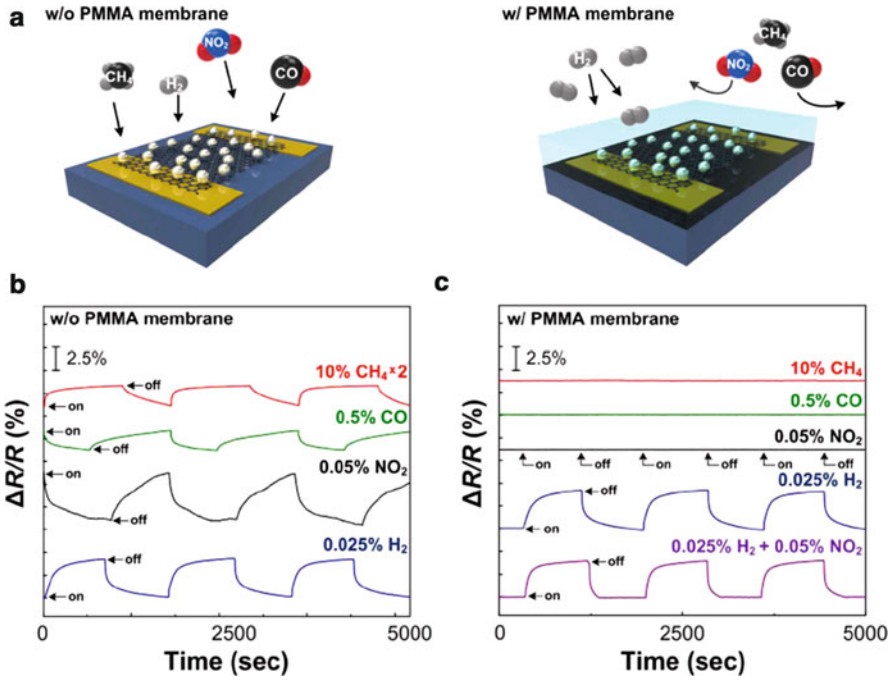

Fig. 4 (**a**) Schematic illustration showing the selective permeation of H_2 through the PMMA membrane layer and reaction with all gases without the PMMA layer. (**b**) Relative resistance changes of the Pd NP/SLG hybrid sensor for different gases: 10% CH_4 (red solid line), 0.5% CO (green solid line), 0.05% NO_2 (black solid line), and 0.025% H_2 (blue solid line). (**c**) Relative resistance changes of the PMMA/Pd NP/SLG hybrid sensor when exposed to 10% CH_4 (red solid line), 0.5% CO (green solid line), 0.05% NO_2 (black solid line), 0.025% H_2 (blue solid line), and mixture gases of 0.025% H_2 and 0.05% NO_2 (purple solid line), respectively (Reproduced from [66], with permission ©The American Chemical Society, 2015)

with palladium nanoparticles. Hydrogen selectivity is achieved via coating the gas-sensitive hybrid nanomaterial with a polymethyl methacrylate (PMMA) membrane. By carefully selecting the thickness of the membrane, hydrogen molecules can easily diffuse through and reach the gas sensing nanomaterial. In contrast, nitrogen dioxide, carbon monoxide, or methane molecules cannot permeate the PMMA membrane and no signal is registered when these species are present in the sensor environment. The simplified description of the sensor fabrication process is as follows. Single-layer graphene is CVD-grown onto a Cu substrate. Pd loading is achieved via galvanic displacement reaction. This enables controlling the amount of Pd loading while respecting the integrity and quality of the single graphene layer. The hybrid nanomaterial is coated with a PMMA supporting layer and the Cu substrate is selectively etched. The hybrid stack is transferred onto a glass sensor substrate comprising Au/Ti electrodes. The PMMA supporting layer acts as filtering membrane in the final device. The thickness of the PMMA membrane can be

adjusted by further coating the device with PMMA. Figure 4 illustrates the concept of achieving selectivity via the PMMA filter membrane.

These sensors show good baseline stability and remarkable hydrogen response (in the 250–10,000 ppm range) when operated at room temperature. Response and recovery times, which are 2 and 6 min, respectively, are slightly higher than those found in other carbon nanomaterial sensors. No data is available on ambient moisture influence and long-term stability.

In [67], a hybrid nanomaterial consisting of Pd nanocubes supported on carbon-nanotube/reduced graphene oxide (rGO) composites was prepared. Pd nanocubes were prepared employing seed-mediated growth. The hybrid material was obtained by mixing and stirring suspensions of Pd nanocubes, functionalized carbon nanotubes, and reduced graphene oxide flakes. The suspension mixture was subsequently assembled on nylon paper via filtration method and drying at 40 °C. Sensors were obtained by cutting a portion of the coated nylon paper and making Ag paste contacts on top. Sensor resistance increases in the presence of hydrogen. This is explained by electrons being transferred from Pd nanocubes toward the *p*-type carbon nanotube/rGO upon adsorption of hydrogen and formation of palladium hydride. Such sensors show room-temperature hydrogen response in a wide concentration range and moderate ambient moisture cross-sensitivity (15% change in hydrogen response when relative humidity changes from 41% to 81%). However, sensors suffer from baseline drift and rather slow response and recovery times (tens of minutes). Cross-sensitivity to potentially interfering gases has been studied, being nitrogen dioxide and acetylene those causing the highest response among those tested.

In an attempt to increase the room-temperature hydrogen sensitivity reached with carbon nanotube or graphene-based materials, the use of graphitic carbon nitride has been suggested [68]. Graphitic carbon nitride (g-C_3N_4) is a 2.7 eV gap, *n*-type semiconductor material. It consists of carbon and nitrogen atoms arranged in a graphite like structure. This material is nontoxic, stable under harsh conditions and can be easily synthesized at affordable cost. In [68], g-C_3N_4 was prepared via a direct pyrolysis of melamine and modified by the loading with Pd nanoparticles employing a modified polyol reduction method. The resulting powders were ground, mixed with organic vehicles, and the paste was drop casted onto an alumina substrate with interdigitated gold electrodes. The sensor device was thermally treated at 150 °C under inert atmosphere. This nanomaterial shows high hydrogen sensitivity and good baseline recovery at operating temperatures that range from room temperature up to 80 °C. It is well adapted for detecting hydrogen in the 1–4% range (i.e., near the lower explosive levels). The gas sensing mechanism is, once more, attributed to the affinity existing between hydrogen and Pd. Hydrogen adsorbs and dissociates in Pd nanoparticles forming a palladium hydride. This lowers the work function of Pd and injects electronic charge toward the g-C_3N_4. As a result, the electrical resistance of the film is lowered in the presence of hydrogen. Ambient oxygen reacts with hydrogen from the surface of Pd nanoparticles forming water molecules that leave the sensor surface. This mechanism explains why the sensor baseline is regained after

hydrogen is removed from the ambient [68]. However, response and recovery times are rather high, near to 100 s and no information is given on cross-sensitivity to other gases or ambient moisture.

Metal-Semiconductor or Metal-Insulator-Semiconductor Structures

In this approach, a catalytic metal is deposited on top of a thin insulator (often a thin oxide layer) lying on top of a semiconductor. The differences in the work functions of the metal and the semiconductor material result in a Schottky barrier developing at the interface. In general, Pd or Pt is used as catalytic metals. Upon exposure to hydrogen, molecules dissociate and H^+ species diffuse toward the metal/oxide interface. This generates a dipole layer, which changes the work function of the metal and shifts the energy levels at the metal–insulator interface. Diodes, metal oxide field effect transistors (MOSFETS), and capacitors are suitable devices for measuring this change in work function and, therefore, estimate hydrogen concentration. The first diode to be reported as hydrogen sensor employed Pd as catalytic metal and SiO_2/Si as insulator and semiconductor layers [69]. Since then, a wide spectrum of semiconductor metal oxides in has been explored too. The first reported hydrogen-sensitive MOSFET employed a porous Pd gate [70]. Since then, MOSFETs employing Pt or Pd/Pt gates have been reported as well. The first capacitive hydrogen sensor was reported in [71]. It consisted of a Pd-gate MOS structure. The reader is referred to [16] for a more detailed description of the working principles for such devices.

More recently, high electron mobility transistors (HEMT) employing Pd-GaAs [72], Pt-GaN [73, 74], or Pd-GaN [75] have been reported as hydrogen sensors. Their sensing mechanism is basically the same already discussed for MOSFETs. The use of wide bandgap materials offers better stability and higher operating temperature limits. The low noise characteristics and good linearity in HEMTs should allow achieving higher sensitivity, especially at low hydrogen concentrations. Figure 5 shows an example of a Pd-GaN hydrogen sensor diode employing the HEMT configuration. Such sensors have a lower detection limit for hydrogen of about 100 ppm and rather long recovery (of a few minutes). In many cases, hydrogen is measured in a background of nitrogen and not in air. No data on cross-sensitivity to other gases and ambient moisture is available.

Devices employing Pt or Pd onto SiC (diodes, capacitors, and FETs) have been also intensively researched as hydrogen sensors since they were introduced more than two decades ago [76, 77]. Despite the higher fabrication costs associated to SiC technology (in comparison to Si technology), SiC has good potential for detecting hydrogen under harsh conditions and at high temperatures, such as in the exhaust of a combustion process. Typical operating temperatures lie in the 400–500 °C range. At such high operating temperatures, besides detecting hydrogen, sensors also show significant response to hydrocarbons, which may be a problem for the reliable estimation of hydrogen concentration in some applications. Some studies have

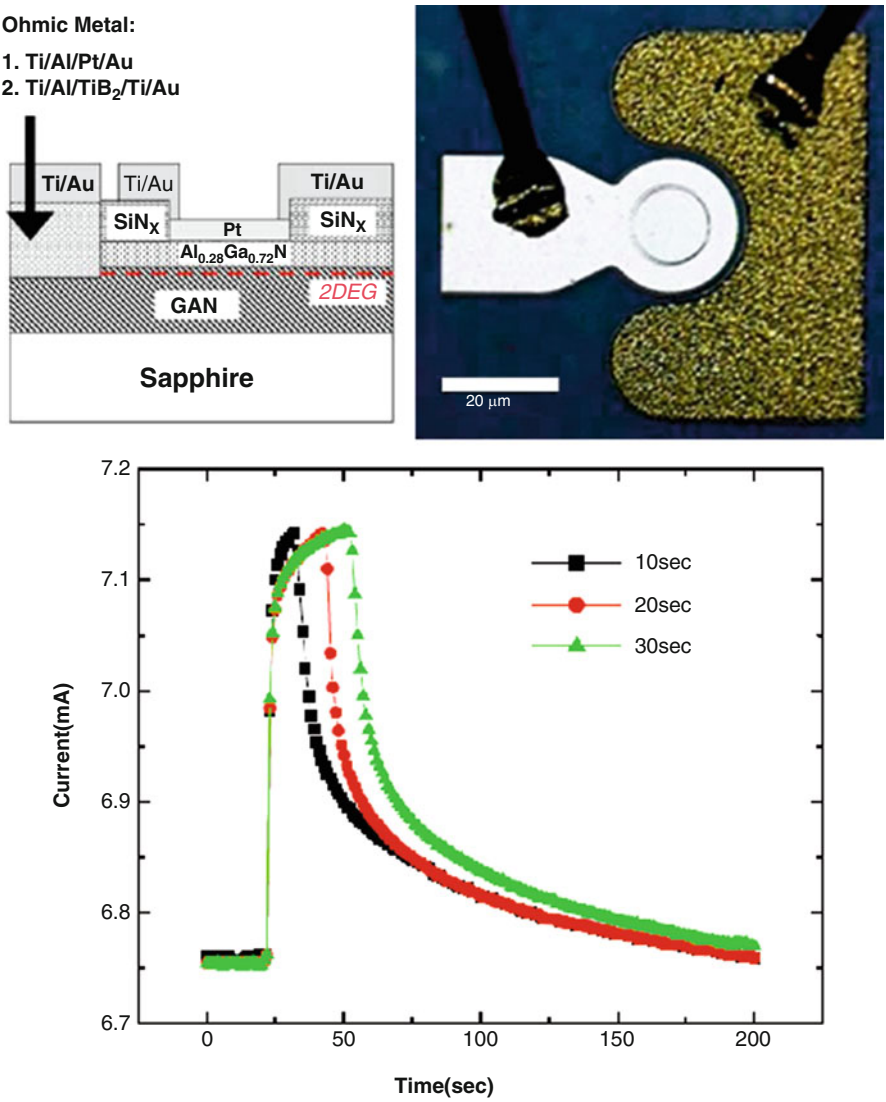

Fig. 5 Schematic cross-sectional of a diode employing an AlGaN/GaN HEMT layer structure (upper left) optical micrograph of a wire bonded device (upper right). Dynamic response of MOS-HEMT-based diode under forward bias of 2 V operated at 25 °C when the ambient is changed stepwise from N_2 to 10%H_2/90%N_2 for periods of 10, 20, or 30 s and then back to pure N_2 (lower panel) (Adapted from [73], with permission ©MDPI 2009)

reported that the oxide employed between the catalytic gate metal and SiC has an impact both in the intensity of hydrogen response and in the response and recovery times. In addition to SiO_2, different metal oxides often employed in resistive gas sensors such as ZnO, TiO_2, WO_3, or In_2O_3 have been explored [78]. In this case, the

gas sensing mechanism cannot be exclusively attributed to the dissociation of hydrogen molecules at the catalytic metal gate and diffusion of ions toward the metal/oxide interface with the formation of a dipole layer. Considering the high operating temperatures, Pt or Pd increase (via a spillover effect) the number of ionosorbed oxygen surface species at the metal oxide layer, and consequently, the amount of electronic charge trapped [79]. Once adsorbed, hydrogen reacts with surface oxygen leading to the formation of water, which is desorbed from the surface. This process releases the electronic charge that was trapped with reacted oxygen adsorbates. This additional mechanism could explain the higher response intensity and faster response dynamics observed.

Gravimetric Hydrogen Sensors

Gravimetric sensors consist either of bulk acoustic wave (BAW) or surface acoustic wave (SAW) resonators. Both types have been employed for detecting hydrogen. In bulk acoustic wave devices, the upper electrode is modified with a catalytic metal film. Different detection mechanisms have been reported including increased mass effects upon hydrogen adsorption [80] and increased operating temperature due to the exothermic decomposition of hydrogen on the catalytic film [81]. When the mass of the system or the operating temperature changes, this translates in a measurable change in the resonance frequency of the acoustic signal. In surface acoustic devices, the propagation channel lying between the excitation and reading electrodes is coated with a hydrogen sensitive film [82]. Once more, hydrogen adsorption results in mass and/or stiffness changes, which lead to a variation in the resonance frequency of the acoustic wave. Since these initial, pioneering works, a significant number of films (metals, metal oxides, organic and hybrids) have been tested for detecting hydrogen using gravimetric transducers [16]. SAWs are more employed than BAWs because the former reach higher sensitivity. Two recent examples consist of using a Pd film [83] or Pd-loaded graphene [84] in SAW devices. In [83], hydrogen in concentrations ranging from 6700 to 20,000 ppm is found to affect density and stiffness of the film, which is studied via measuring changes in phase velocity under the presence of hydrogen. In [84], the negative frequency shifts observed upon exposure to H_2 indicate a mass effect caused by adsorption of hydrogen in the Pd-graphene coating. The lower hydrogen concentration tested was 2500 ppm and this value is close to the detection limit. In gravimetric hydrogen sensors, baseline stability issues and strong humidity cross-sensitivity have prevented this technology to be commercially adopted so far.

Optical Hydrogen Sensors

Once more, Pd has been by far the most studied material for developing optical hydrogen sensors because it offers interesting properties. Upon exposure to hydrogen, Pd films change their optical transmittance in the visible region [85]. Pd, like Au

or Ag, supports surface plasmon resonance (SPR) phenomena and this characteristic has been exploited in hydrogen sensing as well [86]. The thermal changes derived from the formation of palladium hydride during exposure to hydrogen have resulted in the development of photothermal reflectance sensors [87]. Alloys of palladium with nickel [88], gold [89], or silver [90] or supporting palladium onto nickel [91], vanadium oxides [92], calcium fluoride [93], or polymer films [94] have also been investigated as a means to stabilize palladium, which is prone to suffer from cracks and delamination after repeated exposures to hydrogen, especially at high concentrations.

Besides palladium, the fact that some oxides present gasochromic behavior has been exploited in optical hydrogen sensing. Tungsten trioxide, the most well-known of these materials, increases absorbance in the visible range upon adsorption of gases. By supporting Pd or Pt nanoparticles onto tungsten trioxide, optical hydrogen sensors have been developed [95, 96]. Pd supported on molybdenum oxide [97] or Au-cobalt oxide films [98] have been studied as well. Finally, some rare-earth hydrides such as lanthanum [99] or yttrium [100] hydrides show also changes in their optical properties when exposed to hydrogen.

Employing the above-mentioned materials, many different measurement techniques have been reported. These can be summarized as follows. In one approach, a Pd micromirror is coated on the cleaved end of a fiber and reflectivity changes caused by the adsorption of hydrogen on the coating are measured [91]. In a second approach, a portion of a fiber is coated with Pd. Since Pd changes its refractive index upon hydrogen adsorption, this translates into a phase shift in the light beam and such a change can be measured employing interferometry [101]. An optical fiber supporting a Pd very thin film (few nanomaters in thickness) can excite surface plasmon resonance. SPR is affected by changes in the structure of the metal such as the formation of palladium hydride in the presence of hydrogen and this can be detected, for example, as a change in the intensity of reflected light. Sensors based on reflectivity changes employing SPR are more sensitive than those employing micromirrors [86]. In another approach, part of the cladding of a fiber is removed and substituted by a hydrogen-sensitive film (e.g., Pd or Pd-WO_3). Changes in the refractive index of this cladding caused by hydrogen affect the evanescent field and this translates in changes in the transmittance that can be measured [95, 102]. In [103], one to five stacked nanometric bilayers of Pd and Au are used and the attenuation of the optical evanescent wave caused by the presence of hydrogen is measured. This approach enables measuring hydrogen (at concentrations higher than 8000 ppm) with few second response and recovery times. Gratings can be etched to the core of the fiber and then coated with Pd so they can be sensitive to hydrogen. Upon adsorption of hydrogen, the expansion of palladium shifts the wavelength of the signal reflected by the gratings [104]. A recent review on the use of optical fiber gratings for hydrogen sensors can be found in [105]. Finally, in optical time domain reflectometry, the fiber is coated with a hydrogen sensitive film (e.g., Pt-WO_3) along the fiber rather that at a single point [106]. The signal can be spatially resolved, which allows for implementing distributed hydrogen sensing. In [107], the reader can find a recent review on fiber optic hydrogen sensors.

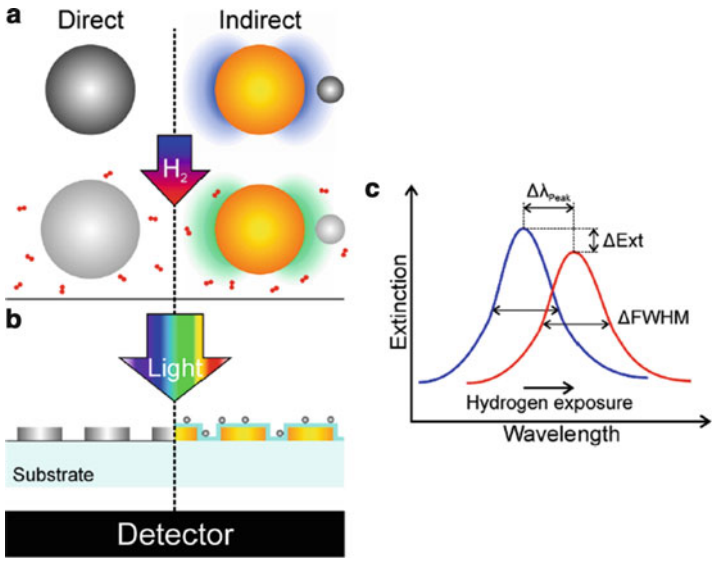

Fig. 6 Scheme describing the working principles of direct and indirect LPRS hydrogen sensors. (**a**) In direct sensing, nanoparticles act both as active material reacting with hydrogen (i.e., transform into a hydride) and as plasmonic signal transducer. In indirect sensing, an inert plasmonic particle (e.g., Au) is used to probe the interaction of hydrogen with the adjacent active material (generally a metal oxide or a palladium alloy). (**b**) LSPR of the sensor is excited by light in the visible range, and scattering or extinction spectra are recorded. (**c**) Tracking characteristic shifts in the spectral position, intensity, or line width of the LSPR peak in the recorded spectra, allows detecting and quantifying hydrogen (Adapted from [108], with permission ©ACS, American Chemical Society 2014)

The last few years have seen the development of nanoplasmonic hydrogen sensors. These employ localized SPR (LSPR) occurring in nanostructures such as nanoparticles, nanodiscs, or nanowires. A good review on this approach can be found in [108]. Both direct and indirect nanoplasmonic detection schemes have been developed. In a direct LPSR hydrogen sensor, the plasmonic entity (generally a Pd nanoparticle) is an active material that interacts with hydrogen forming a hydride and also acts as plasmonic transducer. In an indirect LPSR hydrogen sensor, the plasmonic entity (generally an Au nanoparticle) is used as a plasmonic antenna to probe the interaction taking place between hydrogen and an active nanomaterial that is in close vicinity. Figure 6 illustrates this approach and shows the differences in the working principles for direct and indirect LPSR sensing.

The problems associated to optical hydrogen sensors are related to mechanical stability issues caused by the transformation from palladium to palladium hydride and back during cycles of exposure to hydrogen. In addition, sulfur-containing species can easily poison palladium. Finally, sensor response to hydrogen is also affected by changes in ambient temperature, light, and humidity. Despite all these drawbacks, serious research efforts are directed to overcome them, since optical hydrogen sensing is an intrinsically safe detection technology. For example,

electronics can be kept far away from the area monitored in which hydrogen concentration in air may reach the explosive range and measurement signals consist of photons and not electrons. Another important aspect is that optical sensing can be used for multipoint hydrogen detection by deploying a single optical fiber and adopting spatially resolved spectrometry. Finally, optical signals are less affected than electrical signals by electromagnetic noise.

Nanoplasmonic sensors are emerging as a technology not only for merely detecting hydrogen but also for gaining deeper insight in the mechanism of the reversible formation of hydrides. Long-term stability of the nanomaterials, the development of simple readout strategies, and effective packaging are issues that need to be addressed in the immediate future.

Conclusions and Outlook

The safe production, transport, storage, and use of hydrogen require the deployment of reliable, sensitive, selective, and durable sensors. The scenarios related to a hydrogen economy are very diverse and widely different are the requirements and specifications of hydrogen sensors. Currently, there is not a single detection technology that meets all these requirements and, therefore, sensor selection should be carefully performed according to the needs of the application considered. The most commercially successful and mature technologies in hydrogen sensing are electrochemical and resistive metal oxide sensors. Electrochemical sensors can still be improved by working toward their miniaturization and reducing their cost. However, the operating and readout electronics will always remain more complex and expensive than those needed for resistive gas sensors. Resistive metal oxide gas sensors show excellent sensitivity to hydrogen. Efforts are needed in the improvement of nanomaterials (stability and robustness), to sustain their promise of ultrasensitivity at moderate operating temperatures. Some advances in the improvement of selectivity towards hydrogen have been achieved, but these need to be enhanced further. Some of the methods that have been reported to grow nanomaterials could be easily scaled up for mass production. In the years to come, we may see the adoption of nanomaterials in commercial metal oxide gas sensors with superior performance. Carbon nanomaterials are still in a too incipient technology readiness level for considering that these could be commercially adopted in the next few years. Lower sensitivity, stability, and repeatability in the reported fabrication processes than standard metal oxide materials are important issues that require further research.

Few commercially available examples of hydrogen-sensitive MOSFET devices exist. With good sensitivity and low detection limits, these devices would benefit from further research devoted to ameliorate their response and recovery dynamics and to reduce ambient temperature and moisture cross-sensitivity. This is one of the best suited approaches for detecting hydrogen in harsh environments, especially at high ambient temperatures.

The development and commercial exploitation of optical hydrogen sensors employing modified optical fibers or plasmonic structures shows great potential.

Suitable for the intrinsically safe detection of hydrogen in potentially flammable atmospheres and capable of implementing distributed sensing, this approach seems a good choice for high-end hydrogen detection applications. Phenomena like SPR, LSPR, and lossy-mode resonance (LMR) [109, 110] in nanostructured films or in nano-objects are leading to extreme hydrogen sensitivities. This may extend the application range of such sensors toward bioanalysis for medical applications. However, more efforts are needed in the long-term stabilization of the active materials employed, in fighting cross-sensitivity to other gaseous species including ambient moisture and poisoning. This is true both for palladium (thin films and nanomaterials) and gasochromic materials. The use of coatings acting as selective filtering membranes may be an approach worth studying.

Acknowledgements E.L is supported by the Catalan Institution for research and Advanced Studies via the ICREA Academia Award. E.N. gratefully acknowledges a pre-doctoral grant from MINECO-FEDER (grant. no. BES-2016-076582).

References

1. World Health Organization, Mortality and burden of disease from ambient air pollution. http://www.who.int/gho/phe/outdoor_air_pollution/burden/en/. Accessed 22 Aug 2017
2. Winter CJ (2006) Energy policy is technology politics: the hydrogen energy case (with an eye particularly on safety comparison of hydrogen energy to current fuels). Int J Hydrogen Energy 31:1623–1631
3. Frolov SM, Medvedev SN, Basevich VY, Frolov FS (2013) Self-ignition of hydrocarbon-hydrogen-air mixtures. Int J Hydrogen Energy 38:4177–4184
4. Gupta RB (2008) Hydrogen fuel-production, transport, and storage, 1st edn. Taylor and Francis Group, New York/Boca Raton
5. Mirza NR, Degenkolbe S, Witt W (2011) Analysis of hydrogen incidents to support risk assessment. Int J Hydrogen Energy 36:2068–2077
6. Najjar YSH (2013) Hydrogen safety: the road toward green technology. Int J Hydrogen Energy 38:10716–10728
7. US Department of Energy, R&D targets for hydrogen safety sensors. http://www1.eere.energy.gov/hydrogenandfuelcells/mypp/pdfs/safety.pdf. Accessed 22 Aug 2017
8. Buttner WJ, Post MB, Burgess R, Rivkin C (2011) An overview of hydrogen safety sensors and requirements. Int J Hydrogen Energy 36:2462–2470
9. Korotcenkov G, Do Han S, Stetter JR (2009) Review of electrochemical hydrogen sensors. Chem Rev 109:1402–1433
10. Liu Y-C, Hwang B-J, Chen Y-L (2002) Nafion based hydrogen sensors: Pt/Nafion electrodes prepared by Takenata-Torikai method and modified with Polypyrrole. Electroanalysis 14:556
11. Lee E, Hwang I, Cha J, Lee H, Lee W, Pak J, Lee J, Ju B (2011) Micromachined catalytic combustible hydrogen gas sensors. Sensors Actuators B 153:392–397
12. Qiu F, Shin W, Matsumiya M, Izu N, Matsubara I, Murayama N (2004) Miniaturization of thermoelectric hydrogen sensor prepared on glass substrate with low-temperature crystallized SiGe film. Sensors Actuators B 103(1–2):252–259
13. Nishibori M et al (2010) Thermoelectric hydrogen sensors using Si and SiGe thin films with a catalytic combustor. Jpn J Ceram Soc 118:188–192
14. Simon I, Arndt M (2002) Thermal and gas-sensing properties of a micromachined thermal conductivity sensor for the detection of hydrogen in automotive applications. Sensors Actuators B 97–98:104–108

15. Aroutiounian V (2007) Metal oxide hydrogen, oxygen, and carbon monoxide sensors for hydrogen setups and cells. Int J Hydrogen Energy 32:1145–1158
16. Hübert T, Boon-Brett L, Black G, Banach U (2011) Hydrogen sensors – A review. Sensors Actuators B 157:329–352
17. Liu B, Cai D, Liu Y, Wang D, Wang L, Wang Y, Li H, Li Q, Wang T (2014) Improved room-temperature hydrogen sensing performance of directly formed Pd/WO3 nanocomposite. Sensors Actuators B 193:28−34
18. Kukkola J, Mohl M, Leino A-R, Mäklin J, Halonen N, Shchukarev A, Konya Z, Jantunen H, Kordas K (2013) Room temperature hydrogen sensors based on metal decorated WO3 nanowires. Sensors Actuators B 186:90−95
19. Wang Z, Li Z, Jiang T, Xu X, Wang C (2013) Ultrasensitive hydrogen sensor based on Pd0-loaded SnO2 electrospun nanofibers at room temperature. ACS Appl Mater Interfaces 5:2013–2021
20. Suematsu K, Shin Y, Hua Z, Yoshida K, Yuasa M, Kida T, Shimanoe K (2014) Nanoparticle cluster gas sensor: controlled clustering of SnO_2 nanoparticles for highly sensitive toluene detection. ACS Appl Mater Interfaces 6:5319−5326
21. Chang C-M, Hon M-H, Leu I-C (2013) Outstanding H_2 sensing performance of Pd nanoparticle-decorated ZnO Nanorod arrays and the temperature-dependent sensing mechanisms. ACS Appl Mater Interfaces 5:135−143
22. Chávez F, Pérez-Sánchez G, Goiz O, Zaca-Morán P, Peña-Sierra R, Morales-Acevedo A, Felipe C, Soledad-Priego M (2013) Sensing performance of palladium-functionalized WO_3 nanowires by a drop-casting method. Appl Surf Sci 275:28−35
23. Gu H, Wang Z, Hu Y (2012) Hydrogen gas sensors based on semiconductor oxide nanostructures. Sensors 12:5517–5550
24. Zhao M, Huang b J, Ong C-W (2013) Feasibility of H2 sensors composed of tungsten oxide nanocluster films. Int J Hydrogen Energy 38:15559–15566
25. Annanouch FE, Haddi Z, Ling M, Di Maggio F, Vallejos S, Vilic T, Zhu Y, Shujah T, Umek P, Bittencourt C, Blackman C, Llobet E (2016) Aerosol-assisted CVD-grown PdO nanoparticle decorated tungsten oxide Nanoneedles extremely sensitive and selective to hydrogen. ACS Appl Mater Interfaces 8:10413–10421
26. Yamazoe N, Sakai G, Shimanoe K (2003) Oxide Semiconductor Gas Sensors. Catal Surv Jpn 7:63–75
27. Chiang Y-J, Lee K-C, Pan F-M (2015) Effects of Pt decoration on the CO sensing reaction mechanism of PdO Nanoflakes thin films. J Phys Chem C 119:17278–17287
28. Yamazoe N (1991) New approaches for improving semiconductor gas sensors. Sensors Actuators B 5:7−19
29. Sun Y, Wang HH (2007) High performance, flexible hydrogen sensors that use carbon nanotubes decorated with palladium nanoparticles. Adv Mater 19:2818−2823
30. Ma N, Suematsu K, Yuasa M, Kida T, Shimanoe K (2015) Effect of water vapor on Pd-loaded SnO2 nanoparticles gas sensor. ACS Appl Mater Interfaces 7:5863−5869
31. Koziej D, Hübner M, Barsan N, Weimar U, Sikora M, Grunwaldt J-D (2009) Operando X-ray absorption spectroscopy studies on Pd-SnO2 based sensors. Phys Chem Chem Phys 11:8620–8625
32. Joshi RK, Krishnan S, Yoshimura M, Kumar A (2009) Pd nanoparticles and thin films for room temperature hydrogen sensor. Nanoscale Res Lett 4:1191–1196. F
33. Kumar MK, Ramachandra Rao MS, Ramaprabhu S (2006) Structural, morphological and hydrogen sensing studies on pulsed laser deposited nanostructured palladium thin films. J Phys D Appl Phys 39:2791–2795
34. Ravi Prakash J, McDaniel AH, Horn M, Pilione L, Sunal P, Messier R, McGrath RT, Schweighardt FK (2007) Hydrogen sensors: role of palladium thin film morphology. Sensors Actuators B 120:439–446
35. Noh J-S, Lee JM, Lee W (2011) Low-dimensional palladium nanostructures for fast and reliable hydrogen gas detection. Sensors 11:825–851

36. Hughes RC, Schubert WK (1992) Thin films of Pd/Ni alloys for detection of high hydrogen concentrations. J Appl Phys 71:542–544
37. Yoshimura K et al (2009) New hydrogen sensor based on sputtered mg-Ni alloy thin film. Vacuum 83:699–702
38. Favier ECW, Zach MP, Benter T, Penner RM (2001) Hydrogen sensors and switches from electrodeposited palladium mesowire arrays. Science 293:2227–2231
39. Xu T, Zach MP, Xiao ZL, Rosenmann D, Welp U, Kwok WK, Crabtree GW (2005) Self-assembled monolayer-enhanced hydrogen sensing with ultrathin palladium films. Appl Phys Lett 86:203104
40. Collins PG, Bradley K, Ishigami M, Zettl A (2000) Extreme oxygen sensitivity of electronic properties of carbon nanotubes. Science 287:1801–1804
41. Valentini L, Cantalini C, Lozzi L, Armentano I, Kenny JM, Santucci S (2003) Reversible oxidation effects on carbon nanotubes thin films for gas sensing applications. Mater Sci Eng C 23:523–529
42. Ionescu R, Espinosa EH, Sotter E, Llobet E, Vilanova X, Correig X, Felten A, Bittencourt C, Van Lier G, Charlier J-C, Pireaux JJ (2006) Oxygen functionalisation of MWNT and their use as gas sensitive thick-film layers. Sensors Actuators B 113:36–46
43. Charlier J-C, Arnaud L, Avilov IV, Delgado M, Demoisson F, Espinosa EH, Ewels CP, Felten A, Guillot J, Ionescu R, Leghrib R, Llobet E, Mansour A, Migeon H-N, Pireaux J-J, Reniers F, Suarez-Martinez I, Watson GE, Zanolli Z (2009) Carbon nanotubes randomly decorated with gold clusters: from nano2hybrid atomic structures to gas sensing prototypes. Nanotechnology 20:375501
44. Espinosa EH, Ionescu R, Bittencourt C, Felten A, Erni R, Van Tendeloo G, Pireaux J-J, Llobet E (2007) Metal-decorated multi-wall carbon nanotubes for low temperature gas sensing. Thin Solid Films 515:8322–8327
45. Leghrib R, Felten A, Demoisson F, Reniers F, Pireaux J-J, Llobet E (2010) Room-temperature, selective detection of benzene at trace levels using plasma-treated metal-decorated multiwalled carbon nanotubes. Carbon 48:3477–3484
46. Kong J, Chapline MG, Dai H (2001) Functionalized carbon nanotubes for molecular hydrogen sensors. Adv Mater 13:1384–1386
47. Sayago I, Terrado E, Lafuente E, Horrillo MC, Maser WK, Benito AM, Navarro R, Urriolabeitia EP, Martinez MT, Gutierrez J (2005) Hydrogen sensors based on carbon nanotubes thin films. Synth Met 148:15
48. Kumar MK, Ramaprabhu S (2006) Nanostructured Pt Functionlized multiwalled carbon nanotube based hydrogen sensor. J Phys Chem B 110:11291–11298
49. Jung D, Han M, Lee GS (2015) Fast-response room temperature hydrogen gas sensors using platinum-coated spin-capable carbon nanotubes. ACS Appl Mater Interfaces 7:3050−3057
50. Dhall S, Sood K, Nathawat R (2017) Room temperature hydrogen gas sensors of functionalized carbon nanotubes based hybrid nanostructure: role of Pt sputtered nanoparticles. Int J Hydrogen Energy 42:8392–8398
51. Jung D, Han M, Lee GS (2014) Room-temperature gas sensor using carbon nanotube with cobalt oxides. Sensors Actuators B 204:596–601
52. Sharma B, Yadav H, Kim J-S (2017) MEMS based hydrogen sensor with the highly porous au-CNT film as a sensing material. J Mater Sci Mater Electron 28:13540–13547
53. Seo SM, Kang TJ, Cheon JH, Kim YH, Park YJ (2014) Facile and scalable fabrication of chemiresistive sensor array for hydrogen detection based on gold-nanoparticle decorated SWCNT network. Sensors Actuators B 204:716–722
54. Kumar R, Varandani D, Mehta BR, Singh VN, Wen Z, Feng X, Müllen K (2011) Fast response and recovery of hydrogen sensing in Pd-Pt nanoparticle-graphene composite layer. Nanotechnology 22(27):275719
55. Johnson JL, Behnam A, Pearton SJ, Ural A (2010) Hydrogen sensing using Pd-functionalized multi-layer graphene nanoribbon networks. Adv Mater 22(43):4877–4880

56. Shafiei M, Spizzirri PG, Arsat R, Yu J, Plessis JD, Dubin S, Kaner RB, Kalantar-Zadeh K, Wlodarski W (2010) Platinum/graphene nanosheet/SiC contacts and their application for hydrogen gas sensing. J Phys Chem C 114(32):13796–13801
57. Lee JS, Oh J, Jun J, Jang J (2015) Wireless hydrogen smart sensor based on Pt/graphene immobilized radio-frequency identification tag. ACS Nano 9(8):7783–7790
58. Phan D-T, Chung G-S (2015) A novel nanoporous Pd-graphene hybrid synthesized by a facile and rapid process for hydrogen detection. Sensors Actuators B 210:661–668
59. Ha NH, Long CT, Nam NH, Hue NT, Phuong NH, Hong HS (2017) Characteristics of hydrogen sensor based on monolayer of Pt nanoparticles decorated on single-layer graphene. J Electron Mater 46(6):3353–3358
60. Alfano B, Massera E, Polichetti T, Miglietta ML, Di Francia G (2017) Effect of palladium nanoparticle functionalization on the hydrogen gas sensing of graphene based chemi-resistive devices. Sensors Actuators B 253:1163–1169
61. Pandey PA, Wilson NR, Covington JA (2013) Pd-doped reduced graphene oxide sensing films for H2 detection. Sensors Actuators B 183:478–487
62. Ghosh R, Santra S, Ray SK, Guha PK (2015) Pt-functionalized reduced graphene oxide for excellent hydrogen sensing at room temperature. Appl Phys Lett 107(15):153102
63. Mansha M, Qurashi A, Ulla N, Bakare FO, Kha I, Yamani ZH (2016) Synthesis of In2O3/graphene heterostructure and their hydrogen gas sensing properties. Ceram Int 42:11490–11495
64. Dutta D, Hazra SK, Das J, Sarkar CK, Basu S (2015) Studies on p-TiO_2/n-graphene heterojunction for hydrogen detection. Sensors Actuators B 212:84–92
65. Esfandiar A, Irajizad A, Akhavan O, Ghasemi S, Gholami MR (2014) Pd-WO_3/reduced graphene oxide hierarchical nanostructures as efficient hydrogen gas sensors. Int J Hydrogen Energy 39(15):8169–8179
66. Hong J, Lee S, Seo J, Pyo S, Kim J, Lee T (2015) A highly sensitive hydrogen sensor with gas selectivity using a PMMA membrane-coated Pd nanoparticle/single-layer graphene hybrid. ACS Appl Mater Interfaces 7:3554−3561
67. Yaqoo U, Iftekhar-Uddin ASM, Chung G-S (2016) Foldable hydrogen sensor using Pd nanocubes dispersed into multiwall carbon nanotubes-reduced graphene oxide network assembled on nylon filter membrane. Sensors Actuators B 229:355–361
68. Raghu S, Santhosh PN, Ramaprabhu S (2016) Nanostructured palladium modified graphitic carbon nitride e high performance room temperature hydrogen sensor. Int J Hydrogen Energy 41:20779–207786
69. Shivaraman MS, Lundström I, Svensson C, Hammarsten H (1976) Hydrogen sensitivity of palladium thin-oxide silicon Schottky barriers. Electron Lett 12:483–484
70. Lundström I, Shivaraman S, Svensson C, Lundkvist L (1975) A hydrogen-sensitive MOS field-effect transistor. Appl Phys Lett 26:55–57
71. Steele MC, Hile JW, MacIver BA (1976) Hydrogen-sensitive palladium gate MOS capacitors. J Appl Phys 47:2537–2538
72. Hung C-W, Lin H-L, Chen H-I, Tsai Y-Y, Lai P-H, Fu S-I, Chuang H-M, Liu W-C (2007) Comprehensive study of a Pd–GaAs high electron mobility transistor (HEMT)-based hydrogen sensor. Sensors Actuators B 122:81–88
73. Anderson T, Ren F, Pearton S, Kang BS, Wang H-T, Chang C-Y, Lin J (2009) Advances in hydrogen, carbon dioxide, and hydrocarbon gas sensor technology using GaN and ZnO-based devices. Sensors 9:4669–4694
74. Irokawa Y (2011) Hydrogen sensors using nitride-based semiconductor diodes: the role of metal/semiconductor interfaces. Sensors 11:674–695
75. Chiua S-Y, Huanga H-W, Huanga T-H, Lianga K-C, Liua K-P, Tsaib J-H, Lour W-S (2009) Comprehensive investigation on planar type of Pd–GaN hydrogen sensors. Int J Hydrogen Energy 34:5604–5615
76. Hunter GW (1992) P.G.Neudeck, G.D. Jefferson, et al., the development of hydrogen sensors technology at Nasa Lewis research Centre, pp. 106141–106118. In: Proc. 4th Ann. Space Syst. Health manage. Technol. Conf., Cincinnati, USA, NASA technical Memo.106141

77. Arbab A, Spetz A, Lundstrom I (1993) Gas sensors for high-temperature operation based on metal-oxide-silicon carbide (MOSiC) devices. Sensors Actuators B 15:19–23
78. Trinchi A, Kandasamy S, Wlodarski W (2008) High temperature field effect hydrogen and hydrocarbon gas sensors based on SiC MOS devices. Sensors Actuators B 133: 705–716
79. Yamazoe N, Tamaki J, Miura N (1996) Role of hetero-junctions in oxide semiconductor gas sensors. Mater Sci Eng B 41:178–181
80. Christofides C, Mandelis CA (1989) Operating characteristics and comparison of photo-pyroelectric and piezoelectric sensors for trace hydrogen gas detection. II. Piezoelectric quartz-crystal microbalance sensor. J Appl Phys 66:3986–3992
81. Miura N (1991) New-type calorimetric gas sensor using temperature characteristics of piezoelectric quartz crystal fitted with noble metal catalyst film. Sensors Actuators B 5:211–217
82. D'Amico A, Palma A, Verona E (1982) Surface acoustic wave hydrogen sensor. Sensors Actuators 3:31–39
83. Kerroum I, Fall ME, Reinhardt A, Domingue F (2016) Hydrogen effect on density and Young's modulus of thin films in acoustic sensors. Sensors Actuators B 223:520–526
84. Ha NH, Nam NH, Dung DD, Phuong NH, Thach PD, Hong HS (2017) Hydrogen gas sensing using palladium-graphene nanocomposite material based on surface acoustic wave. J Nanomater 2017:9057250
85. Wang C, Mandelis A, Au-Ieong KP (2001) Physical mechanism of reflectance inversion in hydrogen gas sensor with Pd/PVDF structures. Sensors Actuators B 73:100–105
86. Chadwick B, Gal M (1993) Enhanced optical detection of hydrogen using the excitation of surface plasmons in palladium. Appl Surf Sci 68:135–138
87. Yarai A, Nakanishi T (2010) Optical fiber hydrogen sensor based on photothermal reflectance detection technique. J Phys Conf Ser 214(1–4):012039
88. Hughes RC, Schubert WK (1992) Thin films of Pd/Ni alloys for detection of high hydrogen concentrations. J Appl Phys 71:542–544
89. Luna-Moreno D, Monzón-Hernández D, Villatoro J, Badenes G (2007) Optical fiber hydrogen sensor based on core diameter mismatch and annealed Pd–Au thin films. Sensors Actuators B 125:66–71
90. Cui L, Chen Y, Zhang G (2009) An optical fiber hydrogen sensor with Pd/ag film. Opt Lett 5:220–223
91. Butler MA (1994) Micromirror optical-fibre hydrogen sensor. Sensors Actuators B 22:142–145
92. Liu P, Lee S, Cheong HM, Tracy CE, Pitts JR, Smith RD (2002) Stable Pd/V2O5 optical H2 sensor. J Electrochem Soc 149:H76
93. Fedtke P et al (2004) Hydrogen sensor based on optical and electrical switching. Sensors Actuators B 100:151–157
94. Wang C, Mandelis A, Garcia JA (1999) Pd/PVDF thin film hydrogen sensor system based on photopyroelectric purely-thermal-wave interference. Sensors Actuators B 60:228–237
95. Sekimoto S et al (2000) A fibre-optic evanescent-wave hydrogen gas sensor using palladium supported tungsten oxide. Sensors Actuators B 66:142–145
96. Chan CC, Hsu WC, Chang CC, Hsu CS (2010) Preparation and characterization of gasochromic Pt/WO3 hydrogen sensor by using the Taguchi design method. Sensors Actuators B 145:691–697
97. Hamagami J, Oh Y, Watanabe Y, Takata M (1993) Preparation and characterization of an optically detectable H2 gas sensor consisting of Pd/MoO3 thin films. Sensors Actuators B 13:281–283
98. Ando M, Kobayashi T, Iijimac S, Harutaa M (1997) Optical recognition of CO and H2 by use of gas-sensitive Au–Co3O4 composite films. J Mater Chem 7:1779–1783
99. Imai Y et al (2004) Optically readable hydrogen sensor using Pd/Y double-layered thin films. Adv Technol Mater Process J 6:57–62

100. Huiberts JN, Griessen R, Rector JH, Wijngaarden RJ, Dekker JP, de Groot DG, Koeman NJ (1996) Yttrium and lanthanum hydride films with switchable optical properties. Nature 380:231–234
101. Butler MA (1984) Optical fibre hydrogen sensor. Appl Phys Lett 45:1007–1009
102. Tabib-Azar M, Suptapun B, Petrick R, Kazemi A (1999) Highly sensitive hydrogen sensor using palladium coated fibre optics with exposed cores and evanescent field interaction. Sensors Actuators B 56:158–163
103. Monzón-Hernández D, Luna-Moreno D, Martínez-Escobar D (2009) Fast response fiber optic hydrogen sensor based on palladium and gold nano-layers. Sensors Actuators B 136:562–566
104. Sutapun B, Tabib-Azar M, Kazemi A (1999) Pd-coated electrooptic fibre Bragg grating sensor for multiplexed hydrogen sensing. Sensors Actuators B 60:27–34
105. Dai J, Zhu L, Wang G, Xiang F, Qin Y, Wang M, Yang M (2017) Optical fiber grating hydrogen sensors: a review. Sensors 17:577
106. Sumida S, Okazaki S, Asakura S, Nakagawa H, Murayama H, Hasegawa T (2005) Distributed hydrogen determination with fiber-optic sensor. Sensors Actuators B 108:508–514
107. Zhang Y-N, Peng H, Qian X, Zhang Y, An G, Zhao Y (2017) Recent advancements in optical fiber hydrogen sensors. Sensors Actuators B 244:393–416
108. Wadell C, Syrenova S, Langhammer C (2014) Plasmonic hydrogen sensing with nanostructured metal hydrides. ACS Nano 8:11925–11940
109. Elosúa C, Vidondo I, Arregui FJ, Bariain C, Luquin A, Laguna M, Matías IR (October 2013) Lossy mode resonance optical fiber sensor to detect organic vapors. Sensors Actuators B 187:65–71
110. Mishra SK, Usha SP, Gupta BD (2016) A lossy mode resonance-based fiber optic hydrogen gas sensor for room temperature using coatings of ITO thin film and nanoparticles. Meas Sci Technol 27:045103

Regarding to their sensing properties, semiconductor metal oxides have been broadly studied, as chemo-resistive sensors, in order to fully understand the mechanism or mechanisms behind gas sensing. In the first place, SMOx are classified under two main categories: n-type and p-type semiconductors depending on the main charge carriers involved. These are electrons in n-type materials and holes in p-type materials. When such materials interact with gases n-type semiconductors such as SnO_2, WO_3, ZnO suffer a lowering in their resistance when interacting with reducing gases (i.e. ethanol, hydrogen, hydrogen sulfide), meanwhile when interacting with oxidizing gases such as nitrogen dioxide or ozone, their resistance is increased. In contrast, p-type semiconductors such as nickel oxide (NiO) and Cobalt Oxides (Co_xO_y) display the opposite behavior. In order to explain the gas sensing mechanism in bulk semiconductor metal oxides, the energy-band bending theory was postulated. Prior to discussing the energy-band bending theory, in the first place it is important to discuss the chemical species present. When gas sensing is underway, the materials are usually heated at temperatures in the range of hundreds of Celsius degrees and, therefore, the molecular water layer typically adsorbed onto the surface of a nanomaterial at low temperatures (i.e. tenth of Celsius degrees) is almost non-existent due to the high adsorption-desorption rate. In contrast oxygen species present in the atmosphere are adsorbed onto the material.

When describing the sensing mechanism is important to note the crucial role of oxygen species adsorbed onto the nanomaterial surface. Such oxygen species act as traps for the electrons from the conduction band of an n-type material. Oxygen gets adsorbed at the surface as ions, thus creating through the immobilization of electron charges a depletion zone which leads to an energy-band bending. The whole system then consists of two main parts: the depletion zone (outer zone) and the conduction zone (inner zone). SMOx films generally consist of packed

grains. When two grains are in contact the depletion zones interact, and a potential barrier is created for the electrons travelling from one grain to another, this barrier is the so-called Schottky barrier. The height of the Schottky barrier that develops at grain boundaries determines the conductivity of the gas sensitive film. The key part of the sensing mechanism is the reaction of adsorbed oxygen species with foreign gas molecules releasing charges that modify the height of the Schottky barrier, thus having an impact on the overall film conductivity. Furthermore, as more charges are released, higher is the impact on the Schottky barrier potential and the material suffers a higher change in conductivity. For this reason, SMOx are used as chemoresistive sensors, their resistance is monitored as a baseline and when under an interaction with a gas, such resistance suffers a modification (due to the previously described interactions) and is then compared to the baseline. The change in resistance experienced is correlated to gas concentration.

In addition, charge transfer is heavily influenced by the grain size (D) to the width of the space-charge layer (L) ratio. Three possible scenarios have been postulated depending on the ratio between them (Figure 3), for instance if grains are large enough (D>>2L) the conductivity of the material depends mainly on the mobility of the carriers inside the grains. In this case surface reactions occurring, have a small impact to the barrier potential and thus the overall conductivity is not heavily affected. Under these conditions, the sensitivity displayed is low. In the second scenario, the grain size and the depletion layer width are similar (D >= L). For this particular scenario, the variations on the material conductivity are more affected by the surface reactions taking place. The third scenario is by far the most interesting, when the size of the grain is significantly lower than the width of the depletion layer, the surface reactions and the charges released by them have a strong impact on the barrier potential thus having a huge impact on the overall material conductivity. This happens because grains may become fully

depleted of charges upon the adsorption of oxygen species. All this has strong effects on the resistance of the gas sensitive film, which enables getting dramatically enhanced responses upon the detection of gases.

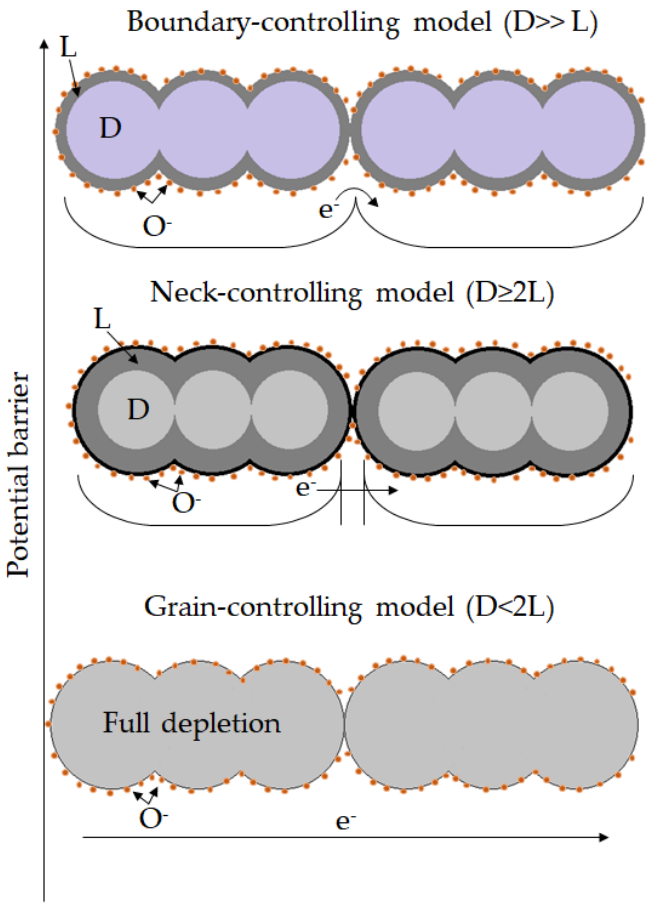

Figure 3. Schematic representation of the three different conductivity scenarios present depending on the depletion zone layer width to particle size ratio.

Once the simplified gas sensing mechanism behind *n*-type SMOx gas sensors has been reviewed, there are other aspects to be considered. In general, such materials may react with a wide spectrum of gas species with higher or lower affinity and, therefore, their selectivity is poor. Furthermore, their operating temperature is a key parameter for gas sensing, since each gas may have an optimal temperature in which the response of the material is maximized. Of course, such maximization strongly depends on the type of semiconductor as well as the nanostructure morphology [29] [30]. Indeed, the amount and the

nature of the adsorbed oxygen species in the form of ions such as O_2^-, O^- and O^{2-} depends not only on the operating temperature, but also on the nanostructure morphology. In the paper "*Gas Sensing Mechanisms Study for 1-D WO_3 Nanowires and 2-D Lamellar WO_3 Nanoparticles*" the difference in the oxygen species present at the surface of a sensing layer when operating at the same temperature two different morphologies of tungsten oxide, sensors is studied.

2.1.2 Gas Sensing Mechanisms Study for 1-D WO_3 Nanowires and 2-D Lamellar WO_3 Nanoparticles

Gas Sensing Mechanisms Study for 1-D WO_3 Nanowires and 2-D Lamellar WO_3 Nanoparticles

Èric Navarrete[1], Koichi Suematsu[2], Eduard Llobet[1], Kengo Shimanoe[2]

[1]*MINOS-EMaS, University Rovira I Virgili, Avda. Països Catalans, 26, 43007 Tarragona, Spain*

[2]*Department of molecular and Material Sciences, Faculty of Engineering Sciences, Kyushu University, 6-1 Kasuga-koen, Kasuga, Fukuoka 816-8580, Japan*

Abstract

Gas sensors were fabricated employing tungsten trioxide (WO_3) nanowires grown via AACVD and lamellar WO_3 nanoparticles were grown via wet acidification methodology. The morphology of both samples was studied and their sensing properties towards hydrogen and ethanol were tested. Furthermore, a partial oxygen dependence study was carried out to determine the possible difference between the oxygen species responsible for the gas sensing mechanism.

1. Introduction

During the last few decades, with the increase in the emission of air pollutants from anthropogenic sources, air quality control and monitoring has become a global concern. There are several reasons for controlling the levels of pollutants in the air. On the one hand outdoor emissions from automobile exhausts and factories such as NO_x, O_3, SO_2, VOCs or particulate matter, only to cite a few, undeniably are a threat to human health. These are responsible for some 4.2 million premature deaths annually worldwide, mainly from heart disease, stroke, chronic obstructive pulmonary disease, lung cancer, and acute respiratory infections in children [1][2]. On the other hand, indoor emissions of carbon monoxide (CO) resulting from the inefficient combustion of fuels in cooking stoves or heaters often causes asphyxia accidents at home [3]. The exposure to high indoor concentrations of VOCs such as acetaldehyde released from

furniture and paints at home or the occupational exposure to benzene and mercaptans in closed areas in factories could lead to serious illnesses or death [4]. Besides air quality control and occupational health, other applications require the detection of gases or vapors. For example, with the development of a greener economy, the use of hydrogen (from efficient reforming or water splitting) in fuel cells may boost the need of hydrogen sensor systems to detect hydrogen leaks, given its flammability [5]. Also, ethanol vapor detectors are necessary in many applications such as in ethanol production plants, in the monitoring of alcoholic fermentation processes or in breath analysis (in medical applications or for preventing drunk driving) [6].

Among the different materials and transducing schemes that are currently commercially available for detecting gases and vapors, metal oxide semiconductors (MOXs) employed as chemoresistors represent a significant part of the market share. MOXs possess outstanding sensitivity for detecting traces of toxic, pollutant and flammable gases in the ambient and their use as chemoresistors enables the development of simple and affordable detectors. The MOX family is quite extensive and comprises materials such as SnO_2, ZnO, In_2O_3, TiO_2, Co_3O_4, Fe_2O_3, NiO, CuO or WO_3, only to cite a few [7]. These materials can be synthetized in a wide variety of morphology, micro and/or nano structures, crystalline phase and stoichiometry through different methodologies, both physical and chemical, in order to achieve the specifications of a given gas/vapor detection application [8]. The most studied material by far is SnO_2, which has been studied for more than 50 years now. It remains the most employed material in commercial MOX sensors. However, in the last few decades tungsten oxide (WO_3) has been extensively studied for its outstanding gas sensing properties and has also gained presence in the market of chemoresistive sensors. Tungsten oxide has been found suitable for the detection of oxidizing gases such as NO_2 or O_3 [9] [10] [11] and it has also been reported as a good gas-sensitive material for reducing species such as H_2, ethanol or H_2S [12][13]. Despite its commercial

success, the gas sensing mechanisms of tungsten oxide are still far from being completely understood. It has been stated that not only the oxygen species adsorbed on the material surface (O_2^-, O^- and O^{2-}) are involved in the sensing mechanism, but also the lattice oxygen O_{lat}^{2-} can play a role, especially in the presence of surface catalysts such as Pt [14]. Furthermore, it has been reported as well that the material synthesis routes have an impact on the material morphology, microstructure, crystalline phase and stoichiometry, which eventually translate into remarkable differences gas sensor response and performance [15]. In the literature, a wide range of synthesis methods have been reported to obtain a large variety of tungsten oxide materials for gas sensing. RF sputtering was used to obtain thin WO_3 films for the detection of O_3 [11], WO_3 nanowires and WO_3 nanoflowers were grown through thermal evaporation and hydrothermal process in order to detect H_2 and ethanol respectively [16] [17]. Tungsten oxide nanorods were prepared through thermal CVD at different substrate temperatures and flow rates to understand the material growth [18]. In addition, tungsten oxide nanoigloos decorated with Pd, Au and Ag were obtained through soft-template method and the film sensing properties towards H_2 and NO_2 were studied [19].

In this paper, we use two different chemical synthesis approaches to obtain WO_3 nanomaterials with different morphologies. Tungsten trioxide nanowires were synthesized employing the aerosol assisted chemical vapor deposition (AACVD) [20] and lamellar WO_3 nanoparticles were obtained through wet acidification of Na_2WO_4 [12]. The gas sensing properties of these materials to hydrogen and ethanol diluted in air are reported and a study showing the dependence of the sensor resistance on the partial pressure of oxygen is conducted, which enables the identification of the oxygen surface species involved in the detection mechanisms for the two morphologies considered. The hydrogen and ethanol sensing mechanisms for lamellar and nanowire tungsten oxides are discussed.

2. Material & methods

2.1. Alumina substrate preparation

In this paper, screen printed interdigitated gold electrodes on top of alumina substrates (13 x 9 mm) were prepared [10]. The alumina substrates were placed in a screen-printing machine to imprint gold electrodes using a gold commercially available paste. Once the electrode pattern had been screen-printed on top of the alumina substrate, a calcination was performed at 850 ºC for 8 hours. The electrode gap was 90 μm, a line with of 180 μm and a total sensing area of 64 mm^2. Substrates with printed electrodes underwent a cleaning step prior the deposition of the sensing layer was performed. The cleaning step consisted of preparing a solution of 100 mL deionized water and 10 mL H_2O_2 heated at 80 ºC, to which 2 mL of NH_3 were added. Once the cleaning solution was ready, the alumina substrates were dropped inside, and bubbling occurred until all the organic impurities had been removed. Finally, the substrates were dried at 100 ºC for 1 hour.

2.2. Tungsten trioxide nanowires

Tungsten oxide nanowires (WO_3 NWs) were synthetized through aerosol assisted chemical vapor deposition employing tungsten hexacarbonyl, $W(CO)_6$, as organic precursor. 50 mg of $W(CO)_6$ were weighted and dissolved under stirring into a solution consisting on 15 ml of acetone and 5 ml methanol until fully solubilized. Then the solution was brought into a spray employing high frequency waves and carried within a N_2 flow set at 0.5 L/min into a 400 ºC preheated, hot-wall, CVD reactor inside which an alumina substrate with interdigitated screen-printed gold electrodes on top was placed. The total synthesis time was 30 minutes. After finishing the synthesis, the reactor was naturally cooled down to room temperature. The as-grown nanowire film presented a deep blue color due to two main factors; the non-stoichiometry of the tungsten oxide, i.e., WO_{3-x} and the presence of amorphous carbon originated

during the combustion of organic solvents. Therefore, to further increase the oxidation of tungsten oxide and remove the remnant amorphous carbon, an annealing step was carried out. The annealing was performed inside a muffle at 500 ºC during 2 hours with a temperature increase rate of 5 ºC/min and letting the system to cool down naturally to room temperature. After the annealing, the nanowire layers presented a pale-yellow color, indicative of the presence of a clean, quasi-stoichiometric WO_3.

2.3. Lamellar tungsten oxide nanoparticles

Lamellar tungsten oxide nanoparticles were obtained via a wet-synthesis route that involved the acidification of sodium tungstate, Na_2WO_4. 1 L of deionized water was heated at 50 ºC in a beaker under soft stirring and the pH adjusted to -0.8 with sulfuric acid (analytic gradient, purity 99%). Then, 2.61 g of Na_2WO_4 were added slowly and, immediately, a yellow precipitated was formed. The solution then was stored and aged for 24 hours. After the aging, the precipitated was filtered, collected and dried at 50 ºC. The precipitated was milled manually inside an agate mortar until fine powders were obtained. These powders were then mixed with α-Terpinol until a paste was formed, which was then screen printed on top of the alumina substrates comprising gold interdigitated electrodes. The sensors were then dried and annealed at 350 ºC during 4 hours in a tubular furnace under a flow of dry air.

2.4. Material characterization

The nanomaterials had their crystalline phase characterized through X-ray diffraction (XRD) and their structural morphology was studied employing scanning electron microscopy (SEM). XRD was performed employing a Bruker-AXS D8-Discover diffractometer with a parallel incident beam. SEM images were acquired using a JEOL 7600F field emission SEM.

2.5. Gas sensing characterization procedure

The sensors were tested to two different species, hydrogen and ethanol at five different concentration levels (dry air was used as carrier and balance gas) and using 4 different operating temperatures (i.e. 150, 200, 250 and 300 ºC). The concentrations tested were 50, 100, 200, 300 and 500 ppm for hydrogen and 20, 40, 60, 80 and 95 ppm for ethanol. The sensors were placed inside a controlled-temperature oven, which was connected to a mass-flow system (MF) able to deliver repeatable and precise gas concentrations. To analyze sensor reproducibility, two sensors of each type (i.e. nanowire or lamellar tungsten oxide) were employed. The gas flow inside the oven where the sensors under test were placed was kept constant at 100 mL/min. Sensors were characterized at 4 operating temperatures (from the highest to the lowest). Every time a new operating temperature was set, sensors were kept overnight under dry air to stabilize to their baseline resistance. In a typical measurement process conducted at any given operating temperature, sensors were exposed to 90-minute step-like increasing gas/vapor concentrations and, 90 minutes after the highest concentration had been reached, the gas/vapor concentration was step-like decreased down to pure dry air. Finally, to check the repeatability of measurements, this measurement cycle was repeated after allowing the full recovery of sensor baseline resistance under dry air for 4 to 5 hours.

In addition, the dependence of the baseline resistance for lamellar and pure WO_3 nanowire sensors on the partial pressure of oxygen was studied as well. The partial pressure of oxygen was set at 1, 2.5, 5.25, 10, 20, 50 and 100 % O_2 and the DC voltage at the load resistances (R_0) of the sensors was recorded using a Keithley multimeter, as it is shown in Figure X, and converted to the DC resistance of the sensor employing the mathematical expression in equation 1.

$$R_{sensor} = R_0\left(\frac{4}{V_{Sensor}} - 1\right) \qquad \text{(eq. 1)}$$

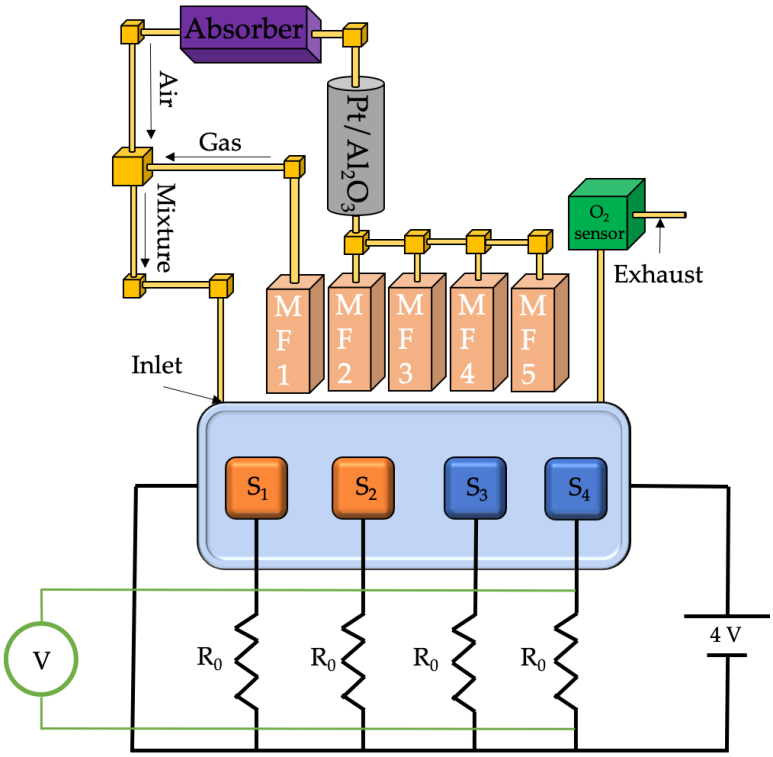

Figure 1. Schematic representation of the experimental set up. Mass-flow systems are connected to a Pt/Al_2O_3 catalyst to burn all possible organic traces. The absorber removes all traces of water present in the commercial synthetic air.

3. Results and discussion

3.1. Material characterization

Tungsten oxide nanowires and lamellar WO_3 nanoparticles were characterized by XRD to understand the crystallinity and analyzed by means of SEM to investigate their morphology. Figure 2 shows the spectra recorded for lamellar WO_3 and pure WO_3 nanowires. The peaks in both spectra are in agreement with those reported in the ICDD card nº 43-1035 corresponding to monoclinic WO_3. The lamellar WO_3 and WO_3 nanowire spectra display also peaks for alumina, which correspond to the substrate and in the case of lamellar tungsten oxide, gold peaks are also present in the spectra due to the electrodes.

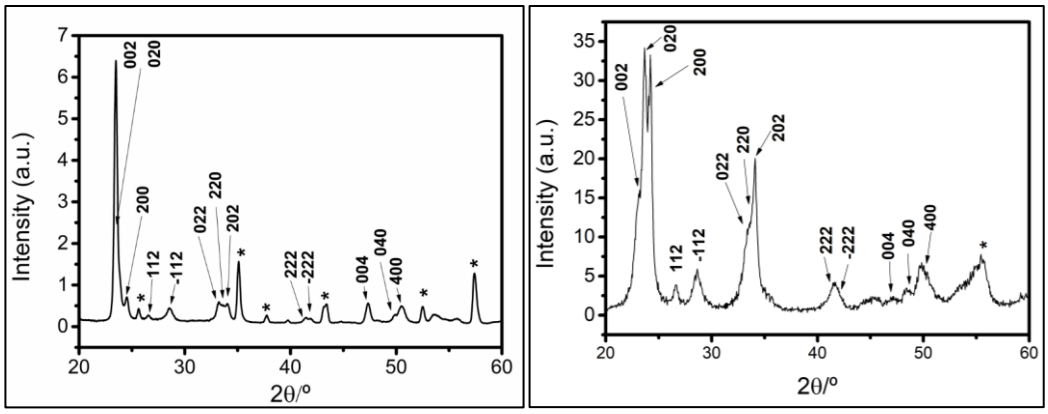

Figure 2. (a) WO_3 Nanowires XRD spectrum; (b) Lamellar WO_3 nanoparticles XRD spectrum.

Figure 3 shows typical SEM images obtained from the surface of the two types of sensors used. Typically, nanowires synthetized through AACVD have a diameter ranging from 50 to 100 nm and a length between 10 to 20 μm with an average of 14 μm layer thickness [13]. Lamellar WO_3 nanoparticles, present a size comprised between 100 to 350 nm in diameter, 25 nm as average thickness and a film thickness estimated to be between 15 to 25 μm.

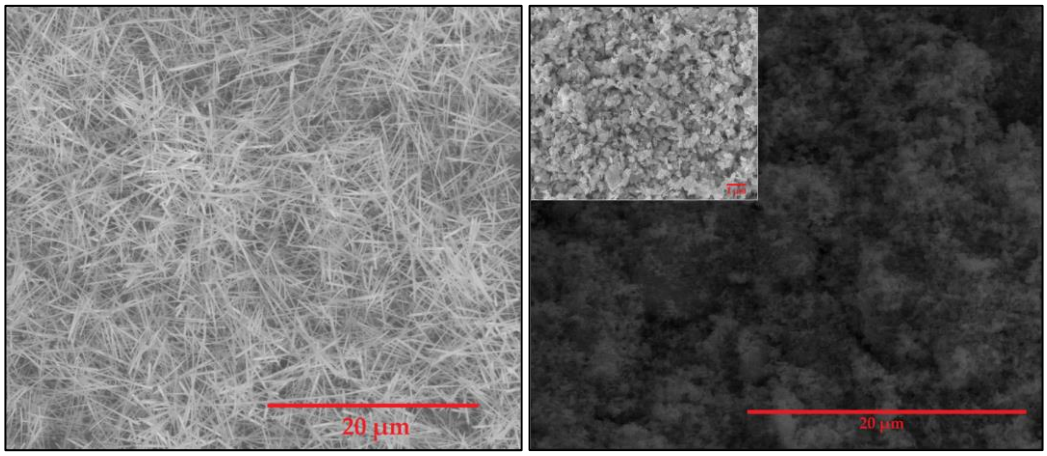

Figure 3. Left panel SEM surface image for a pure WO_3 nanowire film. Right panel shows a SEM image of the lamellar WO_3 nanoparticles with a close zoom inset.

3.2. Gas sensing results

The gas sensors responses towards hydrogen and ethanol were studied under dry air conditions.

3.2.1. Hydrogen

All tungsten oxide based-sensors were exposed to hydrogen at 50, 100, 200, 300 and 500 ppm under dry air conditions. Figure 4a shows that increasing the operating temperature for pure WO_3 nanowire sensors enhances their response towards hydrogen for all the concentrations tested. Tungsten oxide nanowire sensors show almost no response towards hydrogen when operated at 150 ºC. The optimal sensing temperature (among the temperatures tested) for nanowire tungsten oxide sensors was found to be 300 ºC, in which the response for all concentrations of hydrogen is maximized. Figure 4b shows the results obtained for lamellar WO_3 nanoparticle sensors. Lamellar-based sensors exhibited a strikingly different behavior compared to nanowire-based sensors when operated at 300 ºC. Lamellar tungsten oxide sensors showed the lowest response to hydrogen at 300ºC and the highest response at 250 ºC, with little difference in comparison to their response at 200 ºC.

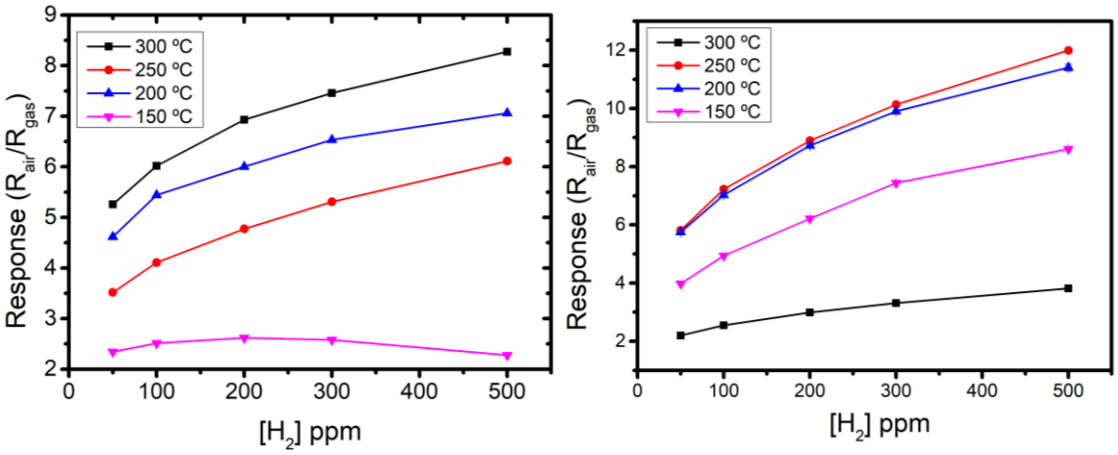

Figure 4. (a) Pure WO_3 nanowires response towards H_2 concentrations; (b) Lamellar WO_3 nanoparticles response towards H_2 concentrations.

3.2.2. Ethanol

The sensors were exposed to different concentrations of ethanol at concentrations of 20, 40, 60, 80 and 95 ppm balanced in dry air. Figure 5a reports these results

for tungsten oxide nanowire sensors operating at the different temperatures tested. When the operating temperature was increased from 150 ºC to 300 ºC nanowire-based sensors increased their response towards ethanol. At 150 ºC the sensor showed little responsiveness towards ethanol vapors and the sensor was rapidly saturated. Figure 5b shows the response to ethanol for lamellar WO_3 sensors. Similarly, to nanowire-based sensors, when lamellar WO_3 sensors were operated at 150 ºC, they showed the lower response towards ethanol. In contrast to nanowire based sensors, no response saturation was observed. In lamellar WO_3 sensors, the optimal operating temperature for detecting ethanol was 250ºC because a slight decrease in responsiveness was observed at 300ºC.

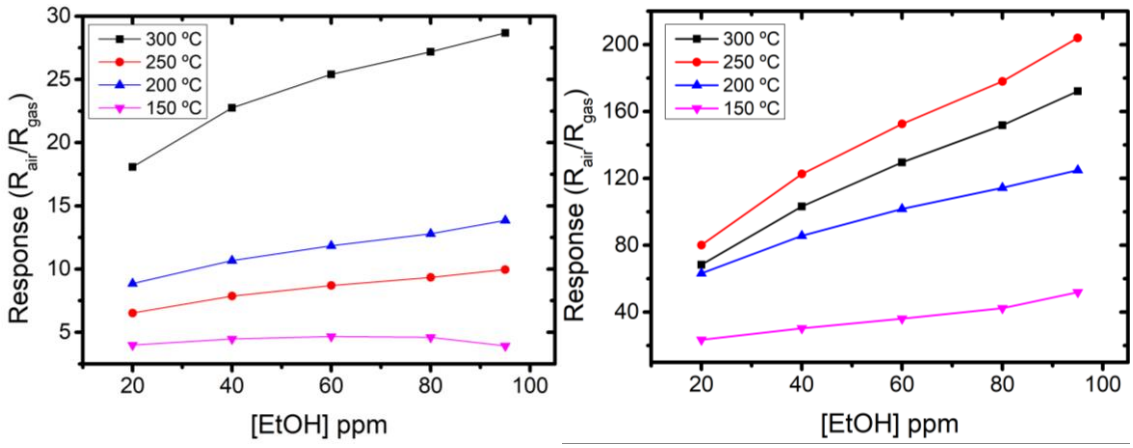

Figure 5. (a) Pure WO_3 response towards ethanol concentrations at different operating temperatures. (b) Lamellar WO_3 nanoparticles response towards increasing concentrations of ethanol at the different temperatures tested.

The intensity of the response towards hydrogen and ethanol is significantly higher for lamellar tungsten oxide sensors than for nanowire based sensors. Given the two different synthesis routes implemented, lamellar sensors comprised far more tungsten oxide material than nanowire sensors. Using more material implies increasing the surface area, which eventually results in higher responsiveness. To verify that the differences in response intensity are due to the reason discussed above, further nanowire sensors were fabricated increasing the amount of precursor. This resulted in nanowire sensors with an increased

amount of tungsten oxide in their sensitive coatings. As a result, response intensity towards hydrogen and ethanol was clearly increased, which confirms our assumption. These results can be found in the Supporting Information.

4. Oxygen partial pressure dependence

In view of better understanding the sensing mechanisms of lamellar and nanowire tungsten oxide sensors, a study was conducted on the evolution of the baseline resistance of the sensors at different oxygen partial pressures. Such a study enables identifying the type of oxygen surface species and understanding the nature of oxygen species involved in the chemical reactions, which play a critical role in the identification of the sensing mechanisms towards reducing species such as hydrogen or ethanol in nanowire and lamellar tungsten oxide. It could be assumed that differences in surface oxygen species can explain the different behavior observed experimentally in this preliminary work. This study was conducted at an operating temperature of 300ºC. This temperature was chosen because it maximizes the response of nanowire based sensors and also results in clear behavioral differences between nanowire and lamellar tungsten oxide sensors (see Figures 4 and 5). In previous works, it has been reported that for tungsten oxide operated at 300 ºC, the oxygen surface species playing a role in the chemical reactions are O^- and O^{2-}, which depend directly at the temperature in which the material is operating. The equilibrium equations for the formation of these oxygen surface species can be expressed as follows:

$$O_2 + 2e^- \rightleftharpoons 2O^- \quad \text{eq. 2}$$

$$(K_1 P_{O2})^{1/2}[e]_s = [O^-] \quad \text{eq. 3}$$

$$O_2 + 4e^- \rightleftharpoons 2O^{2-} \quad \text{eq. 4}$$

$$(K_2 P_{O2})^{1/2}[e]_s = [O^{2-}] \quad \text{eq. 5}$$

Furthermore, a quantitative relationship between the electrical resistance of a tungsten oxide sensor and the oxygen partial pressure (P_{O_2}) has been established. [15] [21] [22] Such a relationship is expressed by equation 6.

$$\frac{R}{R_0} = \frac{1}{2}\left(c + \frac{3}{a} * K_1^{1/2} * P_{O2}^{1/2}\right) + \{\frac{1}{4}(c + \frac{3}{a} * K_1^{\frac{1}{2}} * P_{O2}^{\frac{1}{2}})^2 + \left(\frac{6N_D}{a} * K_2^{\frac{1}{2}} * P_{O2}^{\frac{1}{2}}\right)\}^{1/2} \text{ eq. 6}$$

In equation 6, R/R_0 is the ratio between the sensor baseline resistance (R) at a given oxygen partial pressure P_{O_2} and the baseline resistance in the absence of oxygen (R_0), i.e., achieved under a N_2 atmosphere. N_D is the donor density or carrier density for the material, a is the crystalline radius, and c is a constant. The values for these parameters, which are specific of the gas sensitive material, its crystallinity and morphology, are reported in Table 1 [18]. K_1 and K_2 are the equilibrium constants for O^- and O^{2-}, respectively. Therefore, by fitting the experimental data to the model described by eq. 6, the values of these two constants can be estimated for the two different morphologies studied. Then, the ratio between the concentration of O^{2-} and O^- species can be obtained. All These values are summarized in Table 2.

Table 1 Values for some of the parameters in eq. 6 for the two different WO_3 morphologies considered.

	WO_3 Nanowires	**Lamellar WO_3**
c	-9	1
a (nm)	25	50
N_D (e/cc)	3.1×10^{-18}	3.1×10^{-18}
R_0 (kΩ)	2.3	38.9

Table 2. Experimental values calculated for the different WO_3 morphologies when sensors were operated at 300 ºC.

	WO_3 Nanowires	**Lamellar WO_3**
K_1 ($nm^2 \cdot atm^{-1}$)	5.8×10^2	1.4×10^8
K_2 ($nm^8 \cdot atm^{-1}$)	3.7×10^{12}	3.8×10^{10}
$[O^{2-}]/[O^-]$	**22.17**	**0.0007**

Figure 6 shows the experimental results about the dependence of R/R_0 on the oxygen partial pressure for nanowire and lamellar tungsten oxide sensors. This

dependence is clearly nonlinear, as the model expressed by eq. 6. Figure 7 further elaborates the experimental results presented in Figure 6 by representing $\boldsymbol{R/R_0}$ as a function of $(P_{O2})^{0.5}$ and $(P_{O2})^{0.25}$. Figure 7 reveals that is $\boldsymbol{R/R_0}$ evolves linearly with the squared root of the oxygen partial pressure for lamellar tungsten oxide sensors only (see the left, lower panel in Fig. 7). This, together with the results shown in Table 2, is indicative that (at 300ºC) for lamellar tungsten oxide there is a clearly dominant oxygen surface species, namely O^-. In fact, the concentration of O^{2-} species is quasi negligible, since it is estimated to be about three orders of magnitude lower than the concentration of O^- species. In contrast, the upper panels in Figure 7 show that for nanowire tungsten oxide, $\boldsymbol{R/R_0}$ does not show a linear behavior with the squared root, nor with the ¼ power of the oxygen partial pressure. This is indicative that at 300ºC, in nanowire tungsten oxide the two types of oxygen species co-exist. The results of the fitting reported in Table 2 show that the concentration of O^{2-} species is about twenty times higher than that of O^- species in nanowire tungsten oxide. The strikingly higher value of the equilibrium constant for O^- ($\boldsymbol{K_1}$) for lamellar tungsten oxide, which is nearly six orders of magnitude higher than that of nanowire tungsten oxide implies that the presence of O^- species is clearly dominant in lamellar tungsten oxide.

The differences in the type of oxygen species could explain the slightly differences observed in gas response between nanowire and lamellar tungsten oxide sensors. It can be assumed that the differences in the nature of oxygen adsorbates arise from the differences in the morphology and defects. Tungsten oxide nanowires are highly crystalline with low number of defects. In nanowires, defects appear mainly at their tips and at nanowire-nanowire junctions [20] Lamellar tungsten oxide consists of rather flat lamellae with uneven shapes and edges where a high number of defects is very likely. Furthermore, the gas diffusion trough the nanowires forest could be occurring at lower pace than the diffusion of the gas on the lamellar surface, reducing the sensor signal measured for a given time. In particular, the decrease in response observed (for hydrogen

and ethanol) when the operating temperature is raised from 250ºC to 300ºC in lamellar WO_3 is possibly due to the disappearance of O^{2-} species.

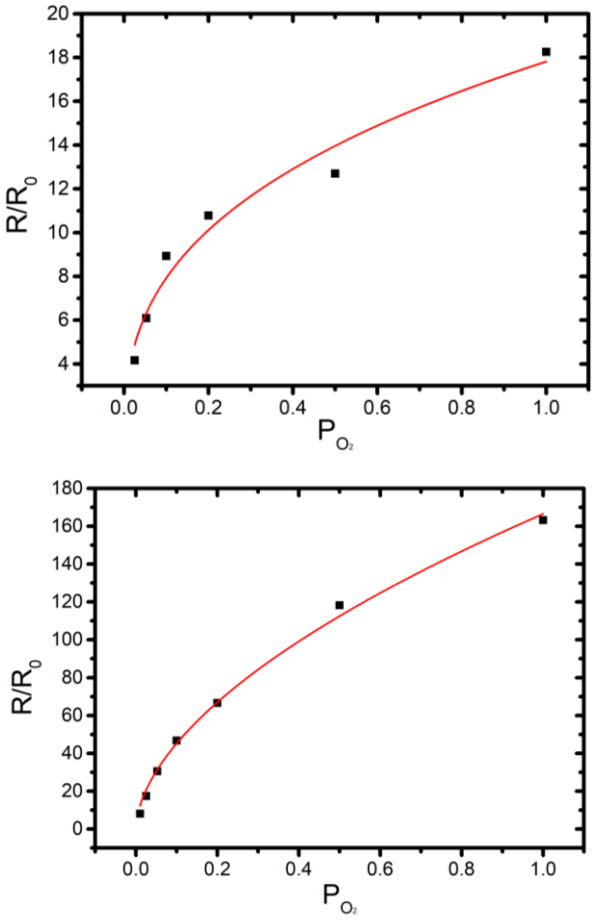

Figure 6. Normalized resistance of nanowire (upper panel) and lamellar (lower panel) tungsten oxide sensors as a function of the oxygen partial pressure (PO_2).

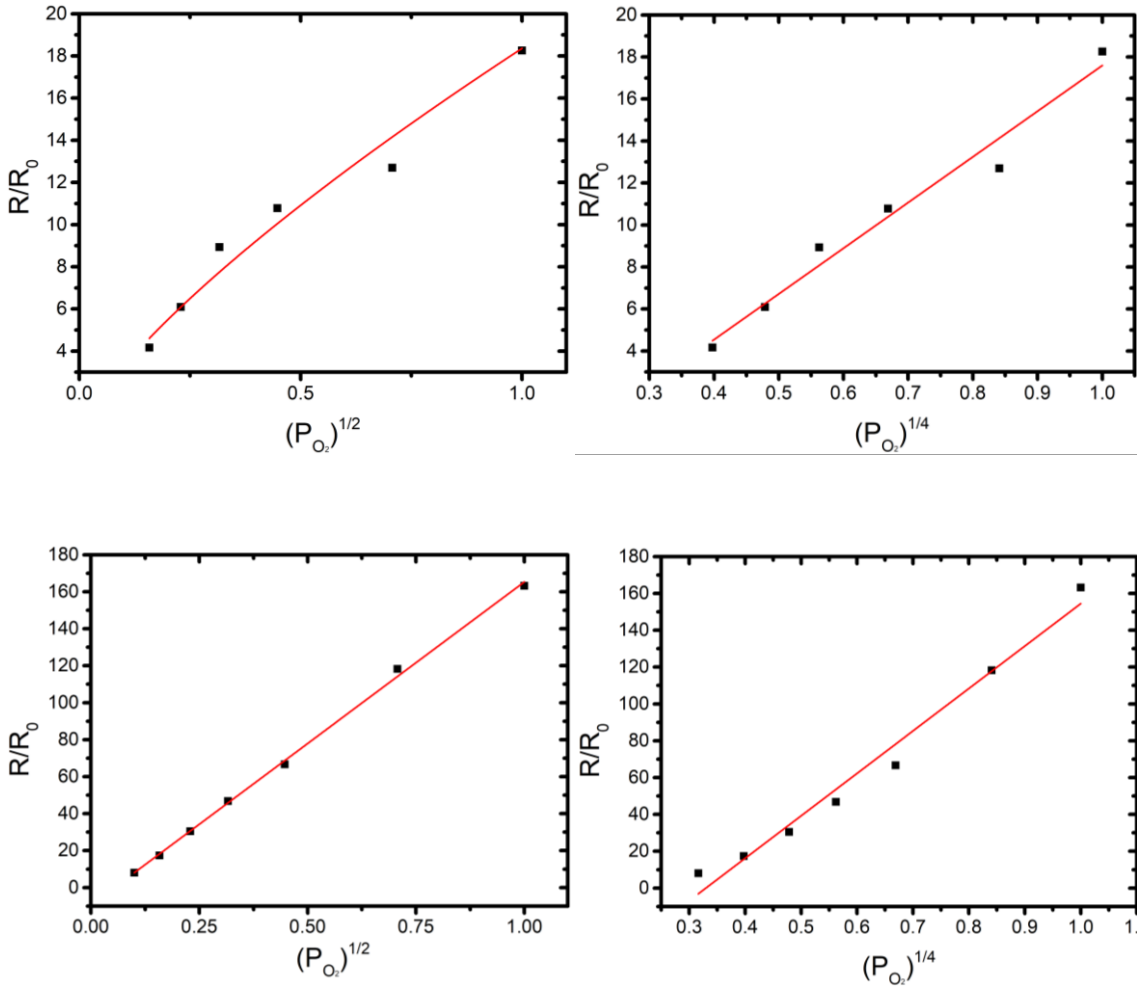

Figure 7. Normalized resistance of nanowire (upper panels) and lamellar (lower panels) WO_3 sensors as a function of two fractional powers of the oxygen partial pressure $(PO_2)^{0.5}$ (left) and $(PO_2)^{0.25}$ (right).

4.1. Suggested mechanism

Due to the study of oxygen partial pressure study performed at 300 ºC, the preliminary results suggest a difference in oxygen species participating in the chemical reactions taking place at the surface of both materials. Figure 8 represents the oxygen species ready to react on the surface, such species keep charges locked on the surface of the material thus narrowing the conductive

channel. When the target gas reacts with those oxygen species electrons are released widening the conduction channel which is translated into an improve of the material conductivity and an overall decrease of the resistance. When we compare at 300 ºC the oxygen species of both materials we could stablish a difference between the WO_3 nanowires which present a mixture of O^- and O^{2-}, as the preliminary results obtained experimentally suggest, having several times more O^{2-} species rather than lamellar WO_3 in which O^- are the main species found to be involved in the reactions occurring at their surface. Taking into consideration both morphologies and the oxygen species, when the target gas reacts with the O^- species in the case of lamellar WO_3, the electron charge that was locked is released to the conduction channel as well as the electrons freed from the chemical reaction occurring, thus widening the conduction channel and decreasing the overall resistance. Meanwhile, nanowires present O^{2-} species, such species lock 2 electron charges thus freeing a higher amount of electrons towards the conduction channel when the reaction with the target gas occurs. Despite the fact of freeing more charges, as the surface area ratio between nanowires and lamellar is higher and also the diffusion of the gas through the nanowires mesh is considerably slower than the surface reaction of lamellar the effect of the oxygen difference is masked.

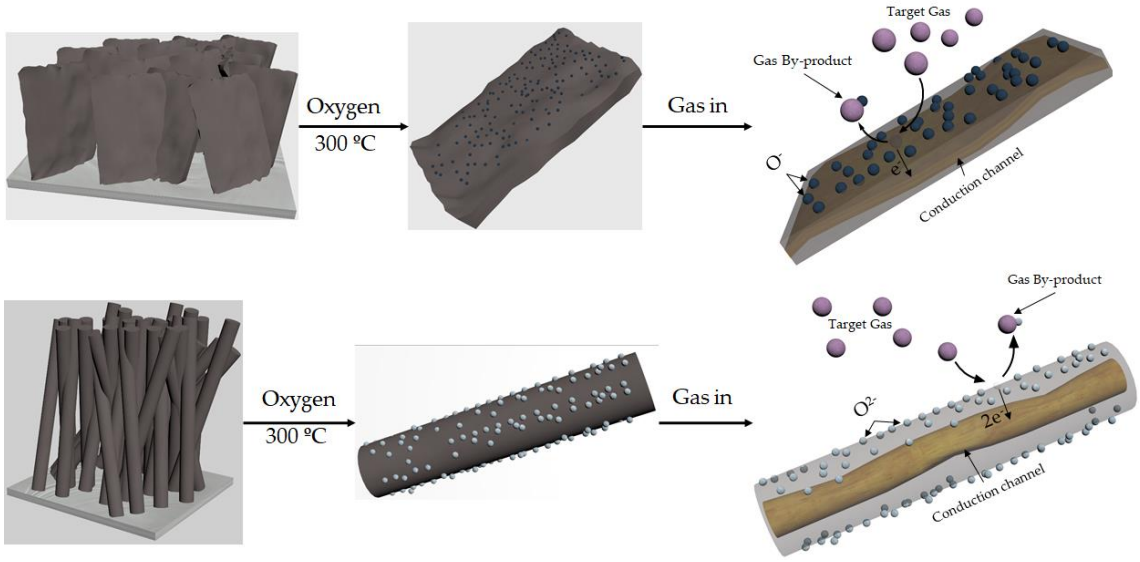

Figure 8. Artistic representation for oxygen species ready to react on both, nanowires and lamellar WO_3, and their interaction with target gas operating at 300 ºC.

5. Conclusions

Tungsten trioxide nanowires and lamellar nanoparticles have been successfully synthetized through two different chemical approaches. Both materials have exhibited responsiveness towards hydrogen and ethanol. Furthermore, due to the differences found in the optimal sensing temperatures, a preliminary oxygen partial pressure dependence study was carried out, revealing a potential difference in the oxygen surface species participating in the sensing mechanism at 300 ºC for the two different materials. From the calculations of both the absorption-desorption constants K1 and K2 and the curve fittings of the resistance materials dependence towards the different oxygen partial pressures, the preliminary results suggested that the oxygen species present in the material at 300 ºC are different depending on the morphology and the synthesis route. Tungsten trioxide nanowires exhibit a mixture of O^{2-} and O^- oxygen types playing both a key role reacting with the target gas with an equilibrium ruled mainly by K_2, meanwhile lamellar WO_3 nanoparticles have mainly O^- oxygen species present in the surface with an equilibrium ruled by K_1. Nevertheless, the differences found in this preliminary work should be assessed with further experimentation with a wider range of samples as well as a wider range of partial oxygen pressure measurements in order to improve the experimental fittings for the constants K1 and K2, which are directly linked towards the different oxygen species taking part in the chemical reactions occurring.

Conflicts of interest

There are no conflicts to declare

Acknowledgement

This work was funded in part by MICIN and FEDER via grants no. TEC2015-71663-R, and RTI2018-101580B100, E.N. gratefully acknowledges a doctoral fellowship from MINECO grant no. BES-2016-076582. E.L. acknowledges the support of the Catalan Institution for Research and Advanced Studies via the 2018 Edition of the ICREA Academia Award.

References

[1] "Air Pollution , Climate and Health."

[2] M. Kampa and E. Castanas, "Human health effect of air polution-Enviro Polution-08.pdf," *Environ. Pollut.*, vol. 151, no. 2, pp. 362–367, 2007.

[3] T. Nandy, R. A. Coutu, and C. Ababei, "Carbon monoxide sensing technologies for next-generation cyber-physical systems," *Sensors (Switzerland)*, vol. 18, no. 10, 2018.

[4] B. Szulczyński and J. Gębicki, "Currently Commercially Available Chemical Sensors Employed for Detection of Volatile Organic Compounds in Outdoor and Indoor Air," *Environments*, vol. 4, no. 1, p. 21, 2017.

[5] T. Hübert, L. Boon-Brett, G. Black, and U. Banach, "Hydrogen sensors - A review," *Sensors Actuators, B Chem.*, vol. 157, no. 2, pp. 329–352, 2011.

[6] J. Goldemberg, "Ethanol for a sustainable energy future," *Science (80-.).*, vol. 315, no. 5813, pp. 808–810, 2007.

[7] S. M. Kanan, O. M. El-Kadri, I. A. Abu-Yousef, and M. C. Kanan, "Semiconducting metal oxide based sensors for selective gas pollutant detection," *Sensors*, vol. 9, no. 10, pp. 8158–8196, 2009.

[8] Y. F. Sun *et al.*, "Metal oxide nanostructures and their gas sensing properties: A review," *Sensors*, vol. 12, no. 3, pp. 2610–2631, 2012.

[9] E. Navarrete, C. Bittencourt, P. Umek, D. Cossement, F. Güell, and E. Llobet, "Tungsten trioxide nanowires decorated with iridium oxide nanoparticles as gas sensing material," *J. Alloys Compd.*, vol. 812, 2020.

[10] T. Kida, A. Nishiyama, M. Yuasa, K. Shimanoe, and N. Yamazoe, "Highly sensitive NO2 sensors using lamellar-structured WO3 particles prepared by an acidification method," *Sensors Actuators, B Chem.*, vol. 135, no. 2, pp. 568–574, 2009.

[11] C. Cantalini *et al.*, "Investigation on the O3 sensitivity properties of WO3 thin films prepared by sol-gel, thermal evaporation and r.f. sputtering techniques," *Sensors Actuators, B Chem.*, vol. 64, no. 1–3, pp. 182–188, 2000.

[12] Z. Hua, M. Yuasa, T. Kida, N. Yamazoe, and K. Shimanoe, "H2 sensing mechanism of Pd-loaded WO3 nanoparticle gas sensors," *Chem. Lett.*, vol. 43, no. 9, pp. 1435–1437, 2014.

[13] E. Navarrete, C. Bittencourt, P. Umek, and E. Llobet, "AACVD and gas sensing properties of nickel oxide nanoparticle decorated tungsten oxide nanowires," *J. Mater. Chem. C*, vol. 6, no. 19, 2018.

[14] N. Barsan and U. Weimar, "Conduction model of metal oxide gas sensors," *J. Electroceramics*, vol. 7, no. 3, pp. 143–167, 2001.

[15] N. Yamazoe and K. Shimanoe, "Roles of shape and size of component crystals in semiconductor gas Sensors: I. Response to oxygen," *J. Electrochem. Soc.*, vol. 155, no. 4, pp. 85–92, 2008.

[16] L. F. Zhu, J. C. She, J. Y. Luo, S. Z. Deng, J. Chen, and N. S. Xu, "Study of physical and chemical processes of H2 sensing of pt-coated WO3 nanowire films," *J. Phys. Chem. C*, vol. 114, no. 36, pp. 15504–15509, 2010.

[17] Y. Yu, W. Zeng, and H. Zhang, "Hydrothermal synthesis of assembled WO3·H2O nanoflowers with enhanced gas sensing performance," *Mater. Lett.*, vol. 171, pp. 162–165, 2016.

[18] Y. T. Hsieh, L. W. Chang, C. C. Chang, and H. C. Shih, "Synthesis of WO3 nanorods by thermal CVD at various gas flow rates and substrate temperatures," *Electrochem. Solid-State Lett.*, vol. 14, no. 7, pp. 73–75, 2011.

[19] Y. S. Shim *et al.*, "Highly sensitive and selective H2 and NO2 gas sensors based on surface-decorated WO3 nanoigloos," *Sensors Actuators, B Chem.*,

vol. 198, no. 2, pp. 294–301, 2014.

[20] È. Navarrete *et al.*, "WO<inf>3</inf> nanowires loaded with cobalt oxide nanoparticles, deposited by a two-step AACVD for gas sensing applications," *Sensors Actuators, B Chem.*, vol. 298, 2019.

[21] N. Yamazoe and K. Shimanoe, "Roles of shape and size of component crystals in semiconductor gas Sensors: I. Response to oxygen," *J. Electrochem. Soc.*, vol. 155, no. 4, pp. 93–98, 2008.

[22] N. Yamazoe and K. Shimanoe, "Theory of power laws for semiconductor gas sensors," *Sensors Actuators, B Chem.*, vol. 128, no. 2, pp. 566–573, 2008.

Another important aspect to be considered for gas sensing are the dynamics of sensor response. Response and recovery times are usually important parameters to assess the performance of a given material towards gas sensing. In addition, baseline stability is also an important feature for SMOxs. It is widely known that all metal oxide gas sensors suffer from long term baseline drift when operating. The drift in the baseline can be attributed to different factors but the main factor responsible for the drift experienced is the modification of the material surface. The surface is constantly exposed to external chemicals that react with the oxygen adsorbed and then the resulting by-products could get irreversibly attached (chemisorbed) onto the surface contributing to irreversible changes of sensor resistance. For example, when NO_2 reacts at the surface of In_2O_3 octahedra, the by-products of the reaction are found to remain at the surface in the form of nitrites [31]. In addition, also the modification of the material morphology is responsible for such a drift. Such modifications usually occur when sensing aggressive gases such as H_2S, which may heavily alter the material surface on the long term or, for instance, the use of high operation temperatures that leads to induced annealing and ion migrations.

SMOxs are typically operated at a given temperature as said before and the kinetics of the chemical reactions occurring when gases interact with the material surface are responsible for the variations on sensor resistance as well as the response time. Such response time usually could be slow due to the chemical reaction dynamics free-will, so it is mandatory to find a solution to cope with both a baseline stabilization as well as improving the material response time. The solution reported in this thesis is the introduction of the Constant Surface Potential Control. When operating the sensors under boundary conditions constraining the surface potential to a constant value through temperature modulations, the overall number of free variables in the system is decreased and a better control is obtained. Under this new approach, what can be correlated

with gas concentration are no longer the changes in the surface potential due to the chemical interactions, but the temperature modulation average applied to the sensing layer to maintain its surface potential constant. Working under a Second Order Sigma-Delta Control drastically improves the response time. Additionally, via applying such control, there is the possibility of stabilizing the baseline to minimize sensor drift, as the heating and cooling loops during the sensor measurement processes confine the electrical resistance at a given value. This was a collaborative research between URV and UPC groups. While URV provided the gas sensitive materials and devices, the UPC group performed the closed loop operation.

2.1.3. Using a Second Order Sigma-Delta Control to Improve the Performance of Metal-Oxide Gas Sensors

sensors

MDPI

Article

Using a Second Order Sigma-Delta Control to Improve the Performance of Metal-Oxide Gas Sensors

Lukasz Kowalski [1], Joan Pons-Nin [1], Eric Navarrete [2], Eduard Llobet [2] and Manuel Domínguez-Pumar [1,*]

[1] Micro and Nano Technologies Group, Electronic Engineering Department, Universitat Politècnica de Catalunya—BarcelonaTech, 08034 Barcelona, Spain; lukasz.kowalski@upc.edu (L.K.); joan.pons@upc.edu (J.P.-N.)
[2] MINOS-EMaS Group, Electronic Engineering Department, Universitat Rovira i Virgili, 43003 Tarragona, Spain; eric.navarrete@urv.cat (E.N.); eduard.llobet@urv.cat (E.L.)
* Correspondence: manuel.dominguez@upc.edu; Tel.: +34-93-401-5679

Received: 31 January 2018; Accepted: 19 February 2018; Published: 23 February 2018

Abstract: Controls of surface potential have been proposed to accelerate the time response of MOX gas sensors. These controls use temperature modulations and a feedback loop based on first-order sigma-delta modulators to keep constant the surface potential. Changes in the surrounding gases, therefore, must be compensated by average temperature produced by the control loop, which is the new output signal. The purpose of this paper is to present a second order sigma-delta control of the surface potential for gas sensors. With this new control strategy, it is possible to obtain a second order zero of the quantization noise in the output signal. This provides a less noisy control of the surface potential, while at the same time some undesired effects of first order modulators, such as the presence of plateaus, are avoided. Experiments proving these performance improvements are presented using a gas sensor made of tungsten oxide nanowires. Plateau avoidance and second order noise shaping is shown with ethanol measurements.

Keywords: sigma-delta modulation; metal-oxide sensors; gas sensors; electrochemical impedance

1. Introduction

Interest in metal-oxide (MOX) gas sensors has grown significantly during the recent years. Different materials, such as SnO_2, WO_3, or ZnO, and specific fabrication techniques have been developed to form the sensing layers of such sensors, often structured as nanoneedles, nanotubes, nanorods, etc. The high surface-to-volume ratios of these nanostructures allow high levels of interaction with the environment, thus providing high sensitivities. Good stability, reduced cost, low power consumption, and compatibility with semiconductor fabrication processes are other advantages of this type of sensors [1–5]. All this makes them excellent candidates in applications such as detection of hazardous gases, pollution observation, or detection of gas leaks [6–8].

The mode of operation of the MOX gas sensors usually consists of monitoring the conductivity of the sensing layer. Since this layer is a semiconductor, its conductance strongly depends not only on the temperature but also on the chemical reactions involved in the gas adsorption and ionization processes [9]. Moreover, the conductivity of the sensor layer can be seen as the result of two simultaneous competing mechanisms that have different time scales. The first mechanism is due to the temperature applied, which produces redistribution in the energies of the charge carriers and causes fast changes in the conductivity of the layer; the second mechanism consists in changes in the chemical reaction rates with the gas species, which generate slow changes in the conductivity of the sensing layer. MOX sensors are usually operated in open-loop at constant-high temperature, of 100 °C

and above, depending on the specific materials of the sensing layer. To reach and maintain constant operating temperature, heaters are usually embedded in the sensors.

However, the performance of MOX-based gas sensors becomes limited by their slow time response to changes in gas concentration and, in some cases, by unwanted long term drifts. As a first step towards studying these issues, dynamic models of the sensors have been proposed [10,11], and it is widely accepted that nonlinear models must be used to describe the evolution with time of the chemical reactions in the layer. As a consequence, complex digital-processing tools, such as neural networks [12], probabilistic state estimation [13], reservoir computing [14], and support vector machines [15] are used to improve sensor performance. Temperature modulations have also been used in works reported in the literature with MOX gas sensors to reduce measurement uncertainty [13], to improve feature extraction [16–19], or to reduce power consumption [20,21]. Additionally, single walled carbon nanotubes have been used in conjunction with MOX modulated in temperature to reduce power consumption [22].

A new approach for smart operation of MOX gas sensors has been proposed recently by the authors [23]. There, a closed-loop technique, inspired in first order sigma-delta modulation, is applied to enforce a sliding mode control on the state variables of the sensor [24]. In particular, the feedback loop produces the temperature modulations necessary to operate the sensor under constant surface potential. In this case, the output of the sensor is the average temperature applied to the sensing layer. This strategy allows the time dynamics of the system to be changed: since the control variable (the surface potential) is constant, the excursion of one or several state variables is reduced and the time response of the system no longer depends on its own free (and slow) dynamics, but on the marginal dynamics obtained within the control surface. This way, fast time responses with a MOX gas sensor have been demonstrated [23].

However, some known issues of first-order sigma-delta modulators can limit the effectiveness of the technique proposed in [23]. One is the presence of a Devil's Staircase fractal, a typical effect when leaky integrators are used [25]; a fractal plateau is in practice a "dead zone" that cannot be observed or controlled, thus hindering the possibility of having a good control in certain cases. Another issue is poor quantization noise shaping, which can pose a problem for retrieving real-time information about the sensing layer. According to this, this paper introduces a new second-order sigma-delta strategy to control the chemical resistance of MOX gas sensors. This method improves the one previously proposed, providing second order quantization noise shaping, smoother sensor responses, and allows for the avoidance of the plateaus observed in the first-order approach. The feasibility and the features of the new method are demonstrated experimentally through extensive comparisons of both control methods in gas sensing applications with tungsten oxide nanowires.

2. Materials and Methods

2.1. First and Second Order Sigma-Delta Loops for Gas Sensing

As it has been mentioned in the Introduction, the typical operation of chemical gas sensors based in semiconductor metallic oxide (MOX) layers consists in keeping such sensing layers at constant temperature and monitor changes in its resistivity. Under this approach, the time response of the sensor is completely determined by the dynamics of the surface adsorption and ionization reactions, which can be generally very slow.

In order to improve the time response of the sensors, the control proposed in [23] operates the sensor under a new condition: Constant Surface Potential Operation. This is done by implementing a sliding mode controller [26] using the scheme of a first order sigma-delta modulator [24]. Sliding mode controllers confine the dynamics of the dynamical system to a predetermined control surface. By doing this, the dynamics of the whole system can be completely changed under some conditions. This control can be performed using the sigma-delta approach, in which the topology of these analog-to-digital

converters is used to obtain the desired sliding motion on the control surface. In our case, then the control surface is constant Surface Potential.

Now, the conductivity of the chemical sensing layer follows this general expression [23]:

$$G = G_0(T) \exp\left(-\frac{qV_s}{kT}\right), \quad (1)$$

in which $G_0(T)$ is a factor depending on temperature, T, q is the electron-elementary charge, V_s is the surface potential, and k is the Boltzmann constant. From this expression it is clear that in order to keep V_s constant, the conductivity of the sensing layer must be kept constant and measured at constant temperature.

The control proposed in [23] is shown in Figure 1a. It achieved the constant SP operation by applying an adequate sequence of temperature waveforms to the sensor. These waveforms, called BIT0 and BIT1, can be seen in Figure 1b. By periodically sampling the conductivity of the sensing layer, at the end of each sampling period, it is possible to monitor changes in Vs, since both waveforms end with the same temperature value T_{high}. The control is designed to apply, for the following sampling period $[nT_s, (n+1)T_s)]$, a BIT1 waveform if $G[nT_s] > G_{target}$ or a BIT0 if $G[nT_s] < G_{target}$. This way, it is possible to change the average temperature in the sensor, while making decisions based on the conductivity of the sensing layer, measured at the same temperature.

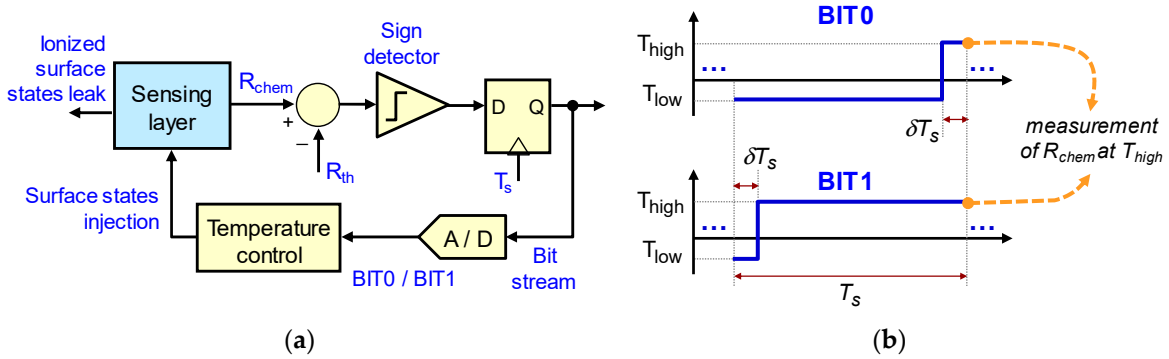

Figure 1. (**a**) First-order sigma-delta modulator topology to control the chemical resistance of the metal-oxide sensing layer. At each sampling time T_S, depending on whether the chemical resistance R_{chem}, measured at the reference temperature T_{high}, is below (or above) the desired value R_{th}, a BIT1 (or BIT0) temperature waveform is applied to the sensor during the next sampling period; (**b**) parameters of the BIT0 and BIT1 waveforms.

This control replicates the usual circuit topology of a 1st order sigma-delta modulator. The sensing layer can be seen as a reservoir of ionized surface states, which can be negatively or positively charged. In an oxidizing atmosphere, increasing (decreasing) the average temperature will increase (decrease) the adsorption of gas molecules that, when ionized, will increase (decrease) the total negative ionized surface states. In this case, the average temperature generated by the control must be able to keep constant the interchange of ionized surface states with the surrounding atmosphere by applying a suitable sequence of temperature waveforms. Changes in the atmosphere are therefore compensated for by changes in the average temperature generated by the control.

As it has been mentioned before, this paper presents a second order sigma-delta topology for surface potential control in MOX-based gas sensors. By adding an integrator to the control loop, it is possible to obtain a second order zero in the quantization noise at zero frequency [27]. This integrator is implemented numerically, see Figure 2, and good values of the α parameter are empirically found. Besides the improvement in the quantization noise, second order modulators do not present plateaus in the case of leaky integrators. On the other hand, they can become unstable under some conditions [27].

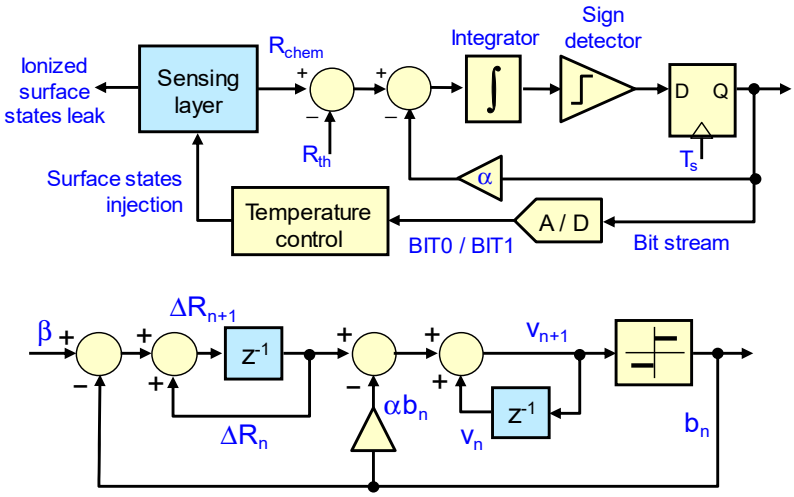

Figure 2. Block diagram (**Top**) and equivalent sampled circuit (**Bottom**) of the 2nd order sigma-delta topology designed to control the chemical resistance of the MOX sensing layer.

Figure 2 presents the qualitative translation of the 2nd order control loop to the standard sigma-delta idealized representation. Parameter β represents the continuous leak of ionized surface states, ΔR_n represents the differences at the sampling times nT_s between the resistivity of the layer and the target value set $R_{chem}(nT_s) - R_{th}$, and v_n are the values of the second numerical integrator. The functions of the first integrator are performed by the sensing layer itself, seen as a reservoir of ionized surface states. The purpose of the control circuit is therefore to cancel the value at the output of this second integrator by applying an adequate sequence of BIT0/BIT1 waveforms to the sensor.

2.2. Description of the Gas Sensors

2.2.1. Sensing Layer Synthesis

The sensing layers consist of pristine tungsten oxide nanowires directly grown on top of the membranes of a 4-element micro-machined silicon transducer employing an Aerosol Assisted Chemical Vapor Deposition (AACVD) process. Each membrane within the 4-element chip contains $POCl_3$-doped polysilicon heaters (16 Ω/sq, 0.47 µm thickness, and TCR = 6.79 × 10^{-4}/°C) and platinum electrodes (0.2 µm thickness, electrode gap = 100 µm). To electrically insulate the electrodes on top from the heater, 800-nm-thick silicon oxide layers were deposited by Low Pressure Chemical Vapor Deposition (LPCVD). In the AACVD growth of tungsten oxide nanowires, tungsten hexacarbonyl (50 mg, Sigma-Aldrich, Saint Louis, MO, USA, ≥97%) dissolved in a mixture of acetone and methanol (15 mL of acetone and 5 mL of methanol, Sigma-Aldrich, ≥99.6%) was used. The solution was kept in a flask and placed in an ultrasonic humidifier.

The resulting aerosol was transported to the reactor by a 500 mL/min flow of nitrogen. The substrates were placed inside the reactor and the whole system was heated up to 370 °C (see Figure 3). A mask was placed on top of the substrate to protect the contact pads of the heater and electrodes, leaving exposed the electrode areas only. The reactor outlet was vented directly into the extraction system of a fume cupboard. The deposition time ranged between 30 to 40 min, until all of the precursor had passed through the reactor. At the end of the growth, the flow of nitrogen was interrupted, and the substrates were kept in the reactor at 370 °C for another 60 min. This helps the removal of the precursor residues and further oxidizes nanowires. Films have a pale-yellow color, which indicates that a close to stoichiometry tungsten oxide is obtained. Finally, the sensors were wire-bonded to standard TO-8 packages.

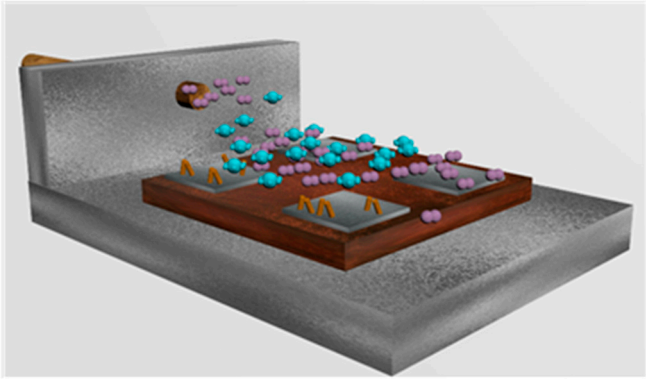

Figure 3. Artistic view inside of the hot wall reactor during the AACVD process. A nitrogen flow carries the aerosol droplets of solvent containing the organic precursor.

2.2.2. Material Characterization

The morphology and crystalline phase of the gas sensitive films were analyzed using an Environmental Scanning Electron Microscope (ESEM) and X-Ray Diffraction (XRD). Figure 4a shows typical XRD results for the films grown. These results indicate that a slightly oxygen-defective tungsten oxide is obtained, which corresponds to $WO_{2.72}$ nanowires that have a P2/m belonging to the monoclinic system, in accordance to the JPCD card no. 73-2177. Figure 4b shows ESEM results. The lower magnification micrograph shows one membrane with interdigitated electrodes and, in light grey, the sensing layer composed of WO_3 nanowires. The higher magnification micrograph shows a closer view of the nanowire film.

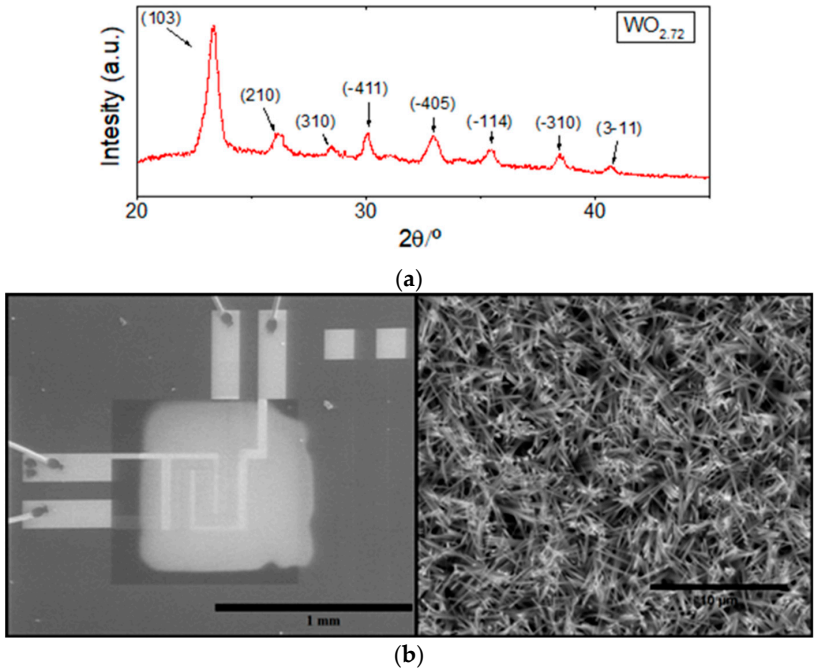

Figure 4. (**a**) XRD results obtained for typical tungsten oxide nanowire films. Tungsten oxide is single crystalline and belongs to the monoclinic phase; (**b**) low magnification micrograph showing the AACVD grown film on top of the electrode area of a sensor within the 4-element transducer (**Left**). Higher magnification micrograph showing the typical microstructure of the AACVD grown tungsten nanowire films (**Right**).

2.3. Experimental Setup

The experiments designed for this work aimed to compare the effectiveness and performance of the first and second order control methods discussed above; they included measurements with the tungsten oxide nanowire sensors that are presented, both in controlled atmospheres of synthetic air and of synthetic air with small concentrations of ethanol.

Accordingly, the measurement setup described in Figure 5 has been used. The sensor was placed inside a gas chamber. To set different target gas concentrations, a calibrated ethanol cylinder with air as balance gas was used. This was further diluted by employing a cylinder of dry air and a computer-controlled mass flow meter system. The total flow into the chamber was kept constant at 100 mL/min throughout the experiments. The dead volume within the gas chamber was 4 mL. The periodical measurements of the chemical resistance of the sensing layer and the application of the BIT0 and BIT1 temperature waveforms are implemented using a standard FPGA-based National Instruments PXIe-1073 acquisition equipment controlled from the same computer. The experimental data was post-processed using standard MatLab software.

In each experiment reported in this paper, a previous characterization of the sensor layer with the temperature was performed to choose the appropriate values of the BIT0 and BIT1 and of the control parameters: T_{high}, T_{low}, R_{th}, etc. Concretely, the same procedure as in [23] was used, e.g., see details in Figure 6 and related text of this reference.

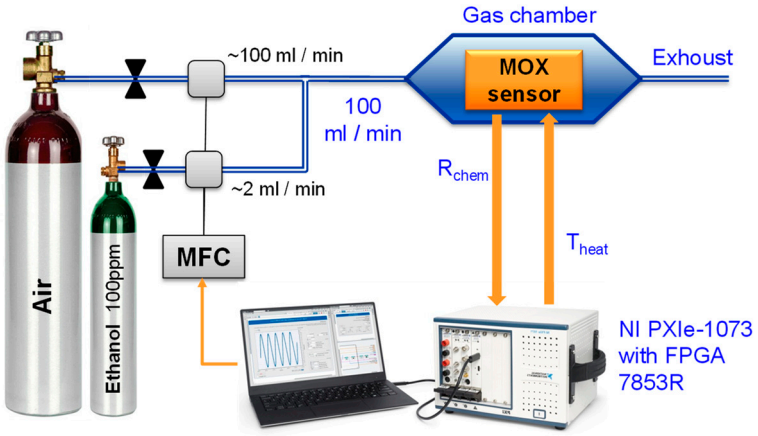

Figure 5. Description of the experimental setup.

3. Results and Discussion

In accordance with the theoretical expectations discussed above, the objective of this section is to demonstrate experimentally that, under certain conditions, the 1st order loop control may suffer from "plateau-related" phenomena, which in practice leads to transient losses of control of the chemical resistance, and that using a 2nd order loop allows for the avoidance this problem. This section also intends to verify the improvement of the quantization noise shaping when higher-order loops are used. All these effects are further investigated using an ethanol gas-sensing application as reference.

3.1. Experiment Set 1—Chemical Resistance Control with First and Second Order Sigma-Delta Loops

The first set of experiments aimed to investigate the feasibility of both control loops to obtain a sequence of arbitrary values of chemical resistance. Accordingly, in the experiment reported in Figure 6a, the sensor was placed in synthetic air, and the 1st order control loop (see Figure 1) with a sampling time T_S = 1 s was used to set seven different values of R_{th} in 15 min intervals. It is seen in Figure 6a that the 1st order control works mostly fine, since the target chemical resistances are successfully achieved and the bit stream average, or the temperature average applied to the sensor, tends to stabilize after each R_{th} step. For example, at t = 10 min R_{chem} must be increased, and therefore

the control loop applies more BIT1s (T_{high} dominant), increasing the oxygen adsorption in the sensing layer, until $R_{chem} = R_{th}$ is reached; from then on, the bit stream/temperature average slowly tends to the value necessary to keep R_{chem} constant. However, two "plateau events", labeled as I and II in Figure 6a, are also observed. During these events, the average temperature injected into the sensor becomes locked to 240 °C (which corresponds to the same average number of BIT1s and BIT0s, i.e., $b_n = 0.5$ or the temperature value $(T_{high} + T_{low})/2$), and, in practice, the system behaves as in open-loop, thus losing control on the value of R_{chem}.

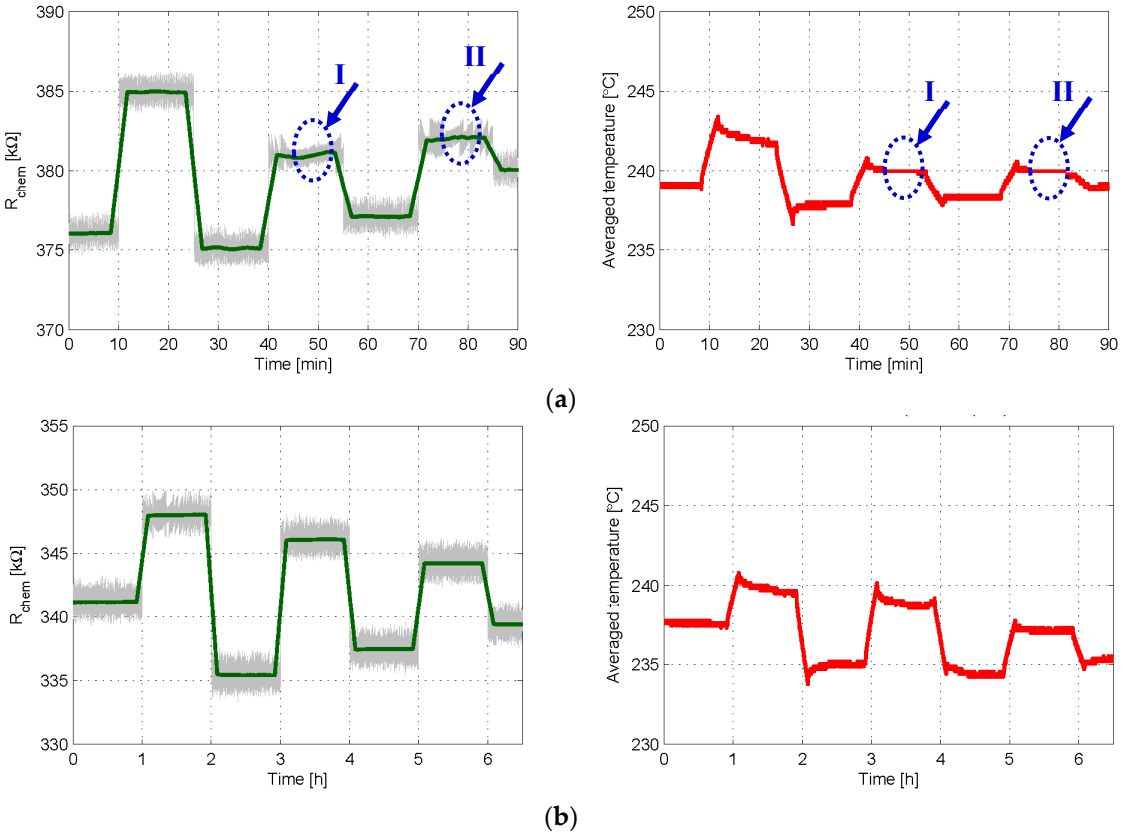

Figure 6. Experimental results in which 1st and 2nd order controls are used to obtain a given sequence of target chemical resistances R_{th}. (**a**) Time evolution of the chemical resistance (**Left**) and of the average temperature provided by the 1st order loop (**Right**); R_{th} was set to 376, 385, 375, 381, 377, 382, and 380 kΩ in 15 min intervals; T_{high} = 280 °C, T_{low} = 200 °C, δ = 25%, and T_S = 1 s; (**b**) same results when 2nd order control was applied to set R_{chem} to 341, 348, 335, 346, 337, 344, and 339 kΩ in 60 min intervals; T_{high} = 280 °C, T_{low} = 200 °C, α = 2 kΩ, δ = 20% and T_S = 2 s. In left plots, the grey lines are the raw signals at the sampling frequency, while the green one is the moving average obtained with 200 samples.

On the other hand, Figure 6b shows the result of an experiment similar to that of Figure 6a, using the 2nd order controller (see Figure 2) with T_S = 2 s. The curves of Figure 6b demonstrate that the 2nd order loop allows for the successful achievement of all target values of R_{chem} and that plateau-related events are no longer seen, even using a slower sampling rate.

In the experiment reported in Figure 7, the sensor is again placed in synthetic air and both control loops are used to obtain the same sequence of target chemical resistances, with T_S = 0.5 s. According to sigma-delta theory, in 1st order loops with leaky integrators the presence of plateaus becomes less evident for increasing values of the sampling frequency $1/T_S$ [25]. Note that, although the sampling frequency doubles that of Figure 6a, plateau-related events are still observed with 1st order control, see Figure 7a. On the other hand, no plateaus are seen in the 2nd order case, see Figure 7b.

This means that even by doubling the sampling frequency of the experiment in Figure 6, first order controls may still produce plateaus (Figure 7). However, using the 2nd order control method allows for the avoidance of these plateau-related events, thereby improving the performance of the sensor as a system.

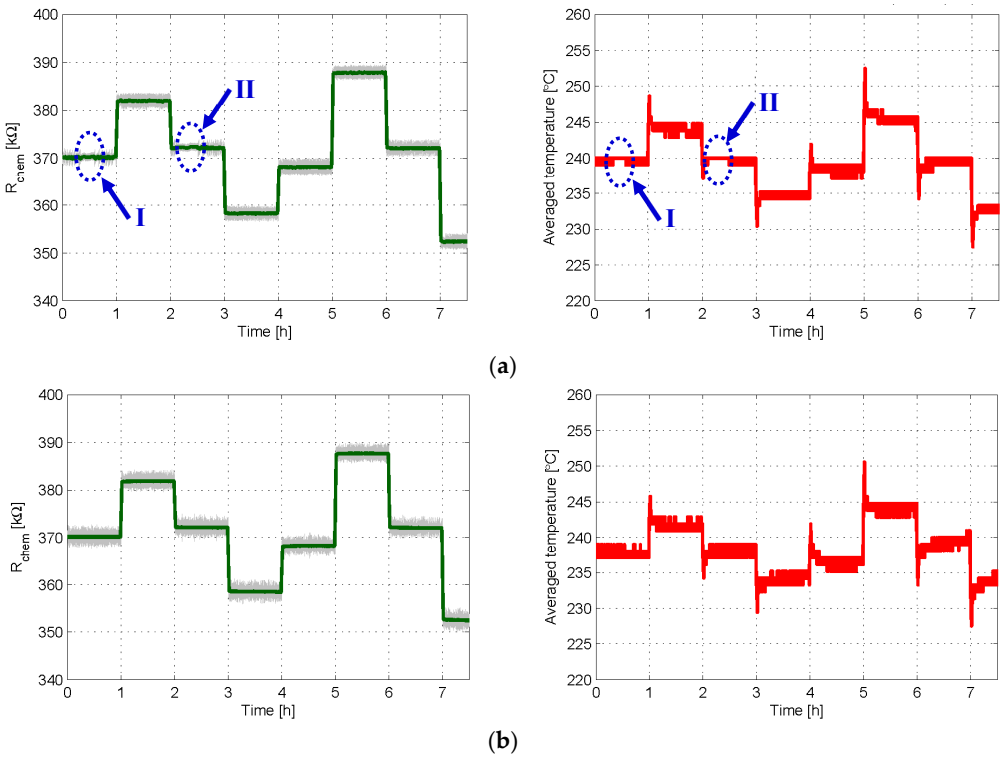

Figure 7. Experimental results in which 1st and 2nd order controls are used to obtain the same sequence of target chemical resistances R_{th} = 370, 382, 372, 358, 368, 388, 372, and 352 kΩ in 60 min intervals. In both cases, T_{high} = 280 °C, T_{low} = 200 °C, δ = 20%, and T_S = 2 s; α = 2 kΩ in the 2nd order case; (**a**) time evolution of the chemical resistance (**Left**) and of the average temperature provided by the 1st order loop (**Right**); (**b**) same results when 2nd order control was applied. In left plots, the grey lines are the raw signals at the sampling frequency, while the green one is the moving average obtained with 50 samples.

The last experiment reported in this section aims to compare the behavior of the two control loops in terms of quantization noise in the output bit stream. As it has been said before, a first order sigma-delta topology produces a zero of first order. This means a slope of approximately 20 dB/decade in the quantization noise near zero frequency. With the second order control, a slope of approximately 40 dB/decade should be obtained. To observe this effect, the sensor was placed again in synthetic air and each type of control with T_S = 0.5 s was applied for 3 h to set a target chemical resistance of 340 kΩ. As shown in Figure 8a,b, constant chemical resistance and constant average temperature are successfully achieved with both control methods.

The spectral power density corresponding to 16,384 samples of stabilized bit stream was calculated in each case. Figure 8c compares the obtained spectra. It is seen there how the presence of the additional integrator in the 2nd order controller produces noticeable differences. With the 2nd order control, the response at low frequencies becomes improved, and the quantization noise is rolled out of the band of interest with a slope of 40 dB/decade, being this figure 20 dB/decade in the 1st order case. Let us note that these results strongly resemble those obtained in other works, in which 1st and 2nd order sigma-delta loops are applied to thermal modulators for flow sensing applications [28] and to control dielectric charging in electrostatic MEMS [29] and CMOS capacitors [30].

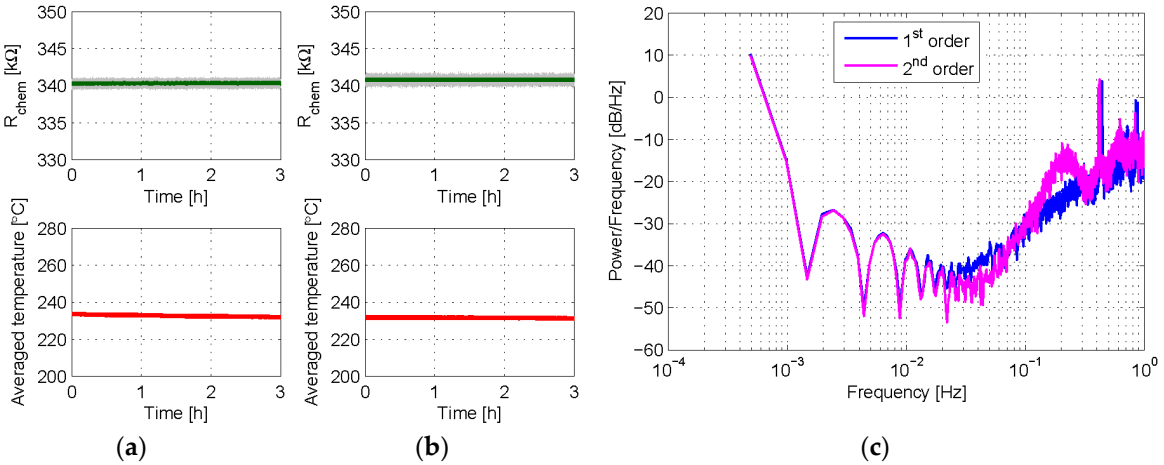

Figure 8. Experimental results in which 1st and 2nd order controls are applied to set R_{chem} to 340 kΩ for 3 h. In both cases, T_{high} = 290 °C, T_{low} = 200 °C, δ = 25%, and T_S = 0.5 s; α = 1.4 kΩ in the 2nd order case. (**a**) Chemical resistance of the sensing layer (**Top**) and averaged temperature provided by the 1st order loop (**Bottom**); (**b**) same results as provided by the 2nd order loop; (**c**) power spectrum densities after 16,384 samples of the bit streams, obtained with standard P-Welch MatLab estimation. In top (**a**,**b**) plots, the grey lines are the raw signals at the sampling frequency, while the green one is the moving average obtained with 200 samples.

3.2. Experiment Set 2—Gas Sensing with First and Second Order Sigma-Delta Loops

This section investigates the improvements introduced by the 2nd order control in the performance of the sensor. To this effect, different ethanol concentrations have been applied, while a control loop is being used to set the condition "constant chemical resistance R_{chem} measured at constant temperature T_{high}" in the sensing layer.

In the first two experiments, the sensor was initially under synthetic air for 20 min, then a concentration of 125 ppb of ethanol was applied for another 20 min, and finally synthetic air was applied again for 20 min. Either a 1st or a 2nd order control loop was applied on each experiment, with the same BIT parameters, to set the chemical resistance to 300 kΩ. A result comparison of these experiments is available in Figure 9. It is seen there that, with both controls, the ethanol step produces a positive step of the average temperature applied, which is the sensor output. This is consistent with the fact that ethanol is a reducing gas, but its mixing with air makes the environment remain still oxidant, and therefore it is necessary to increase the ratio of BIT1s (T_{high} dominant or temperature increase) to keep almost constant the chemical resistance. These results indicate that the sensor response under both controls is rather similar and, in particular, that the 2nd order controller does not reduce its speed, a key feature of this kind of sensors. Additionally, due to the improved response against quantization noise provided by the integrator, a noticeably smoother control of the chemical resistance is achieved when using the 2nd order loop.

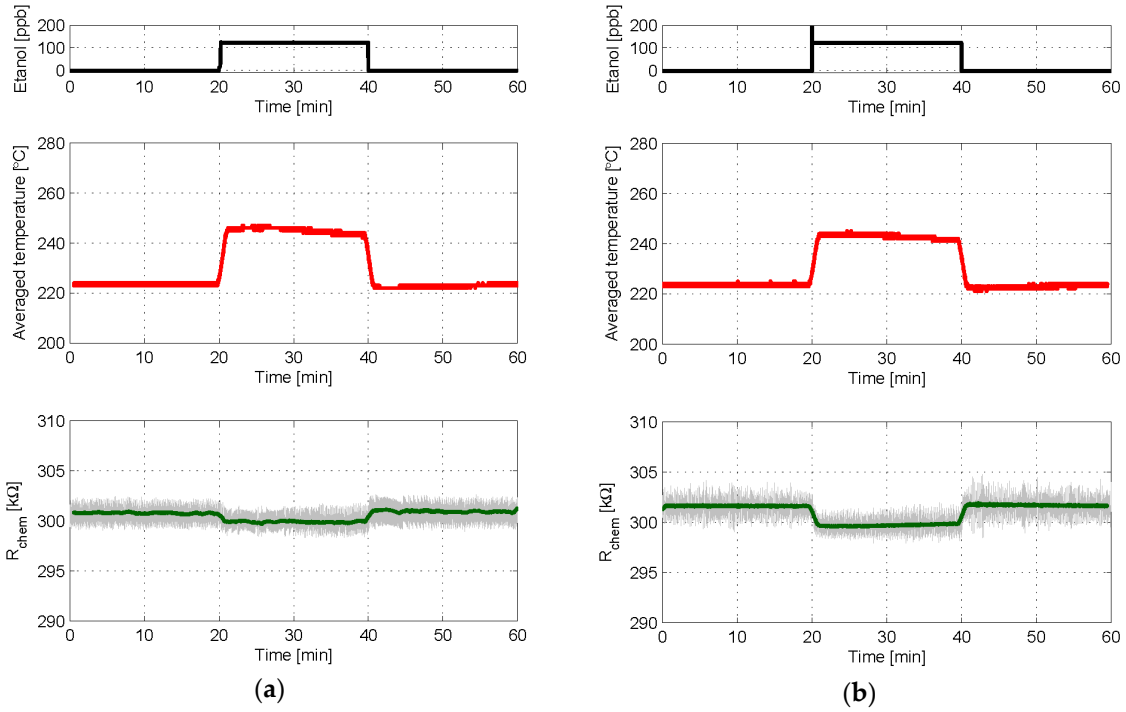

Figure 9. Experimental results in which either a 1st or a 2nd order control loop is used to set R_{chem} to 300 kΩ while a step of ethanol concentration was applied to the sensor. T_{high} = 290 °C, T_{low} = 160 °C, δ = 25%, and T_S = 1 s in both cases; α = 3 kΩ in the 2nd order case. (**a**) Evolution with time of the ethanol concentration (**Top**), the average temperature provided by the control loop (**Middle**), and the chemical resistance (**Bottom**) when 1st order control was used; (**b**) same results for 2nd order control. In bottom plots the grey lines are the raw signals at the sampling frequency, while the green one is the moving average obtained with 60 samples.

The last two experiments reported consist in applying a sequence of small-increasing steps of ethanol concentration to the sensor, while either a 1st or a 2nd order control loop is configured to set the chemical resistance of the sensing layer to 155 kΩ. Each step increases the ethanol concentration in 25 ppb and lasts for 10 min. The same set of BIT0 and BIT1 parameters was used in both controls, and the results are shown in Figure 10. The unwanted effect of a plateau is clearly seen in the case of the 1st order control, Figure 10a. Specifically, the sensor becomes locked to a constant average temperature (again corresponding to $(T_{high} + T_{low})/2$, b_n = 0.5), thus producing the same output value, for two different steps of gas concentration.

This insensitivity to changes in gas concentration does not exist in the case of the 2nd order control, which provides an output behavior that clearly follows the increasing-step shape of ethanol concentration applied, see Figure 10b. We can conclude that the 2nd order controller ensures a 1-to-1 relationship between gas excitation and sensor response.

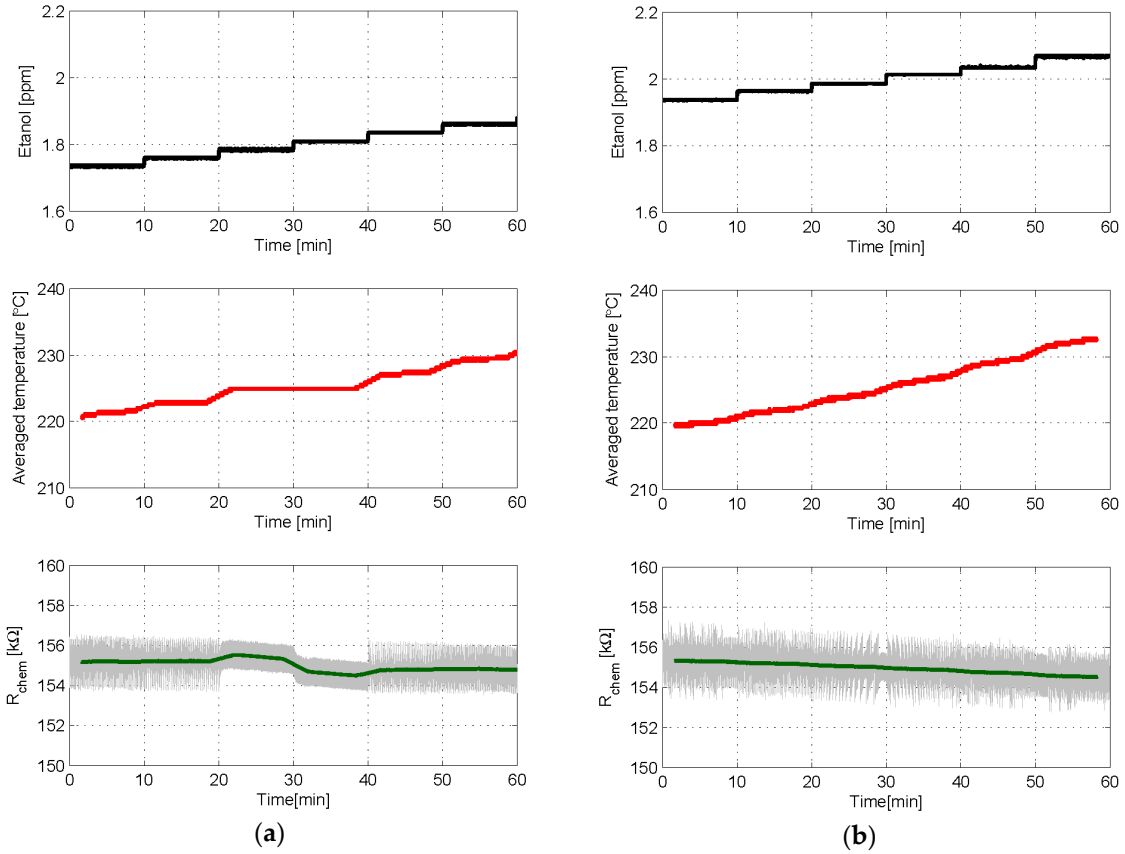

Figure 10. Experimental results in which either a 1st or a 2nd order control loop has been used to set R_{chem} to 155 kΩ when a sequence of small steps of ethanol of 25 ppb concentration was applied to the sensor in 10 min intervals. T_{high} = 290 °C, T_{low} = 160 °C, δ = 25%, and T_S = 1 s in both cases; α = 3 kΩ in the 2nd order case. (**a**) Evolution with time of the ethanol concentration (**Top**), the averaged bit stream provided by the control loop (**Middle**), and the chemical resistance (**Bottom**) when 1st order control was used; (**b**) same results when 2nd order control was used. In bottom plots the grey lines are the raw signals at the sampling frequency, while the green one is the moving average obtained with 200 samples.

4. Conclusions

A new second-order delta sigma method that is used to control the chemical resistance of MOX-based gas sensors has been introduced. This method improves one previously proposed by the authors, providing second-order quantization noise shaping, providing smoother responses, and allowing for the avoidance of the unwanted plateau-related phenomena that are typical of first-order strategies. The feasibility and the features of the new method have been demonstrated experimentally. Future work will be oriented towards optimizing controller parameters and architecture, improving the electronic readout of the sensor, and optimizing the sensor physical structure.

Acknowledgments: This work was supported, including the funds for covering the costs to publish in open access, by the Spanish Ministry MINECO under Project grant no. ESP2016-79612-C3-2R. The development of the gas sensor was funded in part by MINECO and FEDER via grant no. TEC2015-71663-R and by AGAUR under grant 2017SGR 418. E.N. gratefully acknowledges a doctoral fellowship from MINECO grant no. BES-2016-076582. E.L. is supported by the Catalan institution for Research and Advanced Studies via the 2012 Edition of the ICREA Academia Award.

Author Contributions: M.D.-P., L.K. and J.P.-N. conceived and designed the experiments; L.K. performed the experiments; M.D.-P., J.P.-N. and L.K. analyzed the data; E.N. and E.L. fabricated the sensors; J.P.-N., M.D.-P. and E.L. wrote the paper.

Conflicts of Interest: The authors declare no conflict of interest. The founding sponsors had no role in the design of the study; in the collection, analyses, or interpretation of data; in the writing of the manuscript; or in the decision to publish the results.

References

1. Sberveglieri, G. Recent developments in semiconducting thin-film gas sensors. *Sens. Actuators B Chem.* **1995**, *23*, 103–109. [CrossRef]
2. Korotcenkov, G. Metal oxides for solid-state gas sensors: What determines our choice? *Mater. Sci. Eng. B* **2007**, *139*, 1–23. [CrossRef]
3. Cheng, J.; Wang, J.; Li, Q.; Liu, H.; Li, Y. A review of recent developments in tin dioxide composites for gas sensing application. *J. Ind. Eng. Chem.* **2016**, *44*, 1–22. [CrossRef]
4. Wang, C.; Yin, L.; Zhang, L.; Xiang, D.; Gao, R. Metal oxide gas sensors: Sensitivity and influencing factors. *Sensors* **2010**, *10*, 2088–2106. [CrossRef] [PubMed]
5. Korotcenkov, G. Gas response control through structural and chemical modification of metal oxide films: State of the art and approaches. *Sens. Actuators B Chem.* **2005**, *107*, 209–232. [CrossRef]
6. Capone, S.; Zuppa, M.; Presicce, D.S.; Francioso, L.; Casino, F.; Siciliano, P. Metal oxide gas sensor array for the detection of diesel fuel in engine oil. *Sens. Actuators B Chem.* **2008**, *131*, 125–133. [CrossRef]
7. Fleischer, M. Advances in application potential of adsorptive-type solid state gas sensors: High-temperature semiconducting oxides and ambient temperature GasFET devices. *Meas. Sci. Technol.* **2008**, *19*, 042001. [CrossRef]
8. Ng, K.T.; Boussaid, F.; Bermak, A. A CMOS single-chip gas recognition circuit for metal oxide gas sensor arrays. *IEEE Trans. Circ. Syst. I* **2011**, *58*, 1569–1580. [CrossRef]
9. Vuong, N.M.; Kim, D. Surface gas sensing kinetics of a WO_3 nanowire sensor: Part 1—Oxidizing gases. *Sens. Actuators B Chem.* **2015**, *220*, 932–941. [CrossRef]
10. Llobet, E.; Brezmes, J.; Vilanova, X.; Sueiras, J.E.; Correig, X. Qualitative and quantitative analysis of volatile organic compounds using transient and steady-state responses of a thick-film tin oxide gas sensor array. *Sens. Actuators B Chem.* **1997**, *41*, 13–21. [CrossRef]
11. Di Natale, C.; Marco, S.; Davide, F.; D'Amico, A. Sensor-array calibration time reduction by dynamic modelling. *Sens. Actuators B Chem.* **1995**, *25*, 578–583. [CrossRef]
12. Pardo, A.; Marco, S.; Samitier, J. Nonlinear inverse dynamic models of gas sensing systems based on chemical sensor arrays for quantitative measurements. *IEEE Trans. Instrum. Meas.* **1998**, *47*, 644–651. [CrossRef]
13. Gosangi, R.; Gutiérrez-Osuna, R. Active temperature modulation of metal-oxide sensors for quantitative analysis of gas mixtures. *Sens. Actuators B Chem.* **2013**, *185*, 201–210. [CrossRef]
14. Fonollosa, J.; Sheik, S.; Huerta, R.; Marco, S. Reservoir computing compensates slow response of chemo sensor arrays exposed to fast varying gas concentrations in continuous monitoring. *Sens. Actuators B Chem.* **2015**, *215*, 618–629. [CrossRef]
15. De Vito, S.; Castaldo, A.; Loffredo, F.; Massera, E.; Polichetti, T.; Nasti, I.; Vacca, P.; Quercia, L.; Di Francia, G. Gas concentration estimation in ternary mixtures with room temperature operating sensor array using tapped delay architectures. *Sens. Actuators B Chem.* **2007**, *124*, 309–316. [CrossRef]
16. Vergara, A.; Martinelli, E.; Llobet, E.; D'Amico, A.; Di Natale, C. Optimized feature extraction for temperature-modulated gas sensors. *J. Sens.* **2009**, *2009*, 716316. [CrossRef]
17. Vergara, A.; Llobet, E.; Brezmes, J.; Vilanova, X.; Ivanov, P.; Gràcia, I.; Cané, C.; Correig, X. Optimized temperature modulation of micro-hotplate gas sensors through pseudo-random binary sequences. *IEEE Sens. J.* **2005**, *5*, 1369–1378. [CrossRef]
18. Sudarmaji, A.; Kitagawa, A. Application of temperature modulation-SDP on MOS gas sensors: Capturing soil gaseous profile for discrimination of soil under different nutrient addition. *J. Sens.* **2016**, *2016*, 1035902. [CrossRef]
19. Fonollosa, J.; Fernández, L.; Huerta, R.; Gutiérrez-Gálvez, A.; Marco, S. Temperature optimization of metal oxide sensor arrays using mutual information. *Sens. Actuators B Chem.* **2013**, *187*, 331–339. [CrossRef]
20. Burgués, J.; Marco, S. Low power operation of temperature-modulated Metal Oxide Semiconductor gas sensors. *Sensors* **2018**, *18*, 339. [CrossRef] [PubMed]

21. Ghafarinia, V.; Maleki, M. Self-regulated bias circuits for efficient adjustment of the operating temperature of chemoresistive gas sensors. *IEEE Sens. J.* **2017**, *17*, 2984–2991. [CrossRef]
22. Magno, M.; Jelicic, V.; Chikkadi, K.; Roman, C.; Hierold, C.; Bilas, V.; Benini, L. Low-power gas sensing using single walled Carbon nano tubes in wearable devices. *IEEE Sens. J.* **2016**, *16*, 8329–8337. [CrossRef]
23. Domínguez-Pumar, M.; Kowalski, L.; Calavia, R.; Llobet, E. Smart control of chemical gas sensors for the reduction of their time response. *Sens. Actuators B Chem.* **2016**, *229*, 1–6. [CrossRef]
24. Sira-Ramirez, H. *Sliding Mode Control: The Delta-Sigma Modulation Approach*; Birkhäuser: Basel, Switzerland, 2015; ISBN 978-3-319-17256-9.
25. Gorreta, S.; Pons-Nin, J.; Blokhina, E.; Feely, O.; Domínguez-Pumar, M. Delta-sigma control of dielectric charge for contactless capacitive MEMS. *J. Microelectromech. Syst.* **2014**, *23*, 829–841. [CrossRef]
26. Utkin, V.I. *Sliding Modes in Control and Optimization*; Springer: Heidelberg, Germany, 1992; ISBN 978-3-642-84381-5.
27. Norsworthy, S.R.; Schreier, R.; Temes, G.C. *Delta-Sigma Data Converters: Theory, Design, and Simulation*; Wiley-IEEE Press: Piscataway, NJ, USA, 1996; ISBN 978-0-7803-1045-2.
28. Makinwa, K.; Huijsing, J. A 2nd order thermal sigma-delta modulator for flow sensing. In Proceedings of the IEEE Sensors, Irvine, CA, USA, 30 October–3 November 2005. [CrossRef]
29. Gorreta, S.; Pons-Nin, J.; Blokhina, E.; Domínguez-Pumar, M. A Second Order Delta-Sigma Control of Dielectric Charge for Contactless Capacitive MEMS. *J. Microelectromech. Syst.* **2015**, *24*, 259–261. [CrossRef]
30. Bheesayagari, C.; Gorreta, S.; Pons-Nin, J.; Domínguez-Pumar, M. Second order sigma-delta control of charge trapping for MOS capacitors. *J. Microelecron. Reliab.* **2017**, *76–77*, 635–639. [CrossRef]

2.2. Semiconductor Metal Oxide growth and synthesis.

Metal oxides present different morphologies depending on the route employed to synthetize them. For instance, we could categorize the structure obtained in 0-D (nanoparticles), 1-D (nanowires, nanotubes), 2-D (Nanofilms) and 3-D (nanomesh). Despite being the same material and belonging to the same crystallographic spatial group, different morphologies could show distinct responses towards gases and also present significant alterations in their sensitivity and selectivity [30]. Metal oxide nanostructures could be crafted from different approaches gathered mainly in physical or chemical synthesis routes; these two synthesis approaches are based on either top down or bottom up techniques.

A physical synthetic route typically used to grow oxide nanostructures from a bottom-up approach is the vapor phase depositions (VPD). VPD consists of evaporating a precursor from the desired metallic oxide at high temperature and then carry the growth units formed in the gas phase towards a cooler substrate were the deposition/growth occurs. By employing such methodology, indium oxide (In_2O_3) nano-octahedra were synthetized inside a tubular furnace at 1000 ºC and a controlled inert atmosphere. The resulting octahedra obtained presented an average range size around 200 nm with a narrow size distribution [31]. Nevertheless, those conditions required high inputs of energy as well as a high control in the growth conditions (i. e. gas pressure, heating and cooling ramps). Therefore, in this thesis a simplified chemical approach was performed to obtain such structures. Starting from indium chloride as a precursor, the material was grown through an annealing process at 500 ºC under an oxidizing atmosphere. Such conditions are enough to reproduce the shape, morphology and crystalline phase of those obtained through VPS except for the resulting nanostructures present a much wide size distribution, from tenth of nanometers

up to some micrometers. On a further step, those nanostructures were manually stenciled on top of a flexible Kapton substrate to analyze their behavior when exposed to different gas concentrations in a controlled atmosphere.

2.2.1 Flexible Gas Sensors Employing Octahedral Indium Oxide Films

sensors

MDPI

Article

Flexible Gas Sensors Employing Octahedral Indium Oxide Films

Miriam Alvarado, Èric Navarrete, Alfonso Romero, José Luis Ramírez and Eduard Llobet *

MINOS-EMaS, Universitat Rovira i Virgili, Avda. Països Catalans, 26, 43007 Tarragona, Spain; miriam.alvarado@urv.cat (M.A.); eric.navarrete@urv.cat (È.N.); alfonso.romero@urv.cat (A.R.); joseluis.ramirez@urv.cat (J.L.R.)
* Correspondence: eduard.llobet@urv.cat

Received: 6 February 2018; Accepted: 27 March 2018; Published: 28 March 2018

Abstract: Indium oxide octahedral nanopowders were obtained from an ionic precursor compound after an oxidation process conducted under a low-oxygen atmosphere. This method was found to produce contamination-free indium oxide nanomaterial with very similar morphological and crystalline properties to the one produced by vapor-phase transport, but at significantly lower temperatures and higher yield. The as-synthesized indium oxide was mixed to an organic vehicle and microdrop deposited to form a film bridging the interdigitated silver electrodes patterned on top of a flexible, polyimide (Kapton®), substrate. The gas sensing properties of the flexible chemoresistors towards ammonia vapors, hydrogen, and nitrogen dioxide were investigated. It was found that these sensors were remarkably sensitive to nitrogen dioxide at a low operating temperature of 150 °C. These results are consistent with the performance of vapor-phase transport synthesized indium oxide octahedra sensors on rigid, ceramic substrates. Therefore, the results presented here pave the way for the mass production of inexpensive gas sensors onto flexible substrates via additive manufacturing.

Keywords: indium oxide; flexible substrates; gas sensors; nitrogen dioxide

1. Introduction

Indium oxide (In_2O_3) belongs to the family of metal oxides, such as tin oxide, tungsten trioxide, and zinc oxide, which have been reported as promising materials for gas sensing applications. In_2O_3 is an n-type semiconductor with a band gap of 2.7 eV. This material has been widely studied for gas sensing. Different shapes and material morphologies (nanofilms, nanowires, nanorods, octahedra) [1,2] have been already tested. Nanostructured In_2O_3 has been reported mainly for detecting nitrogen dioxide (NO_2), hydrogen (H_2), and ammonia (NH_3) [3–5]. Sol-gel, chemical vapor deposition, laser ablation, or vapor phase deposition have been employed to grow In_2O_3 nanomaterials. Recently, we reported the growth of In_2O_3 nano-octahedra employing vapor-phase transport (VPT) at 1000 °C under an Ar atmosphere [6]. In_2O_3 octahedra obtained by VPT possess sharp edges and vertices, and were found to be highly sensitive and remarkably selective to NO_2 when operated at moderate temperatures (i.e., 130 °C). However this growth method has the disadvantage—besides the high operating temperatures needed—of producing small quantities of the nanomaterial. Here we report an alternative process for obtaining high quantities of octahedral In_2O_3 at a significantly lower temperature of 500 °C. Additionally, this growth method is conducted without using any solvent or carrier gases.

Chemoresistive metal oxide sensors require simple transducers, basically consisting of an inert substrate comprising a pair of interdigitated electrodes onto which the gas sensitive film is deposited or printed and a heating resistor. Ideally, substrates are required to withstand high temperatures, show chemical inertness, and behave as barriers to gases and moisture [7]. Ceramic (e.g., alumina) and

silicon based substrates have been, by far, the most used substrates for developing gas sensors [8,9]. However, the replacement of these conventional, rigid materials by flexible ones would bring some advantages such as lowering cost and heat losses and widening the field of applications to wearable or disposable sensing systems. Nowadays, flexible devices—such as photodetectors, light emitting diodes, pressure sensors, artificial electronic skin, and biomedical sensors—have been fabricated [10]. The most used materials for implementing flexible substrates have been plastic films, metal foils, and fibrous materials (including paper and textiles) [11]. Among polymers, polyimide (PI), polyether ether ketone (PEEK), polyethylene terephthalate (PET), and polyethylene naphthalate (PEN) have been determined to be suitable materials for the fabrication of flexible substrates and devices [12,13]. Moreover, all these polymeric materials have been often selected to fabricate flexible devices for sensing applications [14]. Among the above mentioned polymeric materials, PI exhibits temperature resistance—essential for metal-oxide deposition and sensor operation—and allows to print circuit tracks. Gas sensors on PI foil have been reported and results were comparable to those obtained on standard silicon micromachined transducers [7]. Additionally, it has been demonstrated that In_2O_3 gas sensors on polymeric transducers behave similarly to those employing ceramic transducers [15]. In this paper, a low-cost, off-the-shelf adhesive polyimide has been used as a substrate to fabricate metal oxide sensors, employing In_2O_3 as a sensing layer. These new results represent a significant advancement in comparison with our previously reported prototypes, as far as fabrication and deposition processes have been improved. Namely, the material synthesis process has been optimized and the coating procedure has been readapted in order to increase reproducibility. Those sensors were tested for three different gases. These devices bring good openings for developing flexible sensors employing metal oxides in the near future.

2. Materials and Methods

2.1. Material Preparation

In_2O_3 was obtained by employing commercially-available indium chloride ($InCl_3$, Sigma Aldrich, St. Louis, MO, USA, 99.8% purity) via an oxidation process. This precursor is stored at 0 °C because indium chloride starts sublimating at 5 °C. In a typical synthesis experiment, 40 mg of $InCl_3$ were weighed and put in a ceramic crucible, which was immediately placed inside a muffle. Three tests were carried out to determine the best oxidizing temperature, setting the muffle at 400 °C, 500 °C, and 600 °C. Generally, in the oxidation process, a current of pure, dry air is used to increase the availability of oxygen species [11]. In our experiments, the oxidation process was conducted without employing an air flow in order to obtain a crystal oxide structure under low oxygen concentration. Once the crucible was placed inside the muffle, its temperature was increased progressively at a 5 °C·min^{-1} rate, until it reached the oxidizing temperature (i.e., 400 °C, 500 °C, or 600 °C). Once reached, the oxidation temperature was kept for 120 min. Finally, the material was left inside the muffle to naturally cool down to room temperature. The success in the oxidation process could be checked by the naked eye, given the change in color experienced from white $InCl_3$ to light yellow In_2O_3. Before any further processing, the obtained materials were placed inside an agate mortar and mashed softly until they turned into a homogenous yellowish dust.

2.2. Sensor Fabrication

Transducers comprise two interdigitated (IDE) silver electrodes over a polymeric substrate. The width of the IDE fingers is 300 μm and the electrode gap was 300 μm. The surface of the electrode area was 2.4 × 5.7 mm. As a substrate, a commercially-available, highly-resistant, adhesive-coated polyimide foil (Kapton® 25 μm) was used. For the fabrication of the electrodes, an additional layer of adhesive-coated polyimide was used as a shadow mask. Over the external layer, a finger-shape electrode pattern was cut by a CO_2 laser. Afterwards, the surface was wiped off with a towel moistened with ethanol (ethanol 96% pure, Sigma Aldrich). Using a pair of tweezers, the material belonging to

the pattern was removed, thus obtaining a negative mask. Silver (Ag) ink (DuPont® 5064H, silver conductor, Wilmington, DE, USA) was stenciled with a spatula onto the polyimide. Then, the ink was dried inside an oven for 20 min at 130 °C. Subsequently, the shadow mask was peeled-off obtaining two IDE deposited on the polymeric substrate.

In order to obtain a sensing layer of In_2O_3 octahedra, a microdrop coating technique was employed to coat the electrode area of the transducer. To implement such a technique, 20 mg of nanomaterial were placed inside an Eppendorf and mixed with 0.5 mL of 1,2-propanediol to obtain a suspension. The suspension was agitated to ensure a homogeneous suspension and using a micropipette, 1 µL droplet was deposited on top of the electrode area. Subsequently, the sensor was placed inside an oven at 150 °C to enable solvent evaporation. This process was repeated up to four times for each device, until film resistance ranged between 3 and 6 MΩ at room temperature.

3. Results

3.1. Material Characterization

The morphology—chemical composition and crystalline phase—of the different In_2O_3 materials obtained were characterized using environmental scanning electron microscopy (E-SEM), energy-dispersive X-ray spectroscopy (EDX) and X-ray diffraction (XRD), respectively. An E-SEM (FEI QUANTA600, Hillsboro, OR, USA) coupled to an EDX (Oxford Instruments, Abingdon, UK) were employed to study the structure and composition of materials. Figure 1 summarizes E-SEM results showing the morphologies of the In_2O_3 nanomaterials for the different synthesis temperatures employed.

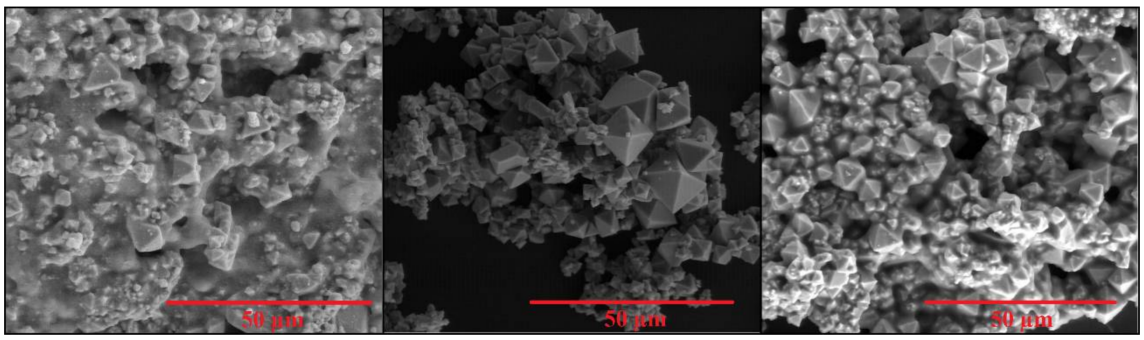

Figure 1. E-SEM micrographs showing the evolution of the morphology of indium oxide materials as a function of the temperature employed during the synthesis. (**Left**), (**middle**), and (**right**) panels correspond to an oxidation step conducted at 400 °C, 500 °C, and 600 °C, respectively.

When the oxidation is conducted at 400 °C the resulting indium oxide contains a few octahedra, however, it mainly consists of particles of irregular shape and amorphous material. In contrast, when the oxidation was conducted at 500 °C, indium oxide appears in the form of octahedra with well-defined surfaces and sharp edges and vertices. At 600 °C even though octahedra are still present, many are fused together and a significant amount of particles re-appear. These studies reveal that when the synthesis is conducted at 500 °C, the octahedral morphology is improved.

EDX results (supporting information) indicate the presence of In, O, and Cl for samples oxidized at 400 °C. In the literature it has been reported the poisoning effect of chlorine ions. Several studies have been conducted to understand the effect of such ions; when there are either on the material surface or included in the metal oxide structure. Chlorine ions can interact with different types of metal oxides in a way that leads to different effects such as their corrosion or breakage, reducing their performance and lifetime [16]. Chlorine contamination is indicative that the precursor has not been fully oxidized and removed by the process conducted at 400 °C. Therefore, in an attempt to eliminate

the Cl surplus, different oxidizing temperatures have been tested. In contrast, for samples oxidized at 500 °C and 600 °C only In and O are detected, indicating that Cl is completely removed or is present at concentrations that are under the limit of detection of the EDX technique.

Considering the morphology and composition results revealed by E-SEM and EDX, the optimal oxidizing temperature was 500 °C. Once the optimal growth temperature is known, a yield study was carried out to determine the efficiency of such a type of growth, 20.5 mg In_2O_3 were obtained employing 50 mg of $InCl_3$ precursor, resulting in an excellent global yield of 65%. Most of these losses occur during the transfer of the material from the ceramic crucible were it is grown to the agate mortar and from there to the Eppendorf where a suspension of indium oxide octahedra is prepared.

Considering the microdrop coating method employed for depositing the gas-sensitive material onto transducers, 20 mg of nanomaterial are enough for producing more than 100 sensors. Additionally, this high-yield synthesis process can be easily scaled up and is simpler to implement than VPT. Unlike VPT, the method employed here is run at 500 °C in a standard muffle under atmospheric conditions, avoiding the use of a tubular quartz furnace under atmospheres of controlled gas flows. Therefore, it represents a good option for the inexpensive, mass production of materials and sensors.

The crystalline phase of samples grown at the optimal temperature of 500 °C was studied by XRD. These results are presented in Figure 2 where the diffraction pattern correlates with the typical cubic structure of In_2O_3 corresponding to space group Ia-3 with an a° = 10.12 Å. The In_2O_3 displays a bixbyite structure belonging to the space group 206 mentioned before. This space group corresponds to a body-centered cubic structure formed by 40 atoms in the primitive cell. Two non-equivalent lattice positions are occupied by indium atoms being surrounded by oxygen in trigonal and octahedral prismatic coordination, which results finally in the octahedral shape of the nanostructures observed by E-SEM.

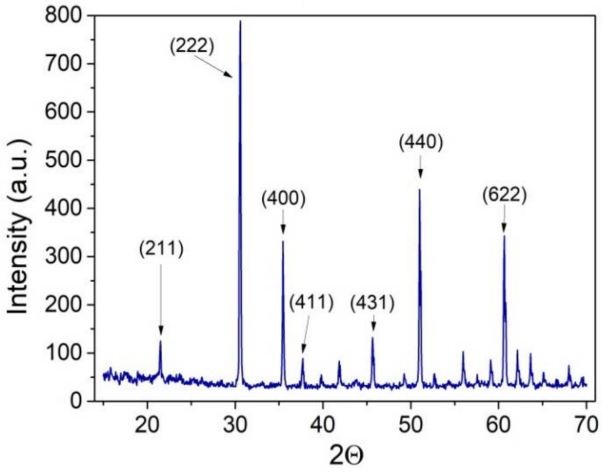

Figure 2. Typical XRD pattern of an In_2O_3 sample synthesized at 500 °C.

All the peaks found in the spectrum correspond to each one of the faces displayed by the material with lower or higher intensity, fitting with the corresponding JCPDS card no. 01-071-2194. The most representative peaks appear labelled in Figure 2. None of the peaks present could be attributed to impurities, confirming the purity of the material synthesized [17]. The results of the XRD analysis for the sample synthesized at 500 °C match those reported previously for In_2O_3 octahedra synthesized at 1000 °C via the VPT method [6], which indicates that the crystalline quality of the samples discussed in this paper is very similar to the one reported before.

Considering these results, chemoresistive gas sensors were produced by depositing films of In_2O_3 synthesized at 500 °C. Figure 3 shows low-magnification E-SEM images of the electrode area of a Kapton transducer before and after being coated with the gas-sensitive film. The microdrop coating

method employed succeeds in completely and homogeneously recovering the electrode area with the gas-sensitive indium oxide film.

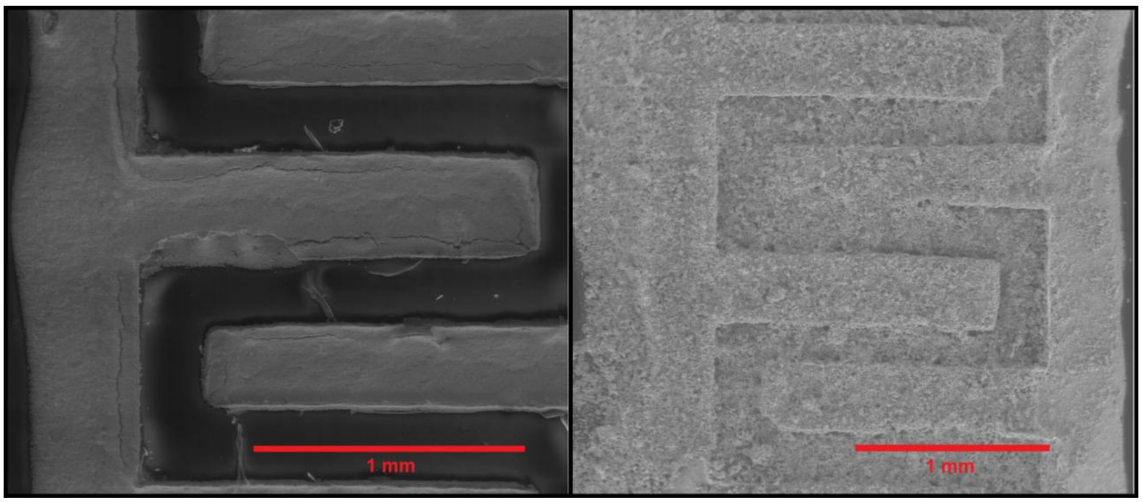

Figure 3. Low-magnification E-SEM images of the electrode area of a chemoresistive sensor employing a Kapton substrate. (**left**) The substrate before coating. (**right**) The same substrate after being coated with a dropped indium oxide gas sensitive film.

3.2. Gas Sensing Results

The sensors were exposed to different concentrations of NO_2, NH_3, and H_2 and tested by means of DC resistance measurements. Different operating temperatures were tested to determine the optimal. Sensing experiments were carried out under dry air conditions. For all measurements, 60 min of synthetic air were employed to clean the sensor surface and stabilize its baseline signal, followed by 30 min pulses of target gas at different concentrations alternated with 30 min pulses of synthetic air to enable the sensors to recover their baseline. All these experiments were conducted with the sensors placed inside a Teflon chamber (14 cm^3) under a constant flow of 100 $mL \cdot min^{-1}$, either of pure, dry air, or of a gas mixture balanced in dry air. Under these conditions, the relative humidity in the test chamber where sensors were housed remained stable at 3% (temperature was 25 °C). In an attempt to determine the optimal operating temperature for the different species measured, sensors were operated at 100 °C, 150 °C, 200 °C and 250 °C. The highest working temperature was set to 250 °C. According to the specifications of the silver ink used to draw the electrodes, it is not recommended to heat the substrates above 250 °C. At higher operating temperatures, electrodes would suffer cracks, oxidation processes, and could even detach from the substrate, which would shorten the sensor lifetime.

Figure 4 shows the typical dynamic evolution of the resistance of a sensor when exposed to successive pulses of increasing concentrations, of the different species tested. For each species, the response displayed was recorded at the optimal operating temperature of the sensor.

In_2O_3 behaves as an n-type semiconductor and sensor resistance decreases for reducing species such as NH_3 or H_2 and increase for oxidizing species like NO_2. Each cycle of increasing concentration pulses is repeated at least two times for each panel in Figure 4. The responses are highly reproducible. Some baseline drift is present that is especially visible for NO_2. This is due to the strong interaction of this oxidizing species with the gas sensitive film—which combined to the relatively low operating temperature of the sensor (i.e., 150 °C)—does not allow for a complete desorption of adsorbed species and baseline recovery during each cleaning phase [18].

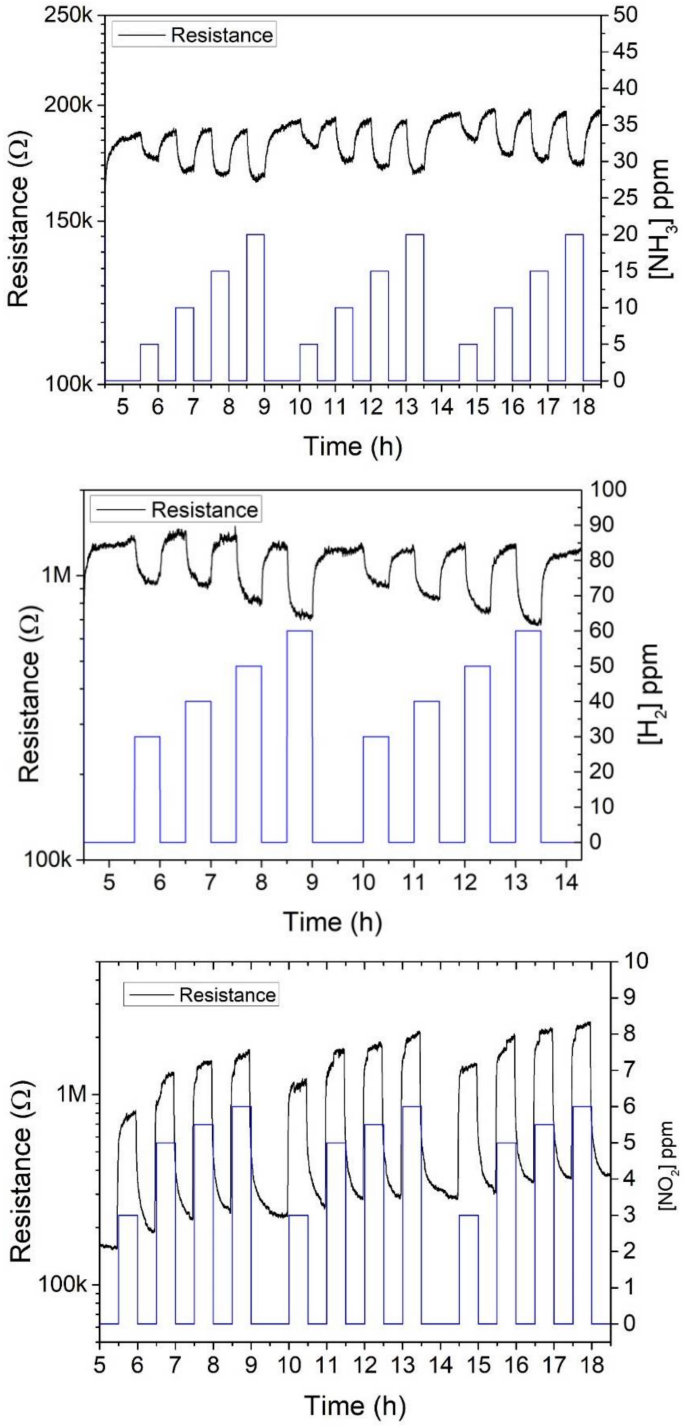

Figure 4. Dynamic evolution of sensor resistance for successive response and recovery pulses of the different species tested. The upper panel corresponds to NH_3 pulses for a sensor operated at 150 °C. The middle panel corresponds to H_2 pulses for a sensor operated at 250 °C. The lower panel corresponds to NO_2 pulses for a sensor operated at 150 °C.

3.2.1. NH_3 Results

Figure 5 (upper panel) shows the effect of the operating temperature on the response to NH_3. The response as a function of temperature curve shows the typical volcano shape for metal oxides [19]. As shown in Figure 5, the response towards NH_3 is maximum when the sensor is operated at 150 °C. Elouali et al. [4] reported an optimum operating temperature of 450 °C to 10 ppm concentration of

NH_3 with a response of 1.76 for In_2O_3 prepared via continuous hydrothermal flow synthesis. In [20] an operating temperature of c.a. 175 °C was reported, with responses of 1.3 and 1.05 for 500 ppm and 100 ppm concentration of NH_3, respectively for In_2O_3 thin films prepared via thermal evaporation. Our sensor showed a response of 1.12 to a 20 ppm pulse of NH_3 comparing favorably with the optimum operating temperature for the sensors mentioned before.

The lower panel in Figure 5 shows the calibration curve for NH_3 when the sensor is operated at 150 °C—i.e., the optimal operating temperature for this species. Measurements present low standard deviation, below 1%, even lower for the higher NH_3 concentrations, which is indicative of high repeatability. The responsiveness towards NH_3 of the indium oxide octahedra sensors is moderated [4,20] and shows a tendency to become saturated for concentrations higher than 30 ppm. When operated at the optimal operating temperature of 150 °C, response and recovery times (t90) for ammonia were 190 and 410 s, respectively.

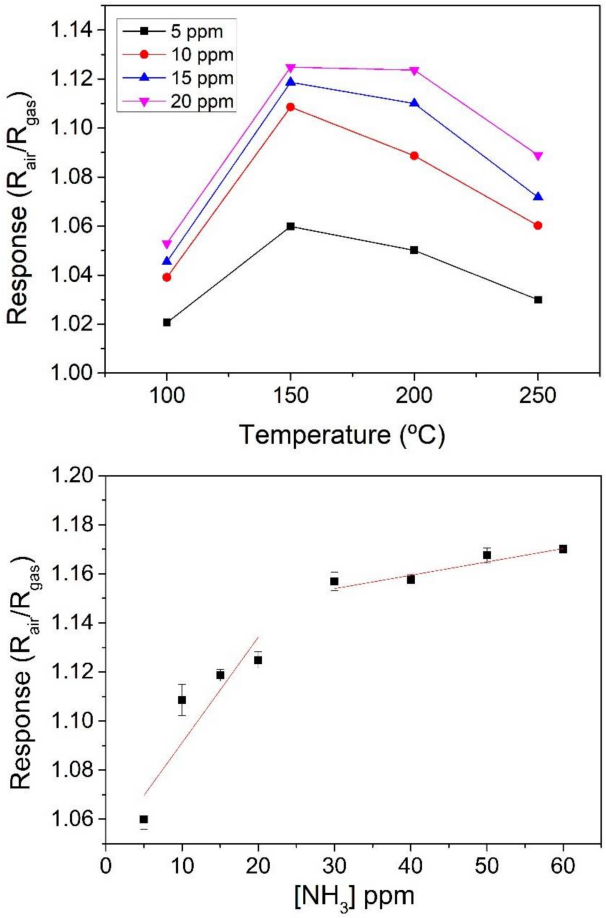

Figure 5. Effect of the operating temperature on the response towards different concentrations of NH_3 (**upper panel**). Calibration curve towards NH_3 for a sensor operated at the optimal working temperature of 150 °C (**lower panel**).

3.2.2. H_2 Results

The sensors fabricated were exposed also to different concentrations of H_2. Following the same approach, in the first place, a temperature study was carried out in order to find the optimal working temperature for this particular gas. The results obtained are shown in the upper panel of Figure 6. The response towards H_2 of the In_2O_3 sensors increased with operating temperature, therefore, the higher responses were obtained at 250 °C. Even though increasing the operating temperature of

the sensors further could lead to even higher responses, the maximum temperature was set to 250 °C in order to prevent the occurrence of electrode damage, as already discussed above.

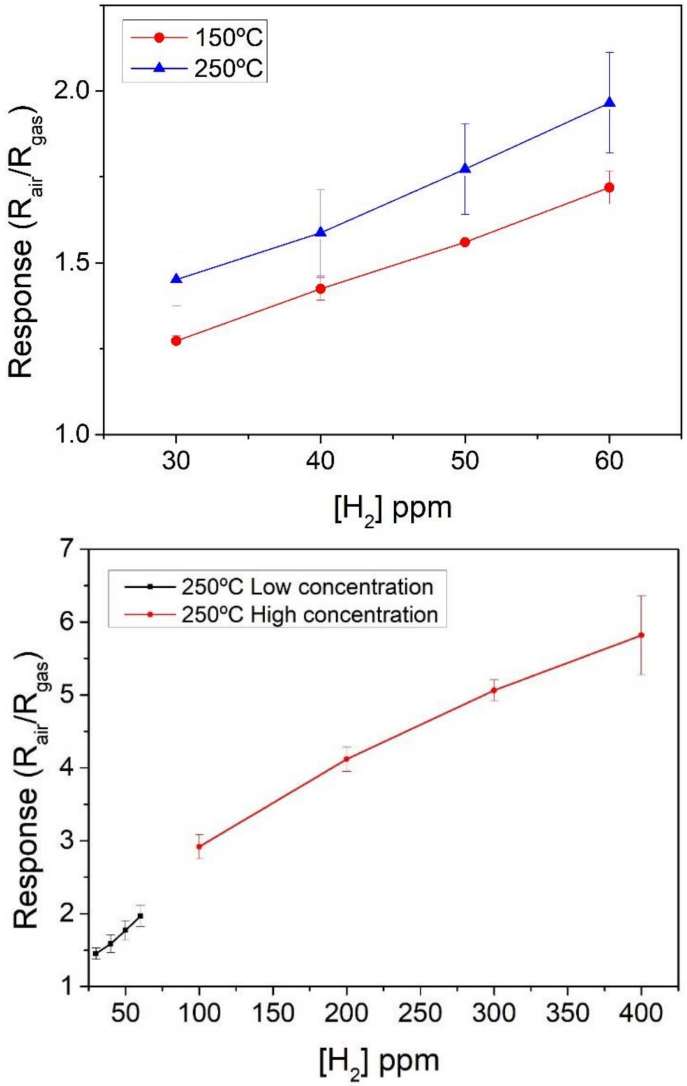

Figure 6. Effect of the operating temperature on the response towards different concentrations of H_2 (**upper panel**). Calibration curve towards hydrogen for a sensor operated at the maximum allowed working temperature of 250 °C, which resulted in the higher responsiveness to hydrogen (**lower panel**).

The standard deviation of H_2 responses when the sensor was operated at 150 °C was lower than 5%. Meanwhile when the sensor was operated at 250 °C, the standard deviation of H_2 responses increased up to 15%. The calibration curve for H_2 shown in the lower panel of Figure 6 indicates that sensor response is quite linear for low H_2 concentrations (up to 100 ppm). The higher concentration measured was 400 ppm of H_2 and, up to this value, the sensor does not show response saturation. When operated at the optimal operating temperature of 250 °C, response and recovery times (t90) for hydrogen were 195 and 850 s, respectively.

Previously-reported In_2O_3 sensors, based on other synthesis techniques (flower-like indium oxide prepared via hydrothermal method, operated at 210 °C, [5]), shown responses magnitudes of 1.4 to H_2 concentrations above 100 ppm. Below this concentration those sensors show no response at all, unlike the linear response reported in this work.

3.2.3. NO_2 Results

Sensors were exposed to low concentrations (3, 5, 5.5, and 6 ppm) of NO_2 at two different temperatures; 100 °C and 150 °C. Figure 7 shows the response of the sensors at both temperatures, which is better at 150 °C. S. Roso et al. [6] reported an optimum operating temperature of 130 °C for a high-temperature grown In_2O_3 (octahedral nanoparticles on top of an alumina substrate), which correlates with our results. When operated at the optimal operating temperature of 150 °C, response and recovery times (t90) for nitrogen dioxide were 105 and 785 s, respectively. These are very similar to the values reported in [6].

Many indium oxide synthesis methods and sensor structures have been reported for detecting nitrogen dioxide. Indium oxide responses to nitrogen dioxide range from 352.3 (@ 100 ppb) for a sensor operating at 120 °C, as reported in [21], to the rather small one of 0.1 (@ 5 ppm) for a sensor operating at 150 °C [2]. In comparison, the response for NO_2 (@ 5 ppm) for the sensors reported in this paper is 5.75, which is a remarkable result for such a simple and inexpensive synthesis and sensor manufacture process. In addition, this response reported here represents almost a five-fold increase in comparison to the response reported previously for indium oxide coated polyimide chemoresistors [15] in which the active film was synthesized at 400 °C. A comparison of the characteristics and gas sensing performance of different indium oxide sensors can be found in the Supplementary Materials.

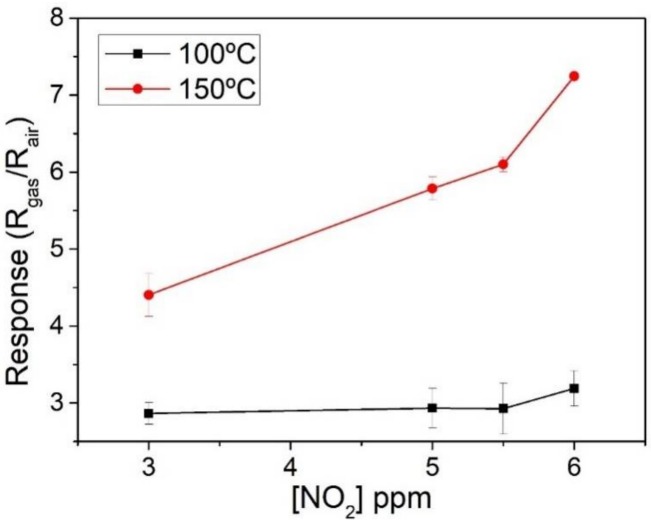

Figure 7. Sensor response towards NO_2 at two different operating temperatures.

4. Discussion

The mechanism of response to reducing species such as ammonia or hydrogen involves the interaction with oxygen species adsorbed on the surface of indium oxide. The nature of oxygen species depends on the temperature of the metal oxide [19,22,23].

$$O_{2(g)} \leftrightarrow O_{2(ads)}$$

$$O_{2(ads)} + e^- \leftrightarrow {O_2}^-_{(ads)} \ (<150\ ^\circ C)$$

$${O_2}^-_{(ads)} + e^- \leftrightarrow 2{O^-}_{(ads)} \ (150–400\ ^\circ C)$$

$${O^-}_{(ads)} + e^- \leftrightarrow {O^{2-}}_{(ads)} \ (>400\ ^\circ C)$$

Considering that the best temperature for detecting ammonia vapors has found to be 150 °C, it can be assumed that both adsorbed molecular oxygen ${O_2}^-$ and O^- species coexist on the surface of indium oxide and, therefore, the following reactions can explain ammonia response:

$$4NH_3 + 3O_2{}^-{}_{(ads)} \leftrightarrow 2N_2 + 6H_2O + 6e^-$$

$$2NH_3 + 3O^-{}_{(ads)} \leftrightarrow N_2 + 3H_2O + 3e^-$$

$$2NH_3 + 4O^-{}_{(ads)} \leftrightarrow N_2O + 3H_2O + 4e^-$$

$$2NH_3 + 5O^-{}_{(ads)} \leftrightarrow 2NO + 3H_2O + 5e^-$$

The release of electrons explains the decrease in sensor resistance observed upon exposure to ammonia.

Indium oxide octahedra show response to hydrogen when operated at 250 °C. At such operating temperature, the response mechanism can be summarized as follows. Hydrogen is adsorbed and reacts with O^- species, resulting in the formation of water molecules, which eventually desorb from the surface of indium oxide:

$$H_2 + O^-{}_{(ads)} \leftrightarrow H_2O + e^-$$

This response to hydrogen could be increased further by loading the film with Pt or Pd nanoparticles [6]. Pt or Pd nanoparticles supported onto n-type metal oxides have been reported to enhance response towards hydrogen via a combination of chemical and electronic sensitization effects [19,22,23].

When operated at 150 °C, pure indium oxide octahedra show a remarkable response towards NO_2 and, considering the small response measured for the other species tested at such low temperature, a certain degree of selectivity towards nitrogen dioxide is achieved. Additionally, ambient moisture facilitates the adsorption of NO_2 on the surfaces of indium oxide octahedra [6] or of indium oxide nanoparticles [18], further increasing sensor response and sensitivity to this species.

Recently we employed diffuse reflectance infrared Fourier transform spectroscopy (DRIFTS) under operando conditions to identify the surface species involved in the sensing of nitrogen dioxide, employing indium oxide [18]. It was found that different sensing mechanisms were in place depending on the operating temperature. While the electrical response of In_2O_3 results from the adsorption of NO_2, this adsorption differs substantially due the changes in the chemical nature of the surface of indium oxide at different temperatures. In particular, when the indium oxide sensor is operated at low temperatures, gas sensing involves surface hydroxyls with and without hydrogen bonds present over the surface. Hydrogen-bonded hydroxyl groups are consumed when the sensor is exposed to NO_2. This facilitates NO_2 adsorption, which withdraws electrons via the conduction band of In_2O_3 and, therefore, increases sensor resistance. In addition, adsorbed NO_2 forms surface nitrites that interact with isolated surface hydroxyls. Surface nitrites irreversibly increase in concentration during successive exposures to NO_2 at low operating temperatures, but this does not directly translate into a drift. In fact, sensor response is dominated by the hydrogen-bonded hydroxyl groups mediated NO_2 adsorption mechanism.

In the experiments reported here, even though dry air was used as carrier gas, the relative humidity inside the sensor chamber stabilized at 3% (@ 25 °C) and, given the fact that the operating temperature for detecting NO_2 was set to 150 °C, the sensing mechanism discussed above holds.

5. Conclusions

Here we have introduced a straightforward process for synthesizing In_2O_3 octahedral nanoparticles. This process requires lower temperatures and obtains a significantly higher yield than a VPT method we reported previously. The quality of indium oxide octahedra (e.g., absence of contamination and crystallinity) is very similar to the one of indium oxide synthesized via the more involved VPT method, which makes the approach reported here very promising for the mass production of high-quality nanomaterials. The synthesized materials were microdrop coated onto flexible polyimide transducers for producing chemoresistive gas sensors. Their performance in the detection of different target gases, namely, H_2, NH_3, and NO_2 was studied. Morphologies like

octahedra offer advantages for gas sensing since they possess sharp edges and tips, providing more active sites and smooth surfaces exposed to their chemical environment. It was found, in agreement with our previous results, that pure indium oxide octahedra films were very sensitive towards nitrogen dioxide, provided that their operating temperature was set to moderate values (e.g., 150 °C). Indium oxide also shows potential for detecting hydrogen, however, loading of indium oxide octahedra with Pt or Pd nanoparticles seems necessary to increase response and lower the optimal operation temperature.

These results demonstrate the feasibility of the material synthesis and sensor production methods discussed here for achieving flexible gas sensors using inexpensive polymeric substrates. Flexible devices show gas sensing properties that match those of sensors onto ceramic or silicon rigid substrates. In the near future the miniaturization and optimization of the flexible transducer together with the development of a flexible smart tag for detecting nitrogen dioxide will be envisaged.

Supplementary Materials: The following are available online at http://www.mdpi.com/1424-8220/18/4/999/s1, Figure S1. EDX from an In_2O_3 sample synthesized at 400 °C. Figure S2. EDX from an In_2O_3 sample synthesized at 500 °C sample. Figure S3. Nitrogen dioxide calibration curves for a sensor consisting of indium oxide synthesized at 400 °C coated onto a polyimide flexible transducer. Table S1. Comparison of gas-sensing performances of In_2O_3 gas sensors using different structures.

Acknowledgments: This work was funded in part by MINECO and FEDER via grant no. TEC2015-71663-R and by AGAUR under grant no. 2017SGR 418. E.N. gratefully acknowledges a doctoral fellowship from MINECO grant no. BES-2016-076582. E.L. is supported by the Catalan institution for Research and Advanced Studies via the 2012 Edition of the ICREA Academia Award.

Author Contributions: M.A. designed and produced the polyimide transducers; E.N. synthesized the gas-sensitive materials, performed the E-SEM and XRD analyses, and coated the gas sensors; A.R. and J.L.R. conceived and designed the experiments, contributed to the data analysis and to the writing of the paper; M.A. and E.N. performed the gas sensing measurements; and E.L. contributed to the discussion of results and to the writing of the paper.

Conflicts of Interest: The authors declare no conflict of interest. The founding sponsors had no role in the design of the study; in the collection, analyses, or interpretation of data; in the writing of the manuscript; or in the decision to publish the results.

References

1. Zhang, D.; Li, C.; Liu, X.; Man, S.; Tang, T.; Zhou, C. Doping dependent NH_3 sensing of indium oxide nanowires. *Appl. Phys. Lett.* **2003**, *83*, 1845–1847. [CrossRef]
2. Domènech-Gil, G.; Barth, S.; Samà, J.; Pellegrino, P.; Gràcia, I.; Cané, C.; Romano-Rodriguez, A. Gas sensors based on individual indium oxide nanowire. *Sens. Actuators B Chem.* **2017**, *238*, 447–454. [CrossRef]
3. Li, C.; Zhang, D.; Han, S.; Liu, X.; Tang, T.; Lei, B.; Liu, Z.; Zhou, C. Synthesis, Electronic Properties, and Applications of Indium Oxide Nanowires. *Ann. N. Y. Acad. Sci.* **2003**, *1006*, 104–121. [CrossRef] [PubMed]
4. Elouali, S.; Bloor, L.G.; Binions, R.; Parkin, I.P.; Carmalt, C.J.; Darr, J.A. Gas sensing with nano-indium oxides (In_2O_3) prepared via continuous hydrothermal flow synthesis. *Langmuir* **2012**, *28*, 1879–1885. [CrossRef] [PubMed]
5. Chen, L.; He, X.; Liang, Y.; Sun, Y.; Zhao, Z.; Hu, J. Synthesis and gas sensing properties of palladium-doped indium oxide microstructures for enhanced hydrogen detection. *J. Mater. Sci. Mater. Electron.* **2016**, *27*, 11331–11338. [CrossRef]
6. Roso, S.; Bittencourt, C.; Umek, P.; González, O.; Güell, F.; Urakawa, A.; Llobet, E. Synthesis of single crystalline In_2O_3 octahedra for the selective detection of NO_2 and H_2 at trace levels. *J. Mater. Chem. C* **2016**, *4*, 9418–9427. [CrossRef]
7. Ramírez, J.L.; Annanouch, F.E.; Llobet, E.; Briand, D. Architecture for the efficient manufacturing by printing of heated, planar, resistive transducers on polymeric foil for gas sensing. *Sens. Actuators B Chem.* **2018**, *258*, 952–960. [CrossRef]
8. Briand, D.; Oprea, A.; Courbat, J.; Bârsan, N. Making environmental sensors on plastic foil. *Mater. Today* **2011**, *14*, 416–423. [CrossRef]
9. Ramírez, J.L.; Annanouch, F.E.; Camara, M.; Llobet, E.; Briand, D. Single layer gold hotplate, printed on polyimide, with heater used as sensing current drain for metal-oxide gas sensor. *Procedia Eng.* **2015**, *120*, 707–710. [CrossRef]

10. Badradeen, E.; Brozak, M.; Keles, F.; Al-Mayalee, K.; Karabacak, T. High performance flexible copper indium gallium selenide core-shell nanorod array photodetectors. *J. Vac. Sci. Technol. A Vac. Surf. Films* **2017**, *35*. [CrossRef]
11. Harris, K.D.; Elias, A.L.; Chung, H.J. Flexible electronics under strain: A review of mechanical characterization and durability enhancement strategies. *J. Mater. Sci.* **2016**, *51*, 2771–2805. [CrossRef]
12. Khan, S.; Lorenzelli, L.; Dahiya, R.S. Technologies for printing sensors and electronics over large flexible substrates: A review. *IEEE Sens. J.* **2015**, *15*, 3164–3185. [CrossRef]
13. Zardetto, V.; Brown, T.M.; Reale, A.; Di Carlo, A. Substrates for flexible electronics: A practical investigation on the electrical, film flexibility, optical, temperature, and solvent resistance properties. *J. Polym. Sci. Part B Polym. Phys.* **2011**, *49*, 638–648. [CrossRef]
14. Han, S.-T.; Peng, H.; Sun, Q.; Venkatesh, S.; Chung, K.-S.; Lau, S.C.; Zhou, Y.; Roy, V.A.L. An Overview of the Development of Flexible Sensors. *Adv. Mater.* **2017**, *29*, 1700375. [CrossRef] [PubMed]
15. Alvarado, M.; Navarrete, E.; Llobet, E.; Ramírez, J.L.; Romero, A. Comparing performance of flexible and rigid substrates for In_2O_3 based gas sensors. In *2017 IEEE SENSORS*; IEEE: Glasgow, UK, 2017.
16. Natishan, P.M.; O'Grady, W.E. Chloride Ion Interactions with Oxide-Covered Aluminum Leading to Pitting Corrosion: A Review. *J. Electrochem. Soc.* **2014**, *161*, C421–C432. [CrossRef]
17. Bierwagen, O. Indium oxide—A transparent, wide-band gap semiconductor for (opto) electronic applications. *Semicond. Sci. Technol.* **2015**, *30*, 24001. [CrossRef]
18. Roso, S.; Degler, D.; Llobet, E.; Barsan, N.; Urakawa, A. Temperature-Dependent NO_2 Sensing Mechanisms over Indium Oxide. *ACS Sens.* **2017**, *2*, 1272–1277. [CrossRef] [PubMed]
19. Yamazoe, N.; Sakai, G.; Shimanoe, K. Oxide semiconductor gas sensors. *Catal. Surv. Asia* **2003**, *7*, 63–75. [CrossRef]
20. Makhija, K.K.; Ray, A.; Patel, R.M.; Trivedi, U.B.; Kapse, H.N. Indium oxide thin film based ammonia gas and ethanol vapour sensor. *Bull. Mater. Sci.* **2005**, *28*, 9–17. [CrossRef]
21. Xiao, B.; Wang, D.; Song, S.; Zhai, C.; Wang, F.; Zhang, M. Fabrication of mesoporous In_2O_3 nanospheres and their ultrasensitive NO_2 sensing properties. *Sens. Actuators B Chem.* **2017**, *248*, 519–526. [CrossRef]
22. Annanouch, F.E.; Haddi, Z.; Ling, M.; Di Maggio, F.; Vallejos, S.; Vilic, T.; Zhu, Y.; Shujah, T.; Umek, P.; Bittencourt, C.; et al. Aerosol-Assisted CVD-Grown PdO Nanoparticle-Decorated Tungsten Oxide Nanoneedles Extremely Sensitive and Selective to Hydrogen. *ACS Appl. Mater. Interfaces* **2016**, *8*, 10413–10421. [CrossRef] [PubMed]
23. Shankar, P.; Bosco, J.; Rayappan, B. Gas sensing mechanism of metal oxides: The role of ambient atmosphere, type of semiconductor and gases—A review. *Sci. Lett. J.* **2015**, *4*, 126.

The above-mentioned materials have been grown or deposited through physical methodologies, yet the best bottom-up methodologies are those based on the chemical growth of the material. Typically, physical methodologies require higher temperatures to evaporate the precursors (VPD), high-vacuum to avoid cross-contamination (Sputtering) or even a combination of both high temperatures and high vacuum in the case of the molecular beam epitaxy (MBE) family techniques. In contrast chemical synthesis methodologies or techniques usually require less energy in terms of temperature as the chemical reactions occur at lower temperatures. For instance, an example of low temperature chemical synthesis route is hydrothermal synthesis. In such methodology, the chemical precursors either organic or inorganic are placed inside a Teflon cartridge and then kept at high pressure and relatively low temperatures ranging from 100 ºC to 250 ºC depending on which type of synthesis is taking place. The high vapor pressure reached with an autoclave forces the crystallization of the materials synthesized. The oxide crystals obtained through this methodology could either be pure or loaded with foreign metals (typically noble or transition-metals) at different loading levels and also present core-shell structures depending on the parameters preset in the reaction. In this these, we synthesized and studied two ZnO structures grown through hydrothermal method. Such structures present different morphologies obtained tuning the growth parameters. ZnO nanorods and ZnO nanoflowers were fully characterized for their chemical composition, morphology and structure by means of scanning electron microscope (SEM) and Electron dispersive X-ray, XPS, high resolution transmission electron microscope (HR-TEM) and X-Ray diffraction (XRD). Furthermore, the ability to detect and measure target gas concentrations was studied for a controlled atmosphere under lab conditions.

2.2.2 Gas sensing properties of ZnO nanostructures (flowers/rods) synthesized by hydrothermal method

Sensors & Actuators: B. Chemical 292 (2019) 24–31

Contents lists available at ScienceDirect

Sensors and Actuators B: Chemical

journal homepage: www.elsevier.com/locate/snb

Gas sensing properties of ZnO nanostructures (flowers/rods) synthesized by hydrothermal method

Sonalika Agarwal[a,*], Prabhakar Rai[b,c,d], Eric Navarrete Gatell[c], Eduard Llobet[c], Frank Güell[e], Manoj Kumar[a], Kamlendra Awasthi[a,*]

[a] Department of Physics, Malaviya National Institute of Technology Jaipur, Rajasthan, 302017, India
[b] Department of Chemical Engineering, Indian Institute of Technology, Kanpur, 208016, India
[c] MINOS-EMaS, Universitat Rovira i Virgili, Avda. Països Catalans 26, 43007, Tarragona, Spain
[d] Wildlife Section, Zoological Survey of India, Kolkata, 700053, India
[e] ENFOCAT-IN2UB, Universitat de Barcelona (UB), C/Martí i Franquès 1, 08028, Barcelona, Catalunya, Spain

ARTICLE INFO

Keywords:
ZnO
Nanoflowers
Nanorods
Hydrothermal method
Gas sensing

ABSTRACT

Here, we report the hydrothermal synthesis of flower-shaped ZnO nanostructures and investigated their morphology-dependent gas sensing properties. Scanning electron microscope (SEM) study confirmed the formation of two kinds of floral structures. At short reaction time, flower-like structures (2–3 μm in size) composed of nanoparticles are formed, whereas floral assemblies (~ 5 μm) of nanorods are formed at long reaction time. X-ray diffraction (XRD) confirmed the formation of the hexagonal wurtzite structure of ZnO. The average crystallite size of prepared nanoflowers and nanorods were found to be 21 nm and 43 nm, respectively. These results are supported by transmission electron microscopy (TEM). The band gap of ZnO nanostructures was calculated from the UV–vis absorption spectrum and found to be 3.0 eV and 3.19 eV for ZnO nanoflowers and nanorods, respectively. Broad absorption peak in the visible region of photoluminescence (PL) spectra confirmed the presence of oxygen vacancies in both specimens. Furthermore, morphology dependent gas sensing property was investigated for ethanol, benzene, carbon monoxide, and nitrogen dioxide at different operating temperatures and concentrations. Although both morphologies have shown good sensitivity and selectivity towards NO_2 at ppb, the response of nanoflower was higher than that of nanorods, which was attributed to its relatively higher surface area and amount of surface defects.

1. Introduction

The tremendous increase in air pollution including both indoors and outdoors containing toxic gases and volatile organic compounds (VOCs), disturbing everyone is a major environmental health problem has been acknowledged by the World Health Organization (WHO) [1]. High levels of VOCs are normally emitted by many precise sources and methods that include exhaust gas, water separation techniques, industrial wastewater, petroleum refining, natural gas processing, petrochemical processes, and paints. It is observed that 50–300 different VOCs has been detected in indoors which is almost ten times higher than outdoors [2]. Therefore, for the detection and monitoring of these harmful and poisonous pollutants, the development of sensors is a topmost priority in the area of research [3]. Metal oxide semiconductor (MOS) gas sensors are currently being widely used in many industrial and domestic applications in detection of toxic, flammable and explosive gases [4]. These gas sensors are highly attractive due to their high sensitivity, flexibility in production, small size, low cost and suitable for detection of both reducing and oxidizing gases [5,6].

Among the various MOS, Zinc Oxide (ZnO), is extensively known as a wide and direct band gap semiconductor of about 3.37 eV at room temperature [7]. Also, ZnO is n-type II-IV semiconductor material and shows useful features such as well chemical stability, excellent optical properties, non-toxicity, suitability to doping, low cost, high surface-to-volume ratio and considerable sensitivity at even low temperatures [8,9]. Due to these distinctive properties, it has been considered as one of the most favorable materials for gas sensing over the past few years. The gas sensing properties of synthesized ZnO nanostructures strongly depend on their shape and size, as well as morphology and crystallinity [10,11]. To date, various morphologies of ZnO have been fabricated such as nanotubes [12], nanorods [13], nanowires [14], nanosheets [15], nanoflowers [16], nanoflakes [17] nanoplates [18] and so on. But

* Corresponding authors.
E-mail addresses: sonalika.phy@mnit.ac.in, sonalika.spsl@gmail.com (S. Agarwal), kawasthi.phy@mnit.ac.in (K. Awasthi).

https://doi.org/10.1016/j.snb.2019.04.083
Received 11 February 2019; Received in revised form 16 April 2019; Accepted 16 April 2019
Available online 25 April 2019

still, a shape controlled ZnO synthesis method is indispensable for exploring the potential of ZnO as a source of smart and functional materials.

The synthesis method and the structure directing agents play an important role in controlling the morphology of these nanostructures. Different methods have been adopted to synthesize these nanostructures including precipitation [19], electro-deposition [20], electrospinning [21], thermal evaporation [22], RF sputtering [23], microwave-assisted solution phase reaction [11] and hydrothermal [24]. Among them, the hydrothermal method has been found to be the most promising route for fabricating the well-crystallized structures [25–29]. The slight changes in experimental parameters like reaction temperature, time and pH value strongly affect the precise morphology [30–35].

Herein, we report a simple shape controlled ZnO synthesis method through a one-pot hydrothermal method to synthesize ZnO nanoflowers and ZnO nanorods (bunches). These nanostructures are characterized by XRD, SEM, TEM and UV–vis spectroscopy. Furthermore, the gas sensing measurement revealed that the hierarchical leaf-like nanoflowers show excellent gas sensing properties as compared to the rod-like nanostructure of ZnO.

2. Materials and methods

2.1. Synthesis of ZnO nanostructures

All chemicals were of analytical grade and used without further purification. The hydrothermal method was used to fabricate ZnO nanostructures [36]. In the typical synthesis, 0.35 *g* of zinc acetate dihydrate ($Zn(CH_3COO)_2{\cdot}2H_2O$) and 0.24 *g* of citric acid monohydrate ($C_6H_8O_7{\cdot}H_2O$) was dissolved into 67 ml deionized water and 13 ml ethanol under vigorous stirring. Then, 10 M NaOH solution was dropped into the above solution with stirring until the pH value reached 13. After some time of fully mixing, the resulting homogeneous solution was transferred into a 100 ml capacity autoclave with a Teflon-liner. Then the autoclave was heated at a constant temperature of 150 °C for 17 h and 19 h, respectively. The autoclave was allowed to cool to room temperature naturally. Finally, the white products were collected by centrifugation and thoroughly washed with deionized water and ethanol several times and dried at 80 °C for 12 h.

2.2. Characterization

The crystallinity of the prepared ZnO nanostructures was characterized by X-Ray diffraction (XRD, Panalytical XPert Pro X-ray diffractometer) using Cu-Kα radiation source at λ = 1.5406 Å ranging from 20° to 80° (2θ) with a scanning step size of 0.020°. Field Emission scanning electron microscopy (FESEM, Nova Nano FE-SEM 450 FEI) was used to examine the surface morphology of the samples. Further, these structures were studied by high-resolution transmission electron microscopy (HRTEM, Tecnai G^2 20 (FEI) S-TWIN). Optical characterization was carried out by UV–vis NIR spectrophotometer (UV–vis, LAMBDA 750 Perkin Elmer) in the wavelength range of 200–800 nm. The Brunauer–Emmett–Teller (BET) nitrogen adsorption-desorption isotherms of the ZnO nanostructures were measured from Quantachrome NOVA touch LX^2 Instrument. Room-temperature photoluminescence (PL) measurements were made with a chopped Kimmon IK Series He-Cd laser (325 nm). Fluorescence was dispersed with a Princeton Instruments Acton SP2750 0.750 m imaging triple grating monochromator, detected using a Hamamatsu H8259-02 with a socket assembly E717-500 photomultiplier, and amplified through a Stanford Research Systems SR830 DSP. To filtering the stray light, a 360 nm filter was used. The optical transfer function of the PL setup was used to correct the emission spectra.

2.3. Sensing device fabrication and measurement

A microdrop coating technique was used for preparing the sensing devices, to coat the electrode region of the alumina transducer as shown in Fig. S1a. To attain such devices, 20 mg of ZnO nanomaterials were dissolved with 0.5 mL of 1, 2-propanediol and obtain a suspended solution, placed inside an Eppendorf. This prepared solution was sonicated and stirred until to confirm a homogeneous suspension. After that 1 μL droplets were dropped on top of the electrode area by using a micropipette. Consequently, for the evaporation of the solvent, sensing devices were placed inside an oven at 150 °C. Lastly, devices were sintered at 500 °C for 2 h in the furnace.

In order to study the gas sensing properties of the resulting ZnO films, the layers were exposed to different concentrations of target gases. The devices were kept inside a Teflon airtight gas chamber for the gas sensing measurements (Fig. S1b). The sensors were stabilized under a flow of zero-grade synthetic dry air at each of the temperatures studied for 2 h before initializing the gas measurements. In this particular study, the gases studied were ethanol vapors measured at 5, 10, 15 and 20 ppm, benzene at 2.5, 5, 7.5 and 10 ppm, carbon monoxide both at 25, 50, 75 and 100 ppm and, finally, nitrogen dioxide at 250, 500, 750 and 1000 ppb. The delivery of reproducible concentrations of the species tested was carried out using an automated computer-driven mass-flow gas control system. Gas sensing studies were performed in repeated cycles that comprised 30 min of exposure to a given gas concentration pulse, followed by 30 min under dry air for cleaning and baseline recovery. The flow rate of gas was adjusted to 100 mL/min throughout the gas sensing measurements. The change in the DC electrical resistance of ZnO films was monitored by using a Keysight 3972 A data acquisition system.

3. Results and discussion

3.1. Structural and morphological studies

The crystal structures and phase of the synthesized ZnO nanoflowers and nanorods were analyzed by XRD as shown in Fig. 1. The diffraction patterns are indexed to hexagonal wurtzite ZnO phase in accordance with JCPDS card no. 01-079-0205. It can be concluded from these characteristic peaks that ZnO has a hexagonal crystal structure and matches the space group of P63mc with lattice constants a = 0.3240 nm and c = 0.5187 nm for nanoflowers and a = 0.3242 nm and c = 0.5193 nm for nanorods. The strong and sharp peaks show the good crystallinity of the synthesized materials. Further, it was noticed that no characteristic peaks from other phases or impurities are observed in the diffraction pattern of both samples, indicating high purity of specimens. The average crystallite sizes of prepared samples were

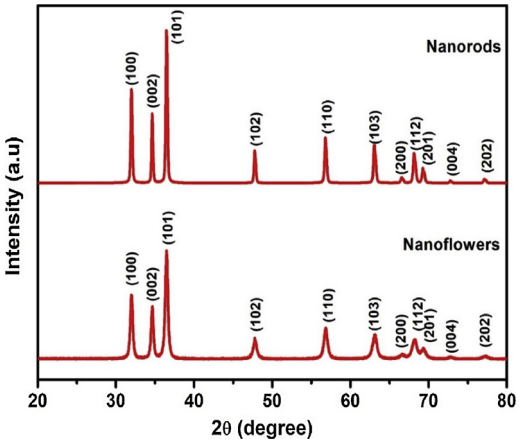

Fig. 1. XRD patterns of as-prepared ZnO nanoflowers and ZnO nanorods.

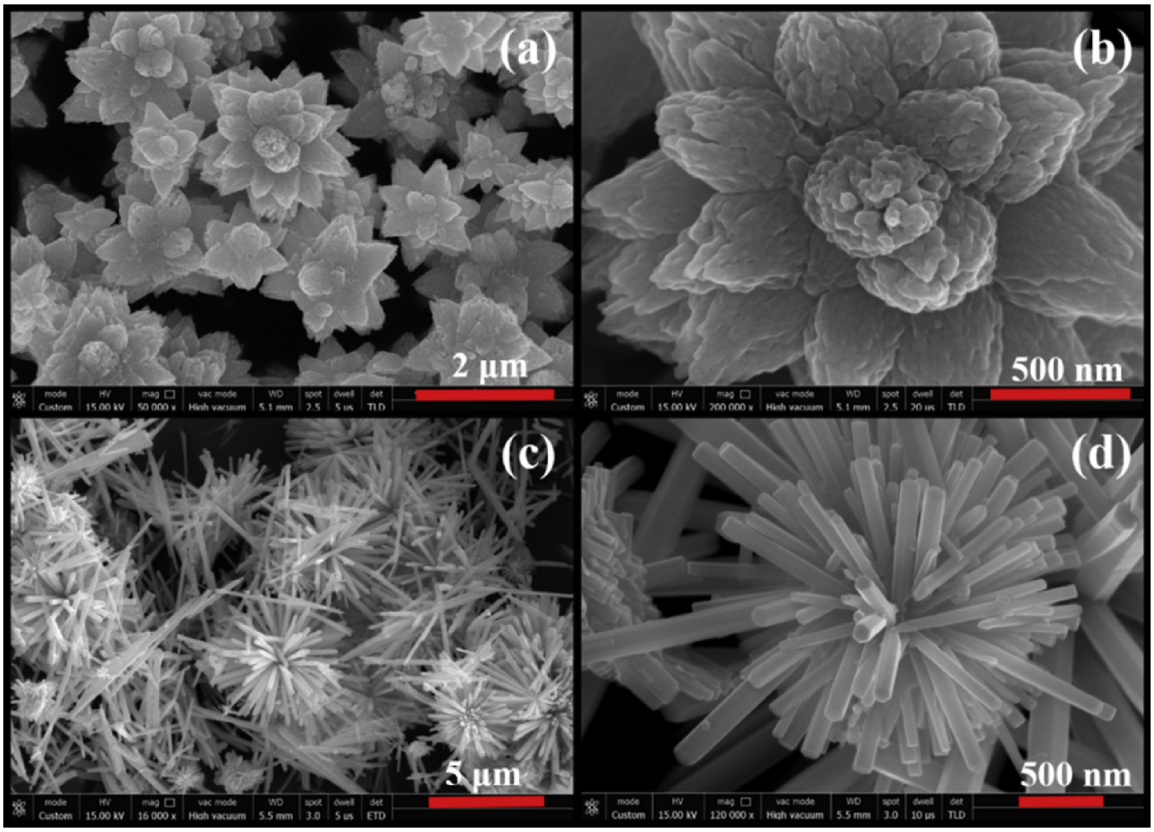

Fig. 2. SEM images of as-prepared ZnO nanostructures; (a) and (b) ZnO nanoflowers; (c) and (d) bunches of ZnO nanorods.

calculated by using the Scherer's formula from the XRD patterns have been found to be about 21 and 43 nm of nanoflowers and floral assemblies of nanorods, respectively.

Surface morphologies of the ZnO nanostructures are analyzed by SEM and displayed in Fig. 2. Flower-like ZnO composed of nanoparticles is formed at short reaction time as depicted in Fig. 2a and b. The size of flower-like geometry was 2–3 micron having 200–500 nm petals. The roughness of the petals surface was attributed to the clustering of nanosized particles (Fig. 2b). Such a distinctive hierarchical flower-like structure has many petals and pores, which are going to play a significant role in improving the gas sensing properties. It is quite interesting that the floral assemblies (~5 µm) of ZnO nanorods are formed when the reaction time was increased as shown in Fig. 2c and d. The whole structure is made from a dozen of ZnO nanorods with a smooth surface and diameters of these nanorods range from 100 to 500 nm and their length is up to several micrometers.

The TEM images of the ZnO nanoflowers and nanorods are shown in Fig. 3a and d, respectively and illustrate that both the size and morphology were similar to the observations of FESEM. Clear lattice fringes are observed correspondingly in both HRTEM images (Fig. 3b and e) of nanoflowers and nanorods. Furthermore, the lattice fringes of 0.246 nm and 0.245 nm were allocated to the (101) plane of wurtzite ZnO nanostructures. Fig. 3c and d show the SAED patterns of ZnO with nanoflowers and nanorods morphology, respectively confirming their high crystalline nature due to presenting sharp spot diffraction patterns. The BET surface areas of these two specimens were measured by nitrogen adsorption-desorption process. The surface area of ZnO nanoflowers ($10.8\,m^2\,g^{-1}$) found to be greater than ZnO nanorods ($7.5\,m^2\,g^{-1}$) as displayed in Fig. S2 (See in supporting information)

During the hydrothermal process following chemical reactions may have been involved:

$$Zn^{2+} + 4OH^- \leftrightarrow [Zn(OH)_4]^{2-}$$

$$2[Zn(OH)_4]^{2-} \leftrightarrow 2ZnO + 4H_2O + O_2$$

It is well-known that by nucleation and crystal growth process, the growth of ZnO can be controlled, where nucleation occurs first followed by crystal growth. The nucleation rate is slow and crystal growth is relatively fast, at higher pH. Due to fewer nuclei and much more growth units, the complex $[Zn(OH)_4]^{2-}$ can be easily linked with the surface at the different site of a ZnO seed and grows along the c axis into petal-like crystal forming flower-like structures. Further increase in reaction time may result in dissolution and re-nucleation of side branches into nanorods connected to the central points. A schematic presentation of a plausible growth mechanism is given in Fig. 4.

3.2. Optical studies

UV-Vis absorption spectroscope was used to study the optical properties of the synthesized ZnO nanostructures. The main absorption peak at room temperature for ZnO nanoflowers is recorded around 380 nm and around 356 nm for nanorods as shown in Fig. 5a. This is attributed to the direct transition of electrons between the valance band and conduction band [37]. The band gap energy of the ZnO nanostructures is calculated by the extrapolation of the linear portion of the graph between the function $(\alpha h\nu)^2$ versus photon energy ($h\nu$) [38], as shown in Fig. 5b. The band gaps of nanoflowers and nanorods are 3.0 eV and 3.19 eV, respectively. A significant increase in the band gap of nanorods was due to the increase in diameter of ZnO rods in comparison to the diameter of leaves in flowers. This shifting in band gap may be attributed to electron confinement as observed in various nanomaterials [39] and also could be due to changes in their morphologies, defects and grain size confinement [40,41].

The PL spectra are shown in Fig. 6. The two emission bands have been observed at room-temperature by pumping at 325 nm. One is narrow excitonic near-band-edge (NBE) emission in the UV range at around 380 nm [42] and second is a broader deep level emission (DLE)

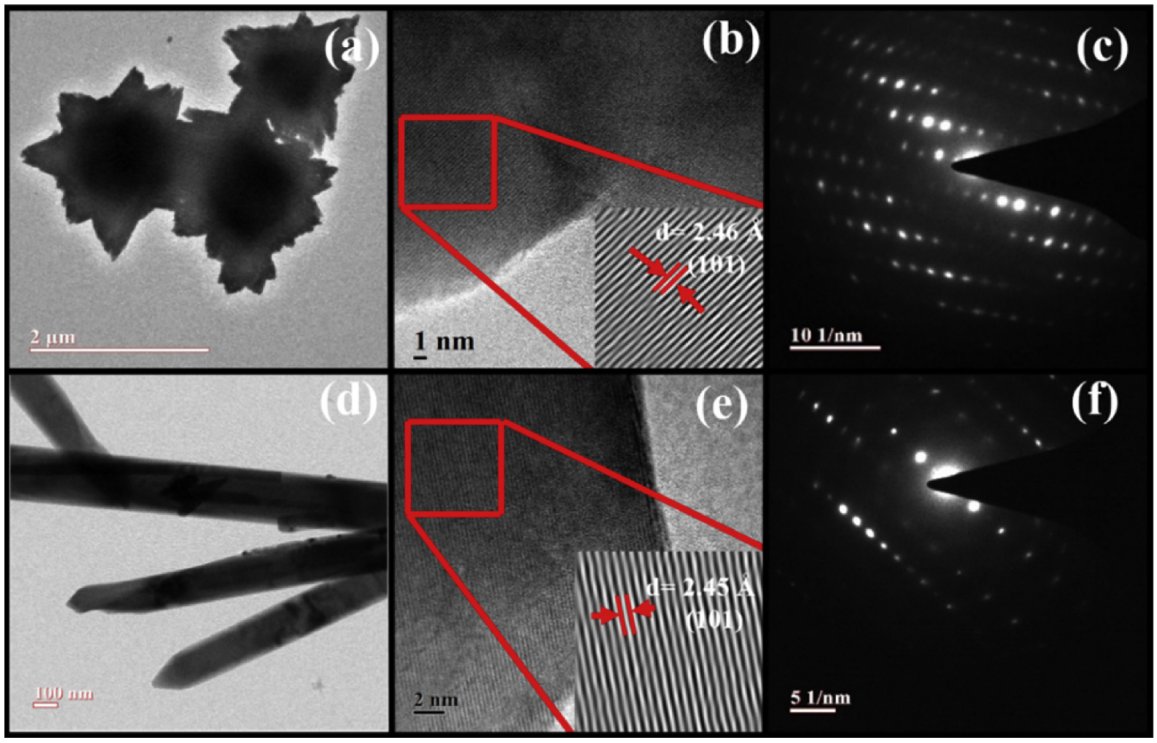

Fig. 3. (a) TEM image, (b) corresponding HRTEM image, and (c) SAED pattern of an individual ZnO nanoflowers; (d) TEM image, (e) corresponding HRTEM image, and (f) SAED pattern of individual ZnO nanorods.

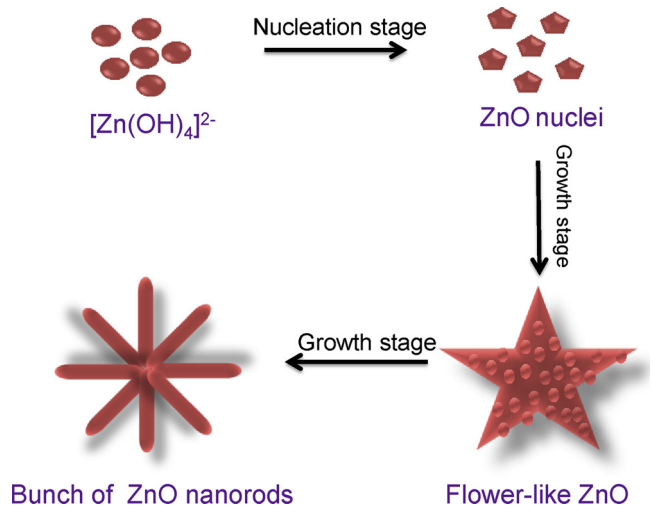

Fig. 4. Schematic presentation of growth mechanism for flower-like structures.

band in the visible range from 430 to 850 nm [43]. For relative comparison, the intensity of every spectrum was normalized to the intensity of the DLE emission. The exciton peak for the ZnO nanorods is situated at 386 nm, whereas for the ZnO nanoflowers is shifted to 380 nm, and the full width at half maximum (FWHM) are around 120 and 200 MeV, respectively. This broadening in FWHM for the ZnO nanoflowers was observed because of the higher quantity of intrinsic defects. The shift in NBE emission agrees well with the absorption results, see Fig. 5. The DLE wide band also shows a shift in the position of the maximum emission intensity. For the ZnO nanorods, the maximum is located near 610 nm, while for the ZnO nanoflowers the maximum is located at around 660 nm. The DLE/NBE ratio is a significant parameter to evaluate the crystal-quality between samples [44]. It is clearly revealed that the crystal quality of the ZnO nanorods is considerably improved as compared to the ZnO nanoflowers.

3.3. Gas sensing studies

The gas sensing properties of the ZnO nanostructures were studied and employed at different operating temperatures i.e., 150 °C, 200 °C, and 250 °C. These nanostructures responded to ethanol and nitrogen dioxide. In contrast, no response towards benzene was obtained for ZnO nanorods and a poor response was obtained for flower-like ZnO sensors. Finally, carbon monoxide was not detected at any of the operating temperatures tested. Fig. 7 shows the typical behavior of an *n-type* semiconductor exposed to repeated response and recovery cycles of increasingly concentrated reducing (ethanol) or oxidizing (nitrogen dioxide) species. While exposures to ethanol (an electron donor) result in a decrease in the resistance of the n-type material (Fig. 7a), exposures to nitrogen dioxide (an electron acceptor) increase sensor resistance (Fig. 7b). Baseline recovery is performed under pulses of pure dry air. It has been found that recovery time was slightly longer for NO_2 as compared to organic compounds (Table S1).

ZnO flower-like structures were exposed to ethanol vapors at concentrations of 5, 10, 15, 20 ppm at different working temperatures. The results are summarized in Fig. 8. When this nanomaterial is operated at the lower temperatures tested of 150 °C and 200 °C, it shows a very similar, moderate responsiveness. When the operating temperature is raised to 250 °C, a nearly 5-fold increase in ethanol responsiveness is observed for any of the concentrations tested. The behavior of ZnO nanorods is very similar to the one displayed by flower-like structures, however, nanorods show slightly lower responsiveness when operated at 150 °C or 200 °C. When operated at 250 °C there is nearly an 8-fold enhancement in ethanol responsiveness, closely matching one of the flower-like structures. It can be concluded that there is no particular difference in the ethanol sensing properties between the two morphologies for any of the working temperatures tested.

Both nanomaterials were exposed to nitrogen dioxide at concentrations of 250, 500, 750, 1000 ppb at different working temperatures. The results are summarized in Fig. 9. In contrast to what was found for ethanol, sensor responses vary significantly depending on the morphology of the gas sensitive nanomaterial. For instance, flower-like

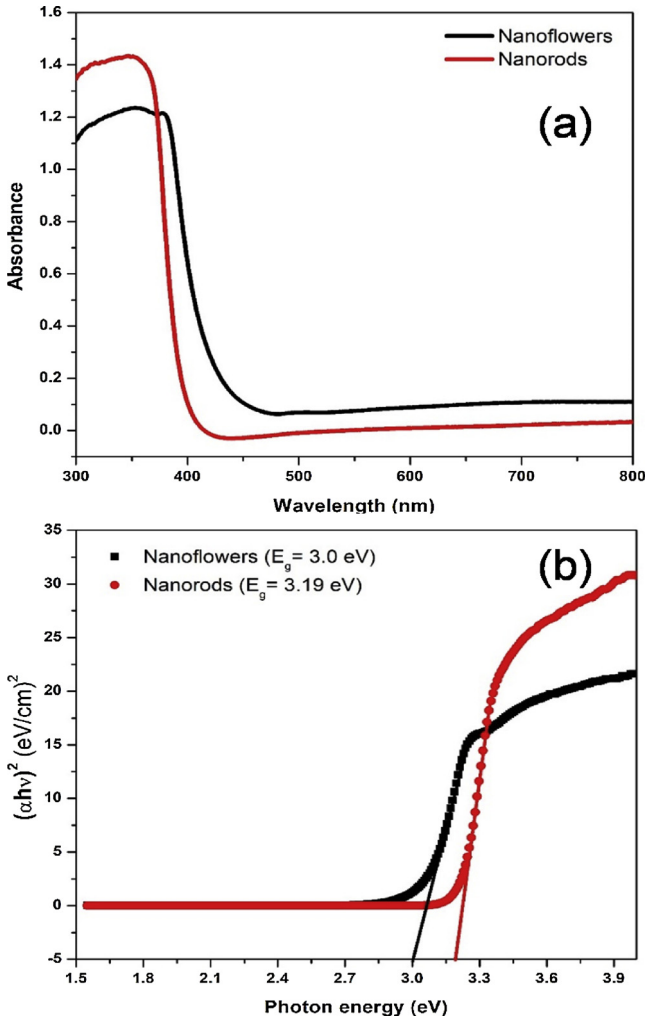

Fig. 5. (a) UV–vis absorption spectra and (b) plot between $(\alpha h\nu)^2$ versus photon energy ($h\nu$) of ZnO nanoflowers and nanorods.

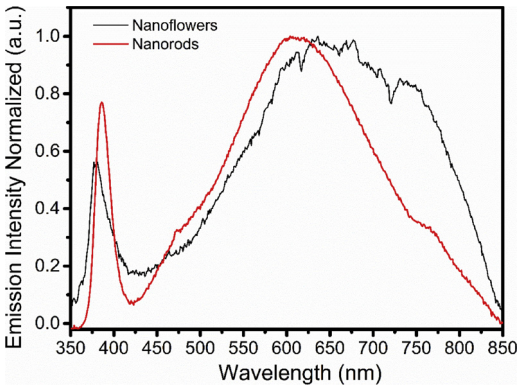

Fig. 6. Room-temperature emission spectra of the ZnO nanoflowers and nanorods.

ZnO displayed the highest responsiveness to nitrogen dioxide at 200 °C, meanwhile 150 °C was the operating temperature at which the lowest responsiveness was achieved (Fig. 9a). On the other hand, ZnO nanorods displayed the highest responsiveness at 200 °C (yet, this was lower than the one of nanoflowers) and its lowest response was obtained at 250 °C (Fig. 9b).

The two types of ZnO nanomaterials were exposed towards benzene vapors at 2.5, 5, 7.5 and 10 ppm. While flower-like ZnO was responsive

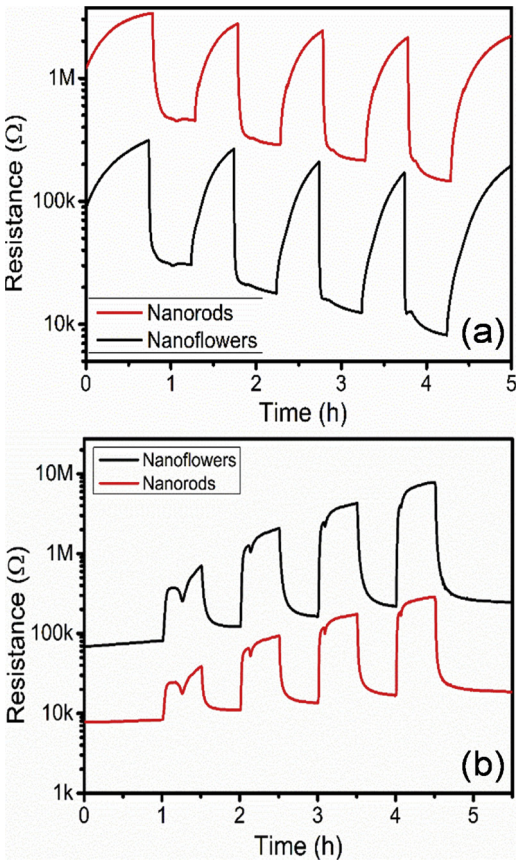

Fig. 7. Sensor resistance changes of two sensors employing ZnO nanorod or nanoflower materials under exposure and recovery cycles to four increasing concentrations of (a) ethanol and (b) nitrogen dioxide. Sensors are operated at their optimal working temperatures for these target gaseous species (i.e., 250 °C for ethanol and 200 °C for NO_2).

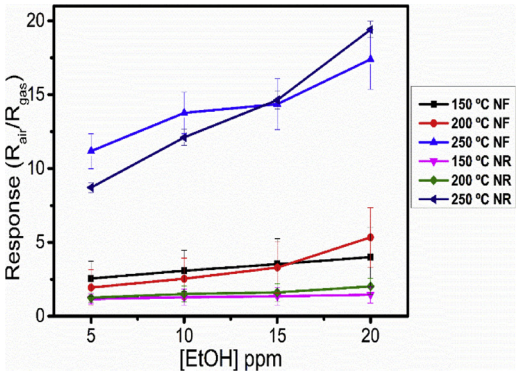

Fig. 8. Temperature dependent sensing results for ethanol vapors for ZnO nanoflowers and nanorods.

to benzene when operated at 250 °C (Fig. 10), ZnO nanorods were not responding at any of the operating temperatures tested. Such a difference can be attributed to the significant differences in the morphology of the two nanomaterials, in which nanoflowers may have a higher surface area and higher amount of surface defects (where the benzene molecule can be better adsorbed) than nanorods [45,46].

Cross-sensitivity effects are summarized in Fig. 11. It can be derived that both nanoflowers or nanorods ZnO are suited to detect nitrogen dioxide when operated at 200 °C, suffering small cross-sensitivity to reducing species such as benzene or ethanol. Despite the fact that ethanol can be detected effectively at 250 °C, ZnO nanomaterials suffer from high cross-sensitivity to NO_2.

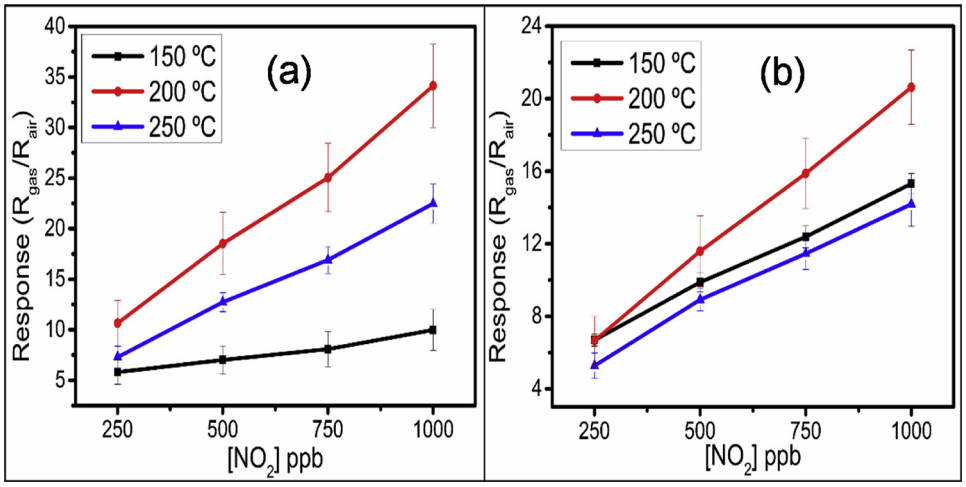

Fig. 9. Sensing results obtained for NO_2 operating at different working temperatures; (a) ZnO nanoflowers and (b) ZnO nanorods.

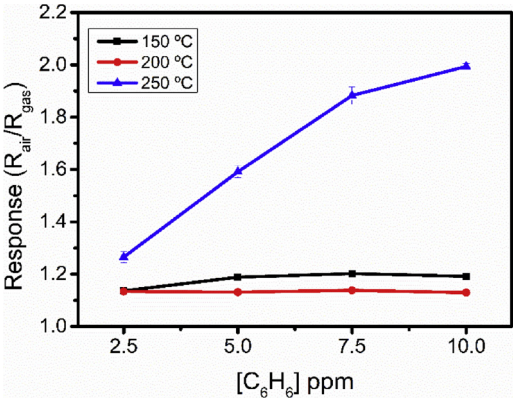

Fig. 10. ZnO nanoflowers response towards benzene vapors at different concentrations and operating temperatures.

Effect of humidity on sensor response was also examined and results are presented in Fig. S3. In the ZnO nanoflowers, there is a decrease in the overall sensor sensitivity when tested under humidity (i.e., a decrease in the slope of the curve while under humid conditions) as displayed in Fig. S3a. This can be attributed to the rough morphology present in such structure, which enhances the number of water molecules adsorbed due to a higher surface ratio. At the same time, this increases the difficulty to desorb such molecules, preventing NO_2 from reaching the material surface and, thus, reacting with it. On the other hand, ZnO nanorods have shown a higher crystallinity than nanoflowers, thus having fewer defects and a smoother surface, easing desorption of water molecules adsorbed on the surface. As a result, nanorods exhibit a stable sensitivity (i.e. the slope for the curves shown in Fig. S3b remains basically unchanged), when exposed to humidity, and the response is of the same order of magnitude as for the one obtained in dry air conditions. Furthermore, long term stability of sensors was tested for a concentration of 1 ppm NO_2. The exposure was done for 30 min and the recovery step was done under 6 h of synthetic air. The results revealed that despite the sensors were kept under storage the response was almost the same for the nanoflower-like sensor and slightly increased for the nanorod sensor (Fig. S4).

3.4. Gas sensing mechanism

Zinc oxide belongs to the n-type metal oxides family such as WO_3, In_2O_3 or SnO_2. When such metal oxides are exposed to atmospheric oxygen, this oxygen is adsorbed to its surface in different molecular or atomic states depending on the temperature. When operating at 100 to 150 °C the dominating oxygen species are O_2^-, when the temperature is raised from 150 up to 200 °C the dominant species are atomic O^- meanwhile further increase on the temperature would lead to the formation of O^{2-} [47]. Therefore, in this work, we presented different

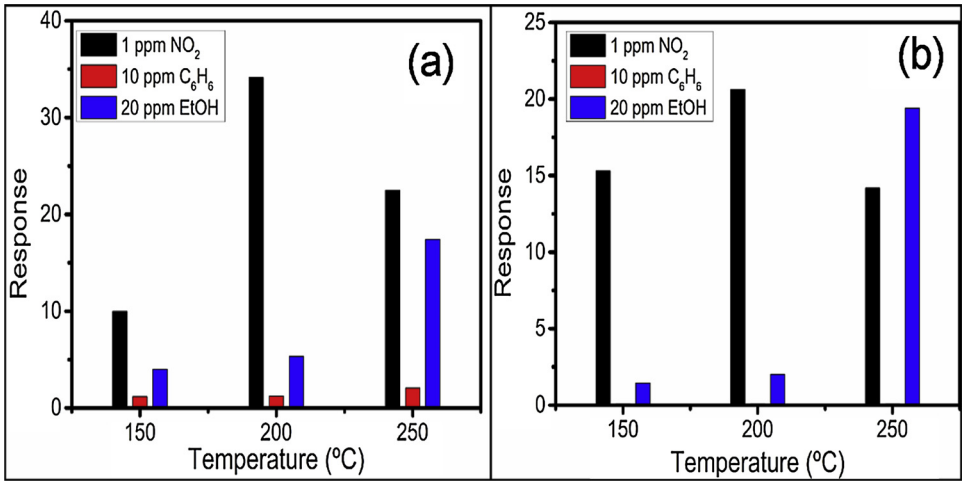

Fig. 11. Sensor responsiveness at each working temperature at different concentrations tested; (a) nanoflowers sensors and (b) nanorods sensor. Response expressed in means of R_{air}/R_{gas} for reducing species and R_{gas}/R_{air} for oxidizing species.

working temperatures 150 °C, 200 °C and 250 °C at which different oxygen species would be found at such temperatures as well as coexist in the transition temperatures. When such oxygen species are chemisorbed in the surface of the metal oxide, a new extrinsic surface acceptor states are created immobilizing conduction band electrons found in the surface area, creating a depletion layer. These chemisorbed oxygen species act as charge carriers, then, when a reducing (i. e. ethanol, hydrogen, benzene) gas reacts it consumes the chemisorbed oxygen extracting them from the surface. This changes the thickness of the depletion layer as well as enhancing the conductivity of the material leading to a decrease of the resistance. Such decrease on the resistance could be correlated with the gas concentration present in the atmosphere, moreover, when the metal oxide is exposed to a clean target gas-free atmosphere, the recovery cycle, the oxygen species removed are renewed again the surface conduction electron is immobilized thus increasing the resistance of the material. All the above-described mechanism for the reducing gases is opposite to the mechanism occurring when an oxidizing gas is present in the atmosphere (i.e. nitrogen dioxide, ozone). When the molecules of an oxidizing gas reach the surface of the metal oxide these get adsorbed in the surface acting also as surface-acceptors immobilizing more conducting electrons, thus increasing the resistance of the material even further. When a cleaning cycle is introduced, these chemisorbed species are removed from the surface recovering the previous resistance values. The above-mentioned mechanism is the reason why our sensors recover in a different way when it is ethanol or NO_2 [48].

Based on the responses obtained, these sensors operating at 200 °C are suitable for the NO_2 detection as little or no cross-sensitivity is found at such temperature. The nitrogen dioxide sensing mechanism can be attributed to the interaction between the oxygen species adsorbed at the zinc oxide surface and the gas molecule. The interaction between NO_2 and such oxygen species has been already reported by Kumar and coworkers [49], establishing the sensing mechanisms as the following; the molecules of nitrogen dioxide present at the atmosphere react with the adsorbed oxygen species present at the surface of the ZnO, suffering a reduction due to the electron transference from the conduction band of ZnO to the gas molecule. Such transfer is translated as a broadening of the electron-depletion layer, which results in the narrowing of the conduction channel thus lowering the conductivity of the material. Han et al. [50] reported the comparison of two zinc oxide nanoparticles groups with different structural defects, one having a larger excess of interstitial oxygen and a second one presenting an excess of zinc, or oxygen deficient. The results showed that an excess of zinc enhances chemisorption of atmospheric oxygen in the zinc oxide surface thus enhancing the amount of available oxygen and subsequently enhancing the response obtained for the gas sensing tests. Zhang et al. [46] also demonstrated that there is an increase in the sensitivity of zinc oxide when its morphology is tuned to have a higher surface area and subsequently increase the oxygen vacancies present in the structure. When NO_2 molecules present in the atmosphere get adsorbed in the surface of the material the effect of immobilizing the electrons from the conduction band has a higher impact in the material rather than the reaction between the adsorbed oxygen with the, i. e. ethanol. As ethanol requires from oxygen to react it is limited at some extend to the amount of active oxygen present on the surface, meanwhile, NO_2 has all the material surface available for absorption thus having a greater impact on materials chemiresistive behavior.

4. Conclusions

Two kinds of ZnO nanostructures, flower-like ZnO nanostructures and floral assembly of ZnO nanorods, were synthesized by a hydrothermal method in order to study the morphology-dependent gas sensing properties. The different nanostructured ZnO materials synthesized by the hydrothermal method have revealed to be a promising material towards NO_2 detection. Both morphologies have shown good sensitivity towards NO_2 at ppb level in comparison to the other gaseous species tested, for which small response (case of ethanol) or no-response (case of carbon monoxide), have been obtained at ppm level. Furthermore, it has been observed a clear effect on the gas sensing properties due to the different morphology obtaining the best results for the nanoflowers shape sensor in comparison to the nanorods. This difference in the sensitivity can be attributed to relatively higher surface area and amount of surface defects in the nanoflowers in contrast to nanorods. Such differences enable the adsorption of several times more target gas molecules thus enhancing the response. It is clearly seen that at higher concentrations the signal difference is almost 2 times between morphologies supporting the idea that nanorods are saturated faster than nanoflowers.

Acknowledgments

Sonalika Agarwal is highly thankful to the Department of Science and Technology, Government of India for financial support vide reference no. SR/WOS-A/PM-72/2016 under Women Scientist Scheme to carry out this work. The authors thankfully acknowledge financial support from DST, New Delhi (ECR/2016/001780) for this research work. E.L. is supported by the Catalan Institution for Research and Advanced Studies via the 2018 ICREA Academia Award. This work is supported in part by MINECO and FEDER under grant no. TEC2015-71663-R and by AGAUR under grant no.2017-SGR 418. Prabhakar Rai is supported by the Department of Science and Technology (DST), New Delhi, India vide DST-INSPIRE Faculty Scheme (DST/INSPIRE/04/2014/001318; IFA14/MS-20). Frank. Guell. is grateful to project MAT2017-87500-P. Authors thank MRC, MNIT Jaipur for providing the research facilities.

Appendix A. Supplementary data

Supplementary material related to this article can be found, in the online version, at doi:https://doi.org/10.1016/j.snb.2019.04.083.

References

[1] M.J.S. Spencer, Gas sensing applications of 1D-nanostructured zinc oxide: insights from density functional theory calculations, Prog. Mater. Sci. 57 (2012) 437–486, https://doi.org/10.1016/j.pmatsci.2011.06.001.
[2] A. Mirzaei, S.G. Leonardi, G. Neri, Detection of hazardous volatile organic compounds (VOCs) by metal oxide nanostructures-based gas sensors: a review, Ceram. Int. 42 (2016) 15119–15141, https://doi.org/10.1016/j.ceramint.2016.06.145.
[3] R. Kumar, O. Al-Dossary, G. Kumar, A. Umar, Zinc oxide nanostructures for no2 gas–sensor applications: a review, Nano-Micro Lett. 7 (2014) 1–24, https://doi.org/10.1007/s40820-014-0023-3.
[4] M. Alvarado, È. Navarrete, A. Romero, L.J. Ramírez, E. Llobet, Flexible gas sensors employing octahedral indium oxide films, Sensors 18 (2018), https://doi.org/10.3390/s18040999.
[5] J.P. Cheng, J. Wang, Q.Q. Li, H.G. Liu, Y. Li, A review of recent developments in tin dioxide composites for gas sensing application, J. Ind. Eng. Chem. 44 (2016) 1–22, https://doi.org/10.1016/j.jiec.2016.08.008.
[6] Mohit Kumar, Rahul Kumar, Saravanan Rajamani, Sapana Ranwa, Mattia Fanetti, Matjaz Valant, Mahesh Kumar, Efficient room temperature hydrogen sensor based on UV-activated ZnO nano-network, Nanotechnology 28 (2017) 365502http://stacks.iop.org/0957-4484/28/i=36/a=365502.
[7] A. Paliwal, A. Sharma, M. Tomar, V. Gupta, Carbon monoxide (CO) optical gas sensor based on ZnO thin films, Sens. Actuators B Chem. 250 (2017) 679–685, https://doi.org/10.1016/j.snb.2017.05.064.
[8] A. Wei, L. Pan, W. Huang, Recent progress in the ZnO nanostructure-based sensors, Mater. Sci. Eng. B Solid-State Mater. Adv. Technol. 176 (2011) 1409–1421, https://doi.org/10.1016/j.mseb.2011.09.005.
[9] L.K. Jangir, Y. Kumari, A. Kumar, M. Kumar, K. Awasthi, Structural and morphological study of PS-ZnO nanocomposite membrane, Macromol. Symp. 357 (2015) 218–222, https://doi.org/10.1002/masy.201500020.
[10] P. Rai, J.N. Jo, I.H. Lee, Y.T. Yu, Fabrication of flower-like ZnO microstructures from ZnO nanorods and their photoluminescence properties, Mater. Chem. Phys. 124 (2010) 406–412, https://doi.org/10.1016/j.matchemphys.2010.06.055.
[11] A. Pimentel, D. Nunes, P. Duarte, J. Rodrigues, F.M. Costa, T. Monteiro, R. Martins, E. Fortunato, Synthesis of long ZnO nanorods under microwave irradiation or conventional heating, J. Phys. Chem. C 118 (2014) 14629–14639, https://doi.org/10.1021/jp5027509.
[12] J. Yang, Y. Lin, Y. Meng, Y. Liu, A two-step route to synthesize highly oriented ZnO

nanotube arrays, Ceram. Int. 38 (2012) 4555–4559, https://doi.org/10.1016/j.ceramint.2012.02.033.
[13] W. Li, H. Xu, H. Yu, T. Zhai, Q. Xu, X. Yang, J. Wang, B. Cao, Different morphologies of ZnO and their triethylamine sensing properties, J. Alloys Compd. 706 (2017) 461–469, https://doi.org/10.1016/j.jallcom.2017.02.223.
[14] D.P. Singh, Synthesis and growth of ZnO nanowires, Sci. Adv. Mater. 2 (2010) 245–272, https://doi.org/10.1166/sam.2010.1093.
[15] W. Guo, T. Liu, H. Zhang, R. Sun, Y. Chen, W. Zeng, Z. Wang, Gas-sensing performance enhancement in ZnO nanostructures by hierarchical morphology, Sens. Actuators B Chem. 166–167 (2012) 492–499, https://doi.org/10.1016/j.snb.2012.02.093.
[16] S. Safa, R. Azimirad, K. Mohammadi, R. Hejazi, A. Khayatian, Investigation of ethanol vapor sensing properties of ZnO flower-like nanostructures, Meas. J. Int. Meas. Confed. 73 (2015) 588–595, https://doi.org/10.1016/j.measurement.2015.06.001.
[17] A.P. Dral, J.E. ten Elshof, 2D metal oxide nanoflakes for sensing applications: review and perspective, Sens. Actuators B Chem. 272 (2018) 369–392, https://doi.org/10.1016/j.snb.2018.05.157.
[18] L. Zhu, Y. Li, W. Zeng, Hydrothermal synthesis of hierarchical flower-like ZnO nanostructure and its enhanced ethanol gas-sensing properties, Appl. Surf. Sci. 427 (2018) 281–287, https://doi.org/10.1016/j.apsusc.2017.08.229.
[19] S.S. Kumar, P. Venkateswarlu, V.R. Rao, G.N. Rao, Synthesis, characterization and optical properties of zinc oxide nanoparticles, Int. Nano Lett. 3 (2013) 30, https://doi.org/10.1186/2228-5326-3-30.
[20] L. Xu, Y. Guo, Q. Liao, J. Zhang, D. Xu, Morphological control of ZnO nanostructures by electrodeposition morphological control of ZnO nanostructures by electrodeposition, J. Phys. Chem. B 109 (2005) 13519–13522, https://doi.org/10.1021/jp051007b.
[21] H. Wu, W. Pan, Preparation of zinc oxide nanofibers by electrospinning, J. Am. Ceram. Soc. 89 (2006) 699–701, https://doi.org/10.1111/j.1551-2916.2005.00735.x.
[22] T. Van Khai, L. Van Thu, L.T.T. Ha, V.M. Thanh, T.D. Lam, Structural, optical and gas sensing properties of vertically well-aligned ZnO nanowires grown on graphene/Si substrate by thermal evaporation method, Mater. Charact. 141 (2018) 296–317, https://doi.org/10.1016/j.matchar.2018.04.047.
[23] A. Singh, A. Sharma, M. Tomar, V. Gupta, Growth of highly porous ZnO nanostructures for carbon monoxide gas sensing, Surf. Coat. Technol. 343 (2018) 49–56, https://doi.org/10.1016/j.surfcoat.2017.11.020.
[24] S. Wei, J. Zhao, B. Hu, K. Wu, W. Du, M. Zhou, Hydrothermal synthesis and gas sensing properties of hexagonal and orthorhombic WO3nanostructures, Ceram. Int. 43 (2017) 2579–2585, https://doi.org/10.1016/j.ceramint.2016.11.064.
[25] C. Peng, J. Guo, W. Yang, C. Shi, M. Liu, Y. Zheng, J. Xu, P. Chen, T. Huang, Y. Yang, Synthesis of three-dimensional flower-like hierarchical ZnO nanostructure and its enhanced acetone gas sensing properties, J. Alloys Compd. 654 (2016) 371–378, https://doi.org/10.1016/j.jallcom.2015.09.120.
[26] J. Xiong, G. Cheng, G. Li, F. Qin, R. Chen, Well-crystallized square-like 2D BiOCl nanoplates: mannitol-assisted hydrothermal synthesis and improved visible-light-driven photocatalytic performance, RSC Adv. 1 (2011) 1542–1553.
[27] H. Wang, T. Liang, X. Yu, W. Zhao, R. Xu, D. Wang, Y. Liu, Hydrothermal synthesis of well-crystallized CuO hierarchical structures and their direct application in high performance lithium-ion battery electrodes without further calcination, RSC Adv. 6 (2016) 96882–96888, https://doi.org/10.1039/C6RA20701D.
[28] S. Bai, T. Guo, D. Li, R. Luo, A. Chen, C.C. Liu, Intrinsic sensing properties of the flower-like ZnO nanostructures, Sens. Actuators B Chem. 182 (2013) 747–754, https://doi.org/10.1016/j.snb.2013.03.077.
[29] Y. Xia, J. Wang, R. Chen, D. Zhou, L. Xiang, A review on the fabrication of hierarchical ZnO nanostructures for photocatalysis application, Crystals 6 (2016) 148, https://doi.org/10.3390/cryst6110148.
[30] S. Cho, J.W. Jang, S.H. Jung, B.R. Lee, E. Oh, K.H. Lee, Precursor effects of citric acid and citrates on ZnO crystal formation, Langmuir 25 (2009) 3825–3831, https://doi.org/10.1021/la804009g.
[31] X. Qu, M. Wang, W. Sun, R. Yang, Hierarchical flower-like ZnO microstructures: preparation, formation mechanism and application in gas sensor, J. Mater. Sci. Mater. Electron. 28 (2017) 14702–14710, https://doi.org/10.1007/s10854-017-7338-z.
[32] W. Guo, One-pot synthesis of urchin-like ZnO nanostructure and its enhanced acetone gas sensing properties, J. Mater. Sci. Mater. Electron. 28 (2017) 963–972, https://doi.org/10.1007/s10854-016-5615-x.
[33] K. Shingange, Z.P. Tshabalala, B.P. Dhonge, O.M. Ntwaeaborwa, D.E. Motaung, G.H. Mhlongo, 0D to 3D ZnO nanostructures and their luminescence, magnetic and sensing properties: influence of pH and annealing, Mater. Res. Bull. 85 (2017) 52–63, https://doi.org/10.1016/j.materresbull.2016.09.003.
[34] J. Luo, S.Y. Ma, A.M. Sun, L. Cheng, G.J. Yang, T. Wang, W.Q. Li, X.B. Li, Y.Z. Mao, D.J. Gz, Ethanol sensing enhancement by optimizing ZnO nanostructure: from 1D nanorods to 3D nanoflower, Mater. Lett. 137 (2014) 17–20.
[35] F. Demoisson, R. Piolet, F. Bernard, Hydrothermal synthesis of ZnO crystals from Zn(OH)2 metastable phases at room to supercritical conditions, Cryst. Growth Des. 14 (2014) 5388–5396, https://doi.org/10.1021/cg500407r.
[36] Y. Yang, H. Li, F. Hou, J. Hu, X. Zhang, Y. Wang, Facile synthesis of ZnO/Ag nanocomposites with enhanced photocatalytic properties under visible light, Mater. Lett. 180 (2016) 97–100, https://doi.org/10.1016/j.matlet.2016.05.117.
[37] H.A. Wahab, A.A. Salama, A.A. El-Saeid, O. Nur, M. Willander, I.K. Battisha, Optical, structural and morphological studies of (ZnO) nano-rod thin films for biosensor applications using sol gel technique, Results Phys. 3 (2013) 46–51, https://doi.org/10.1016/j.rinp.2013.01.005.
[38] F.K. Shan, B.I. Kim, G.X. Liu, Z.F. Liu, J.Y. Sohn, W.J. Lee, B.C. Shin, Y.S. Yu, Blueshift of near band edge emission in Mg doped ZnO thin films and aging, J. Appl. Phys. 95 (2004) 4772–4776, https://doi.org/10.1063/1.1690091.
[39] R. Al-Gaashani, S. Radiman, A.R. Daud, N. Tabet, Y. Al-Douri, XPS and optical studies of different morphologies of ZnO nanostructures prepared by microwave methods, Ceram. Int. 39 (2013) 2283–2292, https://doi.org/10.1016/j.ceramint.2012.08.075.
[40] L. Kumar Jangir, Y. Kumari, A. Kumar, M. Kumar, K. Awasthi, Investigation of luminescence and structural properties of ZnO nanoparticles, synthesized with different precursors, Mater. Chem. Front. 1 (2017) 1413–1421, https://doi.org/10.1039/C7QM00058H.
[41] M. Ghosh, A.K. Raychaudhuri, Shape transition in ZnO nanostructures and its effect on blue-green photoluminescence, Nanotechnology 19 (2008) 1–16, https://doi.org/10.1088/0957-4484/19/44/445704.
[42] J.S. Reparaz, G. Callsen, M.R. Wagner, F. Güell, J.R. Morante, C.M. Sotomayor Torres, A. Hoffmann, Spatial mapping of exciton lifetimes in single ZnO nanowires, Appl. Mater. 1 (2013) 12103.
[43] F. Güell, P.R. Martínez-Alanis, Tailoring the Green, Yellow and Red defect emission bands in ZnO nanowires via the growth parameters, J. Lumin. (2019).
[44] F. Güell, P.R. Martínez-Alanis, S. Khachadorian, J. Rubio-García, A. Franke, A. Hoffmann, G. Santana, Raman and photoluminescence properties of ZnO nanowires grown by a catalyst-free vapor-transport process using ZnO nanoparticle seeds, Phys. Status Solidi 253 (2016) 883–888.
[45] S. Roso, F. Güell, P.R. Martínez-alanis, A. Urakawa, E. Llobet, Sensors and Actuators B : chemical Synthesis of ZnO nanowires and impacts of their orientation and defects on their gas sensing properties, Sens. Actuators B. Chem. 230 (2016) 109–114, https://doi.org/10.1016/j.snb.2016.02.048.
[46] Y. Zhang, J. Xu, Q. Xiang, H. Li, Q. Pan, P. Xu, Brush-like hierarchical ZnO nanostructures : synthesis, photoluminescence and gas sensor properties, J. Phys. Chem. C. 113 (2009) 3430–3435, https://doi.org/10.1021/jp8092258.
[47] N. Barsan, U. Weimar, Conduction model of metal oxide gas sensors, J. Electroceramics. 7 (2001) 143–167.
[48] A. Ponzoni, C. Baratto, N. Cattabiani, M. Falasconi, V. Galstyan, E. Nunez-carmona, F. Rigoni, V. Sberveglieri, G. Zambotti, D. Zappa, Issues Addressed at the SENSOR Lab, Brescia (Italy), (n.d.). doi:https://doi.org/10.3390/s17040714.
[49] R. Kumar, O. Al-Dossary, G. Kumar, A. Umar, Zinc oxide nanostructures for NO2gas–sensor applications: a review, Nano-Micro Lett. 7 (2015) 97–120, https://doi.org/10.1007/s40820-014-0023-3.
[50] N. Han, X. Wu, L. Chai, H. Liu, Y. Chen, Counterintuitive sensing mechanism of ZnO nanoparticle based gas sensors, Sens. Actuators B Chem. 150 (2010) 230–238, https://doi.org/10.1016/j.snb.2010.07.009.

An outstanding chemical synthesis route methodology is Chemical Vapor Deposition (CVD), a bottom-up technique. Chemical vapor deposition is widely used in the industry as wells as in laboratories to produce thin films on top of different substrates. Not only thin films but also a wide range of morphologies can be achieved by tailoring the substrate, design of precursors, adjusting temperatures or flows and by taking advantage of processes like self-assembly occurring in nanostructures. Chemical vapor deposition has three main parts; the volatilization of the organic precursors, their transfer to the reactor and the growth stage (Fig 4.). When growing metal oxide nanostructure through this methodology, organic precursors such as coordination compounds are mainly used.

The main requirement to be a suitable precursor is presenting a low vapor pressure to be brought to gas phase. Furthermore, chemical vapor deposition reactors work under vacuum or ultra-high vacuum to ensure that the chemical compounds present inside the reactor are the ones generated by the precursor. Therefore, the main drawbacks of such methodology are mainly regarding the complexity of the equipment to create and maintain the vacuum and the finding of suitable precursors to be employed. In order to overcome these major drawbacks in this thesis, the Aerosol Assisted Chemical Vapor Deposition (AACVD) has been employed in order to obtain single crystalline semiconductor metal oxide nanomaterials, in particular tungsten trioxide nanowires. The aerosol assisted chemical vapor deposition is a methodology that operates under the same principles as traditional chemical vapor deposition, except that it works at atmospheric pressure and, therefore, the use of vacuum is avoided. In addition, the precursors are dissolved in organic solvents. Such solvents present low vapor pressure and through high frequency waves (via an ultrasonic generator) are easily brought into an aerosol mist which, in a further step, would be transferred from a flask towards the reactor employing a stream of an inert gas, i.e. nitrogen (N_2) or argon (Ar). Employing the AACVD enables the usage of

a wide range precursors that have a high vapor pressure and are by no other means suitable to be used as precursors in traditional CVD. In figure 4 a schematic diagram of an AACVD system is shown.

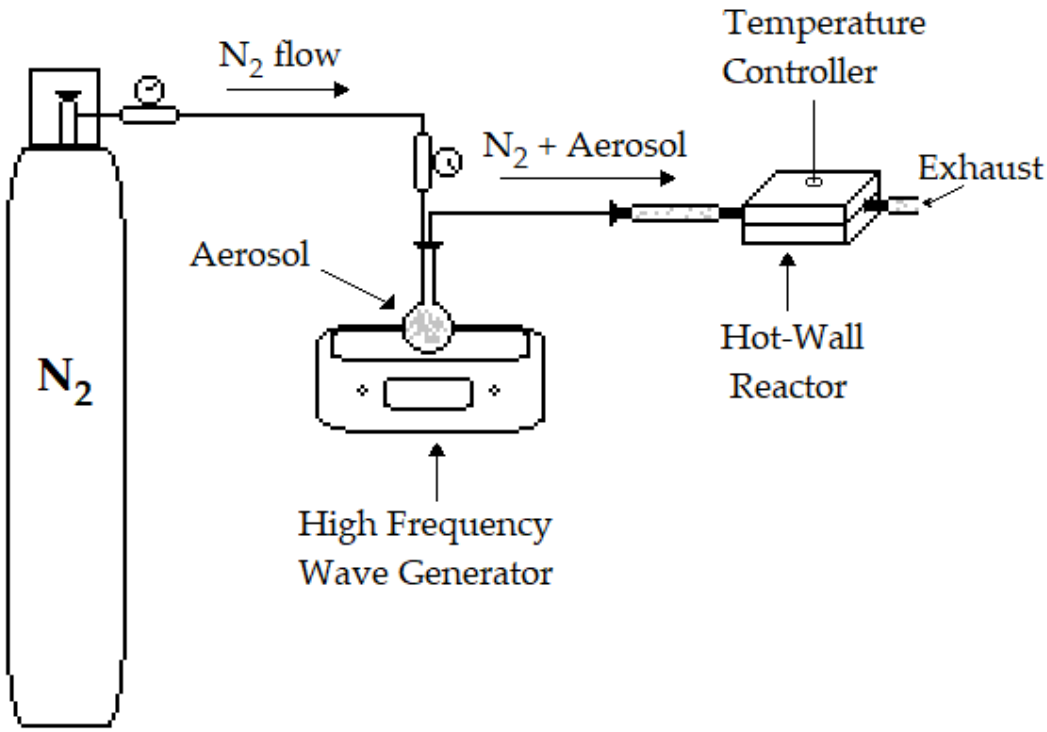

Figure 4. Schematic AACVD representation of the whole methodology set up.

2.3. Heterojunction gas sensors

As discussed before, SMOX present some drawbacks such as the issues regarding baseline stability and response time in the article "Using a second order…". However, the more important drawback to be overcome is their lack of selectivity. As we explained before, the nanomaterials present oxygen adsorbed species at their surface and such species react in higher or lower proportion with the gases present in the environment of the sensors. Therefore, employing an active layer based on a single metal oxide for performing an analysis of a complex mixture of gases is extremely challenging due to the lack of selectivity experienced. There have been different approaches to overcome such drawback,

for instance applying filters to the system to constrain the interaction of the sensing layer with a specific target gas or, to a much more complex approach, the chemical/ electronic sensitization of the sensing layer. Chemical/ electronic sensitization consists of the enhancement of either the chemical interactions of the sensing layer with the gases in the environment or an enhancement on the electronic properties of the material. Ideally, this sensitization is achieved for a very specific gas target of gas family, thus boosting selectivity. A suitable approach employed for achieving such sensitization effects has been the use of heterojunction semiconductor metal oxides [33][34][35].

Achieving heterojunction nanomaterials consists of growing combined n-type and p-type semiconductor metal oxides. In the approach employed in this thesis, when combined, one of the materials is the host and has the higher percentage in weight and the other is the loading element, which has the lower percentage in weight (n-p heterojunction or p-n heterojunction). Three different scenarios could be distinguished when a heterojunction is formed: chemical sensitization, electronic sensitization and the combination of both. The most common host materials employed are n-type semiconductors such as SnO_2, WO_3, ZnO among others, loaded with nanoparticles from noble metals or noble metal oxides, i.e. gold (Au), Platinum (Pt), Palladium (Pd). In the first scenario a nanoparticle is placed on to the surface of the sensing layer (Fig. 5. a). This nanoparticle acts as a catalyst with a higher affinity towards a specific gas. For instance, the most common example is an n-type semiconductor loaded with palladium oxide nanoparticles for hydrogen sensing. When hydrogen molecules reach the palladium oxide nanoparticle surface, their get chemisorbed and subsequently split. Then, through a spill over mechanism, the hydrogen atoms start their migration towards the n-type part of the sensing layer surface and react with the oxygen species there present. Such chemical sensitization boosts dramatically the

sensor response towards hydrogen, leaving the response attributed to other gases almost negligible [36].

On the other hand, an electronic sensitization occurs in the areas where the depletion zone from the n-type semiconductor is in contact with a p-type material (see Fig 5. b). Due to the nature of both semiconductors a flow of electrons is transferred from the n-type material towards the p-type material charging both and developing a depletion zone by creating potential wells. In the first place, the loading of an n-type host material with nanoparticles of a p-type material increases the overall resistance of a film in comparison to a film in which only pristine material were used. For example, the conduction channel of a tungsten oxide (n-type) nanowire is narrowed in the different areas were p-type nanoparticles are located due to the development of multiple depletion zones due to the mentioned migration of charges. Secondly, the p-type material nanoparticles become strongly charged and, therefore, can react in higher proportion to a specific gas from the sensor environment. When a chemical reaction takes place at the surface of the p-type material, the electrons released from such reaction flow back towards the n-type host, widening the conduction channel. For instance, when measuring different gases, a pristine sensor could produce a slightly stronger signal towards a gas and lower signals for others but, when electronically sensitized, the stronger signal is boosted meanwhile the weak signals remain not so affected. In the third scenario, a combination of chemical and electronic sensitization occurs for specific gases.

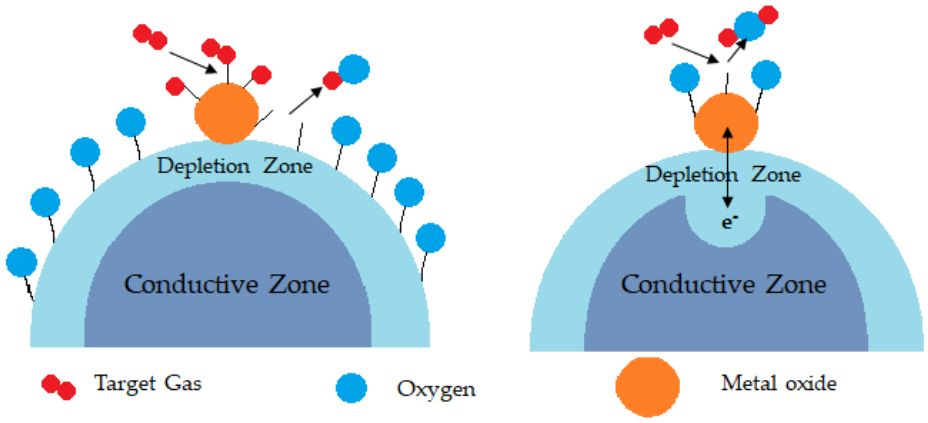

Figure 5. Schematic representation of an p-n heterojunction. Left; Chemical sensitization. Right; Electronic sensitization.

The most studied materials as p-type loading semiconductors by far are noble metals for their outstanding properties as their chemical stability, chemical reactivity and thermal properties. Despite being suitable candidates to be employed, there are also expensive in comparison to most of the transition-metals. Furthermore, transition-metals apart from being less expensive than noble metals, are interesting candidates to act as loading elements due to their higher reactivity. When synthetizing a new heterojunction with a transition metal it is important to perform a screening of different gases at different operating temperatures in order to determine the ability of such *p-n* heteromaterial to distinguish among gases. In this thesis, we presented tungsten trioxide nanowires loaded with nickel oxide, cobalt oxide or iridium oxide synthetized through aerosol assisted chemical vapor deposition in order to improve the response of the sensing layer towards hydrogen sulfide, ethanol and nitrogen dioxide respectively.

2.3.1 AACVD and gas sensing properties of nickel oxide nanoparticle decorated tungsten oxide nanowires

Journal of Materials Chemistry C

PAPER

View Article Online
View Journal

Cite this: DOI: 10.1039/c8tc00571k

AACVD and gas sensing properties of nickel oxide nanoparticle decorated tungsten oxide nanowires†

Eric Navarrete, [a] Carla Bittencourt,[b] Polona Umek[c] and Eduard Llobet *[a]

Here, we show that the aerosol assisted chemical vapor deposition process is suitable for growing single crystalline tungsten oxide nanowires loaded with nickel oxide nanoparticles. This method allows achieving of a wide range of nickel oxide loadings on tungsten oxide nanowires with high effectivity. It also allows for the direct growth of these nanomaterials onto application substrates for developing resistive metal oxide gas sensors. Different morphological and compositional analysis tools have been employed for the characterization of the nanomaterials, finding that nickel oxide nanoparticles are homogeneously distributed over the tungsten oxide nanowire surface. However, at high Ni loadings, even though the size of the nanoparticles remains unchanged, they form agglomerates, especially at the tips of tungsten nanowires. The gas sensing properties of the different nanomaterials grown towards methane, ethanol, nitrogen dioxide and hydrogen sulfide have been studied. The optimized loading of tungsten oxide with nickel oxide nanoparticles has a positive effect on increasing the sensitivity and selectivity of the resulting nanomaterial to hydrogen sulfide, reaching a five-fold increase in the response towards this species. This improvement is attributed to combined chemical and electronic sensitization effects. Therefore, these nanomaterials show good potential for developing inexpensive resistive sensors able to monitor the presence of hydrogen sulfide in the environment.

Received 2nd February 2018,
Accepted 17th April 2018

DOI: 10.1039/c8tc00571k

rsc.li/materials-c

1. Introduction

The growth in worldwide industrial activity, the ever-growing number of circulating cars and the associated increase in energy demands are boosting global gas emissions.[1] This is becoming a serious threat to our environment and to human health.[2] As a result, there is a strong demand for developing rugged, sensitive, selective and inexpensive detection systems that could become ubiquitous for reliably monitoring air quality (indoors and outdoors). Resistive metal oxide gas sensors have been the object of sustained research efforts in the last few decades, since they meet many of the requirements for integrating inexpensive air-quality monitoring systems.[3,4] Highly sensitive to toxic and flammable gases, metal oxides can be mass-produced by employing a wide range of synthesis routes.[4,5] However, the lack of selectivity and cross-sensitivity to ambient moisture remain the most important drawbacks to be overcome.

Most research efforts have been directed towards the study of n-type metal oxides such as SnO_2, ZnO, In_2O_3 or WO_3 because these are, generally, more sensitive than p-type metal oxides.[6–9] The loading of metal oxides with nanoparticles of metal catalysts has been employed extensively both for enhancing sensitivity and tuning the selectivity of gas sensors.[10] Such nanoparticles can induce chemical sensitization effects. For example, by increasing the amount of reactive oxygen species adsorbed on the surface of the semiconductor metal oxide and/or by dissociating the target molecules and favoring their reaction with oxygen adsorbates *via* spillover effects.[11] More recently, with the development of single-crystalline, nanostructured metal oxides (*e.g.* nanorods, nanowires), the synthesis of n-type metal oxide nanowires decorated with p-type metal oxide nanoparticles has been reported.[12] In such a structure, multiple n–p heterojunctions are formed at the nanoscale, which may lead to important electronic sensitization effects.[12,13] Upon the formation of n–p heterojunctions, electrons are transferred from the n-type metal oxide to the p-type nanoparticles and depletion zones develop. When gaseous species adsorb onto nanoparticles, this results in additional electronic charge transfer between the p-type nanoparticles and the supporting n-type metal oxide, modifying the width of depletion zones and dramatically altering the overall electrical conductance of a film. Recently, we have developed two

[a] MINOS-EMaS, Universitat Rovira i Virgili, Avda. Països Catalans, 26, 43007 Tarragona, Spain. E-mail: eduard.llobet@urv.cat; Tel: +34 977 558 502
[b] Chimie des Interactions Plasma – Surface (ChIPS), Research Institute for Materials Science and Engineering, Université de Mons, Avenue Copernic 1, 7000 Mons, Belgium
[c] Jožef Stefan Institute, Jamova cesta 39, 10000 Ljubljana, Slovenia
† Electronic supplementary information (ESI) available. See DOI: 10.1039/c8tc00571k

examples of such an approach. In the first case, films of single-crystalline, n-type tungsten oxide nanowires decorated with p-type copper oxide were devised for the selective detection of hydrogen sulfide. When in the presence of H_2S, p-type copper oxide becomes metallic copper sulfide by a mechanism of oxygen–sulfur replacement. While p–n heterojunctions are destroyed, a large number of electrons are released to the n-type metal oxide nanowires and the conductivity of the film is highly increased.[14] In a second example, n-type tungsten oxide nanowires decorated with p-type palladium oxide were employed for the selective detection of hydrogen. In this case, similarly to the previously described situation, p-type palladium oxide becomes metallic palladium hydride in the presence of hydrogen at low operating temperatures.[15] These sensors are reversible because copper sulfide and palladium hydride again become copper or palladium oxides when hydrogen sulfide or hydrogen are removed from the sensor environment, respectively.[14,15]

Late transition metals, such as the already mentioned copper and palladium or platinum,[16] oxidize to p-type metal oxides due to normal operation during gas sensing. In that sense, it is worth exploring the loading of n-type metal oxides with other p-type, late transition metal oxide nanoparticles and studying the implications on sensitivity and selectivity. This paper addresses the loading of tungsten oxide nanowires with nickel oxide (NiO) nanoparticles. NiO has been known to be a p-type metal oxide for a long time, with a reported large work function of 5.4 eV and an optical bandgap ranging from 3.6 to 4.0 eV.[17] Its p-type character is attributed to the spontaneously formed Ni vacancies.[18] The use of NiO for gas sensing has been reported already. For example, Kim and co-workers[19] and Yoon and co-workers[20] employed Fe-doped, p-type NiO for detecting 100 ppm ethanol. Cho and co-workers reported Pt-doped, p-type NiO nanotubes for detecting ethanol.[21] Huo and co-workers reported a high response of NiO nanowall arrays to hydrogen sulfide.[22] Additionally, loading p-type NiO nanoparticles onto n-type metal oxide structures has been shown to increase gas sensing performance (*e.g.*, by lowering response times or humidity cross-sensitivity).[23] NiO supported by ZnO structures has been reported for detecting ammonia[24] and nitrogen dioxide.[25] NiO combined with indium oxide[26] or NiO supported onto tin oxide nanofibers[27] has been studied for detecting ammonia and nitrogen dioxide, respectively. Nickel oxide supported by thin or thick tungsten oxide films has been reported as well. Noh and co-workers employed a sol–gel method to incorporate NiO into a tungsten oxide matrix for developing a nitrogen dioxide sensor.[28] Vuong and co-workers loaded a sputtering-deposited tungsten oxide thin film with Ni_2O_3.[29] They grew *via* arc-discharge carbon nanotubes on top of the tungsten oxide film employing Ni as a catalyst, which was followed by a calcination process to burn out the carbon nanotubes, leaving nickel oxide nanoparticles. These films were applied to the detection of ammonia vapors. One of the problems associated with the use of high temperatures during calcination steps is the formation of $NiWO_4$ species, which act as a charge barrier, decreasing sensor performance.

Here, we report the growth and gas sensing properties of NiO nanoparticles supported by tungsten oxide nanowires. An aerosol assisted chemical vapor deposition (AACVD) method is used, which is run at temperatures that avoid the formation of $NiWO_4$. This paper presents an in-depth characterization of the morphology and chemical composition of the nanomaterials synthesized, and it addresses the effects of NiO loading on their gas sensing properties. It explores the selectivity and cross-sensitivity to ambient moisture and discusses gas sensing mechanisms, with special emphasis on the detection of hydrogen sulfide. To the best of our knowledge, the loading of tungsten oxide nanowires with nickel oxide nanoparticles for sensing hydrogen sulfide has been reported only once before. This was a conference paper in which we presented very preliminary and incomplete results.[30] In this preliminary work, the nickel oxide loading was not optimized. Despite the fact that the amount of precursors used was high, the synthesis methodology employed allowed only for a rather inhomogeneous and low concentration loading of nickel oxide nanoparticles on tungsten oxide nanowires. This resulted in nanomaterials with a significantly lower hydrogen sulfide response than the ones reported here (about four times lower). In addition, the effect of ambient moisture on sensor response was not studied, in contrast to what is reported here.

A significant amount of research has been conducted on metal oxide hydrogen sulfide sensors. Zhang and co-workers described the use of Pt-doped, α-Fe_2O_3 nanoparticles[31] while Zheng and co-workers studied α-Fe_2O_3 nanochains[32] or nanoparticles[33] for developing chemoresistive hydrogen sulfide sensors. Iron oxide is a good candidate for detecting H_2S because it has been widely employed as a catalyst in the oxidation of hydrogen sulfide in desulfurization processes.[34] However, one of the main drawbacks for these nanomaterials is their strong cross-sensitivity towards ethanol. Yu and co-workers suggested using $NiFe_2O_4$ and obtained a high response towards low concentrations of H_2S. However, their sensor displayed important cross-sensitivity to hydrogen.[35] Kapse and co-workers introduced a spinel ($Ni_{0.6}Zn_{0.4}Fe_2O_4$) displaying a good response towards H_2S, but this material also presented a significant cross-sensitivity towards ethanol, propane, butane and ammonia.[36] Many reports can be found in the literature about employing nano-sized CuO supported on different n-type metal oxides such as SnO_2,[37] ZnO[38] or WO_3.[14] The transformation of CuO, a p-type semiconductor, into CuS, which shows metallic characteristics, upon exposure to H_2S is the reason for the high H_2S responses observed.[14,37] However, CuO supported on SnO_2, ZnO or WO_3 shows important hydrogen cross-sensitivity. Furthermore, CuO–ZnO exhibits a cross-sensitivity towards methane too and CuO–WO_3 sensors suffer from additional cross-sensitivity towards nitrogen dioxide. Finally, an exception is made in the case of CuO–WO_3,[14] and no data are available on the cross-sensitivity to ambient moisture for the above-discussed materials. Table 1 summarizes the main characteristics of recently reported metal oxide nanomaterials and their performance in the detection of hydrogen sulfide. The interested reader is referred to a recent paper[39] on hydrogen sulfide sensors for a more comprehensive review.

Table 1 Summary of results obtained in the chemo-resistive detection of H_2S employing different metal oxide nanomaterials

Nanomaterial	Operating temperature	Response to H_2S	Range	Response time	Selectivity (not affected by, unless otherwise indicated)	Ref.
α-Fe_2O_3 nanochains	285 °C	20 (100 ppm)[a]	1–100 ppm	8.6 s	NA[c]	32
α-Fe_2O_3 nanoparticles	300 °C	5 (10 ppm)[a]	0.05–100 ppm	30 s	NA[c]	33
Pt-doped α-Fe_2O_3 film	160 °C	330 (100 ppm)[a]	10–1000 ppm	>1 min	Ethane, carbon monoxide, significant cross-sensitivity to ethanol and ammonia. Effect of ambient moisture not available.	31
$NiFe_2O_4$	300 °C	35.8 (5 ppm)[a]	5–200 ppm	15 s	Liquefied petroleum gas, methane, carbon monoxide, butane, significant cross-sensitivity to hydrogen. Effect of ambient moisture not available.	35
$Ni_{0.6}Zn_{0.4}Fe_2O_4$	225 °C	0.8 (50 ppm)[b]	NA[c]	10 s	Significant cross-sensitivity to ethanol, liquefied petroleum gas, ammonia. Effect of ambient moisture not available.	36
CuO–SnO_2	150 °C	0.81 (1000 ppm)[b]	200–2500 ppm	53 s	Hydrogen, carbon monoxide, liquefied petroleum gas, sulfur dioxide. Effect of ambient moisture not available. Response saturates for H_2S concentrations higher than 1500 ppm.	37
CuO–ZnO	200 °C	83.5 (5 ppm)[a]	5–100 ppm	572 s	Carbon monoxide, ammonia, hydrogen, methane. Effect of ambient moisture not available.	38
Copper oxides–WO_3	390 °C	26 (5 ppm)[a]	0.3–5 ppm	2 s	Hydrogen, carbon monoxide, ammonia, benzene, nitrogen dioxide. Resilient to changes in the background humidity.	14
Nickel oxides NP–WO_3 nanowires	**250 °C**	**13 (50 ppm)[a]**	**5–50 ppm**	**88 s**	**No significant cross-sensitivity. 30% R.H. enhances response towards low concentration H_2S.**	**This work**

[a] R_{air}/R_{gas}. [b] $(R_{air} - R_{gas})/R_{air}$. [c] NA: not available.

2. Experimental

2.1. Material synthesis

Pure and Ni-decorated forests of tungsten oxide nanowires were grown by aerosol assisted chemical vapor deposition (AACVD). Tungsten hexacarbonyl ($W(CO)_6$) of 97% purity and nickel(II) acetylacetonate ($Ni(acac)_2$) of 95% purity, both from Sigma-Aldrich, were used without further purification for obtaining tungsten oxide and nickel oxide nanoparticles, respectively. Two approaches, *i.e.* single-step or two-step growth, were considered for the synthesis of the nanomaterials. At first, a single step growth was implemented. In this strategy, $W(CO)_6$ and $Ni(acac)_2$ are dissolved in a mixture of acetone and methanol and the AACVD process is run to obtain Ni-decorated tungsten oxide nanowires. Despite our efforts in optimizing the acetone/methanol ratio and deposition temperature (these two parameters have a strong influence on the morphology of the resulting nanomaterials), this one-step approach failed to produce homogeneously decorated tungsten oxide nanowires with a wide enough range of Ni loadings (see the ESI†). In the second approach, at first, pure tungsten oxide nanowires are grown *via* AACVD. Then, a second AACVD process is conducted to decorate some of the previously grown tungsten oxide nanowire samples with nickel oxide nanoparticles. Employing this two-step approach, samples of tungsten oxide nanowires with four different levels of Ni loading were obtained.

When growing the pure tungsten oxide nanowires, the precursor solution was prepared by dissolving 50 mg of tungsten hexacarbonyl in an acetone : methanol (ratio 3 : 1) mixture. This solution was placed under ultra-sonication to form an aerosol, which was input to the reactor chamber using a 0.5 L min^{-1} nitrogen flow. The reactor was kept at 400 °C during the whole deposition process, which lasted until the total consumption of the precursor solution. The deposition took place, *via* a shadow mask, onto the electrode area (2.5 × 2.5 mm^2) of commercially available alumina transducers (Ceram Tech GmBH, Plochingen, Germany). Transducers consist of a pair of Pt interdigitated electrodes (front side) with an electrode gap of 300 μm, and a Pt heating resistor (back side). As-deposited tungsten oxide nanowire films display a dark-blue color, which is due to tungsten oxide being sub-stoichiometric and to carbon residues from the precursors and solvents used. Coated transducers were then placed inside a muffle to undergo an annealing treatment at 500 °C under a flow of pure dry air. Annealed samples display a pale-yellow color, indicating that most of the carbon contamination has been removed and tungsten oxide is close to stoichiometric. For those samples in which tungsten oxide was loaded with different amounts of Ni, a second AACVD process was conducted. For achieving 4 different levels of Ni loading, in this second step, four methanol solutions having different $Ni(acac)_2$ concentrations (*i.e.*, 2.5, 5, 10 and 15 mg of nickel precursor dissolved in 10 mL of methanol) were used. Nitrogen flow and deposition temperature were identical to the ones employed during the first step. A second annealing process was performed as well employing the same conditions described above.

The crystalline phase, morphology and chemical composition of the different nanomaterials grown on transducer substrates were investigated employing X-ray diffraction (XRD), scanning electron microscopy (SEM), high-resolution electron transmission microscopy (HR-TEM), energy-dispersive X-ray (EDX) spectroscopy and X-ray photoelectron spectroscopy (XPS). XRD was performed employing a Bruker-AXS D8-Discover diffractometer with a parallel

incident beam. Scanning electron microscopy images were acquired using a SU8020 Microscope from Hitachi and a JEOL 7600F field emission SEM. The image resolution was set to 512 × 384 pixels while the corresponding map resolution was set to 128 × 96 pixels, meaning a pixel size of 0.01 μm in the image and 0.05 μm in the map. EDX spectra were acquired using a microanalysis tool from Oxford Instruments. HRTEM characterization of the samples was performed on a Jeol 2100 microscope, working at 200 kV. XPS was conducted using a VERSAPROBE PHI 5000 from Physical Electronics, equipped with a monochromatic Al Kα X-ray source. The X-ray photoelectron spectra were collected at the take-off angle of 45° with respect to the electron energy analyzer operated in the CAE (constant analyzer energy) mode. For the compensation of built-up charge on the sample surface during the measurements, a dual beam charge neutralization composed of an electron gun (≈1 eV) and an Ar ion gun (≤10 eV) was used. Binding energies are all referenced to the C1s peak at 284.6 eV.

2.2. Gas sensing experiments

The gas sensing properties of the different nanomaterials were investigated. In particular, the main objective was to study how different levels of Ni loading affected the gas sensing properties of tungsten oxide nanowires. For doing so, AACVD-grown, pure tungsten oxide and Ni-loaded tungsten oxide nanowire sensors were placed inside an inert, airtight Teflon® chamber. Calibrated gas bottles of ethanol, methane, hydrogen sulfide and nitrogen dioxide balanced in air were employed. The carrier gas was zero-grade dry air. A computer-driven, automated mass-flow control system was employed to deliver reproducible concentrations of the different gases and vapors tested to the sensor chamber. The concentrations measured were 5, 10, 15 and 20 ppm for ethanol and methane; 10, 15, 25 and 50 ppm for hydrogen sulfide and 10 ppm for nitrogen dioxide. The baseline of the sensors was recovered under dry air. A 100 mL min^{-1} constant flow was input to the gas sensor chamber. During experiments, the dc electrical resistance of the sensors was monitored, acquired and stored employing a Keysight 3972A data acquisition system. The heating resistors of the sensors were driven by an Agilent U8001A power supply to set the operating temperature. Operating temperatures were set at 150, 200 and 250 °C. Achieving good sensing performance at low–moderate operating temperatures is essential to reduce power consumption. A liquid mass flow was employed as well in some specific measurements to humidify the gas flow and analyze the effect of moisture cross-sensitivity.

3. Results and discussion

3.1. Initial assessment of gas sensing properties

An initial screening of gas sensing properties was conducted to determine whether it was worth studying in depth all four levels of Ni loading. The responses to different concentrations of hydrogen sulfide, ethanol and nitrogen dioxide were measured for pristine and the Ni-loaded samples. Sensor response was defined as R_{air}/R_{gas} for reducing species and R_{gas}/R_{air} for oxidizing species, where R_{air} is the resistance of the sensor in pure air (*i.e.*, baseline resistance) and R_{gas} is the resistance of the sensor exposed to a given gas or vapor. Fig. 1 shows the dynamic response and recovery for the different nanomaterials and species tested. For ease of comparison, the responses of each sensor appear normalized (*i.e.* for each sensor, the instantaneous resistance is divided by its initial baseline resistance value). Two main conclusions can be derived from these results. Some levels of Ni loading result in higher responses to the different species tested than those observed for pristine tungsten oxide. The higher levels of Ni loading, *i.e.*, those achieved employing 10 and 15 mg of nickel precursor during the AACVD process, resulted in decreased responsiveness. In metal oxide gas sensors, it is well known that too high a level of metal loading results in decreased responsiveness.[5]

Considering these results, from now on, the high levels of Ni loading are no longer studied. Only samples consisting of pure tungsten oxide and Ni loaded samples obtained employing 2.5 and 5 mg of nickel precursor are discussed. These samples are labelled as WO_3, Ni/LC and Ni/HC, respectively.

3.2. Material characterization

An XRD study was performed to obtain the crystallographic structure of the pure and Ni-loaded WO_3 nanowires. No reflection peaks due to the presence of Ni were observed in the Ni/LC or Ni/HC samples. This is generally the case for AACDV grown, metal loaded tungsten oxide nanowires.[14–16] These results are summarized in Fig. 2. The diffraction pattern of the pure WO_3 nanowire sample corresponds to the monoclinic structure of WO_3 (space group $P2/m$, JPCDS 73-2177), while diffraction patterns of both Ni-loaded samples (Ni/LC and Ni/HC) correspond to the triclinic structure of WO_3 (space group $P\bar{1}$, JPCDS 73-0305). These differences are attributed to the fact that pure tungsten oxide samples undergo only one annealing step after the AACVD growth. In contrast, the Ni-loaded samples undergo a second annealing step, which is run after the second AACVD process used to load pure tungsten oxide with Ni.

Fig. 3 shows the SEM micrographs for pure (Fig. 3 left panel) and for Ni-loaded (Fig. 3 right panel) tungsten oxide films. Both films show a similar morphology consisting of a carpet of randomly oriented nanowires. The length of the nanowires typically ranges between 4 and 12 μm and their diameter ranges from 60 to 150 nm. Some dendritic, flower-like structures are visible for both pure and Ni-loaded samples in the higher magnification insets in Fig. 3. These structures are more apparent in the Ni-loaded samples. Fig. 4 shows a higher magnification SEM micrograph taken from a Ni-loaded sample (Ni/HC). This micrograph shows that tungsten oxide nanowires are decorated with small nanoparticles. At the tip of the nanowires, these particles form bigger agglomerates in broccoli-shaped structures. EDX (see the ESI†) spectroscopy confirms the presence of Ni in the Ni-loaded samples.

SEM and TEM micrographs of the Li/LC sample shown in Fig. 5 reveal that the tips of the WO_3 nanowires are covered with particles. Similar results were observed for the Ni/HC sample (Fig. 4), however, the size of the particles and their amount are

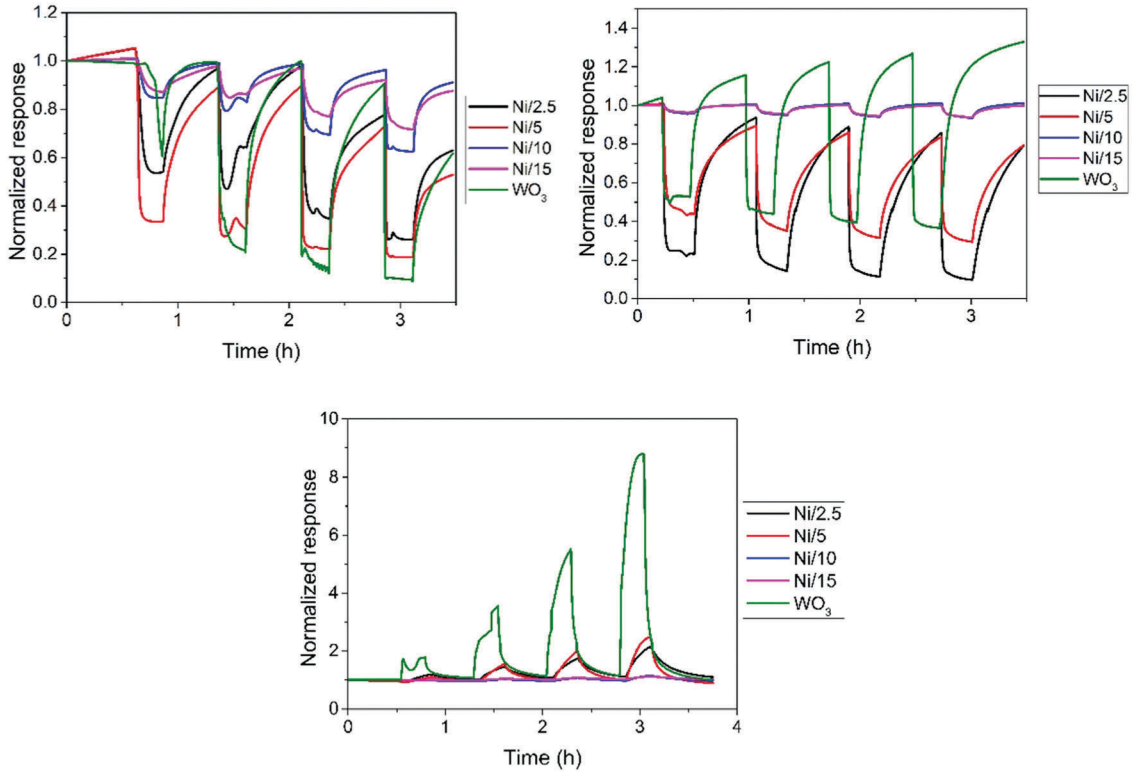

Fig. 1 Normalized dynamic response and recovery cycles of sensors that correspond to the full range of Ni loading levels. Sensors were operated at 200 °C. The different panels correspond to H_2S (upper left), ethanol (upper right) and NO_2 (lower).

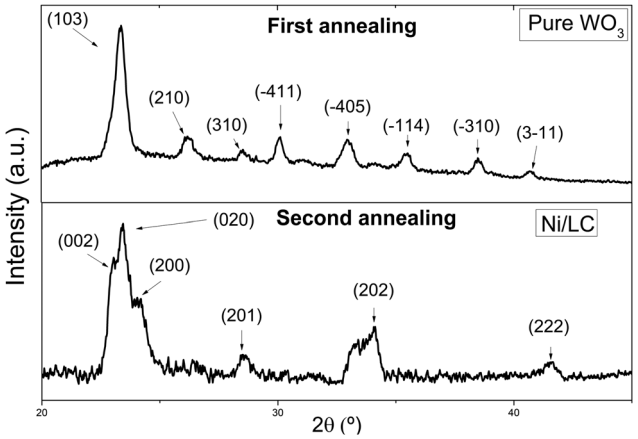

Fig. 2 Typical XRD patterns recorded on a pure tungsten oxide nanowire film, $W_{2.72}$ $P2/m$ (upper panel) and a Ni-loaded tungsten oxide nanowire film, WO_3 $P\bar{1}$ (lower panel) (Ni/LC). Pure tungsten oxide samples have undergone one annealing step only and show a monoclinic structure. Ni-Loaded tungsten oxide samples have undergone two annealing steps and show a triclinic structure.

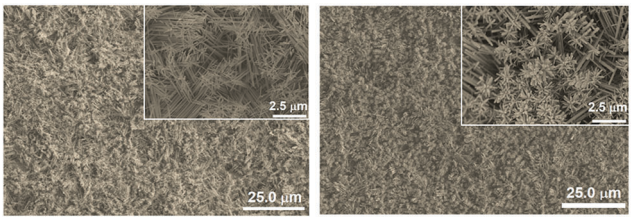

Fig. 3 Typical ESEM micrographs for pure tungsten oxide nanowire films (left panel) and for Ni-loaded tungsten oxide nanowire films (right panel) (Ni/HC). The insets show that flower-like nanostructures appear in both types of samples, however these are more visible in the Ni-loaded samples. Ni loaded tungsten oxide nanowires were grown employing the two-step AACVD procedure.

significantly lower than in the case of the Ni/HC sample. This agrees well with the fact that for the coverage of the WO_3 nanowires for the Ni/LC sample, a lower concentration of the nickel precursor was used. From the inset in the TEM micrograph, it is evident that particles observed at the surface are actually agglomerates composed of nanoparticles with diameters up to 2 nm. Nanoparticles appear to be amorphous and therefore the presence of Ni was only proved through EDX analysis (see the ESI†) and its chemical nature was studied with XPS (results are discussed later). In addition, WO_3 nanowires in both Ni-loaded samples are crystalline (see the ESI†); clear lattice fringes of 0.39 nm were observed, corresponding to the interplanar spacing of (002) planes in WO_3 with a triclinic structure (JPCDS 71-0305), thus agreeing with the results of XRD analysis (Fig. 2).

XPS was used for elemental and chemical analysis of the Ni-loaded, nanostructured active layers. Fig. 6a shows the typical survey spectrum recorded on the Ni doped samples in the range of 0–950 eV binding energy. In addition to the

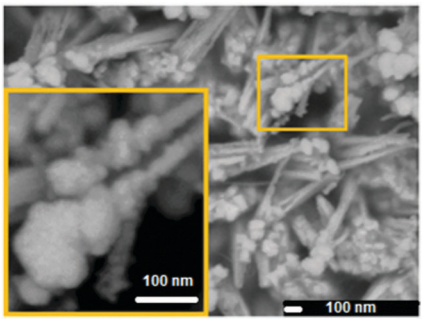

Fig. 4 SEM micrographs of the Ni/HC sample. A micrograph was taken at higher magnification for an area previously shown in the right panel of Fig. 3. Few-nanometer sized nanoparticles appear decorating the surface of the tungsten oxide nanowires. Bigger agglomerates of such nanoparticles appear at the tips of the nanowires (see the inset).

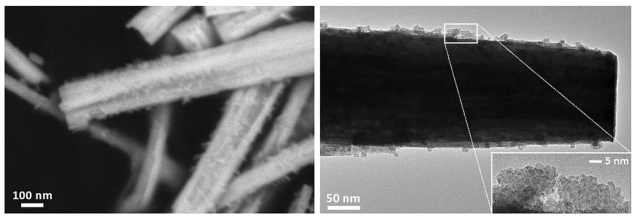

Fig. 5 SEM (left) and TEM (right) micrographs obtained from the Ni/LC sample. The inset in the TEM image is an enlargement of the area indicated.

expected characteristic peaks related to the photoelectrons emitted from tungsten and oxygen atoms, we can observe the presence of peaks related to the presence of nickel and carbon. The adventitious carbon contamination due to exposure to the atmosphere is used as a charge reference, the C–C peak at 284.6 eV. Fig. 6b shows the W 4f XP spectrum recorded on the Ni/HC sample and its fitting analysis; the spectrum was fitted using two doublets, a singlet and the Shirley background. The components centered at 41.2 eV, 37.6 and 35.5 eV are generated by photoelectrons emitted from the W $5p_{3/2}$, W $4f_{5/2}$ and W $4f_{7/2}$ core level states, respectively, in stoichiometric WO_3 (oxidation state 6+).[40] In stoichiometric WO_3, the W ions have their 5d shell empty, *i.e.*, there are no cation d-electrons available to be transferred to adsorbates. The second W 4f doublet, at 36.4 eV and 34.1 eV corresponding to W 4f5/2 and W 4f7/2 core level states, was associated with photoelectrons emitted from tungsten atoms near oxygen vacancies VO.[41] In this case, the d-electron orbitals on adjacent cations are partially occupied. These reduced cations provide active sites for chemisorption and catalytic activity, *i.e.*, influencing the gas-sensing activity of the films.[42] From the area ratio of the components used to fit the W 4f peak, we evaluated that nearly 3.5% of the tungsten atoms are near oxygen vacancies, thus contributing to gas detection.

In order to increase the sensing activity of WO_3, Ni atoms were added. Inspecting the typical XPS spectrum recorded before sensing, we observe the presence of peaks that can be associated with photoelectrons emitted from Ni, W, carbon and oxygen atoms (Fig. 6a). The relative concentration of elements is shown in Table 2. The low intensity component in the 4f W peak suggests that the WO_3 is slightly reduced (Fig. 6b). The XPS spectrum of the Ni $2p_{3/2}$ peak clearly demonstrates that NiO (Ni^{2+}, 854.7 eV), Ni_2O_3 (Ni^{3+}, 855.8 eV) and metallic (Ni^0, 853.1 eV) phases coexist. After sensing, we observed the presence of sulfur atoms at the sample surface; the XPS sulfur spectra recorded on the samples confirm the formation of Ni–S in the form of Ni_xS_x and $Ni_xS_xO_x$.

3.3. Gas sensing properties

The sensors were tested with several concentrations of methane, ethanol, nitrogen dioxide and hydrogen sulfide balanced in pure dry air. Three different operating temperatures were considered, *i.e.* 150 °C, 200 °C and 250 °C. Lower operating temperatures were not considered because these often resulted in increased response times. Higher operating temperatures were not considered either, because these significantly increased power consumption. The detection of reducing species involves the interaction with oxygen adsorbed on the surface of the metal oxides, and the nature of surface oxygen species heavily depends on temperature.[5] At operating temperatures below 150 °C, adsorbed molecular oxygen is the dominant species (O_2^-) and for temperatures ranging between 150 °C and 400 °C, O^- is the dominant species. In addition, target gas molecules are adsorbed on metal oxides, then diffuse and react with oxygen adsorbates. These adsorption and diffusion processes are also affected by temperature. While increasing the operating temperature helps to increase the number of adsorbed oxygen species, when temperature becomes higher than a certain threshold, it causes difficulties in the adsorption of the gas molecules to be detected. This is why response–temperature curves show a volcano shape and there is an optimal operating temperature for detecting a given species.[5]

3.3.1. Methane results. The sensors were tested under a flow of methane at concentrations that ranged from 5 to 20 ppm. The response towards methane of the tungsten oxide based sensors was small. When operated at 150 °C, sensors showed no response to methane. Methane response slightly increased with operating temperature. Fig. 7 summarizes these results. It was necessary to operate the sensors at 250 °C to obtain reliable results. Pure tungsten oxide shows a very small response to methane. Loading with Ni results in a slightly increased response and the lower level of Ni loading results in the highest response enhancement towards methane.

3.3.2. Ethanol results. Sensors were exposed to ethanol vapors at concentrations of 5, 10, 15 and 20 ppm balanced in dry air. The results of ethanol detection are summarized in Fig. 8. When sensors are operated at 150 °C, pure tungsten oxide shows a better ethanol responsiveness than Ni-loaded tungsten oxide. In contrast, when the operating temperature is raised, Ni-loaded tungsten oxide samples show a higher responsiveness to ethanol vapors than pure tungsten oxide. In this case, the higher Ni loading level results in the highest increase in response. However, ethanol sensitivity, *i.e.* the slope of the curves shown in Fig. 8, is very similar for pure tungsten

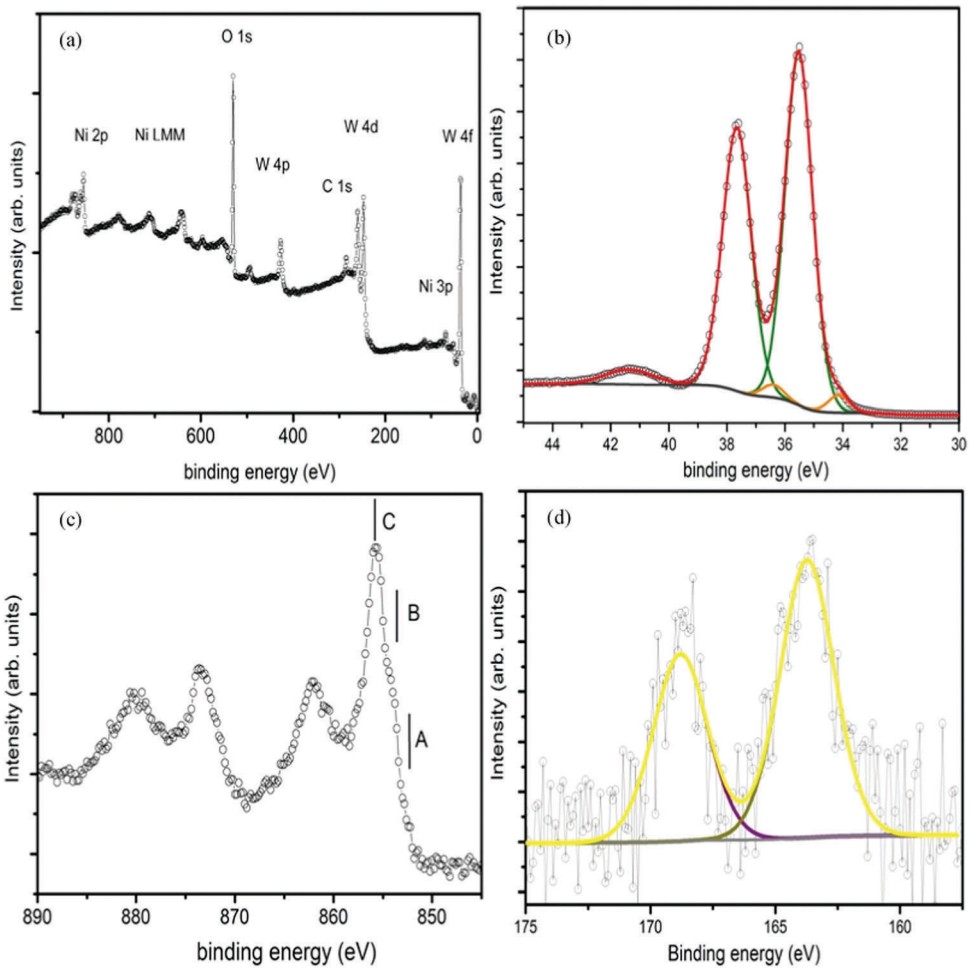

Fig. 6 (a) XPS spectrum of WO_3:Ni/HC; (b) W 4F XPS spectra of the sample WO_3:Ni/HC; (c) Ni 2P XP spectrum (WO_3:Ni/HC); (d) fitting of sulfur peaks showing Ni–S in the form of Ni_xS_x and $Ni_xS_xO_x$.

Table 2 Sensing layer average composition in atomic percentage (atom%) before gas exposure, as obtained from the XPS analysis

	W	O	Ni
Ni/LC	17.5	72.0	10.5
Ni/HC	20.0	65.0	15.0
WO_3	25.0	75.0	0

oxide operated at 150 °C (best sensitivity for pure WO_3) and for Ni-loaded tungsten oxide operated at 250 °C (best sensitivity for Ni-loaded WO_3). It can be concluded, therefore, that Ni loading is not clearly advantageous for increasing ethanol sensitivity.

3.3.3. Nitrogen dioxide results. In order to analyze the response of the different materials towards oxidizing species, the response towards NO_2 was studied. In this case, a single concentration of 10 ppm was measured at the three different operating temperatures. Results are shown in Fig. 9. The loading of tungsten oxide with Ni results in an increased nitrogen dioxide responsiveness. For both pure WO_3 and Ni-loaded tungsten oxide (lower Ni concentration), the best response was obtained at a lower operating temperature. In the case of Ni-loaded tungsten oxide (higher Ni concentration), 200 °C was the best operating temperature for detecting nitrogen dioxide. In fact, highly loaded Ni–WO_3 operated at 200 °C resulted in the highest response value for NO_2.

3.3.4. Hydrogen sulfide results. The responses towards different concentrations of hydrogen sulfide that ranged between 10 and 50 ppm in a balance of pure dry air were measured. When operated at 150 °C, the loading of the sensing layer with Ni has negative effects on sensor response, because lower responses towards hydrogen sulfide were recorded for Ni-loaded tungsten oxide than for the pure WO_3 samples. As the operating temperature increases, this behavior is gradually reversed and the response towards hydrogen sulfide is significantly increased for the Ni-loaded samples in comparison to pure tungsten oxide. Highly loaded Ni–WO_3 samples show the highest responsiveness towards hydrogen sulfide when operated at 250 °C with the Ni/HC sensor. A 5-fold increase in responsiveness is obtained. These results are summarized in Fig. 10.

In the detection of hydrogen sulfide, the loading of tungsten oxide nanowires with nickel oxide nanoparticles is clearly beneficial, since it significantly increases the response. Further details on the influence of the amount of nickel oxide loading on hydrogen sulfide response can be found in the ESI.† This is

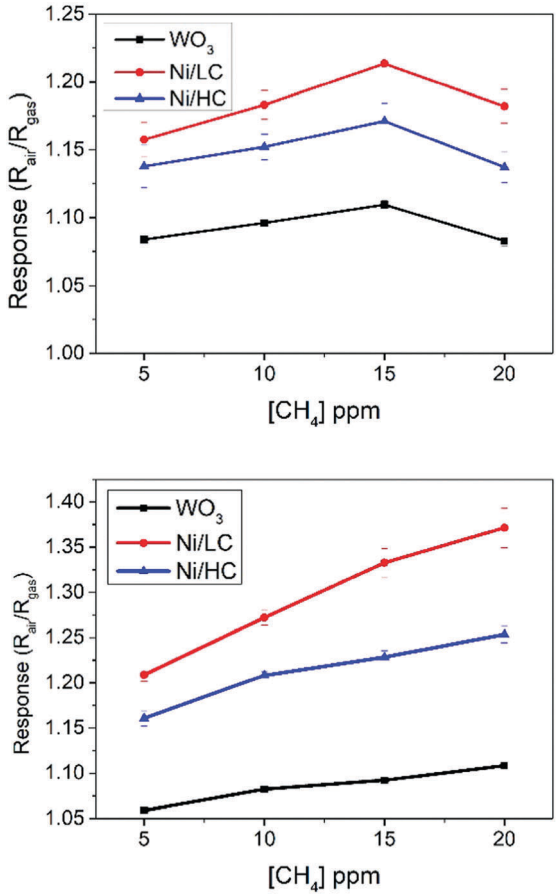

Fig. 7 CH_4 detection results for the different sensors operated at 200 °C (upper panel) and 250 °C (lower panel). When operated at 150 °C (not shown), the sensors showed no response towards methane.

summarized in Fig. 11, which confirms that the nickel oxide loading of tungsten oxide enhances the response and selectivity towards hydrogen sulfide. For better establishing the degree of selectivity towards hydrogen sulfide, it would have been optimal to measure mixtures of H_2S with interfering species such as methane, ethanol or nitrogen dioxide. However, the important differences in response intensity shown in Fig. 11 (*i.e.*, high response to hydrogen sulfide and low responses to the other species tested) clearly indicate that the NiO-loaded sensor is reasonably selective towards H_2S. In addition, the response time of this sensor to hydrogen sulfide is about 88 s, which compares favorably to its response times to the other species tested (further details can be found in the ESI†).

3.3.5. Effect of ambient humidity on the response towards hydrogen sulfide. So far, the analysis of the gas sensing properties has been conducted under dry conditions. However, to better simulate the normal working conditions of the sensors in a real application, the effect of ambient humidity needs to be considered as well. Therefore, hydrogen sulfide diluted in humid air was measured in order to study humidity cross-sensitivity in Ni-loaded tungsten oxide nanowire sensors. The results obtained (see Fig. 12) show that the presence of ambient moisture increases the intensity of the sensor response for low hydrogen sulfide concentrations

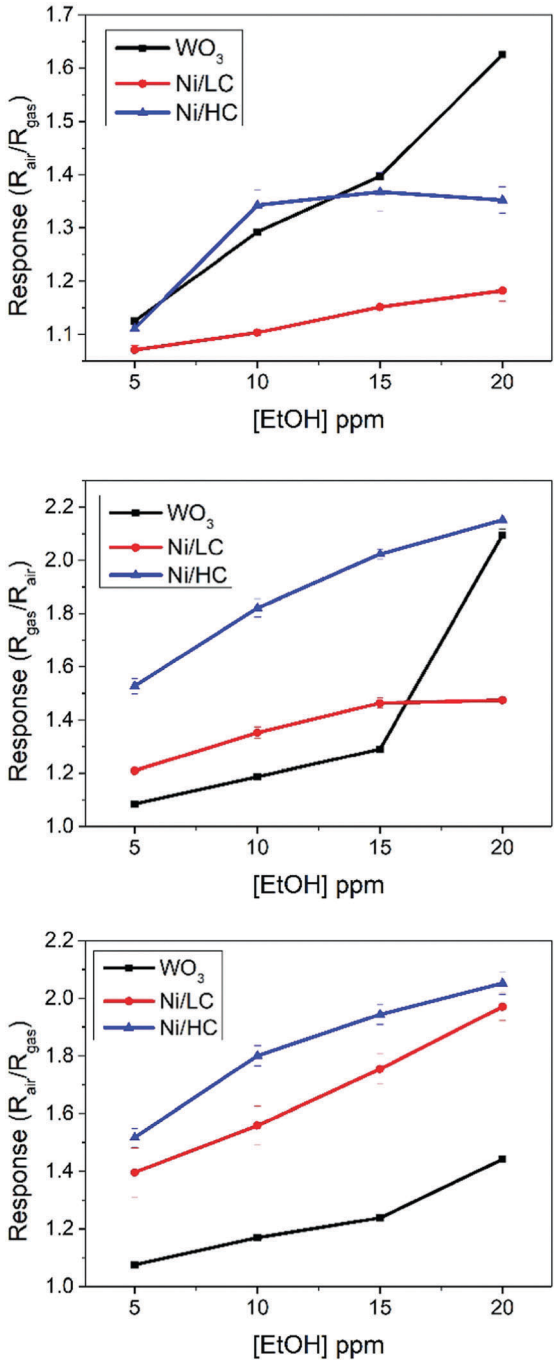

Fig. 8 Ethanol detection results for the different sensors operated at 150 °C (upper panel), 200 °C (middle panel) and 250 °C (lower panel).

(*i.e.* ≤25 ppm). However, at higher hydrogen sulfide concentrations (*e.g.* 50 ppm), the response decreases in the presence of moisture. This response saturation results in a loss of sensitivity. However, in a real application, hydrogen sulfide should be measured in the units of ppm range rather than in the tens of ppm range. For example, the Association Advancing Occupational and Environmental Health recommends a threshold limit value (TLV) of 1 ppm as an 8-hour time weighted average (TWA) and a short-term exposure limit (STEL) of 5 ppm for hydrogen sulfide.[43] These concentrations

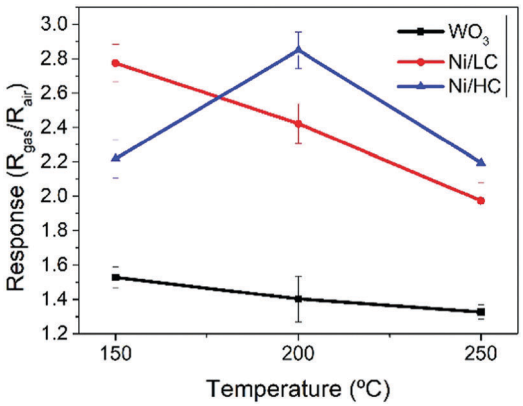

Fig. 9 NO_2 sensing results for the different materials studied as a function of the sensor operating temperature.

would be easily detectable by the Ni-loaded sensor under humid conditions.

It has been reported that in p-type metal oxide nanoparticles supported on n-type metal oxide surfaces, when ambient humidity is present, the host n-type substrate remains drier due to the higher affinity between the p-type metal oxide (*i.e.*, nickel oxide) and water molecules.[44,45] At normal operating temperatures, dissociative adsorption of water molecules takes place, resulting in the formation of hydroxyl groups[8] at the surface of nickel oxide nanoparticles and, to a lesser extent, at the surface of tungsten oxide nanowires. The competitive reaction with surface oxygen species of hydrogen sulfide and water molecules could explain the overall decrease in sensitivity caused by the presence of ambient moisture. However, the interaction of hydrogen sulfide with hydroxyl groups and subsequent relaxation of the space charge zone at the p–n interfaces resulting in electronic charge transfer towards the tungsten oxide nanowires could explain the higher responses recorded for low hydrogen sulfide concentrations.

3.4 Hydrogen sulfide detection mechanism

The hydrogen sulfide sensing mechanism of the Ni-loaded tungsten oxide nanowires is temperature dependent, as the oxygen species adsorbed on the surface of the nickel oxide differ with temperature:[46]

$$O_{2(g)} \leftrightarrow O_{2(ads)}$$

$$O_{2(ads)} + e^- \leftrightarrow O_2^-{}_{(ads)} \quad (<150\ ^\circ C)$$

$$O_2^-{}_{(ads)} + e^- \leftrightarrow 2O^-{}_{(ads)} \quad (150\text{–}400\ ^\circ C)$$

$$O^-{}_{(ads)} + e^- \leftrightarrow O^{2-}{}_{(ads)} \quad (>400\ ^\circ C)$$

Based on the results observed, one reaction that governs the process of the detection of H_2S consists of an oxidation process that consumes adsorbed surface species and results in the generation of free electronic charge. This process is as follows:

$$2H_2S + 3O_2^- \rightarrow 2SO_2 + 2H_2O + 3e^-$$

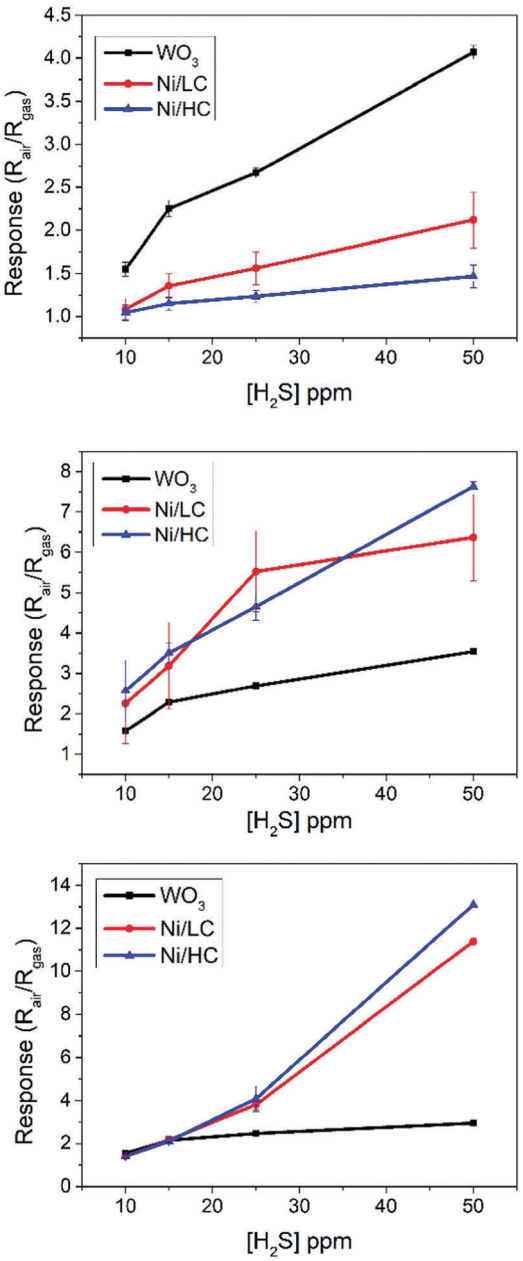

Fig. 10 Hydrogen sulfide detection results for the different sensors operated at 150 °C (upper panel), 200 °C (middle panel) and 250 °C (lower panel).

which holds when the operating temperature is 150 °C and surface oxygen species consist basically of adsorbed molecular oxygen. Alternatively,

$$H_2S + 3O^- \rightarrow SO_2 + H_2O + 3e^-$$

which holds when the operating temperature is 200 °C or 250 °C.

Additionally, another sensing mechanism derived from an electronic sensitization effect caused by the presence of p-type NiO nanoparticles has to be taken into account as well. This mechanism consists of the sulfurization of NiO into Ni_xS_x when

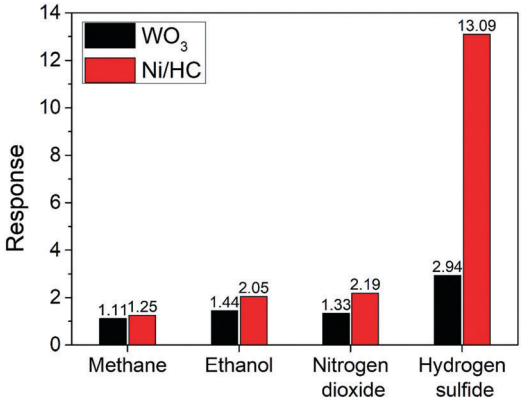

Fig. 11 Comparison of response intensities (R_{air}/R_{gas} for reducing gases and R_{gas}/R_{air} for oxidizing gases) for a pure WO_3 sensor and a Ni/HC WO_3 sensor both operated at 250 °C. The concentrations are 20 ppm for methane and ethanol, 10 ppm for nitrogen dioxide and 50 ppm for hydrogen sulfide.

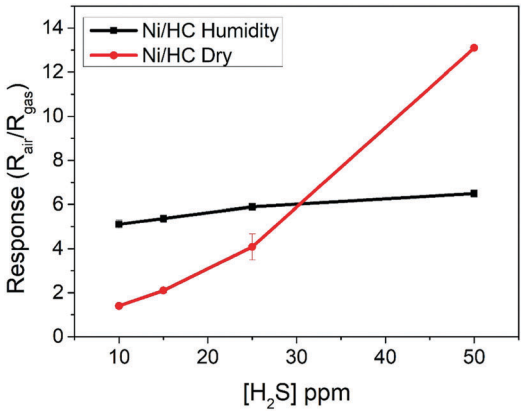

Fig. 12 Comparison of H_2S sensing results between dry conditions and those obtained under 35% R. H. at 250 °C.

the surface of the Ni-loaded tungsten oxide nanowire film is exposed to hydrogen sulfide:

$$NiO_{(s)} + H_2S_{(g)} \rightarrow NiS_{(s)} + H_2O_{(g)}$$

As a result of this sulfurization process, the p–n heterojunctions are destroyed and the overall electrical conductivity of the gas-sensitive film is increased. However, a recovery process is also proposed to regenerate the nickel oxide nanoparticles when hydrogen sulfide is removed from the sensor environment:[47]

$$3NiS_{(g)} + 2H^+_{(aq)} \rightarrow Ni_3S_{2(s)} + H_2S_{(g)}$$

$$Ni_3S_{2(s)} + 7/2O_{2(g)} \rightarrow 3NiO_{(s)} + 2SO_{2(g)}$$

$$Ni_3S_{2(s)} + 9/2O_{2(g)} \rightarrow 2NiSO_{4(s)} + NiO_{(s)}$$

However, this recovery may only be partial as XPS analysis confirms the presence of Ni_xS_x and $Ni_xS_xO_x$ species on the surface of used sensors. Further details can be found in the ESI.† This sulfurization mechanism that destroys the p–n heterojunctions upon the exposure of NiO-loaded tungsten oxide nanowires to hydrogen sulfide explains the higher response observed for this species than for methane, ethanol or nitrogen dioxide and thus explains the selectivity achieved.

4. Conclusions

An AACVD process has been employed to grow Ni loaded tungsten oxide nanowires employing tungsten hexacarbonyl and Ni(II) acetylacetonate as precursors. A two-step strategy is needed in which pure tungsten oxide nanowires are grown at first, and these are loaded with Ni-containing nanoparticles in the second step. This ensures that a wide range of metal loading can be achieved with high efficiency. HR-TEM analysis has shown that tungsten oxide nanowires are single crystalline and that Ni-containing nanoparticles are about 2 nm in diameter. In general, Ni nanoparticles are homogeneously distributed over the tungsten oxide nanowire surface. At high Ni loadings, the size of the nanoparticles remains unchanged, however they show a tendency to form agglomerates, especially at the tips of the tungsten nanowires. XPS analysis has revealed that nanoparticles consist of nickel oxides.

The gas sensing properties of the different nanomaterials grown have been studied. The loading of tungsten oxide with nickel oxide nanoparticles has a positive effect, increasing the sensitivity and selectivity of the resulting nanomaterial to hydrogen sulfide (*e.g.* it shows a poor response towards methane and a low response towards ethanol or nitrogen dioxide). A five-fold increase in the response towards hydrogen sulfide has been measured upon nickel oxide loading. This improvement can be attributed to a chemical sensitization effect in which the nickel oxide nanoparticles increase the amount of adsorbed, reactive surface species, combined with an electronic sensitization effect in which p-type nickel oxide nanoparticles become metallic Ni_xS_x upon exposure to hydrogen sulfide. Furthermore, Ni-loaded tungsten oxide nanowire sensors show enough responsiveness in the units of ppm range of hydrogen sulfide concentrations, even in the presence of humidity. Therefore, this nanomaterial possesses outstanding characteristics that clearly outperform other state-of-the-art materials, showing good potential for the development of resistive sensors able to monitor the presence of hydrogen sulfide in the environment under real application conditions.

Conflicts of interest

There are no conflicts of interest to declare.

Acknowledgements

This work was funded in part by MINECO and FEDER *via* grant no. TEC2015-71663-R, by AGAUR under grant. 2017SGR 418 and by FNRS *via* PLAFON and FITTED projects. E. N. gratefully acknowledges a doctoral fellowship from MINECO grant no. BES-2016-076582. E. L. is supported by the Catalan institution for Research and Advanced Studies *via* the 2012 Edition of the

ICREA Academia Award. C. B. is a research Associate of the FNRS (Belgium).

References

1 H. Akimoto, Global Air Quality and Pollution, *Science*, 2003, **302**(5651), 1716–1719, DOI: 10.1126/science.1092666.

2 M. Kampa and E. Castanas, Human health effects of air pollution, *Environ. Pollut.*, 2008, **151**(2), 362–367, DOI: 10.1016/j.envpol.2007.06.012.

3 G. F. Fine, L. M. Cavanagh, A. Afonja and R. Binions, Metal Oxide Semi-Conductor Gas Sensors in Environmental Monitoring, *Sensors*, 2010, **10**(6), 5469–5502, DOI: 10.3390/s100605469.

4 S. M. Kanan, O. M. El-Kadri, I. A. Abu-Yousef and M. C. Kanan, Semiconducting Metal Oxide Based Sensors for Selective Gas Pollutant Detection, *Sensors*, 2009, **9**(10), 8158–8196, DOI: 10.3390/s91008158.

5 N. Yamazoe, G. Sakai and K. Shimanoe, Oxide Semiconductor Gas Sensors, *Catal. Surv. Asia*, 2003, **7**(1), 63–75, DOI: 10.1023/A:1023436725457.

6 K. Galatsis, L. Cukrov, W. Wlodarski, P. Mccormick, K. Kalantar-Zadeh, E. Comini and G. Sberveglieri, p- and n-type Fe-doped SnO_2 Gas Sensors Fabricated by the Mechanochemical Processing Technique, *Sens. Actuators, B*, 2003, **93**(1–3), 562–565, DOI: 10.1016/s0925-4005(03)00233-8.

7 E. Kanazawa, G. Sakai, K. Shimanoe, Y. Kanmura, Y. Teraoka, N. Miura and N. Yamazoe, Metal oxide semiconductor N_2O sensor for medical use, *Sens. Actuators, B*, 2001, **77**(1–2), 72–77, DOI: 10.1016/s0925-4005(01)00675-x.

8 S. Roso, C. Bittencourt, P. Umek, O. González, F. Güell, A. Urakawa and E. Llobet, Synthesis of single Crystalline In_2O_3 Octahedra for the Selective Detection of NO2 and H2 at trace levels, *J. Mater. Chem. C*, 2016, **4**, 9418.

9 M. Newref1 Hübner, C. Simion, A. Tomescu-Stănoiu, S. Pokhrel, N. Bârsan and U. Weimar, Influence of humidity on CO sensing with p-type CuO thick film gas sensors, *Sens. Actuators, B*, 2011, **153**(2), 347–353, DOI: 10.1016/j.snb.2010.10.046.

10 S. Matsushima, Y. Teraoka, N. Miura and N. Yamazoe, Electronic Interaction between Metal Additives and Tin Dioxide in Tin Dioxide-Based Gas Sensors, *Jpn. J. Appl. Phys.*, 1988, **27**(Part1, No. 10), 1798–1802, DOI: 10.1143/jjap.27.1798.

11 W. C. Conner and J. L. Falconer, Spillover in Heterogeneous Catalysis, *Chem. Rev.*, 1995, **95**(3), 759–788, DOI: 10.1021/cr00035a014.

12 V. B. Kamble and A. M. Umarji, Effect of Pt doping on the gas sensing properties of porous chromium oxide films through a kinetic response analysis approach, *RSC Adv.*, 2015, **5**(35), 27509–27516, DOI: 10.1039/c5ra02186c.

13 C. Wang, L. Yin, L. Zhang, D. Xiang and R. Gao, Metal Oxide Gas Sensors: Sensitivity and Influencing Factors, *Sensors*, 2010, **10**(3), 2088–2106, DOI: 10.3390/s100302088.

14 F. E. Annanouch, Z. Haddi, ,. S. Vallejos, P. Umek, P. Guttmann, C. Bittencourt and E. Llobet, Aerosol-Assisted CVD-Grown WO_3 Nanoneedles Decorated with Copper Oxide Nanoparticles for the Selective and Humidity-Resilient Detection of H_2S, *ACS Appl. Mater. Interfaces*, 2015, **7**(12), 6842–6851, DOI: 10.1021/acsami.5b00411.

15 F. E. Annanouch, Z. Haddi, M. Ling, F. Di Maggio, S. Vallejos, T. Vilic, Y. Zhu, T. Shujah, P. Umek, C. Bittencourt, C. Blackman and E. Llobet, Aerosol-Assisted CVD-Grown PdO Nanoparticle-Decorated Tungsten Oxide Nanoneedles Extremely Sensitive and Selective to Hydrogen, *ACS Appl. Mater. Interfaces*, 2016, **8**(16), 10413–10421, DOI: 10.1021/acsami.6b00773.

16 S. Vallejos, P. Umek, T. Stoycheva, F. Annanouch, E. Llobet, X. Correig, P. de Marco, C. Bittencourt and C. Blackman, Single-Step Deposition of Au- and Pt-Nanoparticle-Functionalized Tungsten Oxide Nanoneedles Synthesized *Via* Aerosol-Assisted CVD, and Used for Fabrication of Selective Gas Microsensor Arrays, *Adv. Funct. Mater.*, 2013, **23**(10), 1313–1322, DOI: 10.1002/adfm.201201871.

17 H. Sato, T. Minami, S. Takata and T. Yamada, Transparent conducting p-type NiO thin films prepared by magnetron sputtering, *Thin Solid Films*, 1993, **236**(1–2), 27–31, DOI: 10.1016/0040-6090(93)90636-4.

18 S. Lany, J. Osorio-Guillén and A. Zunger, Origins of the doping asymmetry in oxides: Hole doping in NiO versus electron doping in ZnO, *Phys. Rev. B: Condens. Matter Mater. Phys.*, 2007, **75**, 241203(R), DOI: 10.1103/physrevb.75.241203.

19 H. Kim, K. Choi, K. Kim, C. W. Na and J. Lee, Highly sensitive C_2H_5OH sensors using Fe-doped NiO hollow spheres, *Sens. Actuators, B*, 2012, **171–172**, 1029–1037, DOI: 10.1016/j.snb.2012.06.029.

20 J. Yoon, H. Kim, I. Kim and J. Lee, Electronic sensitization of the response to C2H5OH of p-type NiO nanofibers by Fe doping, *Nanotechnology*, 2013, **24**(44), 444005, DOI: 10.1088/0957-4484/24/44/444005.

21 N. G. Cho, H. Woo, J. Lee and I. Kim, Thin-walled NiO tubes functionalized with catalytic Pt for highly selective C_2H_5OH sensors using electrospun fibers as a sacrificial template, *Chem. Commun.*, 2011, **47**(40), 11300, DOI: 10.1039/c1cc13876f.

22 T. Yu, X. Cheng, X. Zhang, L. Sui, Y. Xu, S. Gao and L. Huo, Highly sensitive H_2S detection sensors at low temperature based on hierarchically structured NiO porous nanowall arrays, *J. Mater. Chem. A*, 2015, **3**(22), 11991–11999, DOI: 10.1039/c5ta00811e.

23 Z. Wang, P. K. Nayak, J. A. Caraveo-Frescas and H. N. Alshareef, Recent Developments in p-Type Oxide Semiconductor Materials and Devices, *Adv. Mater.*, 2016, **28**(20), 3831–3892, DOI: 10.1002/adma.201503080.

24 J. Wang, P. Yang and X. Wei, High-Performance, Room-Temperature, and No-Humidity-Impact Ammonia Sensor Based on Heterogeneous Nickel Oxide and Zinc Oxide Nanocrystals, *ACS Appl. Mater. Interfaces*, 2015, **7**(6), 3816–3824, DOI: 10.1021/am508807a.

25 R. L. Fomekong, D. Lahem, M. Debliquy, S. Yunus, J. L. Ngolui and A. Delcorte, $Ni_{0.9}Zn_{0.1}O$/ZnO nanocomposite prepared by malonate coprecipitation route for gas sensing, *Sens. Actuators, B*, 2016, **231**, 520–528, DOI: 10.1016/j.snb.2016.03.099.

26 C. Sun and P. K. Dutta, Selective detection of part per billion concentrations of ammonia using a p–n semiconducting

oxide heterostructure, *Sens. Actuators, B*, 2016, **226**, 156–169, DOI: 10.1016/j.snb.2015.11.085.

27 W. Li, X. Zhang and X. Guo, Electrospun Ni-doped SnO_2 nanofiber array for selective sensing of NO_2, *Sens. Actuators, B*, 2017, **244**, 509–521, DOI: 10.1016/j.snb.2017.01.022.

28 W. Noh, Y. Shin, J. Kim, W. Lee, K. Hong, S. A. Akbar and J. Park, Effects of NiO addition in WO_3-based gas sensors prepared by thick film process, *Solid State Ionics*, 2002, **152–153**, 827–832, DOI: 10.1016/s0167-2738(02)00341-7.

29 N. M. Vuong, T. N. Trung, T. T. Hien, N. D. Chinh, N. D. Quang, D. Lee and D. Kim, Ni_2O_3 Decoration of WO_3 Thin Film for High Sensitivity NH_3 Gas Sensor, *Mater. Trans.*, 2015, **56**(9), 1354–1357, DOI: 10.2320/matertrans.ma201572.

30 T. Vilic and E. Llobet, Nickel Doped WO_3 Nanoneedles Deposited by a Single Step AACVD for Gas Sensing Applications, *Procedia Eng.*, 2016, **168**, 206–210, DOI: 10.1016/j.proeng.2016.11.163.

31 Y. Wang, S. Wang, Y. Zhao, B. Zhu, F. Kong, D. Wang, S. Wu, W. Huang and S. Zhang, H_2S sensing characteristics of Pt-doped α-Fe_2O_3 thick film sensors, *Sens. Actuators, B*, 2007, **125**, 79–84, DOI: 10.1016/j.snb.2007.01.037.

32 J. Ma, L. Mei, Y. Chen, Q. Li, T. Wang, Z. Xu, X. Duan and W. Zheng, α-Fe_2O_3 nanochains: ammonium acetate-based ionothermal synthesis and ultrasensitive sensors for low-ppm-level H_2S gas, *Nanoscale*, 2013, **5**, 895–898, DOI: 10.1039/C2NR33201A.

33 Z. Lia, Y. Huang, S. Zhang, W. Chen, Z. Kuang, D. Ao, W. Liu and Y. Fu, A fast response and recovery H_2S gas sensor based on α-Fe_2O_3 nanoparticles with ppb level detection limit, *J. Hazard. Mater.*, 2015, **300**, 167–174, DOI: 10.1016/j.jhazmat.2015.07.003.

34 A. Davydow, K. T. Chuang and A. R. Sanger, Mechanism of H_2S oxidation by ferric oxide and hydroxide surfaces, *J. Phys. Chem. B*, 1998, **102**, 4745–4752, DOI: 10.1021/jp980361p.

35 Y. L. Liu, H. Wang, Y. Yang, Z. M. Liu, H. F. Yang, G. L. Shen and R. Q. Yu, Hydrogen sulfide sensing properties of $NiFe_2O_4$ nanopowder doped with noble metals, *Sens. Actuators, B*, 2004, **102**, 148–154, DOI: 10.1016/j.snb.2004.04.014.

36 V. D. Kapse, S. A. Ghosh, F. C. Raghuwanshi and S. D. Kapse, Nanocrystalline spinel $Ni_{0.6}Zn_{0.4}Fe_2O_4$: A novel material for H_2S sensing, *Mater. Chem. Phys.*, 2009, **113**, 638–644, DOI: 10.1016/j.matchemphys.2008.08.017.

37 R. B. Vasiliev, M. N. Rumyantseva, N. V. Yakovlev and A. M. Gaskov, CuO:SnO_2 thin film heterostructures as chemical sensors to H_2S, *Sens. Actuators, B*, 1998, **50**, 186–193, DOI: 10.1016/S0925-4005(98)00235-4.

38 N. M. Vuong, N. D. Chinh, B. T. Huy and Y. I. Lee, CuO-Decorated ZnO Hierarchical Nanostructures as Efficient and Established Sensing Materials for H_2S GasSensors, *Sci. Rep.*, 2016, **6**, 26736, DOI: 10.1038/srep26736.

39 E. Llobet, J. Brunet, A. Pauly, A. Ndiaye and C. Varenne, Nanomaterials for the Selective Detection of Hydrogen Sulfide in Air, *Sensors*, 2017, **17**, 391, DOI: 10.3390/s17020391.

40 F. Y. Xie, L. Gong, X. Liu, Y. T. Tao, W. H. Zhang, S. H. Chen, H. Meng and J. Chen, XPS Studies on Surface Reduction of Tungsten Oxide Nanowire Film by Ar^+ Bombardment, *J. Electron Spectrosc. Relat. Phenom.*, 2012, **185**, 112–118.

41 C. Bittencourt, E. Llobet, P. Ivanov, X. Vilanova, X. Correig, M. A. P. Silva, L. A. O. Nunes and J. J. Pireaux, Ag induced modifications on WO_3 films studied by AFM, Raman and X-ray photoelectron spectroscopy, *J. Phys. D: Appl. Phys.*, 2004, **37**(24), 3383–3391.

42 L. Ottaviano, F. Bussolotti, L. Lozzi, M. Passacantando, S. La Rosa and S. Santucci, Core Level and Valence Band Investigation of WO_3 Thin Films with Synchrotron Radiation, *Thin Solids Films*, 2003, **436**, 9–16.

43 UNITED STATES DEPARTMENT OF LABOR. (n.d.). Retrieved January 21st, 2018, from https://www.osha.gov/SLTC/hydrogensulfide/standards.html.

44 E. Lackner, J. Krainer, R. Wimmer-Teubenbacher, F. Sosada, C. Gspan, K. Rohracher and A. Koeck, CMOS Integrated Nanocrystalline SnO_2 Gas Sensors for CO Detection, *Procedia Eng.*, 2016, **168**, 297–300, DOI: 10.1016/j.proeng.2016.11.200.

45 K. Choi, M. Hübner, A. Haensch, H. Kim, U. Weimar, N. Barsan and J. Lee, Ambivalent effect of Ni loading on gas sensing performance in SnO_2 based gas sensor, *Sens. Actuators, B*, 2013, **183**, 401–410, DOI: 10.1016/j.snb.2013.04.007.

46 D. V. Ahire, G. E. Patil, D. D. Kajale, V. B. Gaikwad and G. H. Jain, Nanostructured Nickel Oxide by Hydrothermal Route for Gas Sensing Applications, *Sensing Technology: Current Status and Future Trends I, Smart Sensors, Measurement and Instrumentation*, vol. 7, pp. 181–193, 2014, DOI: 10.1007/978-3-319-02318-2_10.

47 A. T. Atimtay and D. P. Harrison, *Desulfurization of Hot Coal Gas*, 2013, Springer Berlin, Berlin.

2.3.2 WO_3 nanowires loaded with cobalt oxide nanoparticles, deposited by a two-step AACVD for gas sensing applications

Sensors & Actuators: B. Chemical 298 (2019) 126868

Contents lists available at ScienceDirect

Sensors and Actuators B: Chemical

journal homepage: www.elsevier.com/locate/snb

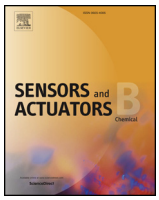

WO_3 nanowires loaded with cobalt oxide nanoparticles, deposited by a two-step AACVD for gas sensing applications

Èric Navarrete[a], Carla Bittencourt[b], Xavier Noirfalise[c], Polona Umek[d], Ernesto González[a], Frank Güell[e], Eduard Llobet[a,*]

[a] MINOS-EMaS, Universitat Rovira i Virgili, Avda. Països Catalans, 26, 43007 Tarragona, Spain
[b] Chimie des Interactions Plasma – Surface (ChIPS), Research Institute for Materials Science and Engineering, Université de Mons, Avenue Copernic 3, 7000 Mons, Belgium
[c] Materia Nova, Avenue Copernic 3, 7000 Mons, Belgium
[d] Jožef Stefan Institute, Jamova cesta 39, 10000 Ljubljana, Slovenia
[e] ENFOCAT-IN2UB, Universitat de Barcelona, C/Martí i Franquès 1, 08028 Barcelona, Catalunya, Spain

ARTICLE INFO

Keywords:
Nanowires
Tungsten trioxide
Cobalt oxide
Gas sensors

ABSTRACT

A two-step procedure was implemented to obtain tungsten oxide nanowires (WO_3) doped with cobalt oxide nanoparticles employing $W(CO)_6$ and the metal-organic precursor $Co(acac)_2$. In the first step, tungsten oxide nanowires were grown at 400 °C using an aerosol assisted chemical vapor deposition system (AA-CVD) and subsequently annealed at 500 ºC for 2 h in dry air. Then, cobalt oxide loading (at different dose levels) of the nanowires was performed via a second AA-CVD process. These hybrid nanomaterials were grown on top of commercial alumina substrates that comprised interdigitated electrodes and a heating element. The response of these nanomaterials toward H_2S, ethanol H_2 and ammonia is investigated and discussed. Co-loaded tungsten oxide is well suited for detecting ammonia under dry conditions and hydrogen sulfide in humid environments.

1. Introduction

Air quality monitoring both indoor and outdoor have become a major issue nowadays due to the global industrial growth and the rise of emissions of harmful gases, such as NO_2, H_2S, or VOCs, which, at high enough concentrations, represent a threat to the environment and human health [1]. Major efforts have been employed for developing new gas sensors with the ability to monitor such gases at low concentrations. Nowadays there are different types of sensor technologies that may possess, at least in part, the requirements to perform a widespread monitoring of harmful gases and vapors. These comprise calorimetric, electrochemical, photoionization detectors (PID) or metal oxide semiconductor gas sensors [2]. Metal oxide semiconductor gas sensors (MOXs) have been continuously researched in the last decades due to their cost-effectiveness, their high sensitivity and their suitability for miniaturization [3]. Among the most popular MOXs are n-type semiconductors such as SnO_2, ZnO, In_2O_3 or WO_3. The main drawback of MOXs remains their lack of selectivity and, very particularly, cross-sensitivity to ambient moisture. Different strategies have been reported to fight cross-sensitivity. Namely, the use of filters to prevent specific gases from reaching the gas sensing surface and thus, interfering in the measurement process [4], the use of sensor arrays with overlapping selectivity and pattern recognition [5,6] or the use of advanced sensor operation techniques such as temperature cycling [7]. However, the major efforts to tackle this problem have consisted of loading MOXs with different metal or metal oxide nanomaterials in an attempt of tailoring gas sensing properties and selectivity towards specific targets [8,9]. In particular, nanoparticles of noble metals such as platinum, palladium or gold nanoparticles have been employed for enhancing gas detection, since these metals display interesting bulk properties and catalytic activity [10]. In addition, the loading of n-type metal oxide nanomaterials with p-type metal oxide nanoparticles has been explored in the last few years because this is a route to achieve both chemical and electronic sensitization effects. For example, upon the formation of many n–p heterojunctions in n-type nanowires decorated with p-type nanoparticles, electronic charge is injected from the nanowires to nanoparticles and depletion zones develop at the interfaces [4–6]. In addition, p-type nanoparticles may help increase the amount of oxygen species that end-up trapped at the surface of the n-type nanowire via their catalytic activity and a spill-over effect [7,9,10]. While these two effects combined translate in an increase in the electrical resistance of decorated nanowire films (in comparison to the resistance for bare nanowire films) when in clean air, they also play a role in the enhancement of sensitivity and selectivity to gases. This result involves

* Corresponding author.
E-mail address: eduard.llobet@urv.cat (E. Llobet).

https://doi.org/10.1016/j.snb.2019.126868
Received 8 March 2019; Received in revised form 22 July 2019; Accepted 23 July 2019
Available online 27 July 2019

different mechanisms occurring at the surface of the hybrid nanomaterial, which alter the overall electrical conductance of the gas-sensitive film. Namely:

- The adsorption of gaseous species onto p-type nanoparticles involves charge-transfer mechanisms that eventually affect the width of the depletion zones.
- Gaseous species can interact directly with oxygen adsorbates on n-type MOX, and we should keep in mind that there is an increased amount of oxygen surface species in hybrid nanomaterials due to the presence of p-type MOX nanoparticles, as stated above.
- Gaseous species can react with p-type nanoparticles resulting in highly reactive radicals that can further react with oxygen adsorbates via a spill-over effect.

It is the choice of the particular p-type MOX to be employed in the hybrid nanomaterial that enables tailoring the system selectivity towards specific targets. Employing this approach Llobet and coworkers reported the use of copper oxide nanoparticles for selectively detecting hydrogen sulfide through a reversible sulfurization of copper oxide upon exposure to H_2S [11]. Similarly, palladium oxide nanoparticle decorated tungsten oxide nanowires have been also reported for the selective detection of H_2 [12]. Hydrogen dissociation at the p-type PdO nanoparticles, followed by spill over onto the n-type nanowires (at high/moderate operating temperatures) or the reversible formation of palladium hydride upon hydrogen exposure (at near room-temperature operation) are the reported sensing mechanisms. More recently, the loading of tungsten oxide nanowires with nickel oxide nanoparticles was found to be of interest for the selective detection of H_2S [13].

Following the approach described above, this paper is focused on the decoration of tungsten oxide nanowires with p-type cobalt oxide nanoparticles. At first, the suitability of the aerosol assisted chemical vapor deposition (AACVD) for growing the hybrid nanomaterial with different cobalt oxide loadings is studied via a morphological and compositional study of the nanomaterials grown. Then, the gas sensing response is investigated and discussed in detail. Here, a two-step AACVD procedure in which WO_3 nanowires are grown at first and subsequently loaded with cobalt oxide nanoparticles was implemented to ensure that the loading could be performed effectively in wide concentration range.

The use of cobalt oxide as a gas sensing material, either standalone or supported by different n-type metal oxides has been reported in the literature and Table 1 summarizes the state of the art. To the best of our knowledge, this is the first time that the growth of tungsten oxide nanowires decorated with cobalt oxide is reported and their use as gas sensing nanomaterial investigated. Cobalt oxide supported on tungsten trioxide nanowires was only reported before in a conference work [14] in which we presented preliminary and incomplete results.

2. Experimental

2.1. Sensing layer synthesis

The AACVD methodology was employed to grow, on top of alumina transducers, a first layer of pristine tungsten oxide. Some of the layers grown underwent a second AACDV process to be loaded with different concentrations of cobalt oxide nanoparticles. The first step consisted of the synthesis of pure WO_3 nanowires employing 50 mg of $W(CO)_6$ as precursor. Such precursor was solubilized in a mixture of methanol and acetone with a 1:3 vol ratio. It has been studied experimentally that higher amounts of methanol lead to the formation of tungsten oxide nanoparticles instead of the desired nanowires, the main reason for this effect is the lower solubility of the organic precursor in methanol than in acetone, leading to a less homogenous solution that, once used in the aerosol generator results in a less effective precursor delivery. The solution was sonicated until all the precursor material was fully solved and then, was placed in an aerosol generator, which used a bath and ultrasonic waves to convert the solution into a micro-droplet spray that contained the precursor. This spray is conveyed via a connecting pipe system using nitrogen as an inert carrier gas at a flow of 1 L/min towards a 400 °C preheated CVD hot-wall reactor where the substrates are placed. Typically, the process for growing tungsten oxide samples took 20–30 minutes to complete and is run at atmospheric pressure. With this procedure and considering the reactor dimensions, up to 3 samples can be produced at the same time. The commercially available alumina substrates employed have interdigitated platinum electrodes screen-printed on the front side and a platinum heating resistor printed on the backside. Three of these substrates placed and kept face up in the reactor chamber during and AACVD process. The resulting tungsten oxide nanowire layers fully coat the electrode are of the substrates. Such layers have a dark-blue color, which is indicative of tungsten oxide being highly oxygen sub-stoichiometric and that some amorphous carbon residues left by the organic precursor and solvents are present. To remove such impurities and enhance oxidation, an annealing step is performed right after the deposition, which is conducted in a muffle at 500 °C for 2 h, with a temperature ramp of 5 °C/min, under pure dry air. After this step, the films show a green-yellowish color, indicative that a slightly oxygen defective tungsten oxide is achieved.

For some of the previously grown tungsten oxide nanowire samples, a second AACVD process is performed for loading them with cobalt oxide nanoparticles. In the first place, different amounts of a cobalt organic precursor, $Co(acac)_2$, are weighed. Here 5 mg or 10 mg of the

Table 1
Summary of results reported for chemo-resistive sensors employing cobalt oxide.

Nanomaterial	Operating temperature	Gas/Range (ppm)	Response (R_{air}/R_{gas})	Response time	Relative humidity	Reference
Co_3O_4 nanoparticles	240 °C	CO/6.7	1.9[a]	110 s	60%	[15]
Co_3O_4 nanorods	300 °C	EtOH/100	25.7[a]	29 s	DA	[16]
$CuCo_2O_4$ nanosheets	23 °C	NH_3/400	1.07[a]	120 s	57%	[17]
Co_3O4/TiO_2 nanotubes	100 °C	H_2/1000	7[a]	660 s	50%	[18]
CoO_x/SnO_2 nanocomposite	250 °C	H_2S/2	10[a]	NS	DA	[19]
Co/SnO_2 NPs	320 °C	H_2/40	15.7[a]	NS	DA	[20]
0-2 wt% Co/SnO_2	350 °C	NO/1000	1637[a]	75	NS	[21]
		C_3H_6O/2000	660[a]	5		
		EtOH/1000	806[a]	1		
0-1 wt% Co/CdO	130 °C	HCHO/100	23[b]	82	DA	[22]
Co/WO_3 thin film	250 °C	O_3/0.8	1.33[a]	–	DA	[23]
WO_3 nanowires/Co_3O_4 loaded	250 °C	H_2 / 20	1.7	819 s	DA & 50%	This work
		EtOH / 20	3.2[a]	150 s		
		H_2S/ 50	5.4[a]	40 s		
		NH_3 / 25	12[a]	308 s		

Notes: [a](Rair/Rgas); [b](%); DA: Dry Air Conditions; NS: Not Specified.

Co precursor were used to produce sensors with different loading levels. The organic precursor is mixed with 10 ml of methanol and subsequently sonicated until its full solubilization. The sensor substrates comprising annealed WO_3 nanowires are placed again inside the CVD reactor and preheated at 350 °C. The solution of the Co precursor is placed at the aerosol generator and delivered into the CVD reactor via a nitrogen flow of 1 L/min. The typical duration of this second AACVD step is 10 to 15 min. Finally, similarly to what was implemented for the first process, an annealing step is performed to clean the surface from carbon residues.

In addition to this two-step approach, a one-step approach for achieving cobalt oxide decorated tungsten oxide nanowires was checked as well. In the one-step approach both the precursors for tungsten and cobalt oxide are mixed and dissolved together. However, the overall efficiency of the cobalt oxide loading achieved in this way was very poor in comparison to the two-step approach described above. This lack of efficiency, which is in agreement with the findings for the AACVD decoration with nickel oxide reported in [13], can be attributed to the difficulty in achieving a good, simultaneous dissolution of the two precursors in the solvent mixture. Therefore, the one-step approach is no discussed further in this paper.

2.2. Material characterization

The nanomaterials had their crystalline phase characterized through X-ray diffraction (XRD), their structural morphology was studied employing scanning electron microscopy (SEM) and high-resolution transmission electron microscopy (HR-TEM). Finally, their chemical composition was characterized using energy-dispersive X-ray spectroscopy (EDX) and X-Ray photoelectron spectroscopy. A Bruker-AXS D8-Discover diffractometer with a parallel incident beam was used to perform the XRD analysis. SEM was carried out using a SU8020 Microscope from Hitachi (Tokio, Japan) operated at 30 kV. XPS was conducted on the sensing layers using a VERSAPROBE PHI 5000 from Physical Electronics, equipped with a monochromatic Al Kα X-ray source. The X-ray photoelectron spectra were collected at the take-off angle of 45° with respect to the electron energy analyzer operated in the CAE (constant analyzer energy) mode. For the compensation of built-up charge on the sample surface during the measurements, a dual beam charge neutralization composed of an electron gun ($\approx$1 eV) and an Ar ion gun ($\leq$10 eV) was used. Binding energies are all referred to the C1s peak at 284.6 eV. TEM analysis was carried out using a JEM-2100 (Jeol, Japan, 200 keV) equipped with an energy dispersive X-ray spectrometer (EDXS). The specimens for TEM investigation were mechanically removed from the growth substrate and ultrasonically dispersed in MeOH and a drop of the dispersion was deposited onto a lacy carbon film supported by a copper grid. In addition, room-temperature photoluminescence (PL) measurements were made with a chopped Kimmon IK Series He-Cd laser (325 nm). Fluorescence was dispersed with an Princeton Instruments Acton SP2750 0.750 m imaging triple grating monochromator, detected using a Hamamatsu H8259-02 with a socket assembly E717-500 photomultiplier, and amplified through a Stanford Research Systems SR830 DSP. A 360 nm filter was used to filtering the stray light. Finally, A cross-section and element mapping was performed employing a FESEM-FIB-field emission gun SEM-focused ion beam.

2.3. Gas sensing studies

These comprised testing the response for four different species (i.e., hydrogen sulfide, ethanol, hydrogen and ammonia vapors) at different concentrations and for three different operating temperatures (150, 200 and 250 °C). The concentrations tested were 10, 15, 25, 50 ppm for hydrogen sulfide, 5, 10, 15 and 20 ppm for both ethanol and hydrogen, and 25, 50 and 100 ppm for ammonia. These species were in calibrated gas cylinders balanced in dry air. The total flow was kept constant at 100 mL/min throughout the measurements. In a typical experiment sensors were exposed to a given species and concentration for 30 min, which was followed by 30 min of dry air for recovering the baseline. The DC resistance of the sensors was recorded. Sensors were placed inside an airtight test chamber made of Teflon®, which was connected to a mass-flow controlled dilution system that delivered reproducible concentrations of the species tested. All sensors were manufactured in duplicate (to test reproducibility). In a standard measurement, each sensor was exposed to 5 cycles of pulses of increasing gas concentration (to check repeatability). On the other hand, to test the reproducibility, two sensors of each type (i.e. 2 pure WO3, 2 Co/LC and 2 Co/HC) were tested and the responses for each concentration were compared. Finally, when all the response values for each concentration had been gathered, a Q Dixon test was run to find possible outliers; and the mean values were calculated together with the standard deviation associated for each concentration to a given operating temperature and plotted in accordance. For the detection of the different species, the cross-sensitivity of ambient moisture was studied. A mass flow controller for liquids was added to the dilution system and samples could be humidified to 50% R.H. at 25 °C.

3. Results and discussion

Fig. 1 shows typical successive response and recovery cycles of pure and cobalt oxide loaded tungsten oxide nanowire sensors to increasing concentrations of ethanol. As it could be expected, the loading of n-type tungsten oxide nanowires with increasingly high amounts of p-type cobalt oxide nanoparticles results in an increase of the baseline resistance. This increase can be due to space charge regions developing at the interfaces between p-type cobalt oxide nanoparticles and n-type tungsten oxide nanowires, but also to cobalt oxide nanoparticles favoring an increase in the concentration of oxygen adsorbates at the nanowires (oxygen surface species trap electrons of the n-type nanowires increasing overall resistance).

The effect of having different amounts of cobalt oxide loading on the sensing properties was screened (see the Supporting Information, Fig. S1). In accordance to the results obtained, two loading levels were considered for further analysis. These corresponded to using either 5 mg or 10 mg of $Co(acac)_2$ during the synthesis step. These low and high loading levels are referred to as Co/LC and Co/HC, respectively.

3.1. Material characterization

The different nanomaterials were characterized by means of XRD to study their crystallinity. All nanomaterials presented peaks in

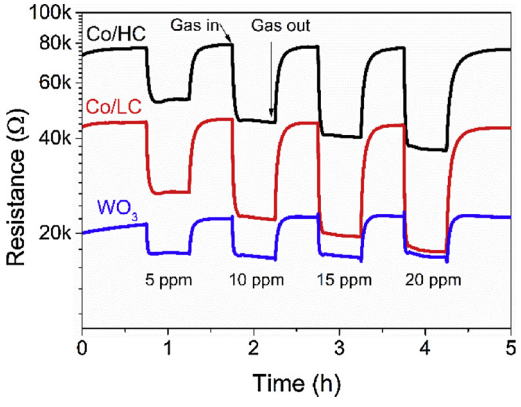

Fig. 1. Typical cycles of response and recovery to increasing concentrations of ethanol pulses for three tungsten oxide nanowire sensors with different loading levels of cobalt oxide nanoparticles. Namely, bare WO_3, low cobalt loaded WO_3 (Co/LC) and high cobalt loaded WO_3 (Co/HC). Sensors were operated at 200 °C under dry air conditions.

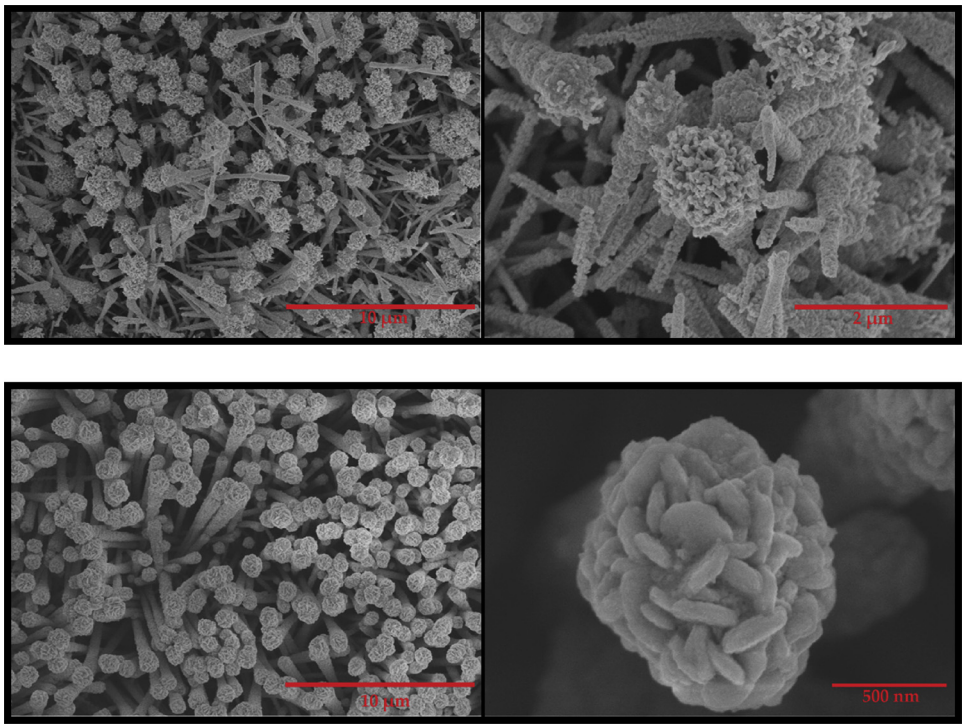

Fig. 2. SEM results. Co/LC tungsten oxide nanowires appear almost covered by clustered cobalt oxide resembling to petal like structures (upper left panel). Close look at the tips (upper right panel). Co/HC tungsten oxide nanowire tips are covered by clustered cobalt oxide with nanoflake-like structure (lower left panel). Close look at the tip of a Co/HC tungsten oxide nanowire (lower right panel).

agreement with those reported in ICDD card no. 43-1035 corresponding to monoclinic WO_3. In addition, cobalt loaded samples showed peaks that corresponded to cobalt oxide. XRD spectra (Fig. S2) and a discussion of these results can be found in the Supporting Information. Tungsten oxide nanowires were single crystalline monoclinic and some peaks recorded in the XRD spectra indicated the presence of Co in Co-loaded samples. Scanning electron microscopy (SEM) and transmission electron microscopy (TEM) were used to understand their morphology.

Fig. 2 shows typical SEM images of tungsten trioxide nanowires loaded with low and high concentrations of cobalt. Nanowires grow randomly oriented, their length ranges from 4 to 12 µm and they are between 50 and 150 nm in diameter. The SEM images indicate that even though cobalt is distributed along the whole length of tungsten oxide nanowires, more cobalt is present at the nanowire tips (see Supporting Information). At high loading levels, cobalt oxide clusters at the tips in a nano-flake morphology. EDX studies confirm the presence of cobalt in both Co/LC and Co/HC samples (see Supporting Information). TEM microscopy of a Co/HC sample confirmed SEM results and further revealed that nanoparticles covering WO_3 nanowires have diameters ranging from 20 nm to 80 nm (see Fig. 3). WO_3 nanowires are crystalline with no amorphous edge observed proving that annealing step at 550 °C in air was efficient. Clear lattice fringes of 0.36 nm are observed (inset in Fig. 3c) corresponding to the interplanar spacing of (200) planes in monoclinic WO_3 (ICDD no. 43-1035), thus supporting XRD results. Nanoparticles deposited at the upper tip of the WO_3 nanowire are polycrystalline, as concluded from selective area electron diffraction (SAED) pattern (see the Supporting Information, Fig. S3a and b). EDX spectrum taken over this area (see the Supporting Information, Fig. S3c), reveals the presence of wolfram, oxygen, and cobalt. In addition, the interplanar spacing measured in some of the deposited CoO_X nanoparticles is 0.46 nm (inset in Fig. 3b), which could correspond to the interplanar spacing of (111) planes in Co_3O_4 (ICDD no. 01-073-1701).

In contrast, on the Co/LC sample, characteristically smaller cobalt-containing agglomerates are found at the surface of WO_3 nanowires (Fig. 4). Also these agglomerates are less densely distributed over the WO_3 nanowires than in the case of the Co/HC sample.

Additionally, an element mapping was performed to confirm the material distribution as well as room-temperature photoluminescence study (these results can be found in the Supporting information). The elemental mapping confirms that cobalt is well distributed along the full length of the tungsten oxide nanowires, with higher presence at the

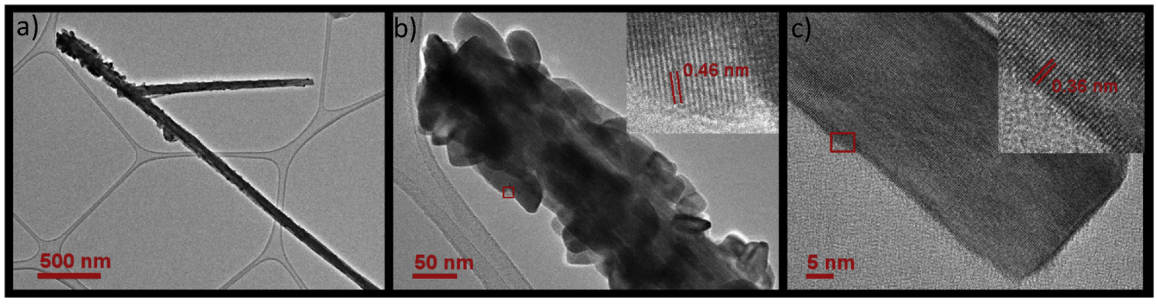

Fig. 3. TEM images of Co/HC sample: (a) TEM image of an individual WO_3 nanowire where (b) the upper end is thickly covered with CoOx nanoparticles (b) while the bottom end is not (c). HR-TEM inset in figure (c) reveals that the WO3 nanowire is crystalline. The measured lattice fringes, inset to figure (b) and (c), are 0.46 nm and 0.36 nm, respectively, which corresponds to the interplanar spacing of (111) planes in Co_3O_4 (ICDD no. 01-073-1701) and (200) planes in monoclinic WO_3. (ICDD no. 43-1035). The red frames in images (b) and (c) indicate areas of the HRTEM insets in images b and c (For interpretation of the references to colour in this figure legend, the reader is referred to the web version of this article).

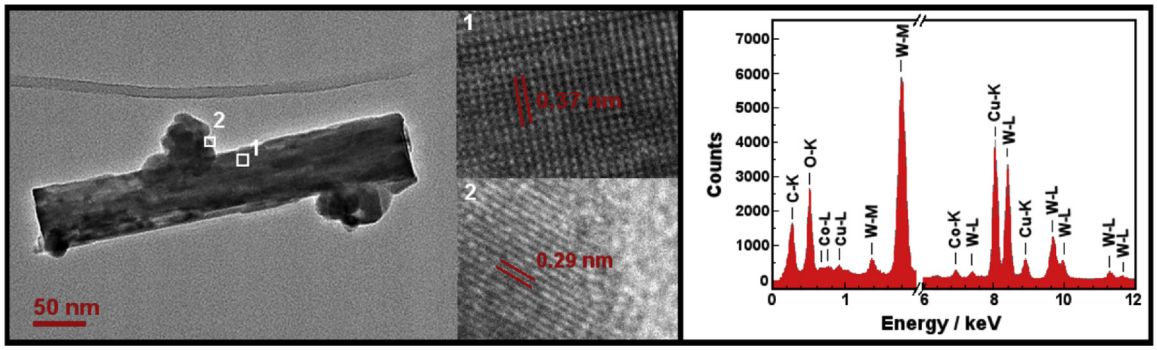

Fig. 4. TEM image of the Co/LC WO_3 nanowire with a corresponding EDX spectrum. HRTEM images of WO_3 nanowire (1) and nanoparticle attached to the surface of WO_3 nanowire (2) reveal that both WO_3 nanowires and nanoparticles are crystalline. The measured lattice fringes in 1 is 0.37 nm, which corresponds to (200) planes in monoclinic WO_3 (ICDD no. 43-1035). The EDX spectrum indicates that the nanoparticle agglomerate at the surface of the WO_3 nanowire contains cobalt.

nanowire tips. The PL study indicates that Co-loaded tungsten oxide nanowires have higher number of defects than pure tungsten oxide nanowires.

To investigate the surface composition and chemical states of the elements in the samples synthesized with different cobalt loading, XPS spectra were recorded. A typical survey spectrum is shown in Fig. 5a. It indicates that the surface of the samples is composed of tungsten and oxygen elements with carbon contamination. In addition, the peaks generated by photoelectrons emitted from cobalt atoms are evident. The relative concentration of elements is shown in the Supporting Information (Table S1), it is clear that by increasing the amount of cobalt loading, the amount of Co incorporated into the material increases. It was observed that the Co/HC sample loaded with the higher concentration of cobalt oxide presented two different regions having dark grey and a light grey colors in SEM images (see Supporting Information, Fig. S4). By studying the concentration of Co in these areas, it is clear that the amount of Co incorporated is higher in the dark grey region.

The high-resolution spectrum of the W4*f* core level (Fig. 5b) shows a doublet with components at 35.3 and 33.1 eV, which are assigned to W4$f_{5/2}$ and W4$f_{7/2}$, respectively. These peaks can be associated to the presence of W atoms with oxidation state 6+ (WO_3) [13]. The detailed inspection of the XPS Co 2p spectra recorded on the different samples and regions (Fig. 5c), shows that for sample Co/LC and light grey region of sample Co/HC, cobalt has the oxidation state 2+, while in the dark grey region of sample Co/HC the oxidation state is 3+ [24,25]. This supports the HRTEM findings, indicating the polycrystalline nature of cobalt oxide in Co/HC samples.

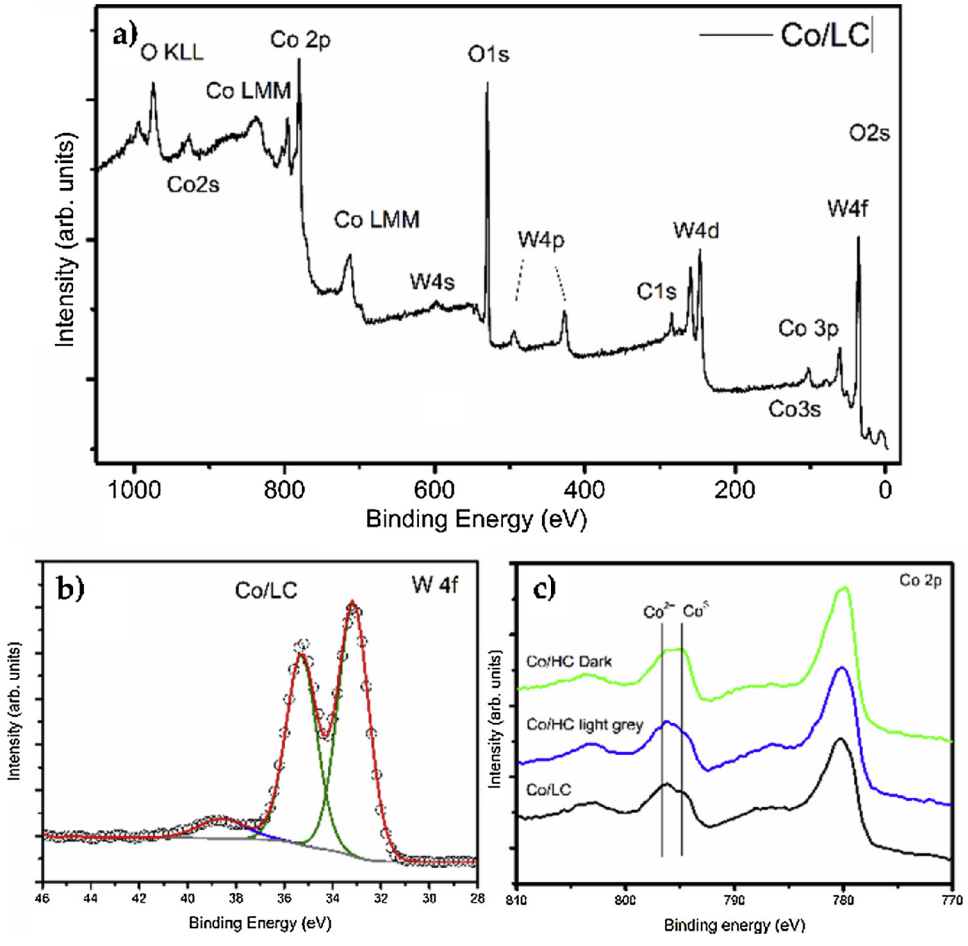

Fig. 5. a) XPS survey showing the composition at the Co/LC sample surface. b) XPS spectrum recorded in the binding energy range of the 4f core level. The spectrum is characterized by a doublet W4$f_{5/2}$ and W4$f_{7/2}$ and a singlet loss feature centered at 38.7 eV. c) Co 2p XP spectrum on both samples Co/LC and Co/HC in the light and dark regions.

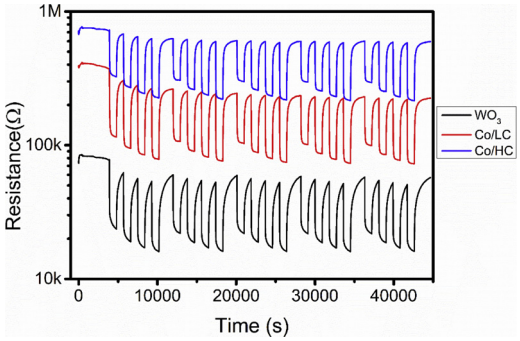

Fig. 6. Sensor resistance behavior when sensors were exposed to 5, 10, 15 and 20 ppm of ethanol while operated at 250 °C. The measurement cycle was repeated 5 times.

3.2. Gas sensing results

The responses of the different materials to ethanol, hydrogen, hydrogen sulfide and ammonia were studied under dry and humid conditions (50% R.H.). Hydrogen and ammonia detection results can be found in the Supporting Information.

3.2.1. Ethanol

The sensors were exposed to different concentrations of ethanol vapors, namely, 5, 10, 15 and 20 ppm in a balance of dry air. Each sensor was exposed to a cycle of four pulses of increasing gas concentrations. Between two consecutive concentration pulses, dry air was used to clean the sensor surface. To test the repeatability of the measurements, such cycle was repeated five times (see Fig. 6). Results indicate that measurements were highly repeatable.

Fig. 7 reports these results for pure tungsten oxide samples operated at three different temperatures (i.e., 150, 200 and 250 °C). Fig. 8 shows that loading tungsten oxide with cobalt has a positive effect in the sensitization towards ethanol vapors. In particular, when loaded at the higher level (Co/HC sample), the higher responsiveness towards ethanol under dry conditions is reached at the lowest operating temperature tested (i.e., 150 °C). The improvement in responsiveness in Co/HC samples is roughly 80% (compared to the responsiveness of pure tungsten oxide samples). Fig. 8 reports as well the responses to ethanol vapors of cobalt loaded tungsten oxide samples, when measured under humid conditions. At 50% R.H., the response towards ethanol is negatively affected. The comparison of the slopes of the curves shown in Fig. 8 clearly indicate that slopes are lower under humid conditions, which is indicative of a decrease in ethanol sensitivity. Fig. 8 shows as well that Co/HC samples operated at the higher temperature tested are more resilient to the presence of moisture, since responsiveness to ethanol remains remarkably high.

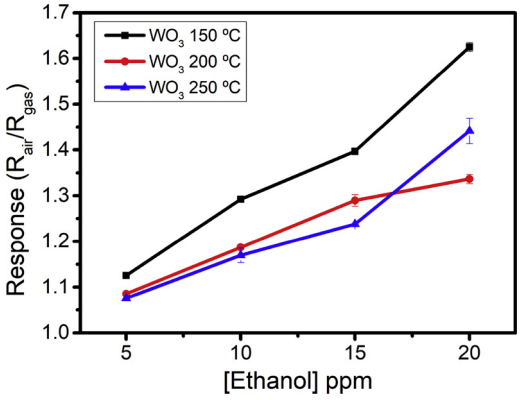

Fig. 7. Effect of the working temperature, to pure WO_3 sensor, on the response to different concentrations of ethanol (diluted in dry air).

3.2.2. Hydrogen sulfide

Finally, the response of the different nanomaterials to hydrogen sulfide was investigated. In the first step, sensors were exposed to hydrogen sulfide at 10, 15, 25 and 50 ppm under dry conditions. These results are summarized in Figs. 9 and 10. The loading of tungsten oxide nanowires with cobalt results in an enhanced response towards H_2S. The improvement in responsiveness towards hydrogen sulfide in Co/HC samples is roughly 60% (compared to the responsiveness of pure tungsten oxide samples). The effect of the operating temperature is very different in pure and cobalt-loaded samples. While the responsiveness towards hydrogen sulfide decreases with the operating temperature in pure tungsten oxide samples, responsiveness increases when the operating temperature is raised for cobalt-loaded samples. This is indicative that the contribution to the response of cobalt oxide nanoparticles decorating tungsten oxide nanowires is a temperature-activated process (catalytic effect). When in the presence of background humidity (see Fig. 10), cobalt-loaded sensors, especially those employing Co/HC samples, remarkably retain high responsiveness towards hydrogen sulfide, provided they are operated at high temperatures (i.e., 250 °C).

The low standard deviations (error bars) associated to the measurements reported in this section are indicative, not only of the good repeatability of measurements, but also of the fair reproducibility of sensors since Figs. 7–10 summarize the results for two sensors per material considered. The gas sensing properties towards hydrogen and ammonia are fully discussed in the Supporting Information. A short summary of these results is as follows. Co-loaded sensors show small responsiveness towards hydrogen. In contrast, under dry conditions, Co/LC sensors operated at 250 °C were found to be remarkably selective to ammonia, since the response to this vapor was 4 times higher than for any of the other species tested (see Fig. 11). However, the presence of ambient moisture heavily influenced (diminished) the response towards ammonia.

Since Co/LC sensors operated at 250 °C were the most promising devices, a long-term stability test was performed for these sensors. Long-term stability measurements consisted of measuring ethanol during November 2018 and then repeating these ethanol measurements in May 2019, after 6 months of continuous operation in which other species such as hydrogen, hydrogen sulfide or ammonia had been measured. Long-term stability results are summarized in Fig. 12, which shows a normalized response towards ethanol (a baseline correction was applied). Results indicate that a fair long-term stability is achieved over a 6-month period.

If compared to the state of the art results reported in Table 1, our Co-loaded sensors have undergone a more in depth study (gas sensing properties, moisture cross-sensitivity and long-term stability). They show promise in the selective detection of low levels of ammonia (if background humidity is filtered out) and in the detection of hydrogen sulfide (in this case with the clear benefit of showing low moisture cross-sensitivity).

3.3. Gas sensing mechanisms

It is generally accepted that, reducing species such as ethanol, hydrogen or hydrogen sulfide are adsorbed on metal oxides and react with oxygen surface species. Electrons trapped at oxygen adsorbates are then freed and contribute to the increase in the electrical conductance that is observed in n-type metal oxide films. As discussed in the introduction, the decoration of an n-type metal oxide (e.g. tungsten oxide) with p-type (e.g. cobalt oxide) nanoparticles can tune the sensitivity and selectivity of the n-type metal oxide via electronic and chemical sensitization effects. In particular, the use of catalytically active metals can enhance sensitivity towards reducing species by increasing the amount of oxygen surface species in their n-type metal oxide host (via a spillover effect). However, this does not seem to be the case here, because

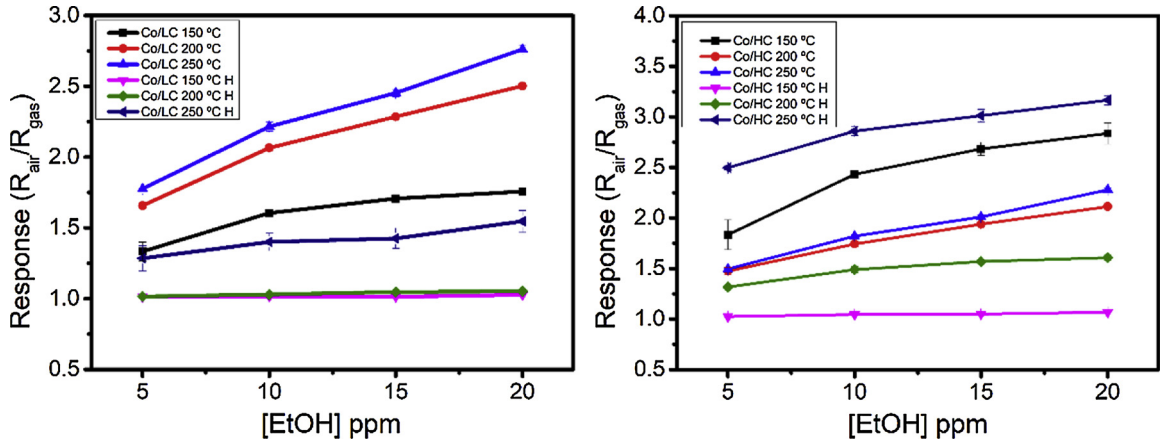

Fig. 8. Humidity effect on ethanol sensing at different operating temperatures for cobalt-loaded samples. Left panel Co/LC results; Right panel Co/HC results.

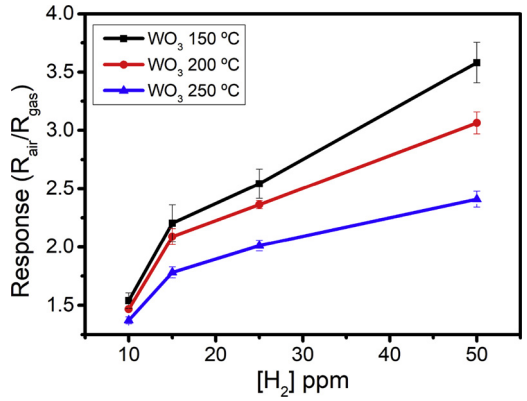

Fig. 9. Effect of the working temperature, to pure WO_3 sensor, on the response to different concentrations of hydrogen sulfide (diluted in dry air).

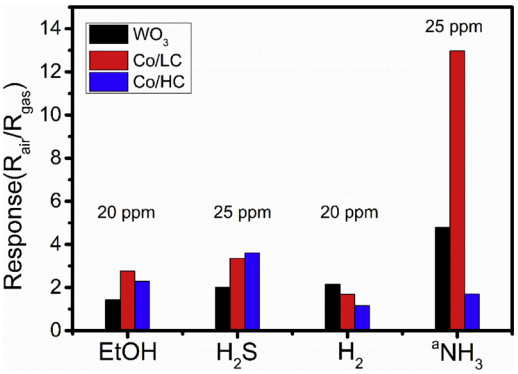

Fig. 11. Sensor response (R_{air}/R_{gas}) comparison for the different species and different nanomaterials used (under dry air conditions). Operating temperature was set to 250 °C. [a]Sensor response calculated as R_{gas}/R_{air}.

such an increase in the number of adsorbed oxygen species would have been very favorable for increasing the response towards hydrogen, which was not observed. Therefore, we have to conclude that the main reasons for the observed enhancement in responsiveness of cobalt oxide-loaded samples towards ethanol and hydrogen sulfide are related to:

- Charge-transfer mechanisms triggered by the adsorption of ethanol or hydrogen sulfide on cobalt oxide nanoparticles, which affect the width of the depletion zones that develop at the p-n interfaces.
- Ethanol or hydrogen sulfide reacting with cobalt oxide nanoparticles and, producing highly reactive radicals that can further react with oxygen species located at the surface of the n-type tungsten oxide via a spill-over effect.

At the operating temperatures tested, we can assume that the dominant oxygen species at the surface of tungsten oxide are O^- [26]. The presence of cobalt oxide nanoparticles could help breaking down the ethanol molecule, favoring its complete oxidation and maximizing the number of electrons released to the conduction band of tungsten

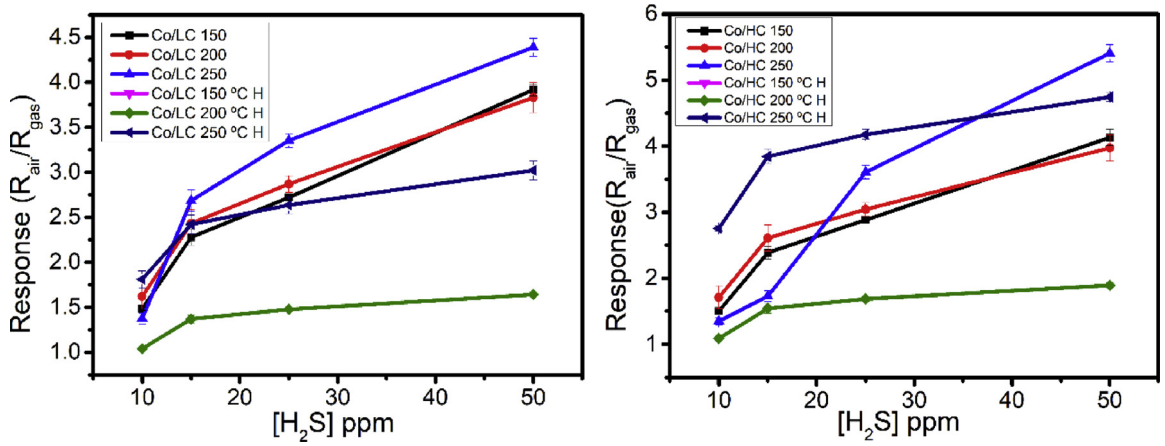

Fig. 10. Humidity effect on hydrogen sulfide sensing at different operating temperatures for cobalt-loaded samples. Left panel Co/LC results; Right panel Co/HC results.

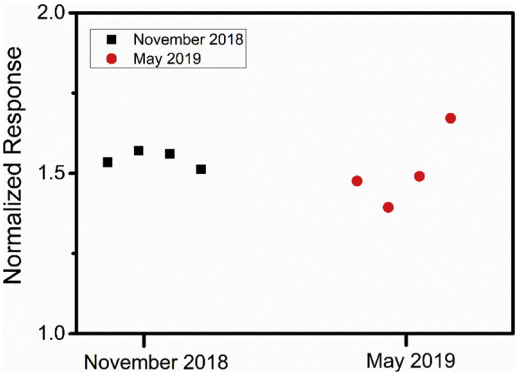

Fig. 12. Long-term stability study for Co/LC sensors operating at the optimal working temperature of 250 °C and detecting ethanol vapors.

oxide (see Eq. 1).

$$C_2H_5OH(g) + 6O^-(ads) \rightarrow 2CO_2(g) + 3H_2O + 6e^- \quad (1)$$

Fig. 13 shows a cartoon of the detection mechanism for ethanol or hydrogen sulfide in which the presence of cobalt oxide nanoparticles contributes to the effective oxidation of ethanol and thus, to response enhancement.

For H_2S, a similar mechanism than the one describe for ethanol applies [17] in which hydrogen sulfide molecules react with oxygen surface species present on tungsten oxide nanowires, releasing electrons as reported in Eq. 2.

$$H_2S_{(g)} + 3O^-_{(ads)} \rightarrow SO_{2(g)} + H_2O + 3e^- \quad (2)$$

According to Eq. 2, a hydrogen sulfide molecule reacts with oxygen adsorbates and undergoes an oxidation that leads to the formation of sulfur dioxide, water and the transferring of three electrons towards the conduction band of tungsten oxide. Furthermore, cobalt oxide nanoparticles can suffer a sulfurization process as expressed by Eqs. 3 and 4, leading to a response enhancement due to electronic sensitization. The width of the depletion layers at the n–p interfaces is altered (reduced) upon this sulfurization process. Such a process is similar, but to a much lower extend, to the one described in tungsten oxide nanowires decorated with copper oxide nanoparticles [9].

$$Co_3O_{4(s)} + H_2S_{(g)} + O_{2(g)} \rightarrow 3CoO + SO_{2(g)} + H_2O \quad (3)$$

$$CoO_{(s)} + H_2S_{(g)} \rightarrow CoS_{(s)} + H_2O_{(g)} \quad (4)$$

The XPS analysis performed after H_2S detection indicates the presence of Sulphur at the sensing layer surface. A close analysis of the S 2p core level spectrum (supplement Fig. S10) suggests the presence of S-O and S-Co supporting the assumptions in Eqs. 3 and 4.

This sulfurization of cobalt oxide nanoparticles can be reversed (at least in part) when the gas sensitive films are cleaned using a flow of pure dry air, as shown by Eq. 5 [25]:

$$Co_{1-y}S_{(s)} + (3\text{-}y/2)O_{2(g)} \rightarrow (1 - y)CoO_{(s)} + S_2O_{(g)} \quad (5)$$

In a humidified background, water molecules compete with target molecules for the adsorption sites available. Exposure to ambient moisture leads to formation of surface hydroxyl groups. In comparison to a dry surface, a hydroxylated surface has a significantly lower number of surface oxygen species that are free to react with ethanol, hydrogen or hydrogen sulfide. This is why the observed responsiveness and sensitivity decreases in a humid atmosphere. When operating at high temperatures (e.g. 250 °C) the desorption of water from the gas-sensitive surface is favored, which explains why at higher operating temperatures, the response towards target species is restored, at least in part. The reversible sulfurization mechanism described above, a detection mechanism that does not rely on the direct interaction of hydrogen sulfide with oxygen surface species, could explain why cobalt-oxide loaded tungsten oxide is quite resilient to the presence of ambient moisture in the detection of hydrogen sulfide.

4. Conclusions

AACVD has been employed in a two steps process to successfully grow tungsten oxide loaded with different amounts of cobalt oxide nanoparticles. ESEM, HR-TEM, XRD, EDX and XPS analysis confirm that single crystalline tungsten oxide nanowires loaded with cobalt oxide nanoparticles are obtained.

The gas sensing properties of the different nanomaterials grown have been studied. There is a clear modification in the gas sensing behavior between films of pure tungsten oxide nanowires and those obtained with cobalt oxide loaded tungsten oxide nanowires. While the loading did not have a positive effect for detecting hydrogen, the presence of cobalt oxide nanoparticles clearly had a positive influence in enhancing responsiveness to ethanol (80% increase) and hydrogen sulfide (60% increase). Co-loading at low levels also had a positive effect for achieving remarkable selectivity towards ammonia. The presence of humidity is, in general, detrimental for the detection of the four reducing species tested. However, it was found that by loading tungsten oxide nanowires with cobalt oxide nanoparticles resulted in a clear decrease in the moisture cross-sensitivity, especially in the detection of hydrogen sulfide at an operating temperature of 250 °C. This result can be attributed to an electronic sensitization mechanism in which a reversible sulfurization of cobalt oxide occurs upon exposure of the gas sensitive film to hydrogen sulfide. Cobalt oxide is regenerated during the recovery phase in which sensors are flown with pure air. In addition, the sensors tested show very good repeatability and good long-term stability.

Declaration of Competing Interest

There are no conflicts of interest to declare.

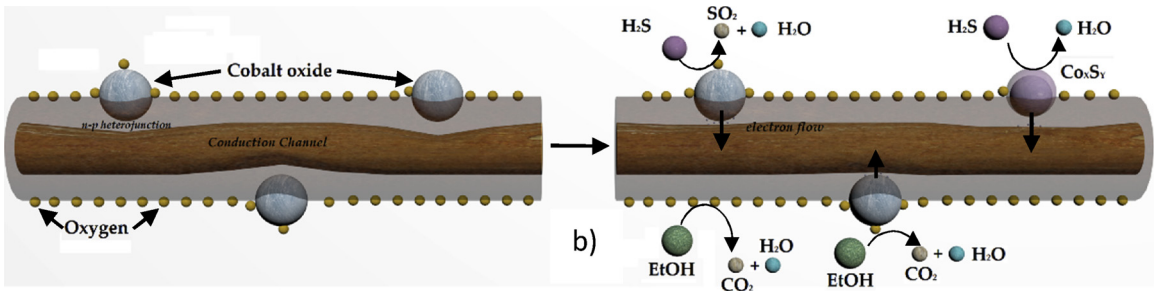

Fig. 13. Representation gas sensing mechanisms for ethanol and hydrogen sulfide. a) Representation of oxidation of H_2S molecules via reaction with adsorbed oxygen species (upper left) and partial cobalt oxide sulfurization (upper right). b) Reaction of ethanol molecules with oxygen molecules adsorbed both at cobalt oxide nanoparticles and the nanowire surface (bottom).

Acknowledgements

The authors are thankful to Ellen Baken, Senior Applications Scientist at Thermo Fisher Scientific for providing the element mapping results. This work was funded in part by MINECO, MICINN and FEDER via grants no. TEC2015-71663-R and RTI2018-101580-B-I00, by AGAUR under grant. 2017SGR 418 and by FNRS via PLAFON and FITTED projects. E.N. gratefully acknowledges a doctoral fellowship from MINECO grant no. BES-2016-076582. E.L. is supported by the Catalan institution for Research and Advanced Studies via the 2012 and 2018 Editions of the ICREA Academia Award. F.G. is supported by MICINN via grant no. MAT2017-87500-P. C.B. is a research Associate of the FNRS (Belgium). P.U. gratefully acknowledges the Slovenian Research Agency for financial support (program P1-0125).

Appendix A. Supplementary data

Supplementary material related to this article can be found, in the online version, at doi:https://doi.org/10.1016/j.snb.2019.126868.

References

[1] H. Akimoto, Global air quality and pollution, Science (80-) 302 (5651) (2003) 1716–1719.
[2] B. Szulczyński, J. Gębicki, Currently commercially available chemical sensors employed for detection of volatile organic compounds in outdoor and indoor air, Environments 4 (1) (2017) 21.
[3] P.J.D. Peterson, et al., Practical use of metal oxide semiconductor gas sensors for measuring nitrogen dioxide and ozone in urban environments, Sensors (Switzerland) 17 (7) (2017) 1–25.
[4] G.F. Fine, L.M. Cavanagh, A. Afonja, R. Binions, Metal oxide semi-conductor gas sensors in environmental monitoring, Sensors 10 (6) (2010) 5469–5502.
[5] Y.-C. Hsieh, D.-J. Yao, Intelligent gas-sensing systems and their applications, J. Micromech. Microeng. 28 (9) (2018) p. 093001.
[6] T. Itoh, T. Akamatsu, A. Tsuruta, W. Shin, Selective detection of target volatile organic compounds in contaminated humid air using a sensor array with principal component analysis, Sensors (Switzerland) 17 (7) (2017).
[7] L. Kowalski, J. Pons-Nin, E. Navarrete, E. Llobet, M. Domínguez-Pumar, Using a second order sigma-Delta control to improve the performance of metal-oxide gas sensors, Sensors 18 (2) (2018) 654.
[8] R. Kumar, O. Al-Dossary, G. Kumar, A. Umar, Zinc oxide nanostructures for NO_2 gas–sensor applications: a review, Nano-Micro Lett. 7 (2) (2015) 97–120.
[9] Z. Yuan, J. Zhang, F. Meng, Y. Li, R. Li, Y. Chang, J. Zhao, E. Han, S. Wang, Highly sensitive ammonia sensors based on Ag-decorated WO_3 nanorods, TNANO 17 (6) (2018) 1252–1258.
[10] P. Strang, Analysis of the noble metal catalytic additives introduced by impregnation of as obtained SnO sol–gel nanocrystals for gas sensors, Lakartidningen 101 (15–16) (2000) 1350–1351.
[11] F.E. Annanouch, et al., Aerosol-assisted CVD-grown WO3 nanoneedles decorated with copper oxide nanoparticles for the selective and humidity-resilient detection of H2S, ACS Appl. Mater. Interfaces 7 (12) (2015) 6842–6851.
[12] F.E. Annanouch, et al., Aerosol-assisted CVD-grown PdO nanoparticle-decorated tungsten oxide nanoneedles extremely sensitive and selective to hydrogen, ACS Appl. Mater. Interfaces 8 (16) (2016) 10413–10421.
[13] E. Navarrete, C. Bittencourt, P. Umek, E. Llobet, AACVD and gas sensing properties of nickel oxide nanoparticle decorated tungsten oxide nanowires, J. Mater. Chem. C 6 (19) (2018) 5181–5192.
[14] E. Navarrete, E. González, T. Vilic, E. Llobet, Cobalt or silver doped WO3 nanowires deposited by a Two-step AACVD for gas sensing applications, Proceedings 1 (4) (2017) 438.
[15] S. Vladimirova, et al., Co3O4as p-type material for CO sensing in humid air, Sensors (Switzerland) 17 (10) (2017) 1–13.
[16] K. Il Choi, H.R. Kim, K.M. Kim, D. Liu, G. Cao, J.H. Lee, C2H5OH sensing characteristics of various Co3O4 nanostructures prepared by solvothermal reaction, Sensors Actuators B Chem. 146 (1) (2010) 183–189.
[17] S. Jain, A. Patrike, S.S. Badadhe, M. Bhardwaj, S. Ogale, Room-temperature ammonia gas sensing using mixed-valent $CuCo_2O_4$ nanoplatelets: performance enhancement through stoichiometry control, ACS Omega 3 (2) (2018) 1977–1982.
[18] O. Alev, A. Kılıç, Ç. Çakırlar, S. Büyükköse, Z.Z. Öztürk, Gas sensing properties of p-Co3O4/n-TiO2nanotube heterostructures, Sensors (Switzerland) 18 (4) (2018).
[19] M.N. Rumyantseva, et al., p-CoOx/n-SnO2nanostructures: new highly selective materials for H2S detection, Sensors Actuators B Chem. 55 (2018) 564–571.
[20] L.P. Oleksenko, N.P. Maksymovych, A.I. Buvailo, I.P. Matushko, N. Dollahon, Adsorption-semiconductor hydrogen sensors based on nanosized tin dioxide with cobalt oxide additives, Sensors Actuators B Chem. 174 (2012) 39–44.
[21] M. Punginsang, A. Wisitsora-At, A. Tuantranont, S. Phanichphant, C. Liewhiran, Effects of Cobalt Doping on Nitric Oxide, Acetone and Ethanol Sensing Performances of FSP-Made SnO2nanoparticles, Elsevier B.V., 2015, p. 210.
[22] P. Velusamy, R.R. Babu, K. Ramamurthi, E. Elangovan, J. Viegas, M. Sridharan, Sensors and actuators B: chemical gas sensing and opto-electronic properties of spray deposited cobalt doped CdO thin films, Sensors Actuators B Chem. 255 (2018) 871–883.
[23] W. Belkacem, A. Labidi, J. Guérin, N. Mliki, K. Aguir, Cobalt nanograins effect on the ozone detection by WO3 sensors, Sensors Actuators B Chem. 132 (1) (2008) 196–201.
[24] M. Hassel, H.J. Freund, High Resolution XPS study of a thin CoO (111) film grown on Co (0001), Surf. Sci. Spectra 4 (3) (1998) 273–278.
[25] D. Kawano, T. Kawai, H. Naito, Y. Goto, M. Odaka, W.D. Bachalo, Comparative measurement of nano-particulates in diesel engine exhaust gas by laser-induced incandescence (LII) and scanning mobility particle sizer (SMPS), Test Lii (2004) 3090–3099.
[26] A. Najbar, M. Bielanski, Metal oxides, J. Catal. 25 (1972) 398–406.

2.3.3 Tungsten trioxide nanowires decorated with iridium oxide nanoparticles as gas sensing material.

Journal of Alloys and Compounds 812 (2020) 152156

Contents lists available at ScienceDirect

Journal of Alloys and Compounds

journal homepage: http://www.elsevier.com/locate/jalcom

Tungsten trioxide nanowires decorated with iridium oxide nanoparticles as gas sensing material

Eric Navarrete [a], Carla Bittencourt [b], Polona Umek [c], Damien Cossement [d], Frank Güell [e], Eduard Llobet [a, *]

[a] MINOS-EMaS, Universitat Rovira i Virgili, Avda. Països Catalans, 26, 43007, Tarragona, Spain
[b] Chimie des Interactions Plasma – Surface (ChIPS), Research Institute for Materials Science and Engineering, Université de Mons, Avenue Copernic 3, 7000, Mons, Belgium
[c] Jožef Stefan Institute, Jamova cesta 39, 10000, Ljubljana, Slovenia
[d] Materia Nova, Avenue Copernic 3, 7000, Mons, Belgium
[e] ENFOCAT-IN2UB, Universitat de Barcelona, C/Martí i Franquès 1, 08028, Barcelona, Catalunya, Spain

ARTICLE INFO

Article history:
Received 27 April 2019
Received in revised form
1 July 2019
Accepted 3 September 2019
Available online 3 September 2019

Keywords:
Tungsten oxide
Iridium oxide
Nanowires
Nanoparticles
Gas sensing
NO_2

ABSTRACT

Tungsten trioxide nanowires were grown employing aerosol assisted chemical vapor deposition (AACVD) and subsequently decorated with different loading levels of iridium oxide nanoparticles. AACVD has been already demonstrated to be a useful tool to load different ranges of nanoparticles on top of an already grown layer. This procedure enables growing the gas sensitive nanomaterials directly onto application substrates for the development of chemo-resistive gas sensors. The morphology and composition of the different materials were characterized via different techniques. It was found that iridium oxide loading resulted in remarkable changes in the morphology and defects of tungsten oxide nanowires. The gas sensing properties of such layers were studied towards ethanol or ammonia vapors, hydrogen, hydrogen sulfide, and nitrogen dioxide. The optimization of the operating temperature and the level of iridium oxide loading results in an improvement in the responsiveness and selectivity towards the species tested. In particular, a dramatically high increase in the response towards nitrogen dioxide is achieved. The mechanisms of gas sensing are discussed in detail.

1. Introduction

There is a worldwide rising concern about air quality monitoring and toxic gas emissions. In this field, extensive efforts have been made in order to discover or manufacture sensors, with the ability to detect a specific gas among a mixture of gases or sensors having the ability to continuously monitor an atmosphere. Semiconductor metal oxides (MOXs) have risen as an outstanding family of promising materials due to their inexpensiveness, outstanding properties, such as chemical resistance, endurance and time stability. MOXs are employed as sensitive layers for sensors in many fields, they are present mostly in the automotive industry, the petrochemical industry and for safety monitoring in domestic premises. One of the most representative examples are MOX sensors employing SnO_2 nanolayers for the indoor detection of CO [1].

N-type semiconductor metal oxides often used for gas sensing such as SnO_2, ZnO, TiO_2, V_2O_4, In_2O_3 or WO_3, present different morphologies depending on the synthesis technique employed. From the abovementioned (MOXs), WO_3 has been extensively researched during the last decades for its outstanding photocatalytic and sensing properties. WO_3 presents a band gap of 2.6 eV, and can be tailored in different nanostructures depending on the growth methodology. WO_3 presents different crystallinity depending on temperature. For example ε-WO_3 with a monoclinic structure (P_m) is the predominant structure between 0 and 230 K. Between 230 and 290 K δ-WO_3 is the predominant structure belonging to the triclinic system (P_{-1}) and, finally, the predominant structure between 290 and 600 K is monoclinic γ-WO_3 belonging to the P2/m spatial group [2].

There are many approaches to synthesize nanostructured layers of WO_3 with different morphologies. The first family of techniques is the liquid-phase synthesis (LPS). In the liquid-phase approach, thin films are usually obtained, even though the product obtained is mostly a hydrate of tungsten trioxide, which will need further steps

* Corresponding author.
E-mail address: eduard.llobet@urv.cat (E. Llobet).

https://doi.org/10.1016/j.jallcom.2019.152156
0925-8388/

of calcination/annealing to become fully oxidized. Another approach consist of using hard templates [3] or soft templates [4], a variation of the sol-gel methodology in which porous thin films of WO_3 can be obtained, yet there is also the need of further annealing steps. Hydrothermal treatment is the most attractive LPS to tailor 1-D WO_3 nanostructures such as nanoplates [5] or nanowires/nanorods [6] through an easy procedure. A second family of procedures can be englobed to vapor-phase synthesis (VPS). In this family there are both chemical and physical approaches such as vapor phase deposition or sputtering. These two aforementioned techniques can produce different nanostructured WO_3 materials. In VPS, nanoparticles, nanorods, thin or thick films can be produced once the correct temperatures, gas flows and precursors are set [7]. For example, sputtering, glancing angle sputtering or oxygen reactive sputtering enables the fabrication of compact, nanostructured or thin metal oxide films, which can be height controlled [8]. Despite the fact that there are several VPS techniques, chemical vapor deposition (CVD) outstands as an easy procedure to obtain a wide range of WO_3 morphologies when using the appropriate conditions [9].

In this work we employ a modification of the above mentioned CVD, in which the precursors are conveyed dissolved in an aerosol into the reactor in which the CVD process is conducted. In aerosol assisted chemical vapor deposition, an organic solution precursor is prepared and then brought to an aerosol with a high-frequency generator. This aerosol is carried towards a preheated hot-wall reactor where a substrate is placed and the growth will take place. As described by Yun-Tsung et al. the supersaturated vapor containing WO_x condenses on top of the substrate forming WO_x clusters, which will act as seeds to develop the growth of nanowires (NWs) [9]. Thanks to the high temperature present inside the reactor (350–400 °C) the organic solvents rapidly decompose and leave WO_x species to act as growing blocks to keep forming the NW structure. Due to the organic precursors used, some remnant amorphous carbon is also present in the NWs forest layer, which is removed in a subsequent annealing step. The AACVD methodology can be employed as well to deliver foreign oxide nanoparticles to sensing layers previously grown. This makes the AACVD a suitable methodology for obtaining pure or late-transition metal oxide loaded tungsten oxide NWs. Typically, extensive research has been done employing noble metals and metal oxides onto tungsten oxide nanowires for gas sensing. For example, Annanouch et al. synthesized, via AACVD, tungsten oxide NWs decorated with core-shell Pd–PdO NPs for the detection of H_2 [10]. Platinum and gold have been also reported by Vallejos et al. [11] for the detection of H_2. Non-noble metals such as copper have been studied and reported by Annanouch et al. as highly selective materials for the detection of H_2S [12] and, nickel oxide reported by Navarrete et al. has also been demonstrated to increase the selectivity towards H_2S [13]. Despite the fact that noble metals display excellent gas sensing properties when decorating tungsten oxide NWs, to the authors' knowledge, iridium oxide has been studied very seldom in the context of gas sensing. Karthigeyan and co-workers presented a field effect transistor employing an iridium oxide thin film as ammonia gas sensor at room temperature [14]. However, studying this material is of interest, since iridium oxide has been widely reported as electrode material, due to its high catalytic activity in water-splitting reactions (OER), or as a pH sensor.

2. Experimental

2.1. Materials synthesis

Pure tungsten oxide (WO_3) NWs and IrO_2-decorated WO_3 NWs were grown employing the AACVD. The precursor for WO_3 NWs was tungsten hexacarbonyl ($W(CO)_6$) (97% purity) purchased from Sigma-Aldrich and the Iridium (IV) oxide (IrO_2) powder (purity 99%) was purchased from Alfa Aesar. Both precursors were employed without further purification. To grow such structures, two approaches can be considered: a 1-Step or 2-Step methodology. In the 1-Step methodology, both the NWs precursor and the iridium oxide are mixed in the same solution and delivered to the reactor during a single deposition. This 1-Step methodology has been already studied in previous works [13] and has been demonstrated to have a low-loading capacity in comparison to the 2-Step methodology, which is a much efficient way to achieve higher loading levels of tungsten oxide nanowires. Therefore, the 2-Step methodology was implemented.

In the first step, a solution of $W(CO)_6$ is prepared mixing 50 mg $W(CO)_6$ with 15 ml of acetone and 5 ml methanol. This solution then is converted into a spray of micro-droplets employing sonication at high frequency. Once the aerosol is created, a flow of nitrogen is used at 0.5 L/min to carry it towards a preheated hot wall CVD reactor. In this particular work, the optimal growth temperature for NWs lies in the range between 370 and 400 °C, since lower temperatures lead to the formation of nano-clustered WO_3 films instead of NWs. In this bottom-up methodology we take advantage of the self-assembly process that occurs once the organic compounds carried by the droplets enters into the high temperature zone were the carbon-based solvents are burned leaving tungsten species that act as building blocks for the NWs. The NW deposition took place onto the electrode area ($2.5 \times 2.5\ mm^2$) of commercially available alumina transducers (Ceram Tech GmBH, Plochingen, Germany).

Once the chemical vapor deposition is finished, the material is let to cool down at room temperature and examined. Due to the use of organic precursors and solvents, the tungsten trioxide NW layers have a dark blue color. This color is attributed to the presence of amorphous carbon and to a non-stoichiometric WO_{3-x}. To remove carbon impurities and increase the oxidation of tungsten, an annealing step is carried out. The annealing takes place inside a muffle with a synthetic air flow at 2 L/min during 2 h at 500 °C, heated at 5 °C/min rate and cooled naturally to room temperature once the process is finished. Finally, the annealed NWs show a yellow-pale color attributed to an almost stoichiometric WO_3 and to the removal of most carbon contamination. As mentioned above, such methodology can be employed also to load different amounts of nanoparticles to already grown NW layers. Following the same procedure several organic solutions were prepared depending on the desired iridium oxide concentration. Different amounts of iridium oxide (i.e., 5 mg, 10 mg and 15 mg) were dispersed in 10 ml methanol. The particle suspension solution was transformed in an aerosol and carried towards the preheated reactor where an already coated sensor had been placed. A commercially available iridium oxide characterized by a very wide dispersion in the dimensions of IrO_2 particles was used. However, the ultrasonic generator produced an aerosol in which only the smaller (nano-sized) IrO_2 particles could be found. These were the particles that were dragged by the carrier gas flow into the reactor and became eventually deposited onto WO_3 nanowires (see the supporting information). Bigger (i.e., heavier) particles remained in the vessel in which the aerosol was generated and these could be recycled, after mechanical milling, in a new loading process. Subsequently to the iridium oxide loading step, another annealing step is implemented to remove the remnant carbon impurities.

The morphology, crystalline phase and chemical composition of the different sensors grown on top of each substrate were studied employing scanning electron microscope (SEM) and high resolution transmission electron microscope (HRTEM), X-ray diffraction (XRD), energy-dispersive X-ray spectroscopy (EDX) and X-ray

photoelectron spectroscopy (XPS). SEM images were acquired using a SU8020 Microscope from Hitachi and a JEOL 7600 F field emission SEM (15 kV, working distance of 15 mm). The image resolution was set to 512 × 384 pixels while the corresponding map resolution was set to 128 × 96 pixels, meaning a pixel size of 0.01 μm in the image and of 0.05 μm in the map. EDX spectra were acquired using a microanalysis tool from Oxford Instruments by scanning a selected area of the sample (pixel resolution as for the SEM analysis) at a working distance of 10 mm at 20 kV with a 137 eV resolution. EDX spectra were analyzed with the aid of the INCA software. HRTEM characterization of the samples was performed on a Jeol 2100 microscope, working at 200 kV. The material was scratched from its alumina substrate and dispersed in methanol. The dispersion was ultrasonicated for 20 min and a drop was deposited on a lacy carbon film supported by a nickel grid. XRD was performed employing a Bruker-AXS D8-Discover diffractometer equipped with parallel incident beam (Göbel mirror), vertical θ-θ goniometer, XYZ motorized stage, and a General Area Detector Diffraction System. A 500 μm X-ray collimator system allowed the analysis of a mean area represented by an ellipsoid with a constant short axis of 500 μm and a variable long axis of 1500 down to 600 μm. The X-ray diffractometer was operated at 40 kV and 40 mA to generate Cu Kα radiation. The detector was an HI-STAR (multiwire proportional counter of 30 cm × 30 cm with a 1024 × 1024 pixel grid) placed at a 15-cm distance from the sample. Experimental diffractograms were fitted with the crystal structure (Rietveld analysis) for the phases identified with the aid of TOPAS 5.0 software. XPS was conducted using a VERSAPROBE PHI 5000 from Physical Electronics, equipped with a monochromatic Al Kα X-ray source (1486.6 eV). The X-ray photoelectron spectra were collected at the take-off angle of 45° with respect to the electron energy analyzer operated in the CAE (constant analyzer energy) mode, the X-ray beam diameter was 200 μm and the pass energy used was 187.5 eV for recording the survey spectrum and 23.5 eV for core level analysis. For the compensation of built-up charge on the sample surface during the measurements, a dual beam charge neutralization composed of an electron gun ($\approx$1 eV) and an Ar ion gun ($\leq$10 eV) was used. Binding energies are all referred to the C1s peak at 284.6 eV. Static ToF-SIMS data were acquired in negative mode using a ToF-SIMS IV instrument from ION-TOF GmbH. An Ar^+ 10 keV ion-beam was used as analysis beam at a current of 0.7 pA (negative ion mode detection), and rastered over a scan area of 100 × 100 μm^2. Three different locations on the surface were accounted for ToF-SIMS analysis.

Room-temperature photoluminescence (PL) measurements were made with a chopped Kimmon IK Series He–Cd laser (325 nm). Fluorescence was dispersed with a Princeton Instruments Acton SP2750 0.750 m imaging triple grating monochromator, detected using a Hamamatsu H8259-02 with a socket assembly E717-500 photomultiplier, and amplified through a Stanford Research Systems SR830 DSP. A 360 nm filter was used to filtering the stray light. It is worth pointing out that the emission spectra were corrected using the optical transfer function of the PL setup.

2.2. Gas sensing study

To study the tungsten trioxide NW ability to detect gases, and the effect of loading iridium oxide onto the NW matrix, the sensors were exposed to 5 different gases; ammonia vapors, ethanol, hydrogen, hydrogen sulfide and nitrogen dioxide. To perform the gas sensing analysis the sensors were placed inside an airtight Teflon® chamber. In this study all gases employed were used from calibrated gas bottles balanced in dry air and the carrier gas was zero-grade dry air. Despite using dry gases, there is always some remnant humidity in the measurement ring. By using a commercially available humidity sensor (SHT71, from Sensirion AG, Switzerland) placed in the sensor chamber, it was established that the relative humidity ranged between 2% and 5%. The concentrations analyzed for ammonia, ethanol vapors, hydrogen and hydrogen sulfide were set to 5, 10, 15 and 20 ppm and for nitrogen dioxide were set to 250, 500, 750 and 1000 ppb. The concentrations were delivered to the gas chamber through a computer-controlled mass-flow system to ensure the reproducibility of the concentrations delivered. The gas analysis was set as pulses consisting of increasing target gas concentrations with intercalated steps of dry air to recover the baseline at a 100 ml min^{-1} constant flow. The sensor DC electrical resistance was measured, acquired and stored employing a Keysight 3972A data acquisition system. An Agilent U8001A was used as power supply for heating the resistors in order to achieve the operating temperatures of 150 °C, 200 °C or 250 °C. Finally, to analyze the interference of ambient humidity, a liquid mass-flow was employed to humidify the carrier gas (to 35% R.H.) and an Arduino controlling the SHT71 humidity and temperature sensor IC was employed to acquire and store the relative humidity data.

3. Results and discussion

3.1. Effective loading study

Previous research done in the group revealed that different loading concentrations can enhance or decrease the response obtained from different gases [13], as well it has been also reported in the bibliography that higher foreign NPs loadings result in a signal decrease [15]. Therefore, in order to determine if it was worth studying all three loading concentrations in depth an initial screening of gas sensing properties was conducted. In this first step, the concentration tested were pristine WO_3 NWs, and 5, 10 and 15 mg IrO_2 loaded NWs. The overall results showed that for all the gases tested 15 mg IrO_2 loaded NWs had a resistance of the order of 30 GigaOhms. Such high a resistance makes very difficult to measure the sensor response towards a gas. As mentioned above, different loading levels can enhance or decrease the sensor response signal towards a gas. According to these preliminary results, the range of IrO_2 loadings achieved is enough to explore/optimize the gas sensing behavior of the loaded nanomaterials. Fig. 1 shows the normalized resistance responses to NO_2 and ethanol as examples of the sensor behavior to oxidizing and reducing gases.

Taking into consideration the high resistance of samples loaded with 15 mg IrO_2, only the samples consisting of pure WO_3 NWs, IrO_2 5 mg loaded WO_3 NWs and IrO_2 10 mg loaded WO_3 NWs will be further analyzed in depth both morphologically and chemically. These samples will be referred to, from here on, as WO_3, IrO_2/LC and IrO_2/HC, respectively.

3.2. Nanomaterial characterization

The NWs were analyzed by XRD to obtain the crystallographic structure of pure and IrO_2-loaded WO_3 NWs. The diffraction pattern of the pure WO_3 NW sample shown in Fig. 2 corresponds to a monoclinic structure, space group P21/n fitting with the ICDD card nº 43–1035. Peaks from the alumina substrate are also present in XRD spectra.

Tungsten trioxide NWs loaded with iridium oxide were studied employing SEM to understand their morphology. Fig. 3 shows both low and high concentration loaded NWs and their differences. On the one hand, pure WO_3 NWs show a smooth surface with few to none attached material particles (see supporting information

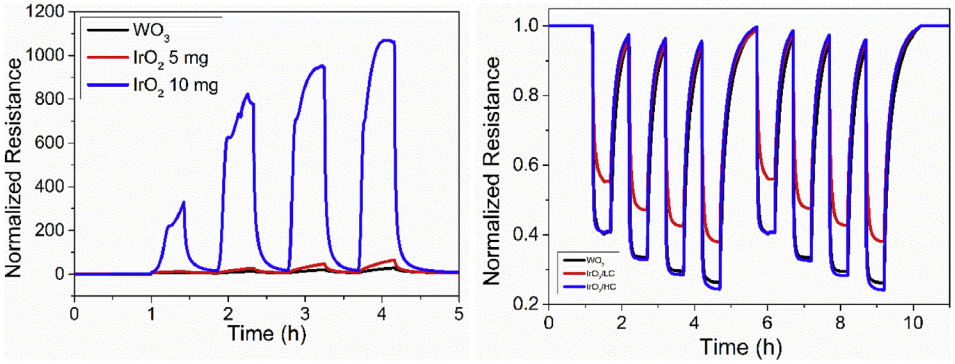

Fig. 1. Normalized dynamic response and recovery cycles of sensors. The left panel corresponds to NO_2 measurements obtained at 150 °C. The right panel corresponds to ethanol measurements obtained at 250 °C.

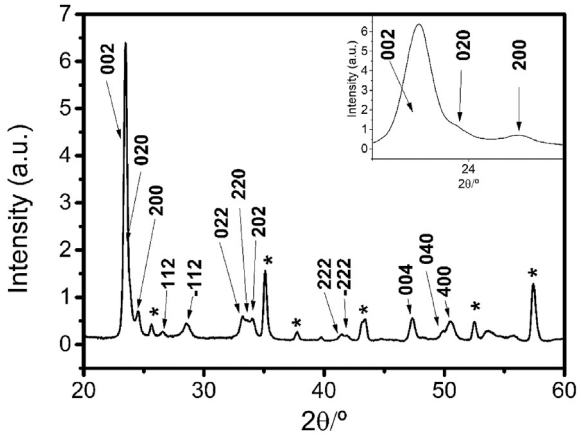

Fig. 2. XRD spectrum recorded on a layer of pristine tungsten trioxide NWs on top of an alumina substrate. All data fitted well with the ICDD card 43–1035 and the (*) labelled peaks correspond to the alumina substrate. The inset corresponds to an enlargement of the first two peaks.

Fig. S4), on the other hand, IrO_2/LC NWs present nanoclusters homogenously spread along the body, meanwhile IrO_2/HC NWs show an increase of such nanoclusters with a higher spread along the NW body.

Then, a HRTEM study was performed in such nanoclusters to determine their morphology, crystallinity and composition. Fig. 4, shows an IrO_2/HC NW with a close look to one of such clusters. The HRTEM inset shows that the nanocluster attached to the NW surface is crystalline. The d-spacing between lattice fringes in the inset is 0.364 nm corresponding to (200) planes in WO_3 with monoclinic structure (ICDD 43–1035) confirming the composition of the clusters present in the surface as tungsten trioxide. Therefore, the increase in iridium oxide loading results in a reshape of the NW morphology with the appearance of granular tungsten oxide on the surface of the NWs. This can possibly affect the specific surface area of the nanomaterial and the amount of structural defects.

X-ray photoelectron spectroscopy and time of flight secondary mass spectrometry were used in the chemical characterization of the sensor active layer. In the XPS survey spectrum we observed tungsten and oxygen peaks, the C 1s peak indicates the presence of contamination that can be associated with the partial removal of organic compounds (see supporting information Fig. S5). The most intense Ir XPS peaks partially overlap with the W XPS peaks, as the relative concentration of Ir is expected to be very small (~1%), the Ir peaks remain buried under the background of secondary electrons. The presence of Ir at the sample surface was confirmed by ToF-SIMS. We observed the presence of peaks at m/z 238.95 and 240.95 with relative intensity corresponding to the relative isotope abundance of 191 Ir and 193 Ir (Fig. 5).

The room-temperature PL spectra are presented in Fig. 6. By pumping at 325 nm, we observed an emission peak of the WO_3 NWs at around 450 nm (2.75 eV) with a full width at half maximum (FWHM) of 370 meV. When loading the WO_3 NWs with iridium oxide, the FWHM increased to about 1040 meV. The intensity of each spectrum was normalized to the maximum emission intensity for easiness of comparison. This broadening observed on the FWHM indicates that the quantity of intrinsic defects (e.g. oxygen vacancies and tungsten interstitials) [16,17] is higher when loading the WO_3 NWs with iridium oxide nanoparticles, which agrees with

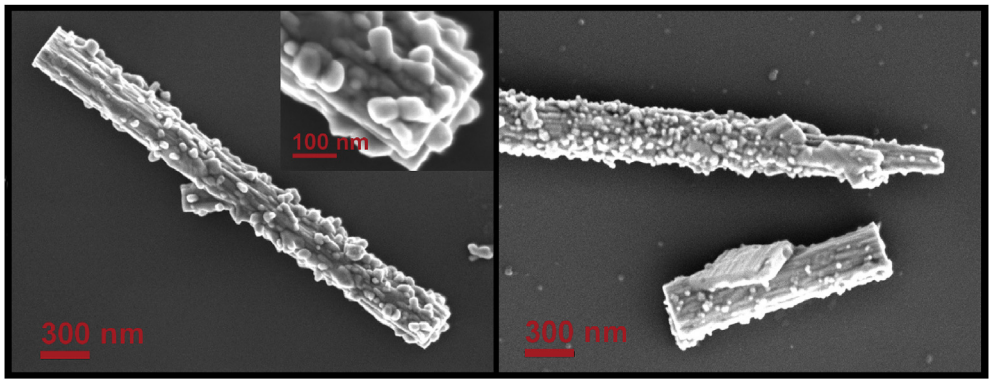

Fig. 3. SEM images for; IrO_2/LC NW (left panel), IrO_2/HC NW (right panel).

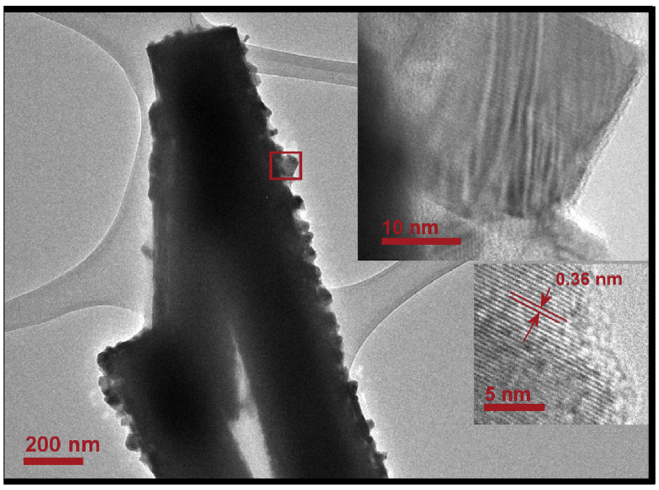

Fig. 4. HRTEM image performed on an IrO_2/HC NW (left panel). Close look at the nanoparticle surface showing structured fringes revealing a high crystallinity (Right panel).

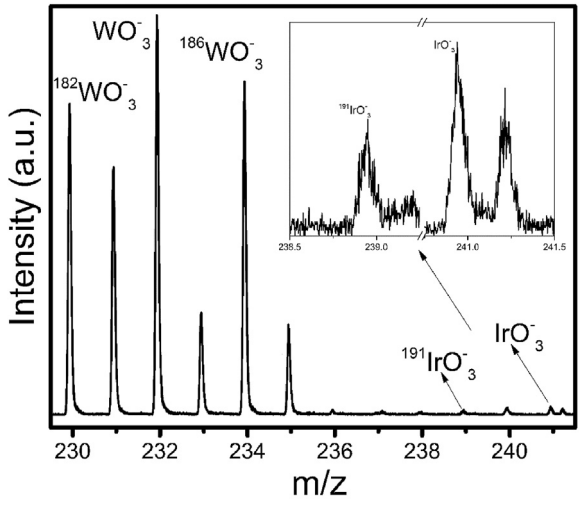

Fig. 5. TOF-SIMS surface analysis revealing the presence of iridium oxide at the surface of tungsten trioxide nanowires.

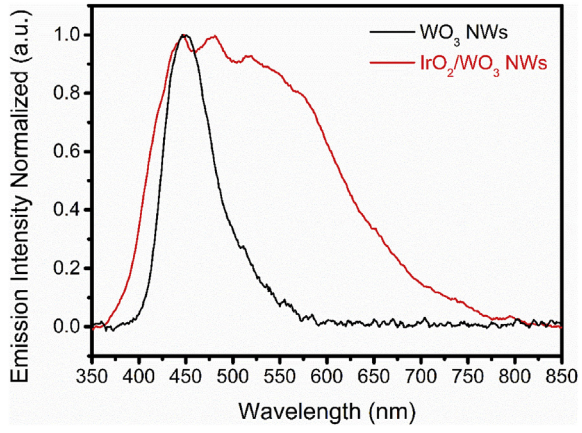

Fig. 6. Room-temperature emission spectra for WO_3 NWs and IrO_2-loaded WO_3 NWs.

the dramatic change in morphology revealed by HRTEM results, see Fig. 4, and is a consequence of the larger surface area of the IrO_2-loaded WO_3 NWs respect to the WO_3 NWs [18]. The photoluminescence of iridium oxide was studied to further verify these assumptions. Pure IrO_2 films did not show PL response, which supports the differences observed being due to differences in morphology and defects.

3.3. Gas sensing responses

The responses towards ethanol, hydrogen sulfide and nitrogen dioxide are presented and discussed in the following paragraphs. The results for hydrogen and ammonia can be found in the supporting information. A table summarizing response times for the different materials and species tested can be found in the supporting information too.

3.3.1. Ethanol results

Sensors were exposed to ethanol vapors balanced in dry air. The results obtained are shown in Fig. 7. When operating the sensor at the lower temperature considered (i.e., 150 °C), the overall responses displayed by all three types of sensors were much lower than the ones recorded at higher temperatures (i.e., 200 °C or 250 °C). At 200 °C or 250 °C, the response pattern for all the three sensor types shows a similar trend. At the operating temperatures tested, the higher iridium oxide loading level (i.e., IrO_2/HC) slightly enhances ethanol response in comparison to the one obtained with pristine WO_3 NWs, meanwhile the lower iridium oxide loading level (i.e., IrO_2/LC), decreases ethanol response. This behavior can be attributed to a competitive reaction between water vapor and ethanol for the active sites available. At higher loadings of iridium oxide, there is a higher amount of active sites available (due to morphological changes and increased number of defects, as revealed by TEM and PL studies), which enhances the reaction with ethanol molecules.

3.3.2. Hydrogen sulfide results

Hydrogen sulfide was studied at concentrations ranging from 5 to 20 ppm. The concentrations studied have been decreased in comparison to previous studies performed in our group due to the negative impact that H_2S may have to sensing layers [13]. As it can be seen from Fig. 8, the overall responses for all three gas sensor types increase as the operating temperatures are increased. From the results obtained it can be concluded that loading iridium oxide to the nanowire matrix has little effect on the responses towards hydrogen sulfide. The sensitivity achieved for this type of loading material is significantly lower than the one obtained in previous studies employing copper oxide [12] or nickel oxide [13].

3.3.3. Nitrogen dioxide results

In view of analyzing the response of iridium oxide loaded tungsten oxide NWs towards oxidizing gases, the response to NO_2 was studied. Fig. 9 summarizes the results obtained with the three different sensor types studied. The loading with iridium oxide clearly enhances the response towards NO_2. At the lowest temperature tested (i.e., 150 °C) the response to 1 ppm of NO_2 increases by a factor of 2 for IrO_2/LC and by a factor of 14 for IrO_2/HC (taking as reference the response of pristine tungsten oxide NWs). At the operating temperature of 200 °C, the highest response for both IrO_2/LC and IrO_2/HC sensor types is achieved (registering 2.3-fold and 95-fold increases in NO_2 response for IrO_2/LC and IrO_2/HC samples, respectively).

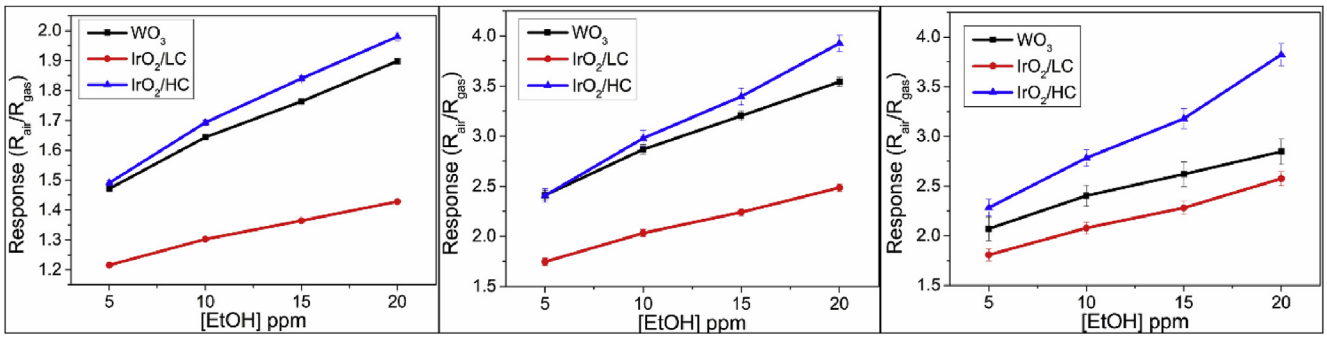

Fig. 7. Ethanol detection results at different operating temperatures. From left to right: 150 °C, 200 °C and 250 °C.

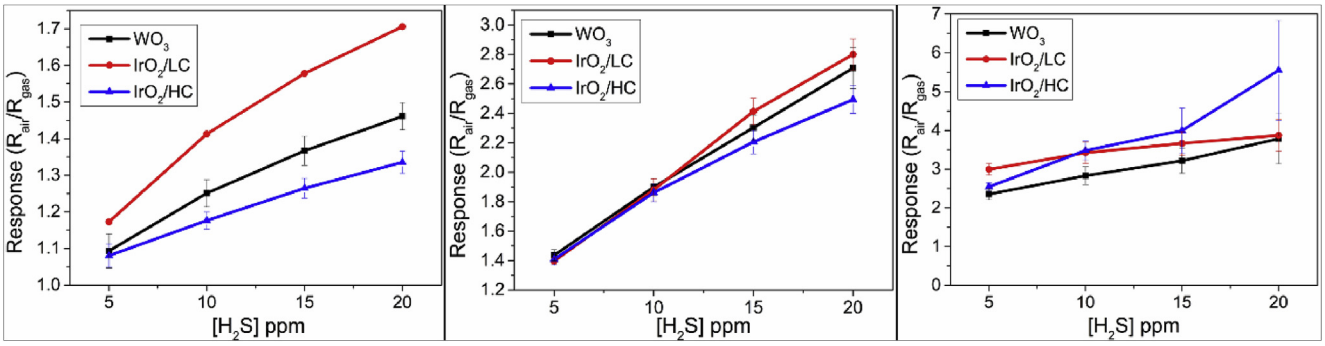

Fig. 8. Hydrogen sulfide detection responses at different working temperatures. From left to right panels: 150 °C, 200 °C and 250 °C.

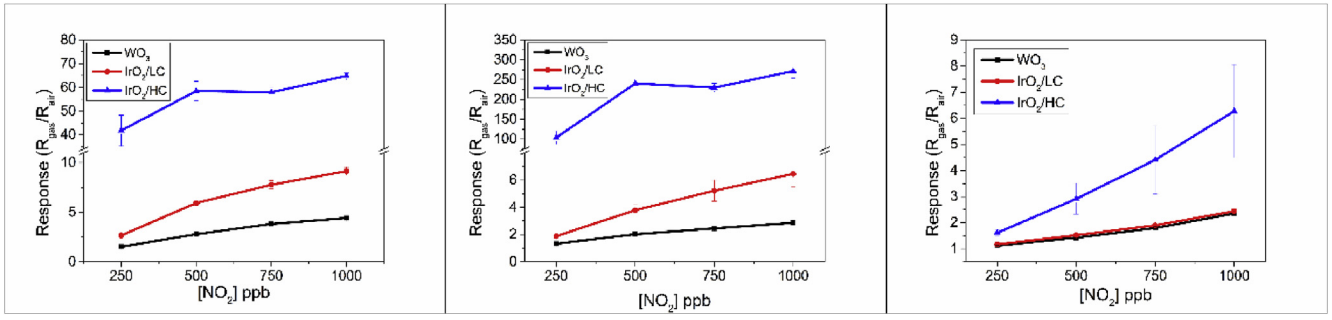

Fig. 9. Nitrogen dioxide responses under dry air conditions at different working temperatures. From left to right panels: 150 °C, 200 °C and 250 °C.

3.4. Humidity effect on the response towards nitrogen dioxide

So far, the analysis of the gas sensing properties has been conducted under dry air conditions. This implies that the actual relative humidity (R.H.) level in the gas-flow measurement set up ranges from 2% up to 5%. However, to emulate real environmental working conditions, measurements conducted at higher R.H. levels are necessary. To do so, different concentrations of NO_2 diluted in dry air were humidified at 35% R.H. and measured. The results are summarized in Fig. 10. They reveal that the presence of moisture results in a decrease in the response towards NO_2. This applies for all three type of sensors studied (i.e., pristine WO_3, IrO_2/LC and IrO_2/HC). Despite these results, IrO_2/LC samples displayed the highest and most stable responses towards NO_2 (higher sensitivity) at the three working temperatures studied.

3.5. Detection mechanisms for nitrogen dioxide

Iridium oxide has been reported as an outstanding material to act as electrode for the oxygen evolution reaction (OER) in water splitting. This reaction occurs at over potentials that range from 1.3 V to 1.6 V, however, the use of metal oxide catalysts can decrease these values, as has been demonstrated in the literature [19]. Iridium oxide belongs to the rutile-type oxides such as RuO_2, MnO_2, PtO_2 [20]. Due to their morphology, non-stoichiometry, band structure and surface electronic structure, these metal oxides display attractive characteristics to be used as materials for electrodes. Considering water splitting on iridium oxide modified electrodes, the OER involves the adsorption of water molecules onto iridium oxide nanoparticles and their reaction with hydroxyls present on the surface of the metal oxide, giving rise to −OOH transition species [21]. During the OER the oxidation states of iridium playing a role are (III), (IV) and (V). The stable oxidation states (i.e., at the end of the OER) present on the surface are Ir (III) and (IV). Iridium (V) has been reported to be a transition oxidation state found only while the OER is occurring [20].

Therefore, Fig. 11 represents the typical mechanism explaining the behavior of iridium oxide during the water splitting oxidation

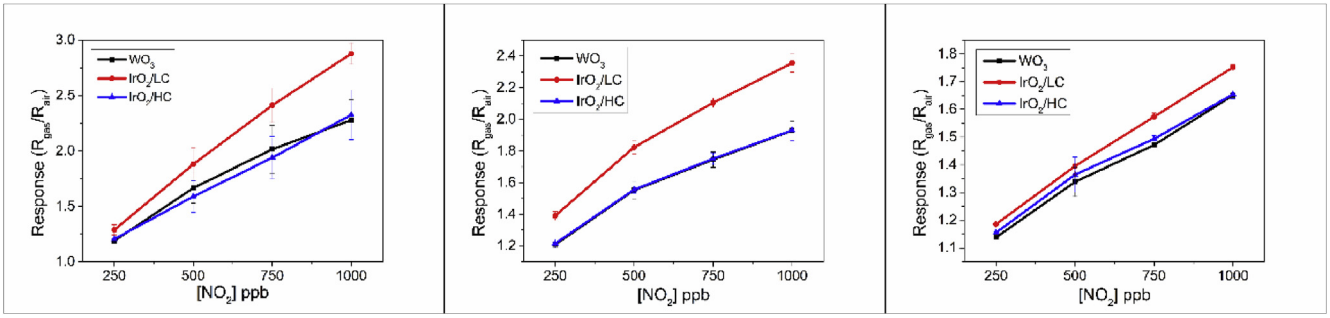

Fig. 10. Nitrogen dioxide responses under 35% R.H. conditions at different working temperatures. From left to right: 150 °C, 200 °C and 250 °C.

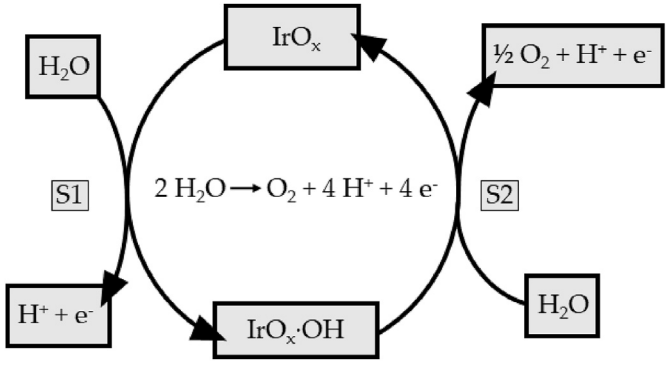

Fig. 11. Typical water splitting path occurring when iridium oxide is used as catalyst.

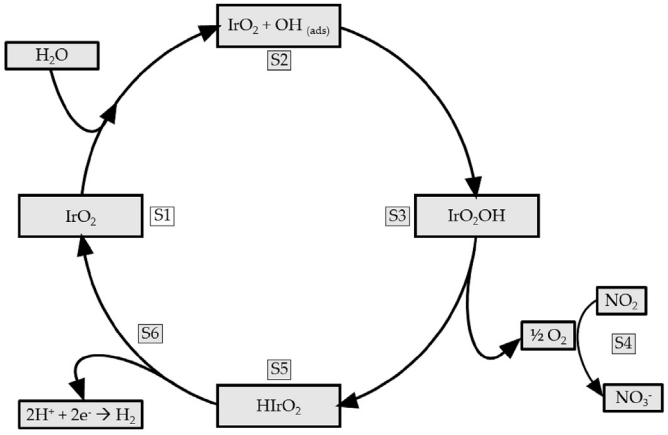

Fig. 12. Schematic pathway mechanism towards the detection of NO_2 at very low relative humidity conditions.

of one water molecule. In this mechanism, water and radical hydroxyl groups adsorb in the first place on the surface of iridium oxide (**S1**) and, subsequently, when another water molecule interacts with the hydroxyl layer, the OER takes place generating a molecular oxygen species (**S2**). This mechanism is supported by experimental data via baseline resistance measurements performed under very low humidity (i.e. <3% R.H.) and humid (35% R.H.) conditions for pure and IrO_2 loaded tungsten oxide sensors (see Fig. S8 and associated discussion in the supporting information).

In order to explain the exceptional capacity of iridium oxide loaded tungsten trioxide nanowires for detecting NO_2, the following mechanism is introduced. At high moisture levels, the interaction with water molecules resulting in the formation of surface hydroxyls is a competitive reaction with the adsorption of NO_2 [22–24]. Surface hydroxyls would react with the highly available water molecules rather than with the traces of NO_2 and, this explains the significant decrease in response towards nitrogen dioxide observed under the presence of moisture. In contrast, when working under dry air conditions, the typical values of relative humidity found inside the test chamber range between 2% and 5%, therefore, a small water content is always present in the atmosphere surrounding the sensors. Under these conditions, few hydroxyl groups are found on the surface of iridium oxide nanoparticles and, NO_2 molecules can easily interact directly with the surface of iridium oxide, which results in a high response signal.

We will now further discuss the sensing mechanism for nitrogen dioxide under low moisture conditions. This is schematized in Fig. 11. Following the water splitting reaction, when iridium oxide is present (**S1**) water molecules and radical hydroxyl groups become adsorbed (**S2**). This leads to the formation of −OOH groups, which have been reported to be found only during the oxygen evolution reaction. The formation of −OOH groups involves surface hydroxyls reacting with lattice oxygen species, changing the oxidation state of iridium to Ir(V) (**S3**) [25,26]. When humidity is in the 2–5% range, NO_2 molecules can easily get adsorbed at the surface of iridium oxide. Adsorbed nitrogen dioxide (an electrophile) can subsequently react with atomic oxygen (a nucleophile), which is made available via the OER taking place at neighboring sites (**S4**). The higher the amount of iridium oxide nanoparticles is, the higher the production of free atomic oxygen is, and more NO_2 molecules react with these oxygen species resulting in the formation of NO_3^-. This increases the total electronic net charge transferred from the host material (i.e., WO_3), which translates into a high resistance change (as shown in Fig. 1). When the atomic oxygen is released and captured by NO_2 molecules, iridium suffers a reduction from Ir(V) to Ir(III), leading to the formation of $HIr(III)O_2$ (**S5**) [27]. When the oxidation of Ir(III) to Ir(IV) occurs (**S6**), the surface of the catalyst is regenerated and a proton is released, leading to the formation of hydrogen. This last step in which hydrogen is produced, could be the reason why the sensor responses towards hydrogen measured for this materials are so weak (see supporting information). The presence of physisorbed NO_2 and chemisorbed NO_3^- species has been confirmed by performing XPS analysis of a sensor exposed to NO_2 (these results can be found in the supporting information). Furthermore, the presence of IrO_2–OH moieties on the surface of the materials exposed to humidity has been confirmed by TOF-SIMS (these results are reported in the supporting information of this paper). These results taken together support the sensing mechanisms depicted in Fig. 12.

A second plausible mechanism for the response enhancement upon IrO_2 loading, complementary to the above mentioned one, is the increase in the number of surface defects and the increased

amount of oxygen species chemisorbed at the surface [23]. This is supported by baseline resistance measurements in pure and IrO_2 loaded tungsten oxide sensors (see the Supporting Information). The increase in the response obtained for both IrO_2/LC and IrO_2/HC can be attributed to the rough morphology of the nanowires, when these are loaded with IrO_2, which enhances the number of surface sites in which NO_2 molecules can be chemisorbed [24]. At the same time, a highly increased roughness makes more difficult for chemisorbed species to leave the material surface and, thus, impeding new molecules to react. When considering sensors using IrO_2/LC, these experience an enhancement in their response towards NO_2 and no response saturation effects are seen. In contrast, sensors employing IrO_2/HC show a dramatically increased response towards NO_2, yet clear response saturation effects are observable within the concentration range tested.

4. Conclusions

Aerosol assisted chemical vapor deposition has been employed to grow tungsten trioxide nanowires loaded with iridium oxide from the precursors tungsten hexacarbonyl and pure iridium oxide powder. To ensure an efficient as well as a homogenous loading, a two-step procedure is followed. Furthermore, different levels of iridium oxide loadings have been achieved, displaying clear differences in gas sensing properties.

XRD has confirmed the synthesis of high-quality crystalline WO_3 NWs. HR-TEM and SEM analysis have shown the occurrence of morphology changes that correlate well with the increase in iridium oxide loading. These results are supported by a photoluminescence study, which reveals an increase in the number of surface defects, when comparing pure WO_3 NWs and IrO_2 loaded WO_3 NWs. XPS and ToF-SIMS analysis have been carried out to confirm the presence of iridium on the sensing layers.

The responses and sensitivity towards different gases, both reducing and oxidizing, of the different materials grown were studied. The loading of iridium oxide nanoparticles to the nanowire matrix dramatically increases the responsiveness towards nitrogen dioxide, as the loading of iridium oxide increases. In contrast, no effect or a slight response enhancement was observed for the other gaseous species tested. When IrO_2/HC samples (operated at 200 °C) were exposed to 1 ppm of NO_2, their response was 95 times higher than the one measured for pristine nanowires. The mechanism behind this response enhancement can be attributed to the catalytic properties of iridium oxide towards the water splitting reaction. In water splitting, the generation of atomic oxygen is dramatically increased, enabling its reaction with adsorbed nitrogen dioxide, thus enhancing sensor response. However, the mechanism that boost NO_2 response in IrO_2/HC samples is hindered at higher relative humidity levels. In contrast, IrO_2/LC samples operated at 150 °C, show fair responsiveness to NO_2 at ppb levels. Furthermore, their responsiveness is little affected by humidity in the 2%–35% R.H. range tested. As a result, IrO_2/LC nanomaterials operated at 150 °C show potential for being employed in resistive sensors to monitor the presence of NO_2 in the ambient (indoor/outdoor), under real atmospheric conditions.

Conflicts of interest

There are no conflicts of interest to declare.

Acknowledgements

This work was funded in part by MINECO and FEDER via grants no. TEC2015-71663-R and RTI2018-101580-B-I00, by AGAUR under grant. 2017SGR 418 and by FNRS via PLAFON and FITTED projects. E.N. gratefully acknowledges a doctoral fellowship from MINECO grant no. BES-2016-076582. E.L. is supported by the Catalan institution for Research and Advanced Studies via the 2018 Edition of the ICREA Academia Award. C.B. is a research Associate of the FNRS (Belgium). F.G. is grateful to project MAT2017-87500-P.

Appendix A. Supplementary data

Supplementary data to this article can be found online at https://doi.org/10.1016/j.jallcom.2019.152156.

References

[1] J. Watson, K. Ihokura, G.S. V Coles, The tin dioxide gas sensor, Meas. Sci. Technol. 4 (7) (1993) 711–719.
[2] S. Vallejos, F. Di Maggio, T. Shujah, C. Blackman, Chemical vapour deposition of gas sensitive metal oxides, Chemosensors 4 (1) (2016) 4.
[3] L. Zhou, Q. Ren, X. Zhou, J. Tang, Z. Chen, C. Yu, Comprehensive understanding on the formation of highly ordered mesoporous tungsten oxides by X-ray diffraction and Raman spectroscopy, Microporous Mesoporous Mater. 109 (1–3) (2018) 248–257.
[4] Y.S. Shim, L. Zhangd, D.H. Kimb, Y.H. Kimb, Y.R. Choib, S.H. Nahme, C.-Y. Kang, W. Leea, H.W. Jang, Highly sensitive and selective H_2 and NO_2 gas sensors based on surface-decorated WO_3 nanoigloos, Sens. Actuators B Chem. 198 (2) (2014) 294–301.
[5] X. Gaoa, X. Sua, C. Yanga, F. Xiaoa, J. Wanga, X. Caob, S. Wangb, L. Zhang, Hydrothermal synthesis of WO_3 nanoplates as highly sensitive cyclohexene sensor and high-efficiency MB photocatalyst, Sens. Actuators B Chem. 181 (2013) 537–543.
[6] X.C. Song, Y.F. Zheng, E. Yang, Y. Wang, Large-scale hydrothermal synthesis of WO_3 nanowires in the presence of K_2SO_4, Mater. Lett. 61 (18) (2007) 3904–3908.
[7] H. Zheng, J.Z. Ou, M.S. Strano, R.B. Kaner, A. Mitchell, K. Kalantar-Zadeh, Nanostructured tungsten oxide - properties, synthesis, and applications, Adv. Funct. Mater. 21 (12) (2011) 2175–2196.
[8] H. Drug, O. Medoxomil, A. Irshad, Growth and characterization of well aligned densely packed IrO_2 nanocrystals on sapphire via reactive sputtering Growth and characterization of well aligned densely packed IrO_2 nanocrystals on sapphire via reactive, J. Phys. Condens. Matter 18 (2006) 1121–1136.
[9] Y.-T. Hsieh, L.-W. Chang, C.-C. Chang, H.C. Shih, Synthesis of WO_3 nanorods by thermal CVD at various gas flow rates and substrate temperatures, Electrochem. Solid State Lett. 14 (7) (2011) K40–K42.
[10] F.E. Annanouch, Z. Haddi, M. Ling, F. Di Maggio, S. Vallejos, T. Vilic, Y. Zhu, T. Shujah, P. Umek, C. Bittencourt, C. Blackman, E. Llobet, Aerosol-assisted CVD-grown PdO nanoparticle-decorated tungsten oxide nanoneedles extremely sensitive and selective to hydrogen, ACS Appl. Mater. Interfaces 8 (16) (2016) 10413–10421.
[11] S. Vallejos, P. Umek, T. Stoycheva, F.E. Annanouch, E. Llobet, X. Correig, P. De Marco, C. Bittencourt, C. Blackman, Single-step deposition of Au- and Pt-Nanoparticle-Functionalized tungsten oxide nanoneedles synthesized via aerosol-assisted CVD, and used for fabrication of selective gas microsensor arrays, Adv. Funct. Mater. 23 (10) (2013) 1313–1322.
[12] F.E. Annanouch, Z. Haddi, S. Vallejos, P. Umek, P. Guttmann, C. Bittencourt, E. Llobet, Aerosol-assisted CVD-grown WO_3 nanoneedles decorated with copper oxide nanoparticles for the selective and humidity-resilient detection of H_2S, ACS Appl. Mater. Interfaces 7 (12) (2015) 6842–6851.
[13] E. Navarrete, C. Bittencourt, P. Umek, E. Llobet, AACVD and gas sensing properties of nickel oxide nanoparticle decorated tungsten oxide nanowires, J. Mater. Chem. C 6 (19) (2018) 5181–5192.
[14] A. Karthigeyan, R.P. Gupta, K. Scharnagl, M. Burgmair, S.K. Sharma, I. Eisele, A room temperature HSGFET ammonia sensor based on iridium oxide thin film, Sens. Actuators B Chem. 85 (1–2) (2002) 145–153.
[15] N. Yamazoe, G. Sakai, K. Shimanoe, Oxide semiconductor gas sensors, Catal. Surv. Asia 7 (1) (2003) 63–75.
[16] F. Güell, P.R. Martínez-Alanis, S. Khachadorian, J. Rubio-Garcia, A. Franke, A. Hoffmann, G. Santana, Raman and photoluminescence properties of ZnO nanowires grown by a catalyst-free vapor-transport process using ZnO nanoparticle seeds, Phys. Status Solidi B 253 (5) (2016) 883–888.
[17] A.H. Romero, F. Widulle, R. Lauck, M. Cardona, "Dispersive phonon Linewidths : the E_2 phonons of ZnO, Phys. Rev. Lett. 90 (5) (2003) 16–19.
[18] F. Güell, P.R. Martínez-Alanis, Tailoring the Green, Yellow and Red defect emission bands in ZnO nanowires via the growth parameters, J. Lumin. 210 (2019) 128–134.
[19] S. Cho, J. Jang, K. Lee, J.S. Lee, "Research Update : strategies for efficient photoelectrochemical water splitting using metal oxide photoanodes Research Update : strategies for efficient photoelectrochemical water splitting using metal oxide photoanodes, Apl. Mater. 2 (2014), 010703.
[20] S. Trasatti, "Electrocatalysis in the anodic evolution of oxygen and chlorine," *Electrochim*, Acta 29 (11) (1984) 1503–1512.
[21] H.G. Sanchezcasalongue, M.L. Ng, S. Kaya, D. Friebel, H. Ogasawara, A. Nilsson, InSitu observation of surface species on iridium oxide nanoparticles during

the oxygen evolution reaction, Angew. Chem. Int. Ed. 53 (28) (2014) 7169–7172.
[22] S. Roso, C. Bittencourt, P. Umek, O. González, Güell Frank, A. Urakawa, E. Llobet, Synthesis of single crystalline in $_2$ O $_3$ octahedra for the selective detection of NO_2 and H_2 at trace levels, J. Mater. Chem. C 4 (40) (2016) 9418–9427.
[23] N. Barsan, U. Weimar, Conduction model of metal oxide gas sensors, J. Electroceram. 7 (2002) 143–167.
[24] A. Ponzoni, C. Baratto, N. Cattabiani, M. Falasconi, V. Galstya, E. Nunez-Carmona, F. Rigoni, V. Sberveglieri, G. Zambotti, Dario Zappa, Metal oxide gas sensors, a survey of selectivity issues addressed at the SENSOR lab, Brescia (Italy), Sensors 17 (2017) 714.
[25] T. Nakagawa, C.A. Beasley, R.W. Murray, Efficient electro-oxidation of water near its Reversible potential by a mesoporous IrO_x nanoparticle film, J. Phys. Chem. C 113 (30) (2009) 12958–12961.
[26] A. Minguzzi, O. Lugaresi, E. Achilli, C. Locatelli, A. Vertova, P. Ghignabc, Sandra Rondinini, Observing the oxidation state turnover in heterogeneous iridium-based water oxidation catalysts, Chem. Sci. 5 (9) (2014) 3591–3597.
[27] O. Kasian, J.P. Grote, S. Geiger, S. Cherevko, K.J.J. Mayrhofer, The common intermediates of oxygen evolution and dissolution reactions during water electrolysis on iridium, Angew. Chem. Int. Ed. 57 (9) (2018) 2488–2491.

Heterojunctions could be employed not only to enhance the selectivity towards a gas but also to cope with humidity cross-sensitivity effects often experienced with metal oxides [37] [38]. For instance, the mixture coating of an inorganic material with a layer of an organic material could lead to an increase in the resilience of the resulting hybrid material towards humidity. This could be attributed to the chemical properties of the organic layer. For example, if this layer is hydrophobic, it will prevent the adsorption of water molecules and the diffusion of water molecules towards the inorganic layer underneath. In the paper Tungsten oxide-lutetium bisphthalocyanine n-p-n heterojunction: From nanomaterials to a new transducer for chemosensing, a hybrid inorganic and organic double layer arrangement is fabricated and its performance in the detection of ammonia under varying humidity conditions is studied. Such gas sensitive hybrid was synthetized as an inorganic resistive layer (WO_3-NWs) covered with an ultra-thin layer of a lutetium bi-phthalocyanine. Basically, in this device the electronic charges are forced to flow throw the layer interfaces, thus enhancing the sensitivity of the materials but also as the exposed layer to the atmosphere is the organic layer, the adsorption of water molecules by the inorganic metal oxide underlayer is minimized.

2.3.4 A tungsten oxide–lutetium bisphthalocyanine n–p–n heterojunction: from nanomaterials to a new transducer for chemo-sensing

Journal of Materials Chemistry C

PAPER

View Article Online
View Journal | View Issue

Cite this: J. Mater. Chem. C, 2019, 7, 6448

A tungsten oxide–lutetium bisphthalocyanine n–p–n heterojunction: from nanomaterials to a new transducer for chemo-sensing†

M. Bouvet, *[a] M. Mateos,[a] A. Wannebroucq,[a] E. Navarrete [b] and E. Llobet [b]

Received 13th December 2018,
Accepted 1st May 2019

DOI: 10.1039/c8tc06309e

rsc.li/materials-c

We report on a new hybrid heterojunction gas-sensitive device by combining a molecular material with a metal oxide. WO_3 was synthesised *via* an aerosol-assisted chemical vapour deposition technique from a tungsten hexacarbonyl precursor. Onto an inorganic film, $LuPc_2$ was vacuum evaporated. The morphology of the WO_3–$LuPc_2$ hybrid films is dominated by the morphological features of the tungsten oxide film, as shown by scanning electron microscopy and atomic force microscopy. Raman spectroscopy of the device confirms the presence of both materials. The non-linear *I*–*V* characteristics demonstrate the existence of an energy barrier at the interface between the inorganic and molecular materials. The interfacial phenomenon was confirmed by means of impedance spectroscopy. Finally, the positive response to ammonia confirms the n-type nature of the charge carriers responsible for the transport properties through the device, in accordance with the n-type conductivity of WO_3. This response is fully reversible whatever the relative humidity value in the range 10–70% r_h. Even though the current is shifted when the relative humidity decreases, ammonia sensitivity remains almost unchanged (2.5 nA ppm^{-1}) for r_h ranging from 30 to 50%. It is worth noting that the present device operates at room temperature with excellent reversibility and stability, showing the lowest limit of detection for ammonia ever reported for this device architecture (250 ppb).

Introduction

Research on heterojunctions formed between inorganic, organic or mixed materials has been attracting significant and sustained efforts. Heterojunctions between two inorganic materials form diodes, which can be used in electronic circuits, but also as photodetectors, light emitting diodes or photovoltaic cells. In the past few decades, heterojunctions between two organic materials have also been studied for their optoelectronic properties.[1–3]

More recently, hybrid organic–inorganic heterojunctions have been reported. For example, n-GaAs–carbon nanotube heterojunctions show a rectifying behavior, potentially usable as diodes for high frequency communications or photovoltaic applications.[4] Poly(3,4-ethylenedioxythiophene)–polystyrene sulfonate–ZnO nanorod p–n heterojunctions have been reported as stretchable photodetectors.[5] The pentacene–MoS_2 p–n heterojunction exhibits a photovoltaic response upon optical irradiation.[6] In addition, a series of organic–inorganic heterojunctions have been reported as possible photodetectors such as spirofluorene derivatives associated with Sb_2S_3[7] or ZnO,[8] or a combination of Cd_3P_2 nanowires with PCBM, a fullerene derivative.[9]

Heterojunctions are mainly used for their optoelectronic properties, and they can also be used for chemosensing.[10] In gas sensing, semiconductor metal oxides have been the most studied materials due to their high sensitivity, simplicity (such gas sensors behave as chemoresistors), wide range of mass-production synthesis routes, low cost and large number of possible applications.[11–13] In an attempt to improve their selectivity, they are often doped or associated with other materials, namely metal or metal oxide nanoparticles.[14–18] Besides these classical chemoresistors, heterojunctions that combine two semiconducting materials offer additional possibilities, since the current through the devices depends not only on the density of charge carriers and their mobility, but also on the energy barrier that develops at the interface between the materials.[19,20]

Inorganic heterojunction materials have been reported for gas sensing. For example, Dutta[21] reported room-temperature

[a] Institut de Chimie Moléculaire de l'Université de Bourgogne (ICMUB), UMR CNRS 6302, Université Bourgogne Franche-Comté, 9 avenue Alain Savary, 21078 Dijon cedex, France. E-mail: marcel.bouvet@u-bourgogne.fr; Fax: +33-380-396-098; Tel: +33-380-396-086

[b] Microsystem Nanotechnology for Chemical Analysis (MINOS-EMaS), Universitat Rovira i Virgili, Avda. Països Catalans, 26, 43007 Tarragona, Spain. E-mail: eduard.llobet@urv.cat

† Electronic supplementary information (ESI) available: SEM micrograph (Fig. S1), XRD (Fig. S2), and EDX (Fig. S3) spectra, an example of I(V) characteristics (Fig. S4) of a WO_3 film and the response of a WO_3/$LuPc_2$ heterojunction to NH_3 in the 1–9 ppm range (Fig. S5) are given. See DOI: 10.1039/c8tc06309e

hydrogen sensing employing Pd/ZnO/p-Si heterojunctions. Hu[22] reported the gas-sensing properties of CuO–ZnO p–n heterojunctions. More recently, single-crystalline n-type WO_3 nanoneedles decorated with p-type Cu_2O nanoparticles led to excellent sensitivity and selectivity to hydrogen sulfide, a 7-fold increase in response compared with that of pristine WO_3 nanoneedles, and a low detection limit, below 300 ppb of H_2S.[23] Hybrid organic–inorganic materials have been reported for gas sensing, as pentacene and ZnO as semiconductors in a transistor-based vapour sensor.[24] Organic–inorganic nanocomposites have been employed in gas sensors for environmental monitoring,[25] but not in the form of heterojunctions. Organic–inorganic polypyrrole–chitosan coated ZnO nanospheres behave as heterojunctions, and their hydrogen response increases linearly with the concentration of ZnO nanoparticles in the material.[26] As reported for polypyrrole–SnO_2 hollow sphere p–n heterojunctions, the modification of the energy barrier height explains the improvement in the response of the sensor.[27] Heterojunctions obtained by the electrodeposition of polyaniline on n-type ZnO or CdS films exhibit high sensitivity to liquefied petroleum gas.[28,29]

Besides classical heterojunctions built from two semiconducting layers in sandwich between two electrodes, a few years ago one of the authors patented a different type of device that combines one poorly conducting semiconductor material deposited onto interdigitated electrodes, which is covered by a more conducting semiconductor.[30,31] The particularity of this device is that the more conducting material is on top and not in contact with the electrodes. Since the interelectrode distance is very high compared to the thickness of the sublayer, typically 70 μm against 100 nm, the lowest resistance pathway from one electrode to the other goes twice across the sublayer, crossing the interfaces as indicated by the arrows in Fig. 1. This device, initially called the molecular semiconductor-doped insulator (MSDI) heterojunction, exhibits nonlinear but symmetrical current–voltage characteristics. MSDIs are neither diodes nor transistors. Till now, the top layer in MSDIs has been a lanthanide bisphthalocyanine, $LuPc_2$, well known for its intrinsic semiconducting behaviour,[32,33] or a lanthanide triple decker phthalocyanine.[34] The energy barrier is particularly high when the sublayer is of n-type. Thus, for a series of poor conducting monometallophthalocyanines, this increases from non fluorinated phthalocyanine (MPc) to hexadecafluoro-phthalocyanine ($M(F_{16}Pc)$),[30] in relation with the stabilization of the frontier orbitals, HOMOs and LUMOs.[35] As expected, an intermediate behaviour is observed with octafluoro-phthalocyanine ($M(F_8Pc)$). The chemosensing properties of MSDIs are unique. Even though the only material in contact with the atmosphere is the top layer, the response can be inverted, depending on the type of conductivity of the sublayer. Thus, the response of the $M(F_{16}Pc)/LuPc_2$ MSDI to ozone, a strong oxidizing agent, is negative whereas it is positive for the $MPc/LuPc_2$ MSDI.

Similarly, upon exposure to an electron-donating species like ammonia, the current in the $M(F_{16}Pc)/LuPc_2$ MSDI increases, but decreases in the $MPc/LuPc_2$ MSDI.

In addition to phthalocyanines,[30,36] MSDI-type heterojunctions have been reported with a series of molecular materials as sublayers, namely sexithiophene[37] as a p-type material and perylene derivatives[37,38] and a triphenodioxazine[39] as n-type materials. However, MSDI-type heterojunction devices that combine inorganic and organic materials have never been reported before. In order to build such heterojunctions, the n-type sublayer needs to be less conductive than $LuPc_2$, which we want to keep as the p-type, highly conductive top layer. Tungsten oxide, WO_{3-x}, known as an n-type semiconductor material was chosen as the sublayer (Fig. 1).

WO_3 is a wide-band gap semiconductor oxide, with an estimated band gap E_g = 2.62 eV. Typically, WO_{3-x} presents a monoclinic structure, stable between 17 °C and 330 °C.[40] Its conductivity depends on oxygen vacancies, related to oxygen substoichiometry (x value). Different techniques are available for performing the growth of a tungsten oxide film. Thin WO_3 polycrystalline films can be grown by reactive RF magnetron sputtering, with appropriate thickness and tuned oxygen stoichiometry.[41] Thick WO_3 films can be obtained using commercially available WO_3 nanopowders sintered at a high temperature (*e.g.*, 900 °C for 2 hours) and subsequently screen-printed on top of the transducer substrate.[42] Chemical vapour deposition is also a methodology employed to grow tungsten oxide, and the main advantages of the technique are the possibility of fine tuning the morphological structure of tungsten oxide crystals and performing oxygen vacancy control.[43–45] Here it was necessary to grow a tungsten oxide film with well-defined crystallinity and oxygen-defects and having a regular and smooth surface that would be, in a second step, totally covered by a p-type organic film. Therefore, in this paper a dense forest of single-crystalline tungsten oxide nanorods and nanoparticles was grown employing an aerosol-assisted chemical vapour deposition (AACVD) method. Inorganic–organic heterojunctions were prepared and characterised by employing different techniques. In particular, their response to ammonia under different relative humidity (r_h) conditions is presented and discussed in detail.

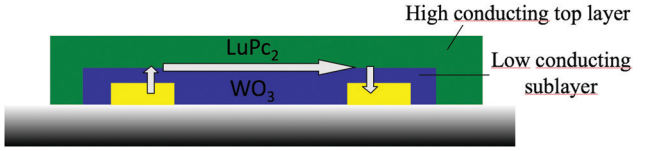

Fig. 1 Scheme of a WO_3–$LuPc_2$ heterojunction; the arrows indicate the pathway of charges across the device.

Results and discussion

Morphology and compositional studies

The morphology of the organic–inorganic heterojunction layers was studied by SEM and AFM. Fig. 2 shows the SEM results. The low magnification SEM images obtained for a sample of WO_3 not covered by $LuPc_2$ show that an homogeneous coating of the application substrate is achieved (Fig. S1, ESI†). Considering previous results,[23] the thickness of the tungsten oxide layer can be estimated to be about 5 microns. This thickness still allows

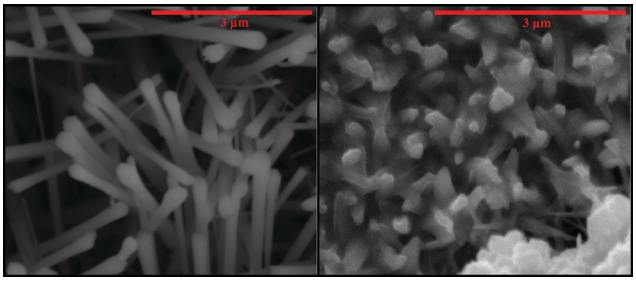

Fig. 2 Typical SEM micrographs of the uncoated WO_3 nanowire layer (left) and of $LuPc_2$-coated layer (right).

observing the pattern of the electrodes underneath the film. The high magnification images reveal that elongated morphologies with granular tips dominate in uncoated films (see the left panel in Fig. 2). These elongated objects, the lateral dimensions of which are below 200 nm, are in good agreement with the nanoneedle-like morphology already reported for the AACVD grown tungsten oxide.[23,46] The right panel in Fig. 2 shows that the organic–inorganic film is not perfectly compact and comprises both granular and elongated morphologies (nanorods). This morphology is confirmed by AFM analysis. While the left panel image in Fig. 3 indicates that the film consists of densely packed particles, the higher magnification image shown in the right panel clearly shows, additionally, the presence of elongated objects (nanorods). The oriented facets visible in some of these elongated structures indicate that these objects comprise bundles of oriented nanoneedles. It can be concluded that the morphology of the WO_3–$LuPc_2$ hybrid films is dominated by the morphological features of a tungsten oxide film.

XRD analysis (Fig. S2, ESI†) indicates that the tungsten oxide (both in coted or uncoated films) shows a monoclinic phase. No peaks associated with the presence of $LuPc_2$ were observed in the XRD spectra of coated tungsten oxide films, which is indicative of the presence of a very thin organic film. EDX analysis was performed on the samples (Fig. S3, ESI†). The main peaks in the spectra revealed the presence of W, O, C and In. While the presence of W can be associated with the tungsten oxide film and the presence of In is related to the ITO electrodes, the presence of carbon could be due to different reasons. Carbon could be contaminated as often found in samples exposed to ambient air, remains from the precursor employed for growing the tungsten oxide film or carbon from

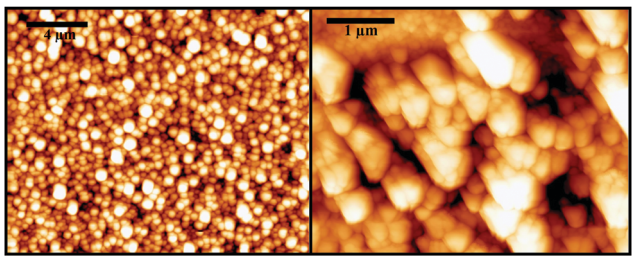

Fig. 3 Typical AFM micrographs of an organic–inorganic heterojunction film.

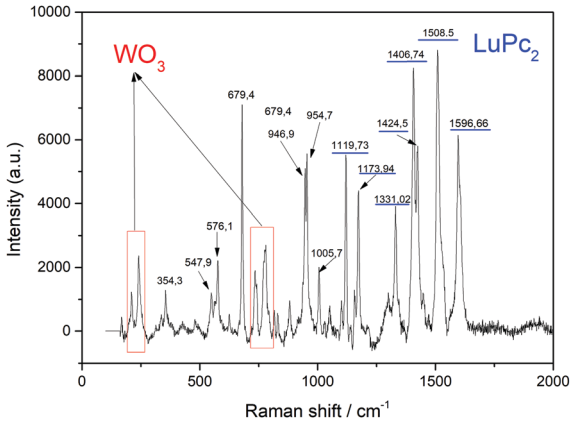

Fig. 4 Raman spectrum of a WO_3–$LuPc_2$ heterojunction layer deposited on top of a glass substrate having a pair of interdigitated ITO electrodes.

the $LuPc_2$ coating. To confirm the presence of the $LuPc_2$ coating in the hybrid films, Raman spectroscopy analysis was conducted. The results are shown in Fig. 4. The Raman spectrum shows peaks that can be directly attributed to tungsten oxide lying in the 200 to 900 cm^{-1} range. In addition, 7 peaks in the region that spans from 1100 to 1600 cm^{-1} can be directly attributed to the $LuPc_2$ layer.[47] In particular the peaks at 1191 cm^{-1} and at 1173 cm^{-1} correspond to C–H bending. The one at 1331 cm^{-1} corresponds to C=C pyrole and benzene stretching and those at 1406 cm^{-1} and 1424 cm^{-1} correspond to isoindole stretching. The peak at 1508 cm^{-1} corresponds to C=C pyrrole stretching and coupling of pyrrole and aza stretching. Finally, the peak at 1596 cm^{-1} corresponds to benzene stretching. These results confirm that a film of $LuPc_2$ coated on top of an AACVD grown tungsten oxide layer has been achieved correctly.

Transport properties

The *I*–*V* characteristics obtained with the WO_3–$LuPc_2$ heterojunction exhibit a nonlinear behavior for both positive and negative polarizations (Fig. 5), contrarily to what is observed for a diode in which a rectification ratio exists between direct and inverse polarizations. The current is 53 µA at 10 V, against 4.6 µA at 2 V. This also confirms that WO_3 covers all the substrate and that $LuPc_2$ does not percolate from one electrode to the other one. Indeed, when this is the case a linear current–voltage characteristic is observed as for a $LuPc_2$ resistor.[48]

The *I*(V) characteristic showed two electrical conduction regimes as we noticed a slope break between 5 and 7 V. So we analyzed the *I*(V) characteristics by means of the space charge limited current (SCLC) model,[49] thanks to the $\log I = f(\log V)$ plot. Above 7 V, the slope is 2.3 (R^2 = 0.9997), *i.e.* only slightly higher than 2. Actually, as soon as traps are present, this slope is higher than 2, and the slope of 2 should be attained only when all the traps are filled.[50,51] Between 0.3 and 3 V, the slope of the $\log I = f(\log V)$ curve is slightly higher than 1 (1.25 with R^2 = 0.99997), showing an ohmic behavior. At low voltages, a part of the current can go through the WO_3 layer, but at higher voltages, the energy barrier between the two materials can be overcome and the charges are also injected from the sublayer to

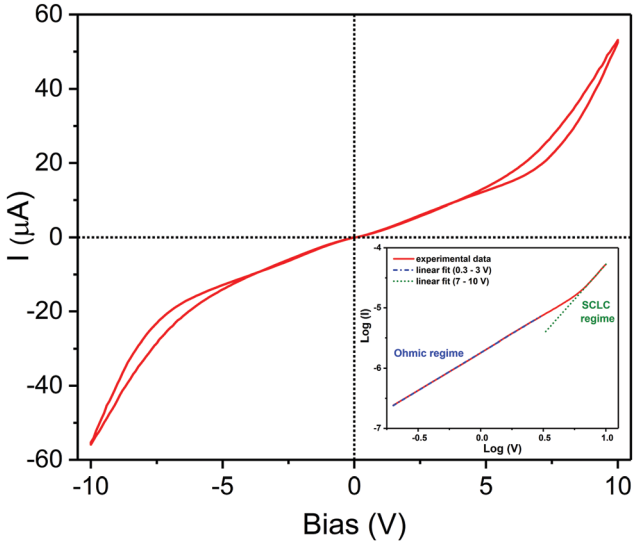

Fig. 5 Typical *I*–*V* characteristics of the heterojunction prepared with WO_{3-x} as a sublayer and $LuPc_2$ as a top layer.

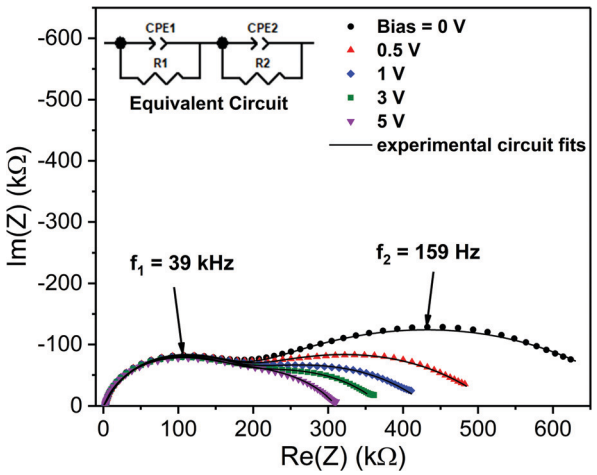

Fig. 6 Complex plane representation (Nyquist plot) of the impedance spectra of a WO_3–$LuPc_2$ heterojunction under a forward bias. The experimental data are fitted to the corresponding equivalent circuit shown in the inset. Ambient atmosphere (T = 19 °C and r_h = 46%).

the top layer and flow through $LuPc_2$ (Fig. 1). This indicates that the annealing conditions, as described in the Experimental section are efficient enough to diminish the conductivity of the oxide.

Elsewhere, we checked whether devices consisting of only the WO_3 layer exhibit linear *I*–*V* characteristics (Fig. S4, ESI†). This means that the contact between the metal oxide sublayer and the electrodes is an ohmic contact. Clearly, the transport properties of the WO_3–$LuPc_2$ heterojunction are governed by the energy barrier between the inorganic and molecular materials.

Impedance spectroscopy and modelling

We completed the study of the transport properties thanks to impedance spectroscopy, which is a conventional technique in electrochemistry,[52] but its application in solid-state organic electronic devices has recently received growing attention.[53–56] Hereafter, we only discuss the complex plane representation, called the Nyquist plot, of the impedance Z defined as: $Z = \mathrm{Re}(Z) + j\,\mathrm{Im}(Z)$, where $\mathrm{Re}(Z)$ and $\mathrm{Im}(Z)$ are the real part and the imaginary part of Z, respectively.

Fig. 6 shows the Nyquist plot of a WO_3–$LuPc_2$ heterojunction acquired between 10 Hz and 1 MHz (f is an implicit variable so we indicated two characteristic frequencies f_1 and f_2) with an ac perturbation voltage of 300 mV and a bias ranging from 0 V to 5 V. We notice two intermixed non-ideal semicircles, which exhibit different behaviours towards bias. The first one, at high frequency (with characteristic frequency f_1), is practically unaffected by the bias, in contrast to the second one, at low frequency (with characteristic frequency f_2), that shrinks as the bias increases. It is worth noting that for a $LuPc_2$ resistor, only one semicircle unaffected by the bias is observed. This means that the electrical properties of the material remain approximately constant over the entire frequency range,[48] suggesting that charge transport is dominated by the bulk material, and not by interfacial traps.[57] In the present heterojunction, the two non-ideal semicircles led us to propose for the data modelling an equivalent circuit, which consists of two *R*-CPE branches (Fig. 6). A constant-phase element (CPE) can be regarded as an imperfect capacitor[58] with an impedance Z_{CPE} defined as follows (eqn (1)):

$$Z_{CPE} = 1/(Q(j\omega)^{\alpha}) \quad (1)$$

with $\omega = 2\pi f$, where f is the frequency, Q is the non-ideal capacitance, and α a value between 0 and 1 that dictates the non-ideality of the capacitive element. When $\alpha = 1$, a CPE equals an ideal capacitor and when $\alpha = 0.5$, it represents a so-called Warburg element that reflects the diffusion phenomenon.[59]

As expected from the Nyquist plot, all parameters (R_1, Q_1 and α_1 in blue Fig. 7) from the R_1-CPE_1 branch, which represents the high frequency semicircle, remain practically constant toward the bias. Therefore, we suggest that these parameters constitute the bulk material properties of the whole device. The values of α are 0.9 for the high frequency loop and 0.5 for the low frequency loop. The collapse of the low frequency semi-circle as the bias increases (Fig. 6) is due to the decrease of R_2 (in red Fig. 7), which deals with an interfacial behaviour.[60] It should be noted that an *R*–*C* element attributed to an interfacial behaviour should have a larger capacitance than the bulk capacitance because an interfacial layer should have a smaller thickness compared to that of the device. The extracted parameter Q does not really have a physical meaning because its unit is dependent on α. However, we can refer to a method proposed by Hsu and Mansfeld[61] to calculate an effective capacitance C_{eff} from the *R*-CPE branch (Fig. 7).

It appears that C_{eff1} has a constant value of 24 pF whereas C_{eff2} has a larger value from 1.75 nF to 0.25 nF which confirms our assumptions: the high frequency semicircle reflects the bulk properties of the device and the low frequency one reflects the interfacial phenomenon similar to an energy barrier as mentioned above in the *I*–*V* characteristics. Finally, α_2 is far from 1, because the charges do not go through a unique pathway but through both layers.

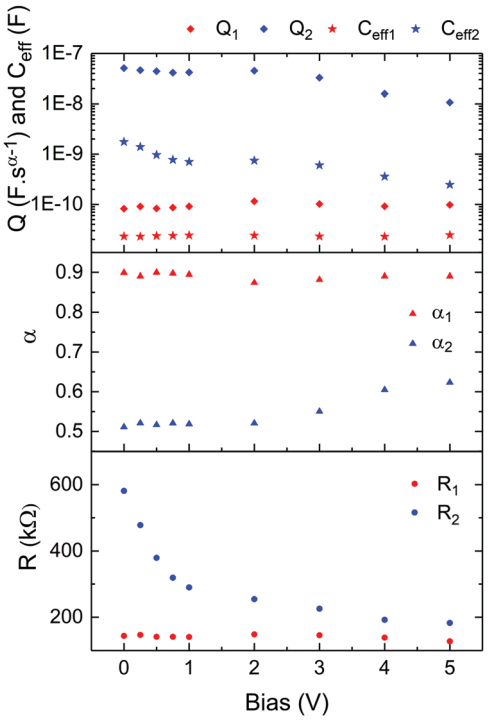

Fig. 7 Variation of the extracted circuit parameters as a function of the bias of a WO_3–$LuPc_2$ heterojunction. The effective capacitance C_{eff} is calculated from $C_{eff} = R^{\frac{1}{\alpha}-1}Q^{\frac{1}{\alpha}}$.[61]

Gas sensing

Ammonia (NH_3), used as a raw material for fertilizers and as a freezing gas instead of freon, is also used in livestock production and in the food industry as a result of biological processes. NH_3 is an important precursor for secondary fine particles in air. This is the reason why policies are established in Europe to reduce NH_3 emissions, for example from agricultural sources.[62] The European labor legislation sets the daily exposure limit at 20 ppm.[63] In most cases, NH_3 needs to be measured under humid atmosphere conditions. Moreover, since we have already studied the response of organic heterojunctions towards NH_3,[30,48] it was of interest to study the present device under the same chemosensing conditions. Upon exposure to NH_3, these heterojunctions exhibit a current increase (Fig. 8), as expected for an n-type MSDI heterojunction prepared from an n-type sublayer as $M(F_{16}Pc)$.[30] This confirms that, in the present device, WO_3 transports negative majority charge carriers. When submitted to repeated exposure/recovery cycles with exposure periods of 1 min separated by a 4 min-long recovery period under a synthetic air flow, the device shows good reversibility, with only a very slight drift. The response depends on the NH_3 concentration, as depicted in Fig. 8 in the 10–90 ppm range.

At 50% r_h, the relative response is 28% at 20 ppm NH_3, which is comparable – or even better – to that of the most sensitive MSDI devices reported so far, namely the MSDIs prepared with perfluorophthalocyanine complexes as a sublayer (Table 1).[48] The only device reported with a higher sensitivity, up to 8% ppm^{-1}, was obtained with a perylene n-type material as the sublayer, but the sensitivity of this device sharply decreased after few days in ambient air.[38]

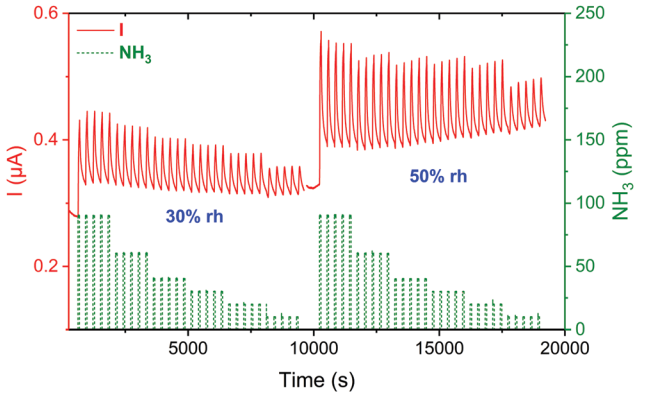

Fig. 8 Variation of the current (red line) as a function of time during exposure to NH_3 in the range 10–90 ppm by steps of 10 ppm (dotted line), at r_h values of 50% and 30% (1 min exposure and 4 min recovery); T = 25 °C.

Table 1 Sensitivities defined as the ratio of the relative response on the NH_3 concentration for a series of MSDI heterojunctions, compared to that of a $LuPc_2$ resistor and to that of the present device, WO_3/$LuPc_2$. All the sensitivity values were determined after a 1 min-long exposure period unless otherwise specified

Device	Conduction type	Sensitivity (% ppm^{-1})	$[NH_3]$ (ppm)	Ref.
$Cu(F_{16}Pc)/LuPc_2$ MSDI	n	0.3 [a]	35	30
$Cu(F_{16}Pc)/LuPc_2$ MSDI	n	1.5	25	64
PTCDA/$LuPc_2$ MSDI	n	5–8 [b]	10–30	38
TPDO/$LuPc_2$ MSDI	n	0.5	30	39
CuPc/Eu_2Pc_3 MSDI	p	0.04	25–200	34
$LuPc_2$ resistor	p	0.02	25	64
WO_3/$LuPc_2$ heterojunction	n	0.2 2.5	20–90 1–9	This work
rGO–Co_3O_4	p	1 [c]	50	65
rGO–PANI	p	1 [d]	20	66
CeO_2–PANI	p	12 [d]	25	67
5% wt MoO_3–WO_3	p	200 [e]	5	68

[a] Mean value after a 15 min-long exposure period. [b] But the sensitivity drops after few days in ambient air. [c] Studied only at 40% r_h. [d] Studied only in dry air. [e] Operating at 450 °C.

The baseline current increases with the r_h value, from 0.32 to 0.4 μA when the r_h value varies from 30% to 50%. As generally observed for conductometric devices, H_2O and NH_3 that are both electron-donating species induce the same response sign. However, when the r_h value increases from 30% to 50%, the qualitative response to NH_3 remains identical, with a stable base line and a current increase during the exposure periods. The baseline is also kept when we carried out experiments at lower ammonia concentrations, in the range 1–9 ppm (Fig. S5, ESI†). The effect of ammonia is the neutralization of positive charge carriers in the $LuPc_2$ layer, leading to a decrease of the energy barrier at the interface between the two materials, which governs the transport properties through the heterojunction. This explains the current increase observed upon exposure to ammonia.

The relative response $RR(\%) = 100 \times (I - I_0)/I_0$ increases quasi-linearly in the range 20–90 ppm NH_3, at 30% and at 50% r_h as well (Fig. 9). In this range, a mean value of the sensitivity, S, defined as the variation of RR on the variation of the NH_3 concentration, $S = \Delta RR/\Delta[NH_3]$, is 0.185% ppm^{-1} and 0.20% ppm^{-1} at 30%

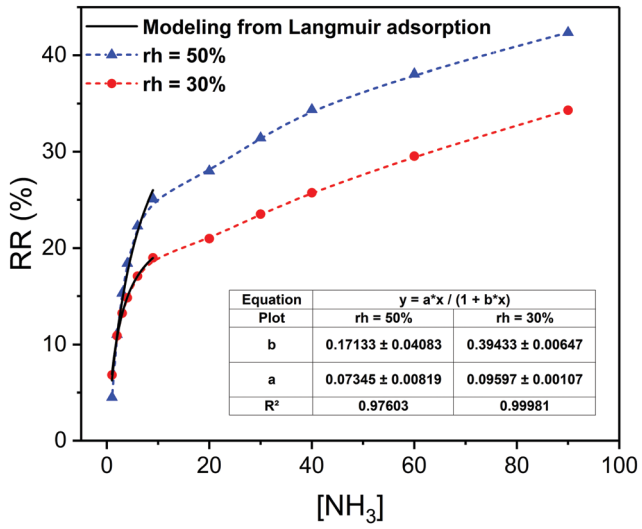

Fig. 9 Relative response, calculated as the mean value over cycles at a given concentration, as a function of NH_3 concentration, at 50% (blue triangle) and 30% (red circle) r_h. At low concentration, the experimental data are fitted with a Langmuir-like model, the parameters of which are shown in the inset.

and 50% r_h, respectively. Actually, the sensitivity is higher at a lower NH_3 concentration. At 10 ppm, the modeling of the relative response as a function of the ammonia concentration shows a Langmuir-like behavior (Fig. 9).[69] It appeared that at 1 ppm the signal to nose ratio stayed correct (>10, Fig. S6, ESI†) meaning that the limit of detection (LOD) was better than 1 ppm, which has never been reported before for MSDI-type heterojunctions. At concentrations lower than 10 ppm, S rose up to 1.52% ppm^{-1} at 30% r_h and 2.56% ppm^{-1} at 50% r_h (Fig. 9).

So, the present device is more sensitive to NH_3 than the previously studied MSDI. Its performances are comparable to many other NH_3 sensors operating at room temperature (Table 1). Thus, reduced graphene oxide (rGO) associated with Co_3O_4 nanofibers[65] or with polyaniline (PANI)[66] showed a sensitivity of 1% ppm^{-1}. However, the latter was studied in dry air whereas the first one was studied only at one r_h value, namely 40%. We added two examples of more sensitive devices. Thus, an heterojunction based on CeO_2 nanoparticles coated by a PANI hydrogel showed a sensitivity of 12% ppm^{-1} at RT, but only studied in dry air.[67] In the second example, a sensitivity of 200% ppm^{-1} was reported with a WO_3 resistor modified by 5% of MoO_3, but this device operates at 450 °C.[68] It is not possible to be exhaustive, but these few examples show that the present sensor favorably competes with previously reported devices operating at room temperature.

The limit of detection was defined as $LOD = 3N/(S \times I_0)$, where N is the noise, determined at 1 ppm on the curve $I(t)$ (Fig. S6, ESI†). With N being 1 nA and I_0 0.36 μA and 0.47 μA, LODs of 550 and 250 ppb were calculated at 30 and 50% r_h, respectively. It is important to remember that, in Europe, the daily exposure limit in NH_3 is 20 ppm.[63] Thanks to its very high signal over noise ratio, the device exhibits a very good LOD. This characteristic comes from the unique properties of $LuPc_2$, which is an intrinsic molecular semiconductor.

Experimental

Synthesis of the inorganic layer

The tungsten oxide layers were synthesized *via* an aerosol-assisted chemical vapor deposition (AACVD) technique. This is a self-catalyzed method conducted at atmospheric pressure. Tungsten hexacarbonyl was purchased from Sigma Aldrich and used as received. A solution was prepared employing 50 mg of the precursor dissolved in 5 ml of methanol and 15 ml of acetone. An ultrasonic aerosol generator was employed to generate fine droplets of the precursor solution, which were input to a hot-wall CVD reactor through a 0.5 ml min^{-1} flow of N_2. The growth time was adjusted to 30 min and the temperature of the reactor was set to 370 °C. Tungsten oxide films were grown onto glass substrates in which ITO interdigitated electrodes separated by 75 μm lithographed on a 1 × 1 cm^2 glass substrate and wire bonding paths had been patterned. To protect bonding paths and allow the growth of the AACVD film onto the electrode area only, Kapton shadow masks were used. These shadow masks were produced employing an excimer laser (DWL 66FS, 420 nm from Ailberg instruments). The as-grown films underwent an annealing process conducted at 400 °C during 2 h under a 3 l min^{-1} flow of dry air.

Morphology and compositional studies

A $LuPc_2$ organic layer was coated on tungsten oxide, by sublimation under secondary vacuum (*ca.* 10^{-6} mbar) in a UNIVEX 250 thermal evaporator (Oerlikon, Germany), and by heating in a temperature range of 450–500 °C at a rate of 1 Å s^{-1}. $LuPc_2$ was synthesized according to a previously reported method.[70,71] The morphology and composition of the resulting hybrid samples were analyzed *via* scanning electron microscopy (SEM), atomic force microscopy (AFM), energy-dispersive X-ray spectroscopy (EDX) and Raman spectroscopy. Environmental SEM was conducted using an FEI QUANTA 600 microscope, which was equipped with an Oxford Instruments microanalysis (EDX) tool. AFM was performed using a Molecular Imaging, Pico SPM II (Pico+) microscope in tapping mode at 190 kHz employing a silicon tip. Raman spectroscopy was conducted employing a Renishaw Raman FT-IR spectrometer and a 514 nm laser.

Device and electrical measurements

The workbench used for NH_3 exposure, at different relative humidity (r_h) values, has been described previously.[38] Ammonia gas, at 985 ppm and 98 ppm (mol/mol) in synthetic air was used from standard cylinders, purchased from Air Liquide, France. The total flow was in the range of 0.5–0.55 NL min^{-1} depending on the ammonia concentration and the volume of the test chamber was 8 cm^3. Gas sensing experiments were carried out in a dynamic fashion, with 4 min-long rest periods alternating with 1 min-long exposure periods. In the present study, all the electrical measurements were carried out at the lab temperature (18–22 °C) unless otherwise specified.

The impedance data were obtained using a Solartron SI 1260 impedance analyser. The frequency range was from 10 Hz to 10 MHz with a fixed ac oscillation amplitude of 300 mV and a

bias ranging from 0 V to 5 V. Commercial software Zview from Ametek was used for impedance data fitting and parameter extraction.

Conclusions

In this paper, the deposition of a highly conductive molecular material, $LuPc_2$, on a layer of an n-type semiconductor metal oxide, WO_3 nanorods and nanoparticles, has led to a conductometric device in which the charge transport properties are governed by the interface between the two types of materials. Thus, as depicted from impedance spectroscopy, the diameter of the low frequency semicircle collapsed under increasing bias conditions, which supports the attribution of this semicircle to interfacial behaviour. The effective capacitance associated with the low frequency semicircle is *ca.* 40 times higher than that associated with the bulk materials, which confirms this hypothesis. The device has been employed for detecting ammonia in a background of humid air in a wide range of moisture levels. In contrast to what is generally observed in conductometric transducers, water and ammonia show opposite effects on the value of the measured current. Ammonia induces a current increase, in accordance with the n-type nature of charge carriers in the oxide sublayer, whereas water molecules lower the energy barrier at the interface between both materials. Clearly, the heterojunction shows better performances than individual materials, in particular as regards stability with respect to humidity. Moreover, all these devices operate at room temperature.

Conflicts of interest

There are no conflicts of interest to declare.

Acknowledgements

The authors acknowledge the Agence Nationale de la Recherche for funding through the ANR projects CAP-BTX ANR-BLAN-2010-917-02 and OUTSMART ANR-2015-CE39-0004-03 and the MENESR for two PhD grants (M. M. and A. W.). Financial support from the European Union and the Conseil Régional de Bourgogne through the FABER and the PARI SMT 08 and CDEA programs is gratefully acknowledged. Also funded in part by MINECO and FEDER *via* grant no. TEC2015-71663-R and by AGAUR under grant 2017SGR 418, E. N. gratefully acknowledges a doctoral fellowship from MINECO grant no. BES-2016-076582. E. L. is supported by the Catalan Institution for Research and Advanced Studies *via* the 2018 Edition of the ICREA Academia Award. We would like to thank the European Union for funding (FEDER and short term missions) through the COST action TD1105 EuNetAir.

Notes and references

1 S. R. Forrest and M. E. Thompson, *Chem. Rev.*, 2007, **107**, 923–925.
2 J. Peet, A. J. Heeger and G. C. Bazan, *Acc. Chem. Res.*, 2009, **42**, 1700–1708.
3 H. Wang and D. Yan, *NPG Asia Mater.*, 2010, **2**, 69–78.
4 C.-W. Liang and S. Roth, *Nano Lett.*, 2008, **8**, 1809–1812.
5 T. Q. Trung, V. Q. Dang, H.-B. Lee, D.-I. Kim, S. Moon, N.-E. Lee and H. Lee, *ACS Appl. Mater. Interfaces*, 2017, **9**, 35958–35967.
6 D. Jariwala, S. L. Howell, K.-S. Chen, J. Kang, V. K. Sangwan, S. A. Filippone, R. Turrisi, T. J. Marks, L. J. Lauhon and M. C. Hersam, *Nano Lett.*, 2016, **16**, 497–503.
7 A. Bera, A. Das Mahapatra, S. Mondal and D. Basak, *ACS Appl. Mater. Interfaces*, 2016, **8**, 34506–34512.
8 O. Game, U. Singh, T. Kumari, A. Banpurkar and S. Ogale, *Nanoscale*, 2014, **6**, 503–513.
9 G. Chen, B. Liang, X. Liu, Z. Liu, G. Yu, X. Xie, T. Luo, D. Chen, M. Zhu, G. Shen and Z. Fan, *ACS Nano*, 2013, **8**, 787–796.
10 K. Potje-Kamloth, *Chem. Rev.*, 2008, **108**, 367–399.
11 D. E. Williams, *Sens. Actuators, B*, 1999, **57**, 1–16.
12 N. Yamazoe, *Sens. Actuators, B*, 1991, **5**, 7–19.
13 N. Barsan, U. Weimar and D. Koziej, *Sens. Actuators, B*, 2007, **121**, 18–35.
14 D. Koziej, N. Barsan, K. Shimanoe, N. Yamazoe, J. Szuber and U. Weimar, *Sens. Actuators, B*, 2006, **118**, 98–104.
15 M. Wallin, H. Grönbeck, A. Lloyd Spetz and M. Skoglundh, *Appl. Surf. Sci.*, 2004, **235**, 487–500.
16 S. Vallejos, T. Stoycheva, P. Umek, C. Navio, R. Snyders, C. Bittencourt, E. Llobet, C. Blackman, S. Moniz and X. Correig, *Chem. Commun.*, 2011, **47**, 565–567.
17 H. Baccar, A. Thamri, P. Clément, E. Llobet and A. Abdelghani, *Beilstein J. Nanotechnol.*, 2015, **6**, 919–927.
18 I. Jiménez, M. A. Centeno, R. Scotti, F. Morazzoni, J. Arbiol, A. Cornet and J. R. Morante, *J. Mater. Chem.*, 2004, **14**, 2412–2420.
19 Y. Tanaka, K. Kanai, Y. Ouchi and K. Seki, *Org. Electron.*, 2009, **10**, 990–993.
20 H. Ma, H.-L. Yip, F. Huang and A. K. Y. Jen, *Adv. Funct. Mater.*, 2010, **20**, 1371–1388.
21 S. Basu and A. Dutta, *Sens. Actuators, B*, 1994, **22**, 83–87.
22 Y. Hu, X. Zhou, Q. Han, Q. Cao and Y. Huang, *Mater. Sci. Eng., B*, 2003, **99**, 41–43.
23 F. E. Annanouch, Z. Haddi, S. Vallejos, P. Umek, P. Guttmann, C. Bittencourt and E. Llobet, *ACS Appl. Mater. Interfaces*, 2015, **7**, 6842–6851.
24 S. Dutta, S. D. Lewis and A. Dodabalapur, *Appl. Phys. Lett.*, 2011, **98**, 213504.
25 A. Kaushik, R. Kumar, S. K. Arya, M. Nair, B. D. Malhotra and S. Bhansali, *Chem. Rev.*, 2015, **115**, 4571–4606.
26 S. Ebrahimiasl and A. Zakaria, *Int. J. Electrochem. Sci.*, 2016, 9902–9916.
27 M. Xu, J. Zhang, S. Wang, X. Guo, H. Xia, Y. Wang, S. Zhang, W. Huang and S. Wu, *Sens. Actuators, B*, 2010, **146**, 8–13.
28 D. S. Dhawale, D. P. Dubal, A. M. More, T. P. Gujar and C. D. Lokhande, *Sens. Actuators, B*, 2010, **147**, 488–494.
29 D. S. Dhawale, D. P. Dubal, V. S. Jamadade, R. R. Salunkhe, S. S. Joshi and C. D. Lokhande, *Sens. Actuators, B*, 2010, **145**, 205–210.

30 V. Parra, J. Brunet, A. Pauly and M. Bouvet, *Analyst*, 2009, **134**, 1776–1778.
31 V. Parra and M. Bouvet, US8450725 B2, 2013.
32 P. Turek, P. Petit, J.-J. André, J. Simon, R. Even, B. Boudjema, G. Guillaud and M. Maitrot, *J. Am. Chem. Soc.*, 1987, **109**, 5119–5122.
33 M. Bouvet and J. Simon, *Chem. Phys. Lett.*, 1990, **172**, 299–302.
34 Y. Chen, M. Bouvet, T. Sizun, G. Barochi, J. Rossignol and E. Lesniewska, *Sens. Actuators, B*, 2011, **155**, 165–173.
35 R. Murdey, N. Sato and M. Bouvet, *Mol. Cryst. Liq. Cryst.*, 2006, **455**, 211–218.
36 A. Wannebroucq, R. Meunier-Prest, J.-C. Chambron, C.-H. Brachais, J.-M. Suisse and M. Bouvet, *RSC Adv.*, 2017, **7**, 41272–41281.
37 M. Bouvet, H. Xiong and V. Parra, *Sens. Actuators, B*, 2010, **145**, 501–506.
38 P. Gaudillat, A. Wannebroucq, J.-M. Suisse and M. Bouvet, *Sens. Actuators, B*, 2016, **222**, 910–917.
39 A. Wannebroucq, G. Gruntz, J.-M. Suisse, Y. Nicolas, R. Meunier-Prest, M. Mateos, T. Toupance and M. Bouvet, *Sens. Actuators, B*, 2018, **255**, 1694–1700.
40 H. Zheng, J. Z. Ou, M. S. Strano, R. B. Kaner, A. Mitchell and K. Kalantar-zadeh, *Adv. Funct. Mater.*, 2011, **21**, 2175–2196.
41 R. S. Vemuri, M. H. Engelhard and C. V. Ramana, *ACS Appl. Mater. Interfaces*, 2012, **4**, 1371–1377.
42 W. Noh, Y. Shin, J. Kim, W. Lee, K. Hong, S. A. Akbar and J. Park, *Solid State Ionics*, 2002, **152-153**, 827–832.
43 S. Vallejos, F. Di Maggio, T. Shujah and C. Blackman, *Chemosensors*, 2016, **4**, 4.
44 C. Bittencourt, R. Landers, E. Llobet, G. Molas, X. Correig, M. A. P. Silva, J. E. Sueiras and J. Calderer, *J. Electrochem. Soc.*, 2002, **149**, H81–H86.
45 L. Ottaviano, F. Bussolotti, L. Lozzi, M. Passacantando, S. La Rosa and S. Santucci, *Thin Solid Films*, 2003, **436**, 9–16.
46 S. Vallejos, T. Stoycheva, F. E. Annanouch, E. Llobet, P. Umek, E. Figueras, C. Canè, I. Gràcia and C. Blackman, *RSC Adv.*, 2014, **4**, 1489–1495.
47 M. Bao, Y. Bian, L. Rintoul, R. Wang, D. P. Arnold, C. Ma and J. Jiang, *Vib. Spectrosc.*, 2004, **34**, 283–291.
48 M. Bouvet, P. Gaudillat, A. Kumar, T. Sauerwald, M. Schüler, A. Schütze and J.-M. Suisse, *Org. Electron.*, 2015, **26**, 345–354.
49 F. Schauer, R. Novotny and S. Nešpůrek, *J. Appl. Phys.*, 1997, **81**, 1244–1249.
50 E. A. Silinsh, *Organic Molecular Crystals, Thier Electronic States*, Springer-Verlag, Berlin, Heidelberg, 1980.
51 M. Bouvet, E. A. Silinsh and J. Simon, *Mol. Mater.*, 1995, **5**, 255–277.
52 J. R. MacDonald, *Ann. Biomed. Eng.*, 1992, **20**, 289–305.
53 J. Scherbel, P. H. Nguyen, G. Paasch, W. Brütting and M. Schwoerer, *J. Appl. Phys.*, 1998, **83**, 5045–5055.
54 Q. Wang, J.-E. Moser and M. Grätzel, *J. Phys. Chem. B*, 2005, **109**, 14945–14953.
55 T. Kuwabara, Y. Kawahara, T. Yamaguchi and K. Takahashi, *ACS Appl. Mater. Interfaces*, 2009, **1**, 2107–2110.
56 C.-H. Kim, H. Hlaing, S. Yang, Y. Bonnassieux, G. Horowitz and I. Kymissis, *Org. Electron.*, 2014, **15**, 1724–1730.
57 K. A. Miller, R. D. Yang, M. J. Hale, J. Park, B. Fruhberger, C. N. Colesniuc, I. K. Schuller, A. C. Kummel and W. C. Trogler, *J. Phys. Chem. B*, 2006, **110**, 361–366.
58 E. Barsoukov and J. R. MacDonald, *Impedance Spectroscopy: Theory, Experiment, and Applications*, John Wiley & Sons, Inc., Hoboken, NJ, USA, 2005.
59 A. Amirudin and D. Thierry, *Prog. Org. Coat.*, 1995, **26**, 1–28.
60 D. Braga, M. Campione, A. Borghesi and G. Horowitz, *Adv. Mater.*, 2010, **22**, 424–428.
61 C. H. Hsu and F. Mansfeld, *Corrosion*, 2001, **57**, 747–748.
62 Guidance document on preventing and abating ammonia emissions from agricultural sources, Economic Commission for Europe, ECE EB.AIR, 2014.
63 Directive 2008/50/EC of the European parliament and of the council of 21May 2008, on ambient air quality and cleaner air for Europe, 2008, vol. L 152.
64 M. Bouvet, P. Gaudillat and J.-M. Suisse, *J. Porphyrins phthalocyanines*, 2013, **17**, 628–635.
65 Q. Feng, X. Li, J. Wang and A. M. Gaskov, *Sens. Actuators, B*, 2016, **222**, 864–870.
66 X. L. Huang, N. T. Hu, Y. Y. Wang and Y. F. Zhang, *Adv. Mater. Res.*, 2013, **669**, 79–84.
67 L. Wang, H. Huang, S. Xiao, D. Cai, Y. Liu, B. Liu, D. Wang, C. Wang, H. Li, Y. Wang, Q. Li and T. Wang, *ACS Appl. Mater. Interfaces*, 2014, **6**, 14131–14140.
68 C. N. Xu, N. Miura, Y. Ishida, K. Matsuda and N. Yamazoe, *Sens. Actuators, B*, 2000, **65**, 163–165.
69 M. G. Chung, D. H. Kim, H. M. Lee, T. Kim, J. H. Choi, D. K. Seo, J.-B. Yoo, S.-H. Hong, T. J. Kang and Y. H. Kim, *Sens. Actuators, B*, 2012, **166–167**, 172–176.
70 I. S. Kirin, P. N. Moskalev and Y. A. Makashev, *Russ. J. Inorg. Chem.*, 1965, **10**, 1065–1066.
71 C. Clarisse and M. T. Riou, *Inorg. Chim. Acta*, 1987, **130**, 139–144.

3. Conclusions

Metal oxide gas sensors have been studied successfully and thoughtfully during this doctoral thesis. The semiconductor metal oxide sensitive layers have been successfully obtained through different synthesis methodologies and their gas sensing performance was also effectively examined. The synthetized materials have been fully characterized by means of ESEM, HR-TEM, XRD, EDX, XPS, PL, ToF-SIMS. These instruments and techniques have been crucial to understand the synthetized layers morphology as well as the gas sensing mechanisms involved for each material.

Through a thermal process, under atmospheric pressure conditions and lower temperatures in contrast to vapor solid deposition growth, indium oxide (In_2O_3) octahedra have been successfully synthetized reducing considerably the overall difficulty and cost of the process. The In_2O_3 obtained was stenciled onto flexible substrates and demonstrated high sensitivity towards low concentrations of NO_2. Two different morphologies of zinc oxide (ZnO), nanorods and nanoflowers, were achieved by means of hydrothermal process. It could be observed that even both morphologies were suitable to be employed for NO_2 detection, their differences had a high impact in the sensing response towards NO_2 as nanoflowers almost doubled sensor response in comparison to nanorods. These differences also confirm that tuning the sensitivity of metal oxides is feasible via a modification in morphology.

Furthermore, wet chemical synthesis and aerosol assisted chemical vapor deposition were carried out to obtain lamellar shaped WO_3 and WO_3 nanowires, respectively. Both structures were fruitfully studied under different sensing conditions under ethanol and hydrogen atmospheres to better understand the difference suffered by a material when its morphology is modified. The results showed a difference in the adsorbed oxygen species at high operating temperatures and a clear enhancing effect of the response signal due to surface

area differences, being the lamellar WO_3 the morphology the one that displays the highest signal towards ethanol due to its higher surface area in comparison to WO_3 nanowires. However, when operating at 300 ºC both morphologies present a difference in the nature of the oxygen species adsorbed at their surfaces. Meanwhile lamellas have mainly O^-, nanowires present a mixture between O^- and O^{2-}. When reacting with ethanol it is clear that having a O^{2-} have a higher impact to the resistance change of the sensor, as reacting with O^{2-} species releases the double of electrons than reacting with O^-. This demonstrated that a sensitivity enhancement is achievable when tuning the material morphology.

On the long term, metal oxide nanowires synthetized via AACVD show an unavoidable baseline drift due to their SMOx nature. Nevertheless, a successful lowering of the baseline drift was achieved using a second order sigma-delta control of the materials surface potential as well as increasing the sensor response towards ethanol.

Aerosol assisted chemical vapor deposition have been demonstrated to be a versatile and easy methodology to obtain different nanostructures such as WO_3 nanowires. In addition, AACVD is a methodology that enables the decoration (at diverse loading levels) of such nanowires with different transition-metal oxides as well as noble metal oxides. Pure tungsten trioxide nanowires layers were tested under different gas laboratory-controlled atmospheres for a wide range of gases at ppb and ppm levels. The results obtained for such layers reveal the expected lack of selectivity and a clear cross-sensitivity for most of the gases due to similar responses values when tested under similar concentration for each gas, except for NO_2 tested at ppb levels. While pure layers suffer from cross-sensitivity effect, the *p-n* heterojunction layers synthetized induced on the sensing materials behavior a major modification, increasing their selectivity. For instance, pure WO_3 NWs and nickel oxide decorated WO_3 NWs were examined under different gases, and the results obtained revealed a 5-times increase in the

response towards hydrogen sulfide in comparison to pure WO_3 NWs layer under the same conditions. This increase was attributed to two main factors, namely the material electronic sensitization thanks to the *p-n* heterojunction presence, but also to the chemical sensitization due to the sulfurization / partial desulfurization of nickel oxide, which enhances further the response. An effective decoration of cobalt oxide nanoparticles was also achieved on a WO_3 NWs layers. The pure and the decorated layers were also exposed to different gases and in this particular case the loaded nanowires revealed and increase in the responses towards ethanol and hydrogen sulfide, but especially ammonia response was boosted. The responses towards ethanol and hydrogen sulfide benefit from the presence of cobalt oxide as they are boosted 60% and 80%, respectively in comparison to pure WO_3 NWs layers. Despite displaying an increase in sensitivity towards the already mentioned gases, the most important increase in the response was for ammonia, which increased by 250%. Both the electronic sensitization, for ethanol, and combined chemical and electronic sensitization for hydrogen sulfide, obtained through the *p-n* heterojunction were responsible for the development of selectivity in cobalt oxide loaded tungsten oxide nanowires. In the case of ammonia, the mechanisms involved and responsible for the sensing response are still under investigation and remain unknown to us. Iridium oxide loaded nanowires were also examined and their selectivity and sensitivity were dramatically increased towards concentrations lower than 1 ppm. In this particular case the heterojunction material acted as a catalyst for a water splitting process, resulting in a 95-fold increase in the overall sensor response in comparison to pristine WO_3 NWs for 1 ppm of NO_2.

The relative humidity cross-sensitivity effect was also studied on the gas sensing properties of WO_3 nanowires. The studies demonstrated a general important impact of ambient moisture on sensor responsiveness and a decrease in a minor or major grade of sensitivity. The main factor responsible for the effects observed

is the formation of an adsorbed layer of water molecules onto the sensors surface, and the subsequent hydroxylation of the metal oxide films. Target gases need to diffuse through this water layer and also face a reduction in the number of available sites at the surface of the gas sensitive material, thus lowering responsiveness.

4. Future Work

Considering all the results obtained, the future research efforts should be focused in three main points. The first and most important aspect is to carry out a deeper research on how to cope with humidity cross-sensitivity effects, as moisture cross-sensitivity remains as an important drawback when thinking in operating such sensors under real conditions. Fluctuations in the relative humidity levels present in the environment have a clear impact in all the sensors tested, typically decreasing their sensitivity. Therefore, the studies carried out in the future should be directed towards the synthesis of nanostructured layers for humidity resilient sensors. Alternatively, the designing of a system with the ability to remove humidity from the atmosphere could be envisaged, understanding atmosphere as the air volume in contact with the sensor surface, in order to operate under quasi-dry or dry air conditions without interfering with the target gas concentration. Secondly, it is necessary to understand and investigate further the behavior of such sensors when interacting with a wide range of possible harmful gases in view of better assessing selectivity. Therefore, there is a clear need to investigate and characterize sensor response towards many different gases (i.e. ozone, carbon monoxide, polycyclic aromatic hydrocarbons, and other organic compounds released to the atmosphere due to anthropologic sources). This study should be conducted not only investigating each gas individually but trying to reproduce more complex matrices with gas mixtures as a way to better study cross-sensitivity effects. Finally, it is also important to investigate towards designing new layer morphologies, with new shapes and metal oxide

heterojunctions, as well as improving the control of sensor surface potential, as it has been demonstrated that both heterojunction design and surface potential control improve considerably the performance of gas sensors.

5. Bibliography

[1] R. Gilbert, "The World Animal Feed Industry," *Protein Sources Anim. Feed Ind.*, pp. 1 - 8, 2003. Available: http://www.fao.org/docrep/007/y5019e/y5019e00.htm.

[2] Food and Aagriculture Organization, "Feeding the Word (part 3) in FAO Statistical Yearbook 2012: World Food and Agriculture," pp. 171-280/369, 2012. Available: http://www.fao.org/docrep/015/i2490e/i2490e00.htm%5Cnhttp://issuu.com/faosyb/docs/fao_statistical_yearbook_2012_issuu#download.

[3] International Labour Organization, *The future of work in textiles, clothing, leather and footwear*, no. 326. 2019. Available: https://www.ilo.org/wcmsp5/groups/public/---ed_dialogue/---sector/documents/publication/wcms_669355.pdf

[4] H. M. Chiu, "The dark side of silicon Island: High-tech pollution and the environmental movement in Taiwan," *Capital. Nature, Social.*, vol. 22, no. 1, pp. 40–57, 2011.

[5] F. G. Babuna, I. Toroz, E. Avsar, and U. Yetis, "Hazardous Waste Generation in Pesticide Synthesis Sector in Turkey," *Pestic. Res. J.*, vol. 26, no. 2, pp. 181–188, 2014.

[6] P. Li, X. Li, C. Yang, X. Wang, J. Chen, and J. L. Collett, "Fog water chemistry in Shanghai," *Atmos. Environ.*, vol. 45, no. 24, pp. 4034–4041, 2011.

[7] J. G. Speight, "Chapter Five - Sources and Types of Inorganic Pollutants," in *Environmental Inorganic Chemistry for Engineers*, J. G. Speight, Ed. Butterworth-Heinemann, pp. 231–282, 2017.

[8] G. Tóth, T. Hermann, M. R. Da Silva, and L. Montanarella, "Heavy metals in agricultural soils of the European Union with implications for food safety," *Environ. Int.*, vol. 88, pp. 299–309, 2016.

[9] R. A. Wuana and F. E. Okieimen, "Heavy Metals in Contaminated Soils: A Review of Sources, Chemistry, Risks and Best Available Strategies for Remediation," *ISRN Ecol.*, vol. 2011, pp. 1–20, 2011.

[10] P. D. Millner, "Chapter 4 - Manure Management," in *The Produce Contamination Problem (Second Edition)*, Second Edition., K. R. Matthews, G. M. Sapers, and C. P. Gerba, Eds. San Diego: Academic Press, pp. 85–106, 2014.

[11] K. Song, Y. Xue, X. Zheng, W. Lv, H. Qiao, Q. Qin and J. Yang., "Effects of the continuous use of organic manure and chemical fertilizer on soil inorganic phosphorus fractions in calcareous soil," *Sci. Rep.*, vol. 7, no. 1, pp. 1–9, 2017.

[12] United Nations Educational, Scientific and Cultural Organization, "The United Nations world water development report 2017: wastewater: the untapped resource." World Water Assessment Programme, 2017. Available: http://www.unesco.org/new/en/natural-sciences/environment/water/wwap/wwdr/2017-wastewater-the-untapped-resource/

[13] D. Bellos and T. Sawidis, "Chemical pollution monitoring of the River Pinios (Thessalia - Greece)," *J. Environ. Manage.*, vol. 76, no. 4, pp. 282–292, 2005.

[14] H. Mayer, "Mayer: Cities," *Atmos. Environ.*, vol. 33, no. 24, pp. 4029–4037, 1999.

[15] D. D. Parrish, H. B. Singh, L. Molina, and S. Madronich, "Air quality progress in North American megacities: A review," *Atmos. Environ.*, vol. 45, no. 39, pp. 7015–7025, 2011.

[16] A. Bougiatioti, M. Kanakidou, and N. Mihalopoulos, "Chapter 19 - Air Quality in European Cities," in *The Quality of Air*, vol. 73 , pp. 517–542, 2016.

[17] R. L. Maynard, "Health effects of urban pollution," *Issues Environ. Sci. Technol.*, vol. 28, pp. 108–128, 2009.

[18] A. J. Cohen, H. R. Anderson, B. Ostro, K. D. Pandey, M. Krzyzanowski, N. Künzli, K. Gutschmidt, A. Pope, I. Romieu, J. M. Samet and K. Smith, "The global burden of disease due to outdoor air pollution," *J. Toxicol. Environ. Heal. - Part A*, vol. 68, no. 13–14, pp. 1301–1307, 2005.

[19] H. Akimoto, "Global Air Quality and Pollution," *Science (80).*, vol. 302, no. 5651, pp. 1716–1719, 2003.

[20] E. Robinson and R. C. Robbins, "Gaseous nitrogen compound pollutants from urban and natural sources," *J. Air Pollut. Control Assoc.*, vol. 20, no. 5, pp. 303–306, 1970.

[21] E. Robinson and R. C. Robbins, "Gaseous sulfur pollutants from urban and natural sources," *J. Air Pollut. Control Assoc.*, vol. 20, no. 4, pp. 233–235, 1970.

[22] V. Soni, P. Singh, V. Shree, and V. Goel, "Effects of VOCs on Human Health," in *Air Pollution and Control*, pp. 119–142, 2018.

[23] C. Holman, "8 - Sources of Air Pollution," in *Air Pollution and Health*, S. T. Holgate, J. M. Samet, H. S. Koren, and R. L. Maynard, Eds. London:

Academic Press, pp. 115–148, 1999.

[24] European Environmental Agency Technical, *Particulate matter from natural sources and related reporting under the EU Air Quality Directive in 2008 and 2009*, no. 10. 2012. Available: https://www.eea.europa.eu/publications/particulate-matter-from-natural-sources

[25] D. Y. H. Pui, S. C. Chen, and Z. Zuo, "PM2.5 in China: Measurements, sources, visibility and health effects, and mitigation," *Particuology*, vol. 13, no. 1, pp. 1–26, 2014.

[26] European Environmental Agency, *Air quality 2018 - EEA report 12 2018*, no. January 2019. 2018. Available: https://www.eea.europa.eu/publications/air-quality-in-europe-2018

[27] European Environment Agency, *Air quality in Europe 2019 report*, no. January 2020. 2019. Available: https://www.eea.europa.eu/publications/air-quality-in-europe-2019

[28] G. Neri, "First fifty years of chemoresistive gas sensors," *Chemosensors*, vol. 3, no. 1, pp. 1–20, 2015.

[29] Y. F. Sun, S. B. Liu, F. L. Meng, J. Y. Liu, Z. Jin, L. T. Kong and J. H. Liu, "Metal oxide nanostructures and their gas sensing properties: A review," *Sensors*, vol. 12, no. 3, pp. 2610–2631, 2012.

[30] N. Yamazoe and K. Shimanoe, "Roles of shape and size of component crystals in semiconductor gas Sensors: I. Response to oxygen," *J. Electrochem. Soc.*, vol. 155, no. 4, pp. 85–92, 2008.

[31] S. Roso, C. Bittencourt, P. Umek, O. González, F. Güell, A. Urakawa, E. Llobet, "Synthesis of single crystalline In_2O_3 octahedra for the selective

detection of NO_2 and H_2 at trace levels," *J. Mater. Chem. C*, vol. 4, no. 40, pp. 9418–9427, 2016.

[32] N. Yamazoe and K. Shimanoe, "Roles of shape and size of component crystals in semiconductor gas Sensors: I. Response to oxygen," *J. Electrochem. Soc.*, vol. 155, no. 4, pp. 93–98, 2008.

[33] L. Zhang, X. Jing, J. Liu, J. Wang, and Y. Sun, "Facile synthesis of mesoporous ZnO/Co_3O_4 microspheres with enhanced gas-sensing for ethanol," *Sensors Actuators, B Chem.*, vol. 221, no. 2, pp. 1492–1498, 2015.

[34] W. C. Conner and J. L. Falconer, "Spillover in Heterogeneous Catalysis," *Chem. Rev.*, vol. 95, no. 3, pp. 759–788, 1995.

[35] D. R. Miller, S. A. Akbar, and P. A. Morris, "Nanoscale metal oxide-based heterojunctions for gas sensing: A review," *Sensors Actuators, B Chem.*, vol. 204, pp. 250–272, 2014.

[36] D. Degler, U. Weimar, and N. Barsan, "Current Understanding of the Fundamental Mechanisms of Doped and Loaded Semiconducting Metal-Oxide-Based Gas Sensing Materials," *ACS Sensors*, vol. 4, no. 9, pp. 2228–2249, 2019.

[37] H. R. Kim, A. Haensch, I. D. Kim, N. Barsan, U. Weimar, and J. H. Lee, "The role of NiO doping in reducing the impact of humidity on the performance of SnO2-based gas sensors: Synthesis strategies, and phenomenological and spectroscopic studies," *Adv. Funct. Mater.*, vol. 21, no. 23, pp. 4456–4463, 2011.

[38] W. Liu, L. Xu, K. Sheng, X. Zhou, B. Dong, G. Lu, H. Song , "A highly sensitive and moisture-resistant gas sensor for diabetes diagnosis with Pt@In_2O_3 nanowires and a molecular sieve for protection," *NPG Asia Mater.*, vol. 10, no. 4, pp. 293–308, 2018.

Annex I

Supporting information

Supporting information for:

Differences in gas sensing mechanisms for 1-D WO_3 Nanowires and 2-D lamellar WO_3 nanoparticles

Èric Navarrete[1], Koichi Suematsu[2], Eduard Llobet[1], Kengo Shimanoe[2]

[1]*MINOS-EMaS, University Rovira I Virgili, Avda. Països Catalans, 26, 43007 Tarragona, Spain*

[2]*Department of molecular and Material Sciences, Faculty of Engineering Sciences, Kyushu University, 6-1 Kasuga-koen, Kasuga, Fukuoka 816-8580, Japan*

The intensity of the response towards hydrogen and ethanol is significantly higher for lamellar tungsten oxide sensors than for nanowire-based sensors. Given the two different synthesis routes implemented, lamellar sensors comprised far more tungsten oxide material than nanowire sensors. Using more material implies increasing the surface area, which eventually results in higher responsiveness. In order to clarify this point and remark the importance of surface area, a gas sensing experiment was conducted employing two nanowire sensors. The first sensor consisted of (WO_3 NWs) grown onto a commercial alumina substrate as it is described in the experimental section of this paper. In the second sensor (H-WO_3 NWs) the amount of precursor employed to produce the nanowire sensing layer was doubled, obtaining a film with a higher amount of nanowire material. These two sensors were operated at 300 ºC and exposed to 100, 300 and 500 ppm of H_2 and 5, 10, 15 and 20 ppm of ethanol vapors balanced in dry air. The results obtained are summarized in Tables S1 and S2.

Table S1. Comparison of response intensities (R_{air}/R_{gas}) towards hydrogen for two sensors with different amounts of tungsten oxide nanowires in their sensing layers. Sensors were operated at 300ºC. The last column indicates the increase in response achieved by increasing the amount of material (surface area) in the sensor.

[H_2] ppm	WO_3 NWs	H-WO_3 NWs	%
100	1.4	1.9	35.7
300	1.7	2.3	35.3
500	1.9	2.5	31.6

Table S2. Comparison of response intensities (R_{air}/R_{gas}) towards ethanol for two sensors with different amounts of tungsten oxide nanowires in their sensing layers. Sensors were operated at 300ºC. The last column indicates the increase in response achieved by increasing the amount of material (surface area) in the sensor.

[Ethanol] ppm	WO_3 NWs	H-WO_3 NWs	%
5	3.0	6.6	120.0
10	3.6	9.1	152.7
15	4.0	11.0	175.0
20	4.4	13.0	195.5

Tables S1 and S2 show that nanowire sensors with an increased amount of tungsten oxide in their sensitive coatings (higher surface area) increase their response towards hydrogen and ethanol by an average factor of 1.3 and 3, respectively. Consequently, these results support our assumption that the higher hydrogen and ethanol responses obtained for lamellar WO_3 nanoparticle sensors are due to their higher effective surface area derived from their higher amount of tungsten oxide than in nanowire sensors.

[Supporting Information]

Gas sensing properties of ZnO nanostructures (flowers/rods) synthesized by hydrothermal method

Sonalika Agarwal[1]*, Prabhakar Rai[2,3,4], Eric Navarrete Gatell[3], Eduard Llobet[3], Frank Güell[5] Manoj Kumar[1], Kamlendra Awasthi[1]*

[1]*Department of Physics, Malaviya National Institute of Technology Jaipur, Rajasthan 302017, India*

[2]*Department of Chemical Engineering, Indian Institute of Technology, Kanpur 208016, India*

[3]*MINOS-EMaS, Universitat Rovira i Virgili, Avda. Països Catalans 26, 43007 Tarragona, Spain*

[4]*Wildlife Section, Zoological Survey of India, Kolkata 700053, India*

[5]*ENFOCAT-IN2UB, Universitat de Barcelona (UB), C/Martí i Franquès 1, 08028 Barcelona, Catalunya, Spain*

*Corresponding Author Email: sonalika.spsl@gmail.com , kawasthi.phy@mnit.ac.in

Table S1 Average t_{90} ZnO sensor response for each gas at different temperatures in seconds.

Nanostructure/ Gas/ Concentration	**150 ºC**	**200 ºC**	**250 ºC**
NR /EtOH - 20 ppm	774	876.4	30.8
NF / EtOH – 20 ppm	1768.4	1322.4	35.9
NF / C_6H_6 – 10 ppm	380	1730	1200
NF / NO_2 – 1 ppm	1230	809.7	1512
NR / NO_2 – 1ppm	794.3	676.5	558.8

Table S2 Summary of results obtained in the chemo-resistive detection of NO_2 employing different metal oxide nanomaterials.

ZnO Morphology	**Synthesis method**	**Target gas / Concentration (ppm)**	**Working Temp.** (ºC)	**Response**	**t_{90} Response time (s)**	**Ref.**
Flower- like	Hydrothermal	Ethanol / 400	350	30.4[a]	10	S[1]
Flower-like	Microwave Hydrothermal	Ethanol / 100	450	9.5[a]	NA [c]	S [2]
Flower-like	Reverse Microemulsion	NO_2 / 40	400	44.8[b]	NA [c]	S[3]
Nanoflowers	Hydrothermal	NO_2 / 10	150	55[b]	8	S[4]
Nanorods	Hydrothermal	Ethanol / 50	320	22[a]	60	S[5]
Nanorods	One-step Solid state reaction	Ethanol / 100	332	13.5[a]	NA [c]	S[6]
Nanorods	Hydrothermal	NO_2 / 1	200	0.3[b]	84	S[7]
Nanorods	Hydrothermal	NO_2 / 10	350	130[b]	NA [c]	S[8]
Nanoflowers	Hydrothermal	Ethanol/ 20 NO_2 / 1	250 200	18.3 [a] 34.1 [b]	31 810	This work
Nanorods	Hydrothermal	Ethanol/ 20 NO_2 / 1	250 200	24.2 [a] 20.6 [b]	36 677	This work

[a] R_{air}/R_{gas}; [b] R_{gas}/R_{air} ; [c] NA: Not available

Fig. S1 (a) Alumina transducer substrates employed. The left image shows the back side with Pt heating element and the right image shows the front side that comprises Pt interdigitated electrodes. (b) Digital picture of your gas sensing test.

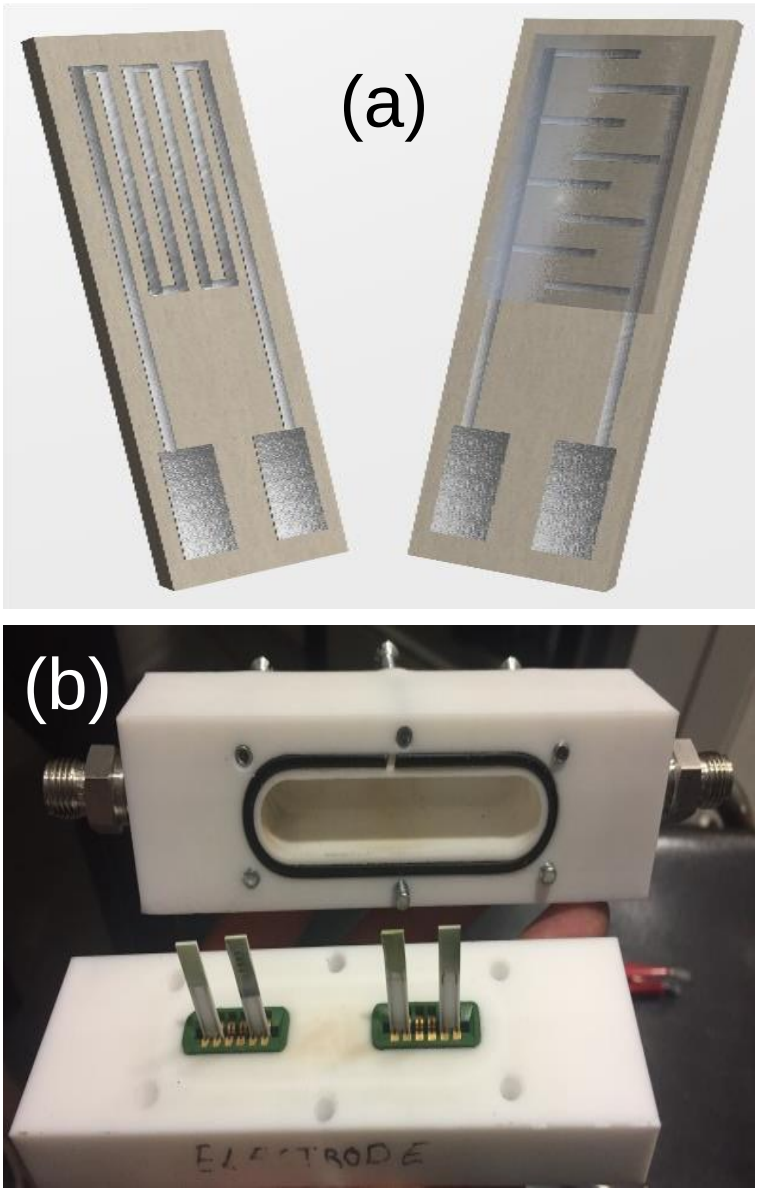

Fig. S2 Typical N_2 gas adsorption-desorption isotherm for BET surface area analysis of ZnO (a) nanoflowers and (b) nanorods.

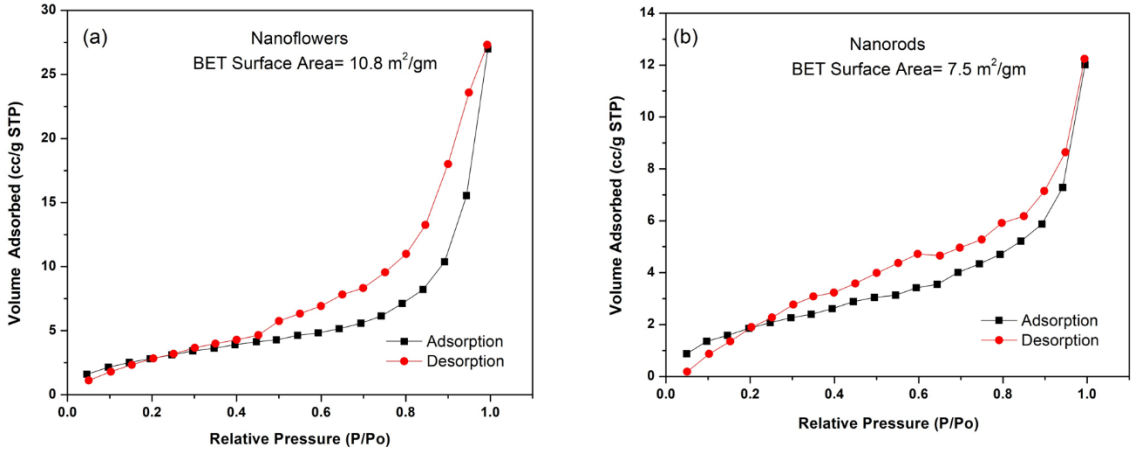

Fig. S3 Response comparison of ZnO (a) nanoflowers and (b) nanorods to NO_2 increasing concentrations exposure at 200ºC working temperature at dry air and 30% relative humidity conditions.

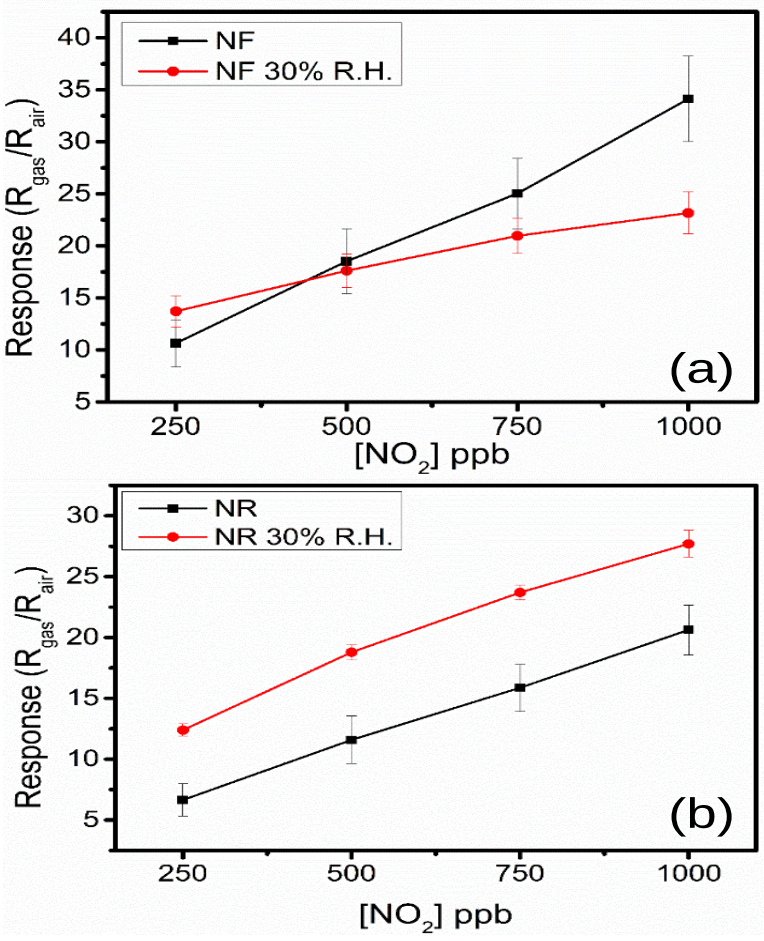

Fig. S4 (a) Resistance measures for ZnO nanoflowers and nanorods sensors exposed to 1 ppm of NO_2 at 200 ºC after 3 months of storage. (b) Sensors response over 3 months' time for 1 ppm NO2 at 200ºC operating temperature.

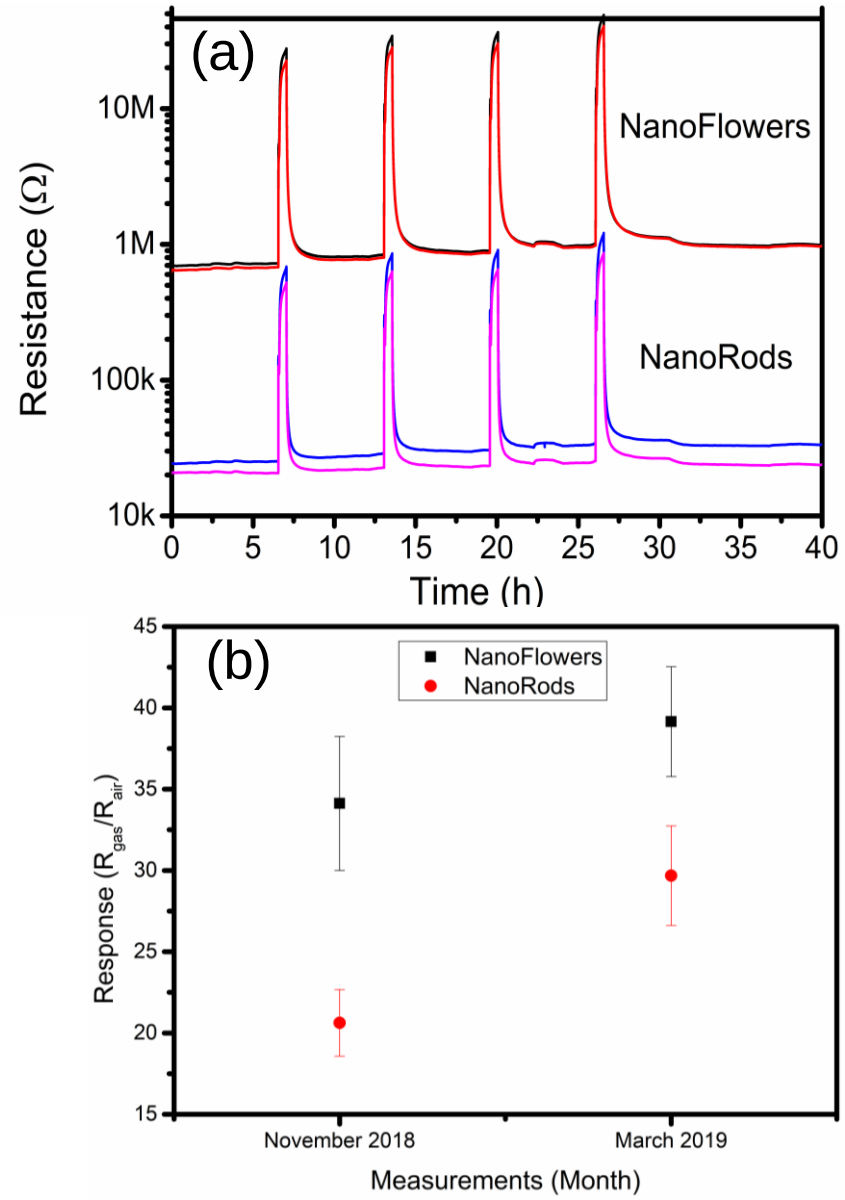

References

S[1] L. Zhu, Y. Li, W. Zeng, Hydrothermal synthesis of hierarchical flower-like ZnO nanostructure and its enhanced ethanol gas-sensing properties, Appl. Surf. Sci. 427 (2018) 281–287. doi:10.1016/j.apsusc.2017.08.229.

S[2] X. Su, H. Zhao, F. Xiao, J. Jian, J. Wang, Synthesis of flower-like 3D ZnO microstructures and their size-dependent ethanol sensing properties, Ceram. Int. 38 (2012) 1643–1647. doi:10.1016/j.ceramint.2011.09.055.

S[3] S. Bai, L. Chen, S. Chen, R. Luo, D. Li, A. Chen, C.C. Liu, Reverse microemulsion in situ crystallizing growth of ZnO nanorods and application for NO2 sensor, Sensors Actuators, B Chem. 190 (2014) 760–767. doi:10.1016/j.snb.2013.09.032.

S[4] S. Bai, T. Guo, D. Li, R. Luo, A. Chen, C.C. Liu, Intrinsic sensing properties of the flower-like ZnO nanostructures, Sensors Actuators, B Chem. 182 (2013) 747–754. doi:10.1016/j.snb.2013.03.077.

S[5] L. Wang, Y. Kang, X. Liu, S. Zhang, W. Huang, S. Wang, ZnO nanorod gas sensor for ethanol detection, Sensors Actuators, B Chem. 162 (2012) 237–243. doi:10.1016/j.snb.2011.12.073.

S[6] Z.P. Sun, L. Liu, L. Zhang, D.Z. Jia, Rapid synthesis of ZnO nano-rods by one-step, room-temperature, solid-state reaction and their gas-sensing properties, Nanotechnology. 17 (2006) 2266–2270. doi:10.1088/0957-4484/17/9/032.

S[7] S. Öztürk, N. Kilinç, Z.Z. Öztürk, Fabrication of ZnO nanorods for NO2 sensor applications: Effect of dimensions and electrode position, J. Alloys Compd. 581 (2013) 196–201. doi:10.1016/j.jallcom.2013.07.063.

S[8] L. Shi, A.J.T. Naik, J.B.M. Goodall, C. Tighe, R. Gruar, R. Binions, I. Parkin, J. Darr, Highly sensitive ZnO nanorod- and nanoprism-based NO2 gas sensors: Size and shape control using a continuous hydrothermal pilot plant, Langmuir. 29 (2013) 10603–10609. doi:10.1021/la402339m.

Supporting information for:

Flexible Sensors Based on Octahedral Indium Oxide Nanopowder for Gas Sensing Applications

Miriam Alvarado [1], Èric Navarrete[1], Alfonso Romero[1] José Luis Ramírez[1] and Eduard Llobet[1,*]

[1] MINOS-EMas, Universitat Rovira i Virgili, Tarragona, Spain
* Correspondence: eduard.llobet@urv.cat

The following figures S1 and S2 correspond to the EDX obtained for the samples grown at 400 ºC and 500 ºC. The as mentioned Cl remnant from the precursor has been found at 400 ºC by means of EDX. At 500 ºC the temperature is high enough to promote its elimination, or at least, resulting its concentration below the limit of detection for such technique.

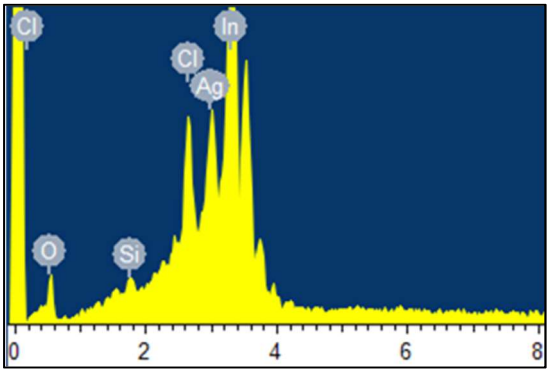

Figure S1. EDX from an In_2O_3 sample synthesized at 400 ºC. The presence of Cl contamination is revealed. The silver (Ag) signal is due to the printed electrodes. Silicon (Si) is present due to the holder.

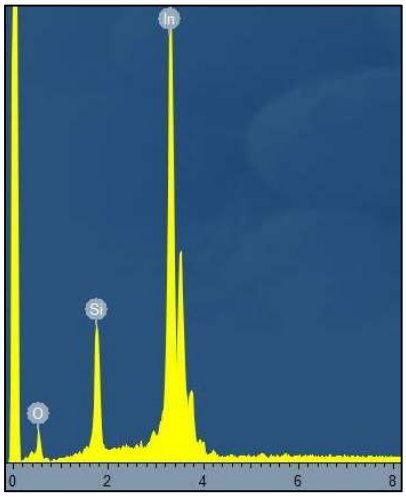

Figure S2. EDX from an In_2O_3 sample synthesized at 500 ºC sample. Silicon (Si) signal is given due to the holder.

Figure S3 summarizes the responses towards nitrogen dioxide of a flexible sensor employing indium oxide synthesized at 400 ºC. These results were reported in [15]. The responses summarized in Figure S3 are about 5 times lower than those we report now for NO_2 (in this work). The reasons for such an increase in response may be due to:

- The elimination of contamination from the gas sensitive film (Cl is present in samples synthesized at 400 ºC and this is no longer the case for samples synthesized at 500 ºC, as shown by EDX analysis).
- Better octahedral morphology and ameliorated homogeneity of the coating.

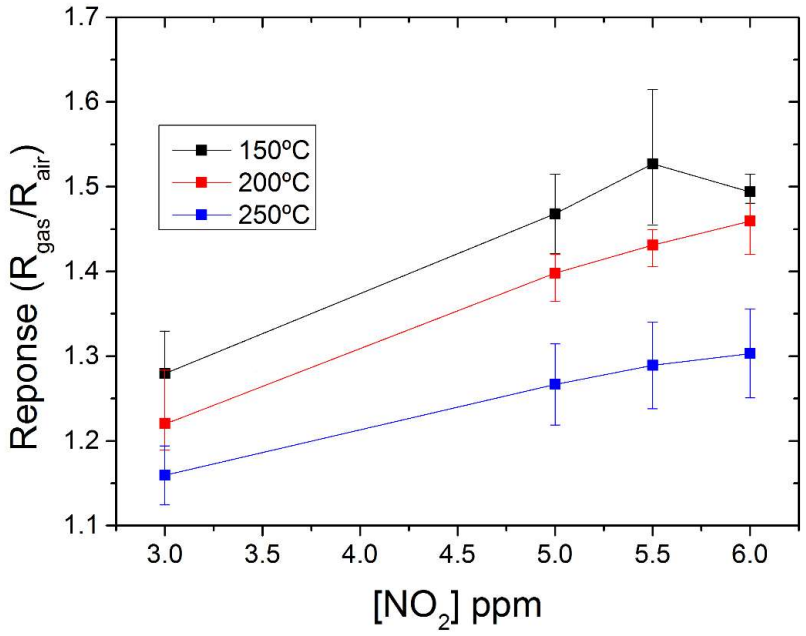

Figure S3. Nitrogen dioxide calibration curves for a sensor consisting of indium oxide synthesized at 400 ºC coated onto a polyimide flexible transducer. The different curves correspond to the different operating temperature tested. Adapted from [15].

Table S1. Comparison of gas-sensing performances of In_2O_3 gas sensors using different structures.

Sensing material	Synthesis strategy	Processing temperature/ Reaction time	Annealing temperature (Time)	Sensor fabrication	Working temperature	Response* for NO_2	Substrate	Ref
In_2O_3 micro-cubes	Low-temperature wet chemical	90 ºC (3 h)	400 ºC (1 h)	Mixed with distilled water	60 ºC	2.9 (500 ppb)	Ceramic tube	[S1]
In_2O_3 nanowires	Wet-chemical	180 ºC (30 h)	400 ºC (5 min)	Mixed with ethanol	250 ºC	2.57 (1 ppm)	Alumina tube	[S2]
In_2O_3 microspheres	Template-free solvent-thermal method	200 ºC (4 h)	600 ºC (3 h)	Sintered at 500ºC (2 h) Aged at 300ºC (7 days)	250 ºC	1.5 (5 ppm)	Alumina tube	[S3]
In_2O_3 nanorod bundles	Microwave hydrothermal	140 ºC (0,5 h)	550 ºC (2 h)	Dispersed in water, dried at RT, aged at 400 ºC (2 h)	100 ºC	87 (1 ppm)	Ceramic tube	[S4]
In_2O_3 nanobricks	Bath heating	96 ºC (2 h)	400 ºC (2 h)	Mixed with ethanol, dried at RT. Aged at 130 ºC (24 h)	50 ºC	402 (500 ppb)	Ceramic	[S5]
In_2O_3 nanospheres	Solvothermal method	100 ºC (24 h)	500 ºC (2 h)	Dispersed in deionized water	120 ºC	371.9 (1 ppm)	Ceramic tube	[S6]
In_2O_3 nanorod clusters	Solvothermal method	160 ºC (12 h)	500 ºC (2 h)	Mixed with deionized water, dried at RT, sintered at 500 ºC (2 h)	150 ºC	41 (500 ppb)	Alumina tube	[S7]
In_2O_3 octahedra	Vapor phase transport	1000 ºC (2 h)		Mixed with 1,2-propanediol	130 ºC	120 (1 ppm)	Alumina	[S8]
In_2O_3 octahedra	Oxidation	500 ºC (2 h)		Mixed with 1,2-propanediol, dried at 150 ºC	150 ºC	5.75 (5 ppm)	Polyimide	This work

* Response calculated $S=R_g/R_a$

Supporting information references

S1. Navale, S. T.; Liu, C.; Yang, Z.; Patil, V. B.; Cao, P.; Du, B.; Mane, R. S.; Stadler, F. J. Low-temperature wet chemical synthesis strategy of In2O3for selective detection of NO2down to ppb levels. *J. Alloys Compd.* **2018**, *735*, 2102–2110, doi:10.1016/j.jallcom.2017.11.337.

S2. Xu, P.; Cheng, Z.; Pan, Q.; Xu, J.; Xiang, Q.; Yu, W.; Chu, Y. High aspect ratio In2O3 nanowires: Synthesis, mechanism and NO2 gas-sensing properties. *Sensors Actuators, B Chem.* **2008**, *130*, 802–808, doi:10.1016/j.snb.2007.10.044.

S3. Cheng, Z.; Song, L.; Ren, X.; Zheng, Q.; Xu, J. Novel lotus root slice-like self-assembled In2O3microspheres: Synthesis and NO2-sensing properties. *Sensors Actuators, B Chem.* **2013**, *176*, 258–263, doi:10.1016/j.snb.2012.09.048.

S4. Li, X.; Yao, S.; Liu, J.; Sun, P.; Sun, Y.; Gao, Y.; Lu, G. Vitamin C-assisted synthesis and gas sensing properties of coaxial In<inf>2</inf>O<inf>3</inf> nanorod bundles. *Sensors Actuators, B Chem.* **2015**, *220*, 68–74, doi:10.1016/j.snb.2015.05.038.

S5. Han, D.; Zhai, L.; Gu, F.; Wang, Z. Highly sensitive NO2gas sensor of ppb-level detection based on In2O3nanobricks at low temperature. *Sensors Actuators, B Chem.* **2018**, *262*, 655–663, doi:10.1016/j.snb.2018.02.052.

S6. Xiao, B.; Zhao, Q.; Wang, D.; Ma, G.; Zhang, M. Facile synthesis of nanoparticle packed In_2O_3 nanospheres for highly sensitive NO_2 sensing. *New J. Chem.* **2017**, *41*, 8530–8535, doi:10.1039/C7NJ00647K.

S7. Xu, X.; Zhang, H.; He, C.; Pu, C.; Leng, Y.; Li, G.; Hou, S.; Zhu, Y.; Fu, L.; Lu, G. Synthesis and NO_2 sensing properties of indium oxide nanorod clusters via a simple solvothermal route. *RSC Adv.* **2016**, *6*, 47083–47088, doi:10.1039/C6RA01958G.

S8. Roso, S.; Bittencourt, C.; Umek, P.; González, O.; Güell, F.; Urakawa, A.; Llobet, E. Synthesis of single crystalline In_2O_3 octahedra for the selective detection of NO_2 and H_2 at trace levels. *J. Mater. Chem. C* **2016**, *4*, 9418–9427, doi:10.1039/C6TC03218D.

Supporting information for:

AACVD synthesis and gas sensing properties of nickel oxide nanoparticle decorated tungsten oxide nanowires

Èric Navarrete[1], Carla Bittencourt[2], Polona Umek[3], Eduard Llobet[*1]

[1]MINOS-EMaS, Universitat Rovira i Virgili, Avda. Països Catalans, 26, 43007 Tarragona, Spain

[2]Chimie des Interactions Plasma – Surface (ChIPS), Research Institute for Materials Science and Engineering, Université de Mons, Avenue Copernic 1, 7000 Mons, Belgium

[3]Jožef Stefan Institute, Jamova cesta 39, 10000 Ljubljana, Slovenia.

[*]Correspondence: eduard.llobet@urv.cat; Tel.: +34 977 558 502

1. Results employing the one-step deposition approach

At first the AA-CVD process was performed in one step mixing both the tungsten oxide and the nickel oxide organic precursors in the same solution and subsequently deposited. The results obtained through this one step procedure revealed a non-homogeneous nickel deposition.

The following table displays the average chemical composition of nickel doped sensors resulting from running the 1 step procedure. This composition has been estimated by XPS. Low-concentration loading (LC) corresponds to using 2.5 mg of Ni precursor and high-concentration loading (HC) corresponds to using 5 mg of Ni precursor.

Table S1. Average composition in weight percentage for the Ni-loaded sensing layers obtained employing the 1-step deposition approach.

	W	**O**	**Ni**
1ST Ni/LC	**22.0**	**76.5**	**1.5**
	W	**O**	**Ni**
1ST Ni/HC	**22.4**	**75.8**	**1.9**

The amount of nickel loading is rather low and does not differ substantially for LC and HC samples. In addition, the morphology of the Ni-loaded samples is not the expected. Even though tungsten oxide nanowires are obtained, in many regions of the samples an unexpected cauliflower shaped morphology appears as revealed by SEM (see the micrographs below in Figure S1). The EDX analysis of the chemical composition of these abnormal microstructures indicates that they contain tungsten and nickel. Considering the poor, inefficient results of Ni loading and the abnormal microstructure of the resulting films, the single step approach was discarded and a two-step approach implemented.

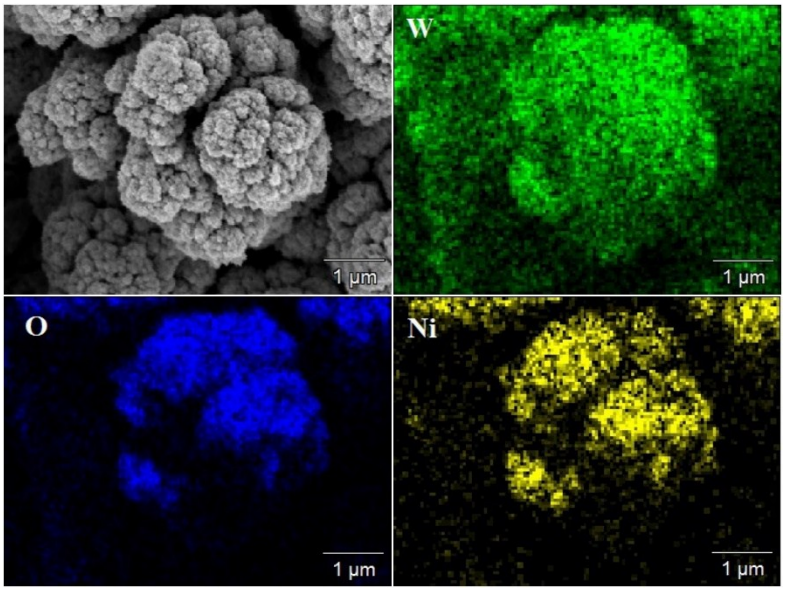

Figure S1. A SEM image and the corresponding elemental maps (W – green, O – blue and Ni – yellow) for the cauliflower structures present in Ni-loaded samples obtained via the single step deposition approach.

2. Additional results on the two-step deposition approach

Sensors were characterized by EDX as qualitative and XPS as quantitative techniques, in order to confirm the presence of nickel. The following figure shows the results of EDX performed on a Ni-loaded tungsten oxide nanowire sample obtained via a two-step deposition approach. EDX confirms the presence of Ni. The Pt peaks in the EDX spectrum correspond to the electrodes of the transducer onto which the gas sensitive film is deposited.

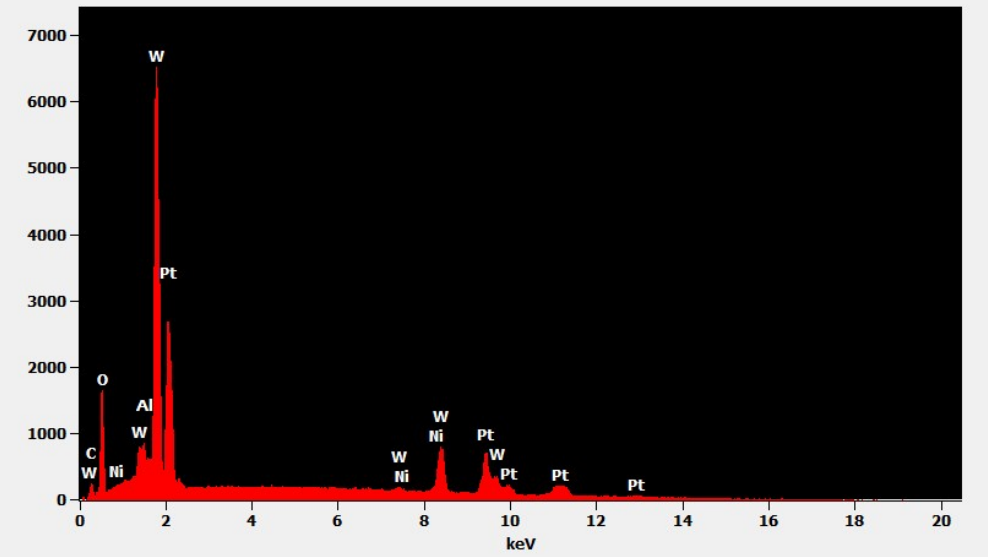

Figure S2. EDX results for a Ni/HC sensor.

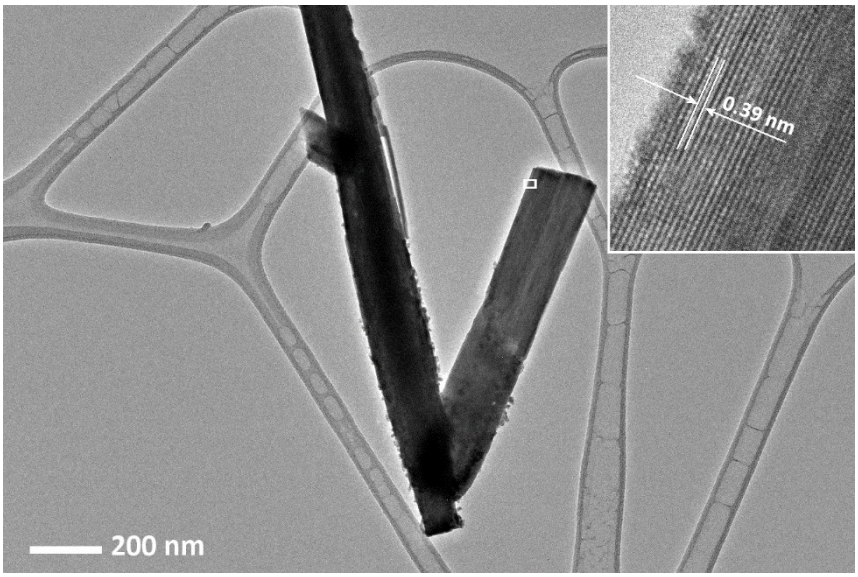

Figure S3. SEM micrograph of the Ni/LC sample. The HRTEM inset shows that the WO_3 nanorod is crystalline. The d-spacing between lattice fringes in the inset is 0.39 nm corresponding to (002) planes in WO_3 with triclinic structure (JPCDS 71-0305).

3. Response times

Tables S2 and S3 summarize the response times for pure and Ni-loaded tungsten oxide sensors. The response time t90 indicates the time needed for the sensor resistance to reach 90% of its steady state value upon a sudden change in gas concentration. Response times decrease when the operating temperature increases, as it could be expected. Despite the fact that the fastest responses are obtained at 250 ºC, this operating temperature it is not always the optimal for achieving the highest response.

Table S2. Case of pure WO_3 sensor. Average t90 response for each gas at different temperatures in seconds. t90 values appear in bold when they correspond to the operating temperature in which sensor response is maximal.

WO_3	150 ºC	200 ºC	250 ºC
CH_4 – 20 ppm	--	450	**255**
Ethanol – 20 ppm	**832**	450	255
NO_2 – 10 ppm	**650**	325	272
H_2S – 50 ppm	**158**	88	119

Table S3. Case of Ni/HC sensor. Average t90 response for each gas at different temperatures in seconds. t90 values appear in bold when they correspond to the operating temperature in which sensor response is maximal.

Ni/HC	150 ºC	200 ºC	250 ºC
CH_4 – 20 ppm	--	363	**199**
Ethanol – 20 ppm	848	494	**149**
NO_2 – 10 ppm	**1720**	1210	568
H_2S – 50 ppm	514	90	**88**

4. H_2S and layer degradation

It is well known that hydrogen sulfide is a compound that poisons metal oxide gas sensors and results in fast aging of the sensing films. The acidity of H_2S leads to a corrosion of the structures, altering the original morphology of the gas sensitive films. This effect is clearly visible after several hours of operation at 250 ºC and under high hydrogen sulfide concentrations (i.e. 50 ppm). As a result the initially observed responsiveness degrades. This effect has been studied for the different gas-sensitive layers produced. Figure S4 shows that morphological changes are visible after the films are exposed continuously to 50 ppm of hydrogen sulfide at 250 ºC. Some corrugation develops on the walls of the Ni-loaded tungsten oxide nanowires, indicative of a corrosion effect. Furthermore, XPS performed on aged samples indicates a clear reduction in the amount of Ni present on the surface of the nanomaterial. These results are summarized in Table S4. Finally, the effects of such degradation in the response towards hydrogen sulfide are shown in Figure S5. In this experiment the sensor is under and accelerated ageing under high concentration of hydrogen sulfide. During the first 9 hours of exposure to 50 ppm H_2S at the different operating temperatures considered, response remains stable. After this period of time, if the sensor surface remains exposed to such a high concentration of hydrogen sulfide, response degrades. This effect is more evident at higher operating temperatures.

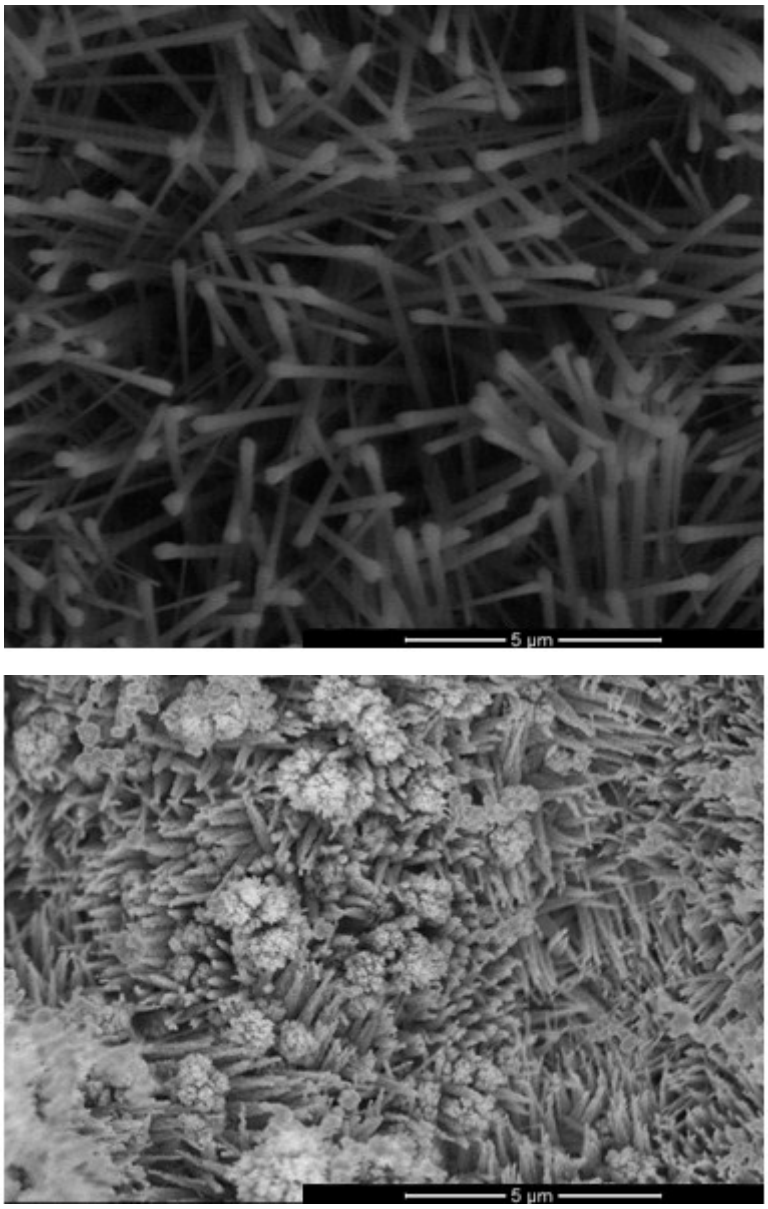

Figure S4. Unexposed sensing layer (upper panel) and H_2S exposed sensing layer (lower panel).

Table S4. Sensing layer average composition in weight percentage after 18 hours of exposure to hydrogen sulfide, 50 ppm.

	W	**O**	**Ni**
Ni/LC	17.6	81.0	1.4
Ni/HC	18.0	80.0	2.0
WO_3	25.0	75.0	0

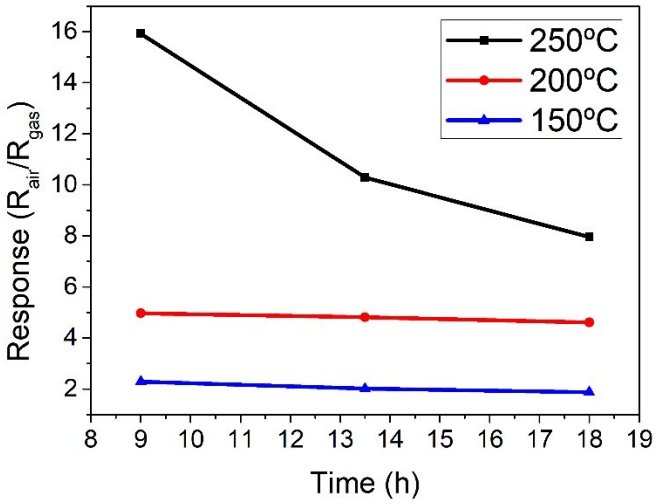

Figure S5. Degradation in sensor response after hours of exposure to 50 ppm H_2S at the operating temperatures of 150 ºC, 200 ºC or 250 ºC.

5. Effect of nickel oxide loading on the response to hydrogen sulfide.

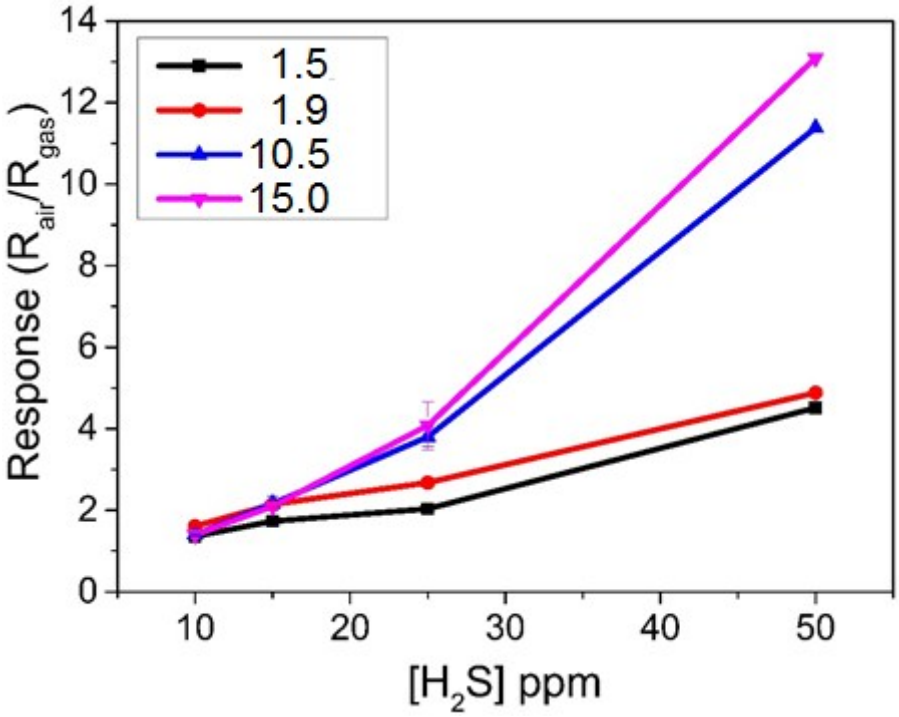

Figure S6. Response for different H_2S concentrations of tungsten oxide nanowires sensors loaded with different amounts of nickel oxide. The legend indicates the atm. % of Ni as revealed by XPS. Sensors were operated at 250ºC.

Supporting information for:

WO_3 Nanowires Loaded with Cobalt Oxide Nanoparticles, Deposited by a Two-Step AACVD for Gas Sensing Applications

Èric Navarrete[1], Carla Bittencourt[2], Xavier Noirfalise[3], Polona Umek[4], Ernesto González[1], Frank Güell[5] and Eduard Llobet*[1]

[1]MINOS-EMaS, Universitat Rovira i Virgili, Avda. Països Catalans, 26, 43007 Tarragona, Spain

[2]Chimie des Interactions Plasma – Surface (ChIPS), Research Institute for Materials Science and Engineering, Université de Mons, Avenue Copernic 3, 7000 Mons, Belgium

[3]Materia Nova, Avenue Copernic 3, 7000 Mons, Belgium

[4]Jožef Stefan Institute, Jamova cesta 39, 10000 Ljubljana, Slovenia

[5]ENFOCAT-IN2UB, Universitat de Barcelona, C/Martí i Franquès 1, 08028 Barcelona, Catalunya, Spain

*Correspondence: eduard.llobet@urv.cat; Tel.: +34 977 558 502

1. Loading level effects on gas sensing properties

To study the effect of cobalt oxide loading on the sensing properties, samples of pure tungsten oxide nanowires were decorated with three different amounts of cobalt oxide nanoparticles. This was achieved by using different weights of the Co metalorganic precursor during the second AACVD process. Namely 2.5, 5 and 10 mg of $Co(acac)_2$ were used to achieve three increasing loading levels. A preliminary study was conducted to determine which amount of loading resulted in better responses to the species tested. Figure S1 summarizes these results, which are shown only for the optimal sensor working temperatures (i.e., 200 ºC for ethanol and 250 ºC for H_2 or H_2S). According to Figure S1, the presence of cobalt oxide increases the response to ethanol and the intermediate loading level (when 5 mg of the Co precursor were used) leads to

be best results. Roughly, a two-fold increase in response is achieved in comparison to bare tungsten oxide. In contrast, the loading with cobalt oxide is not suitable for detecting hydrogen, since the response and sensitivity towards hydrogen decrease for cobalt oxide loaded materials. For the detection of H_2S, the loading with cobalt oxide has a clear beneficial effect. While the intermediate loading level leads to higher responses at low H_2S concentrations, the high loading level works slightly better for H_2S concentrations equal or higher than 25 ppm. According to these results, only two cobalt oxide loading levels are retained for performing further studies, these are the amounts that correspond to using 5 mg and 10 mg of the Co precursor, which from now on are referred as Co/LC and Co/HC.

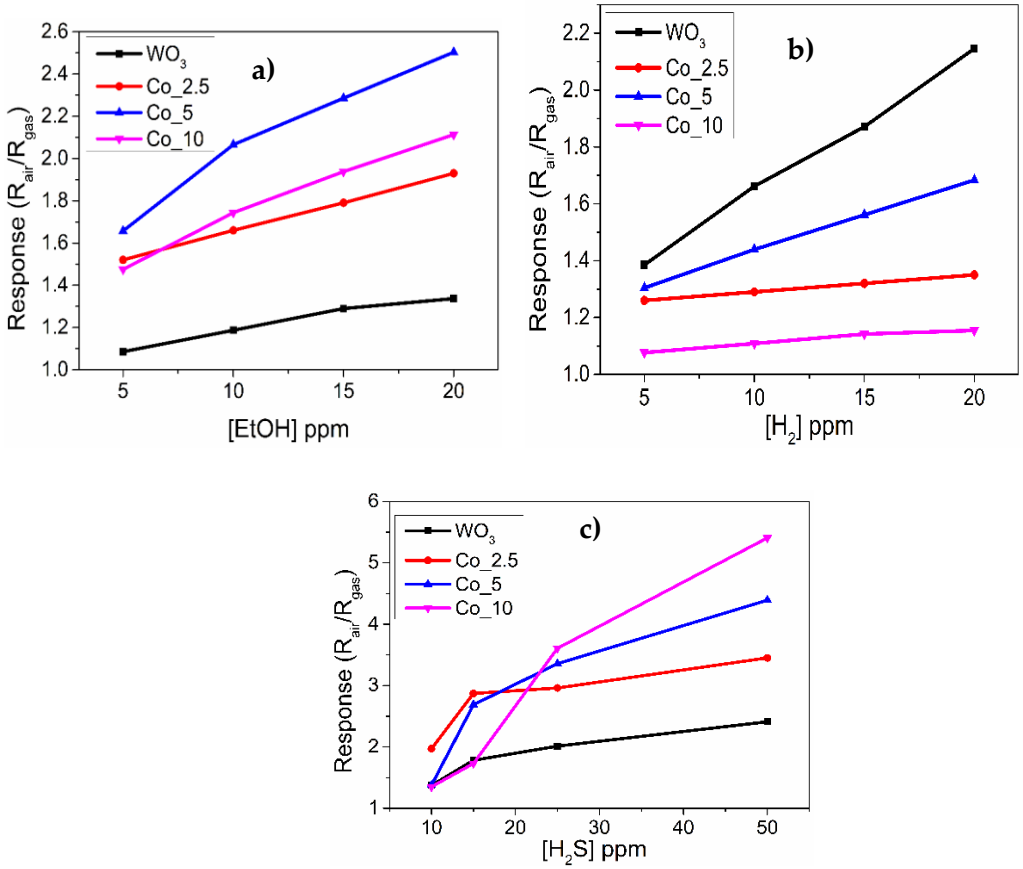

Figure S1. (a) Ethanol responsiveness comparison among sensors at 200 ºC. (b) H_2 responsiveness comparison among sensors at 250 ºC. (c) H_2S responsiveness comparison among sensors at 250 ºC. All displayed responses are under dry air conditions.

2. Additional results for material characterization

Figure S2 shows a typical XRD spectrum of Co/HC loaded WO_3 nanowires. The peaks in the spectrum are in agreement with those reported in the ICDD card nº 43-1035 corresponding to monoclinic WO_3. The WO_3 nanowires are grown on an interdigitated platinum electrode on top of an alumina substrate, therefore the XRD spectra show different peaks corresponding to the alumina and the electrodes. Despite the fact of showing these peaks, the 3 peaks remarked in the spectra are attributed to cobalt oxide species corresponding to ICDD card nº 73-1701.

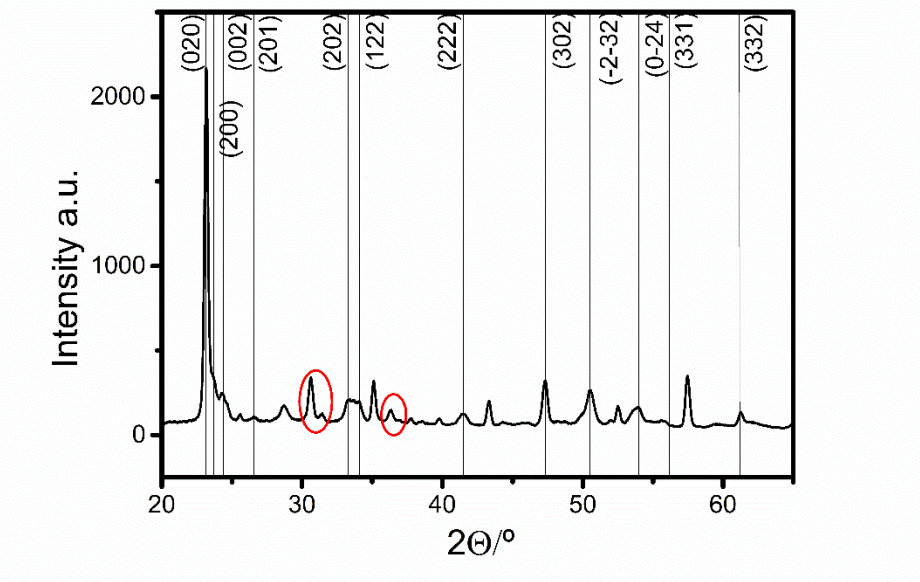

Figure S2. Typical XRD spectrum recorded on Co/HC sensor. The loaded sensors undergo two annealing steps leading to a monoclinic structure with a space group P2/m.

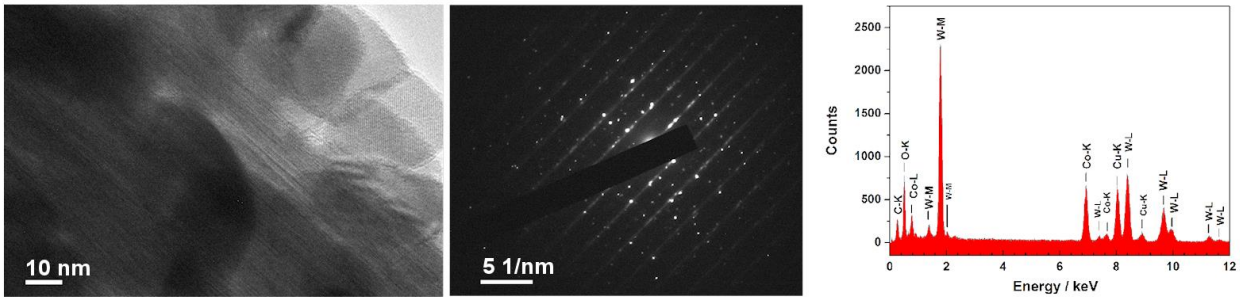

Figure S3: TEM image (a) of Co/HC sample. Selective area electron diffraction (SEAD) pattern (b) and EDX spectrum (c) were taken over the area shown in image a. Appearance of carbon and copper in the EDX spectrum originate from the TEM grid.

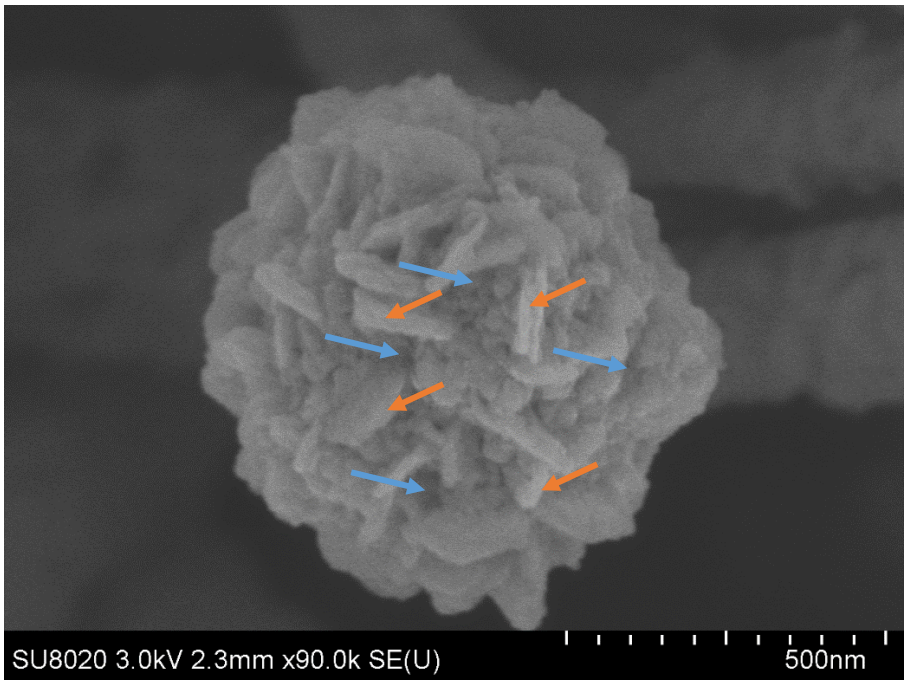

Figure S4: SEM image of Co/HC sample showing the presence of light grey and dark grey areas. Red arrows indicate light grey areas and blue arrows indicate dark grey areas in the sample.

A cross-section and element mapping were performed at Thermo Fisher Scientific employing a FESEM-FIB-field emission gun SEM-focused ion beam (Figure S5). The nanowires present nearly a core-shell structure (WO_3 core, Co_xO_y shell) spreading from the nanowires tip to their body. The highest amount of cobalt oxide is found at nanowire tips.

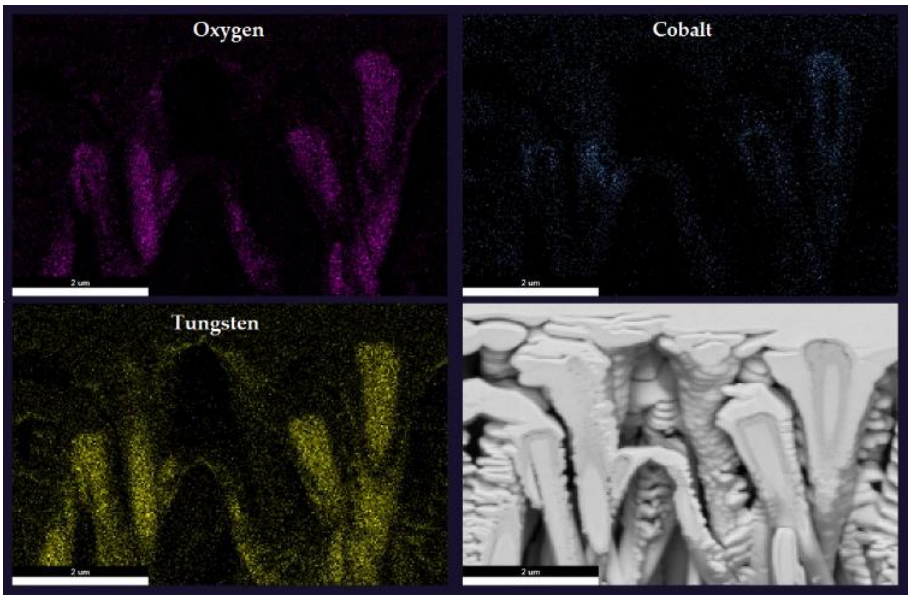

Figure S5. FESEM-FIB element mapping image from a Co/HC sensor surface.

Additionally, room-temperature photoluminescence (PL) measurements were made with a chopped Kimmon IK Series He-Cd laser (325 nm). Fluorescence was dispersed with an Princeton Instruments Acton SP2750 0.750 m imaging triple

grating monochromator, detected using a Hamamatsu H8259-02 with a socket assembly E717-500 photomultiplier, and amplified through a Stanford Research Systems SR830 DSP. A 360 nm filter was used to filtering the stray light. It is worth pointing out that the emission spectra were corrected using the optical transfer function of the PL setup.

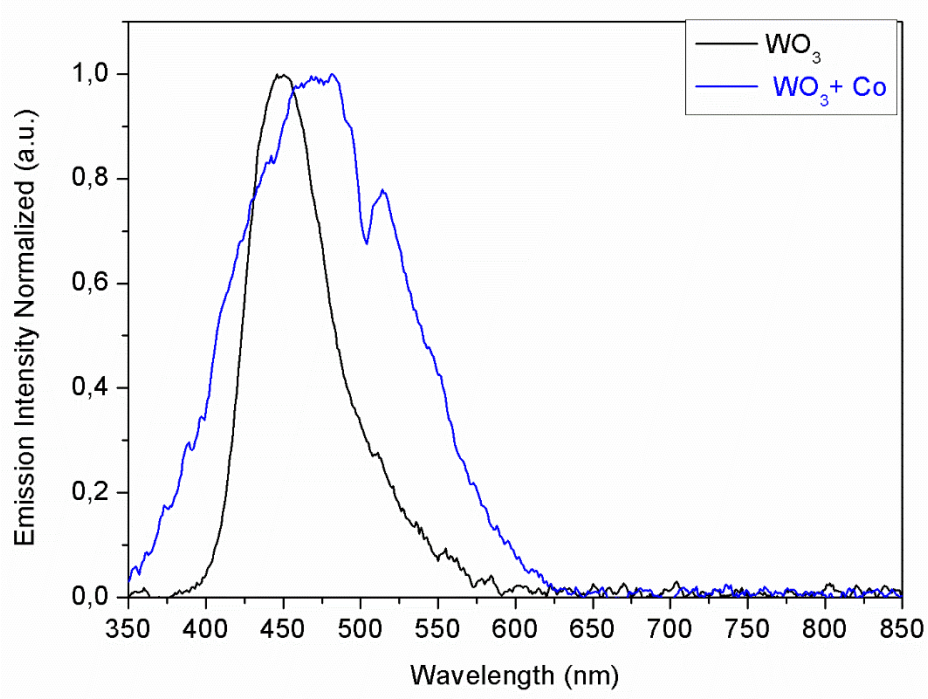

Figure S6. Room-temperature PL spectra recorded for pure WO_3 and Co/LC samples.

The room-temperature PL spectra are presented in Figure S6. By pumping at 325 nm, we observed an emission peak of the WO_3 NWs at around 450 nm (2.75 eV) with a full width at half maximum (FWHM) of 370 meV. When loading the WO_3 NWs with the cobalt nanoparticles the emission peak is shifted to 480 nm (2.58 eV) and the FWHM is around 750 meV. The intensity of each spectrum was normalized to the maximum emission intensity for relative comparison. This broadening observed on the FWHM indicates that the quantity of intrinsic defects is higher when loading the WO_3 NWs with the cobalt nanoparticles.

Additional results obtained from XPS analysis revealed the sample composition at atomic percentage.

Table S1. XPS results for the average composition for the different sensing layers in atomic percentages (atom. %) before gas exposure.

Sample	Carbon	Oxygen	Cobalt	Tungsten
Co/LC	10.3	58.0	21.1	10.6
Co/HC (light)	12.0	54.0	25.0	9.0
Co/HC (dark)	11.0	55.0	29.0	5.0

3. Additional gas sensing measurements

3.1. Hydrogen gas

In a similar approach to the one reported for ethanol or hydrogen sulfide, the sensors employing pure and cobalt-loaded tungsten oxide were exposed to hydrogen at 5, 10, 15 and 20 ppm under dry air conditions. Figure S9 shows how increasing the operating temperature of the sensors enhances the response and sensitivity towards hydrogen. Pure tungsten oxide operated at 250°C shows the highest response and sensitivity towards hydrogen. Therefore, it can be derived that loading tungsten oxide nanowires with cobalt is not useful for enhancing their response to hydrogen. Figure S10 reports the responses to hydrogen of cobalt loaded tungsten oxide samples, when measured under humid conditions. Similarly, to what was found for ethanol, Co/HC samples operated at high temperatures retain their responsiveness to hydrogen when there is humidity in the background (50% R.H.). However, this responsiveness is rather low.

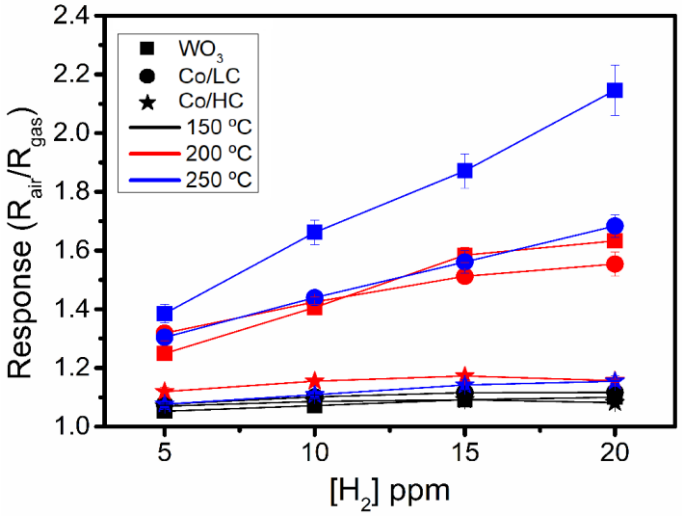

Figure S7. Effect of the amount of cobalt loading and operating temperature on the response to different concentrations of hydrogen (diluted in dry air).

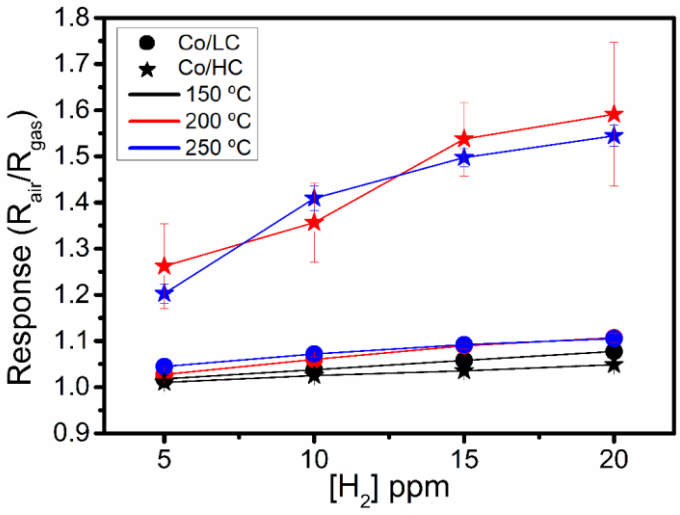

Figure S8. Humidity effect on hydrogen sensing at different operating temperatures for cobalt-loaded samples.

3.2. Ammonia vapors

Ammonia at 25, 50, 75 and 100 ppm was tested under dry air conditions at 3 different temperatures (i.e. 150°C, 200°C and 250°C) following the same procedure as for the other gases characterized. Sensors displayed a tendency to saturation when exposed to ammonia concentrations higher than 25 ppm. Therefore, only ammonia 25 ppm results are discussed in detail. Ammonia displays an unusual behavior being found to act as a reducing species when tested with Co-loaded sensors operated at 150°C and 200°C. On the other hand, it exhibits an oxidizing behavior for pure WO_3 (at any of the operating temperatures tested) and for Co-loaded sensors operated at 250°C. This abnormal behavior when ammonia is detected employing tungsten oxide has been reported previously [S1,S2]. Furthermore, operating temperature has a high impact on sensor response. For example, 200°C is the optimal temperature for detecting ammonia using pure tungsten trioxide, meanwhile 250C is the optimal temperature for a Co/LC sensor. Co/HC shows the lowest ammonia response and thus, higher levels of cobalt oxide loading are detrimental for detecting ammonia. Figure S12 indicates that, under dry conditions, a Co/LC sensor operated at 250°C is quite selective to ammonia. The effect of ambient moisture in the detection of ammonia vapors was studied as well. In the presence of moisture (35% R.H. at 25°C), the response towards 25 ppm of ammonia for

a Co/LC sensor operated at 250°C was 2.3 (this response was nearly 13 under dry conditions). Therefore, the presence of humidity heavily influences the response towards ammonia.

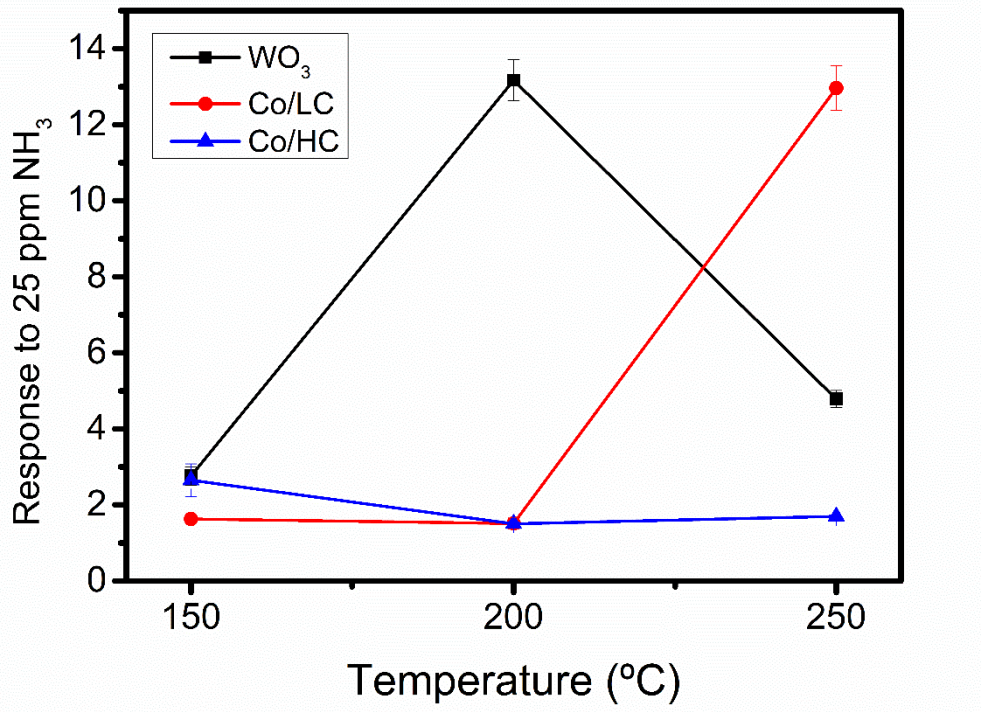

Figure S9. Sensors response for ammonia vapors operated at different temperatures under dry air conditions. Response calculated as R_{air}/R_{gas} for Co/LC and Co/HC at 150°C and 200°C; Response calculated as R_{gas}/R_{air} for WO_3 at all temperatures tested and 250 ºC for both Co/LC and Co/HC.

4. Additional results for gas sensing mechanism

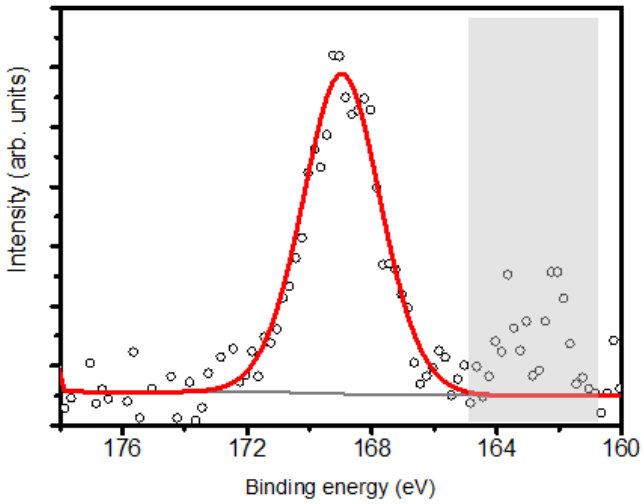

Figure S10. Sulphur 2p core level spectrum recorded after H_2S detection. The relative amount of sulphur at the active layer surface was 1%. The peak centered at 168.8 eV indicate the presence of S-O bonds while the apparent increase in the counts around 162 eV suggest the presence of S-Co bonds [S3][S4]. The noise in the spectrum can be explained by the relative low amount of sulfur atoms.

[S1] Dac Dien Nguyen, Duc Vuong Dang and Duc Chien Nguyen, Hydrothermal synthesis and NH3 gas sensing property of WO3 nanorods at low temperature, Adv. Nat. Sci.: Nanosci. Nanotechnol. 2015, 6, 035006

[S2] Han Li, Wuyuan Xie, Tianjie Ye, Bin Liu, Songhua Xiao, Chenxia Wang, Yanrong Wang, Qiuhong Li, and Taihong Wang, Temperature-Dependent Abnormal and Tunable p-n Response of Tungsten Oxide–Tin Oxide Based Gas Sensors, ACS Appl. Mater. Interfaces 2015 7 (44), 24887–24894

[S3] K. Huang, J. Zhang, G. Shi, and Y. Liu, "One-step hydrothermal synthesis of two-dimensional cobalt sul fi de for high-performance supercapacitors," *Mater. Lett.*, vol. 131, pp. 45–48, 2014.

[S4] X. Meng, J. Deng, J. Zhu, H. Bi, E. Kan, and X. Wang, "Cobalt Sulfide / Graphene Composite Hydrogel as Electrode for High- Performance Pseudocapacitors," *Nat. Publ. Gr.*, pp. 1–9, 2016.

Supporting information for: Tungsten Trioxide Nanowires Decorated with Iridium Oxide Nanoparticles as Gas Sensing Material

Eric Navarrete[1], Carla Bittencourt[2], Polona Umek[3], Damien Cossement[4] , Frank Güell[5], Eduard Llobet*[1]

[1]MINOS-EMaS, Universitat Rovira i Virgili, Avda. Països Catalans, 26, 43007 Tarragona, Spain

[2]Chimie des Interactions Plasma – Surface (ChIPS), Research Institute for Materials Science and Engineering, Université de Mons, Avenue Copernic 3, 7000 Mons, Belgium

[3]Jožef Stefan Institute, Jamova cesta 39, 10000 Ljubljana, Slovenia.

[4] Materia Nova, Avenue Copernic 3, 7000 Mons, Belgium

[5]ENFOCAT-IN[2]UB, Universitat de Barcelona, C/Martí i Franquès 1, 08028 Barcelona, Catalunya, Spain

*Correspondence: eduard.llobet@urv.cat; Tel.: +34 977 558 502

Additional material characterization.

The iridium oxide nanoparticles are dispersed in a suspension in methanol prior to their loading of WO_3 nanowire layers. Such a suspension presents a wide range of particle sizes, which range from several micrometers to few nanometers. The AACVD system acts as a filter, as its N_2 flow can only carry small nanoparticles ranging from few nanometers up to hundreds of nanometers as it can be seen from the images obtained by TEM S1 and S2. Only small nanoparticles are actually dragged by the carrier gas flow into the reactor and become eventually deposited onto the WO_3 nanowires. Bigger (i.e., heavier) particles are not wasted because they remain in the vessel in which the aerosol is generated. Once a loading experiment finishes, all the remnant material (IrO_2 micro-particles) can be recovered and, after a milling treatment to decrease their size, they can be recycled in a new loading process.

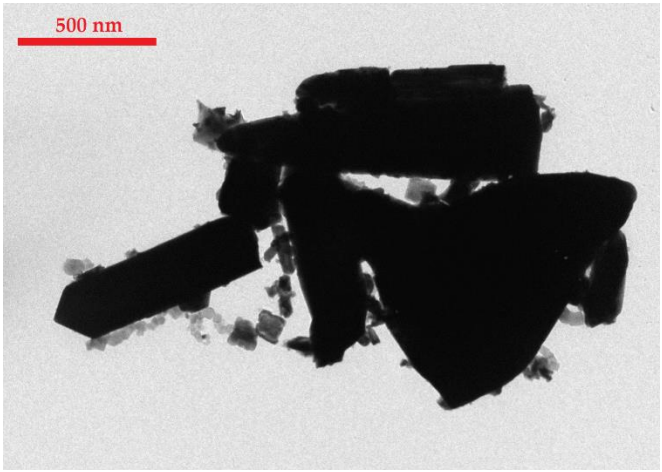

Figure S1. TEM image of commercial iridium powder. The particles present a wide range of morphologies as well as a size dispersion.

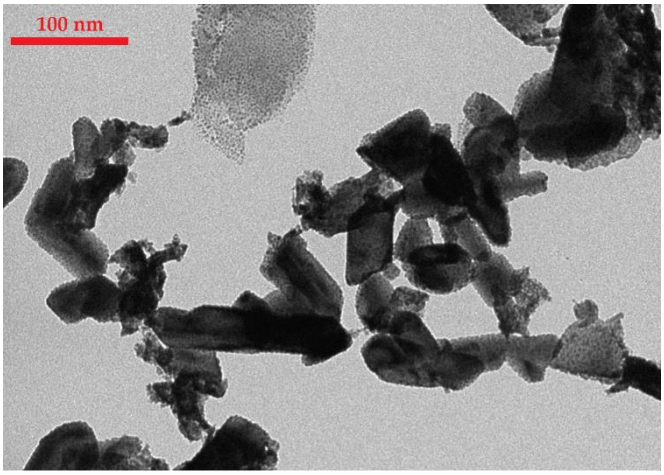

Figure S2. TEM image of nanoparticles able to reach the WO_3 nanowire surface ranging from few nanometers up to 100 nm.

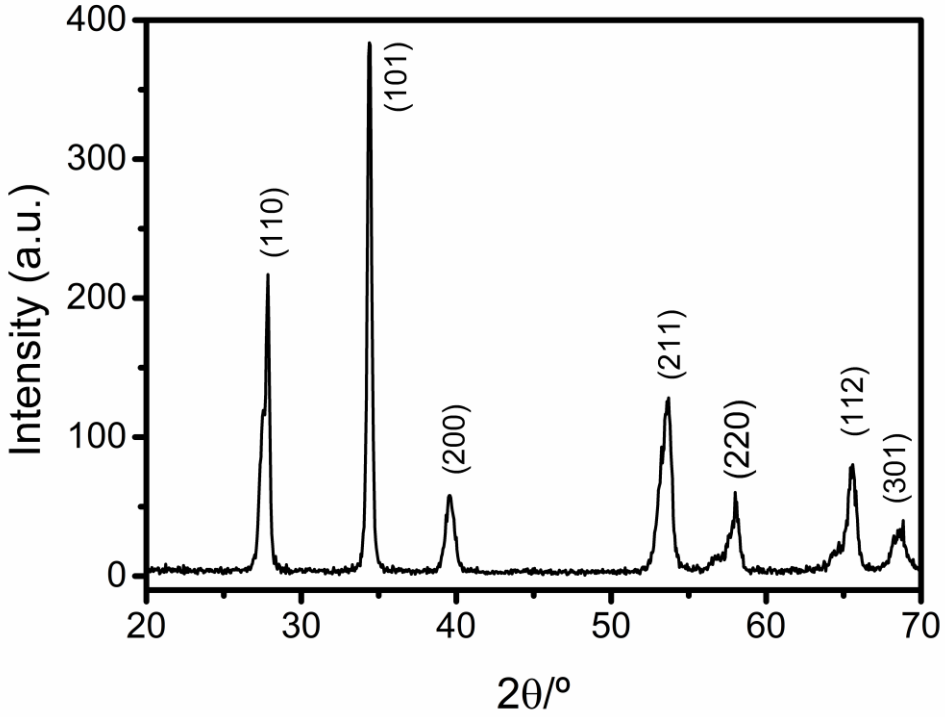

Figure S3. XRD performed to the commercial IrO_2 powder. The material presents a high crystallinity having a tetragonal lattice with a spatial group P42/mnm matching the ICDD card nª 01-088-0288.

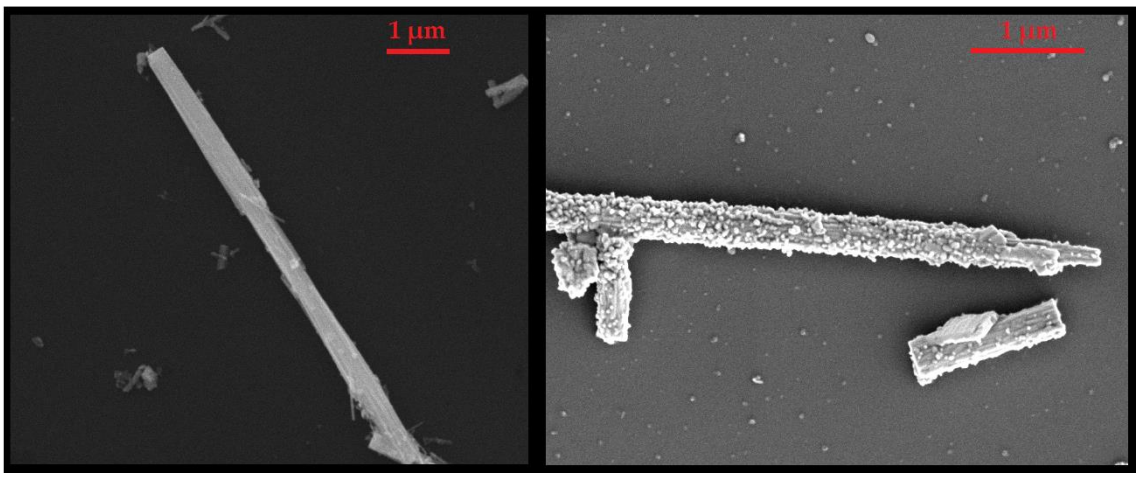

Figure S4. shows SEM images of pure and iridium oxide loaded tungsten oxide nanowires. The two images have similar magnification, showing clearly the striking differences in morphology that exist between pure and iridium oxide loaded samples.

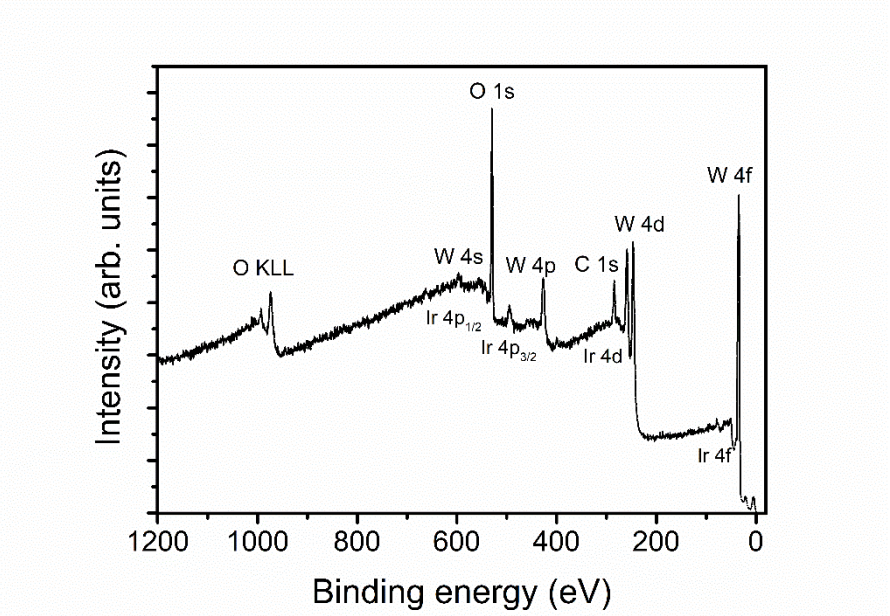

Figure S5. XPS survey spectrum showing the expected position for W, O, C and Ir XPS peaks, in WO_3:IrO_2. Due to the low amount of Ir oxide nanoparticles at the WO_3 nanoribbons surface the peaks generated by photoelectrons emitted form Ir atoms are buried under the background due to secondary electrons.

Additional gas sensing results

Hydrogen results

Sensors were exposed to hydrogen diluted in air at concentrations of 5, 10, 15 and 20 ppm. The results obtained for each sensor are summarized in Figure S5. Sensor responsiveness, both for pristine and iridium oxide loaded samples is low. Measurements conducted at 150 ºC revealed the lack of response of iridium oxide loaded sensors and the very small response of pristine WO_3 sensors. At higher operating temperatures, both IrO_2/LC and IrO_2/HC, showed a small response, which increased as the operating temperature raised.

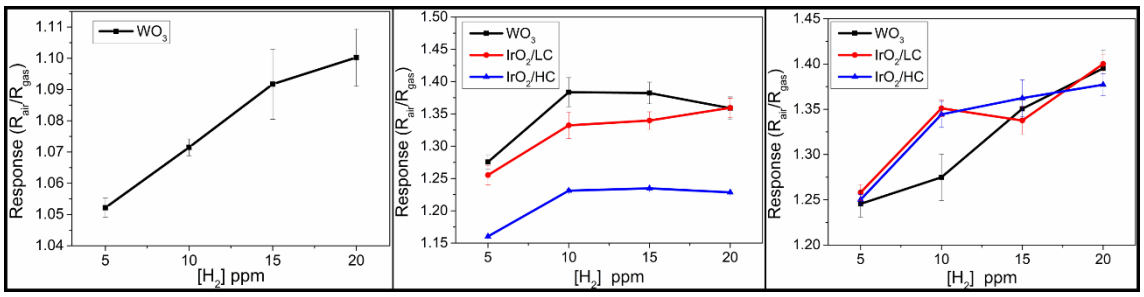

Figure S6. Sensor response for hydrogen detection at different working temperatures, from left to right panels; 150 ºC, 200 ºC and 250 ºC.

Ammonia Vapors results

Sensors were exposed to ammonia vapors at concentrations of 5, 10, 15 and 20 ppm. The results obtained for each type of sensor are summarized in Figure S6. Overall, sensor responsiveness when exposed towards ammonia is low. Measurements conducted at 150 ºC had revealed the occurrence of sensor response saturation at concentrations of 10 ppm and higher. At 200 ºC sensitivity is slightly improved in spite of the fact that the response of pristine WO_3 sensors is equal or better than the one obtained with iridium loaded sensors. When humidity is present, pristine WO_3 nanowire samples display a similar response to the ones obtained under dry air conditions for the lower working temperatures. On the other hand, iridium oxide loaded sensors increase their response in particular IrO_2/LC showing that the presence of humidity enhances sensor response towards ammonia vapors.

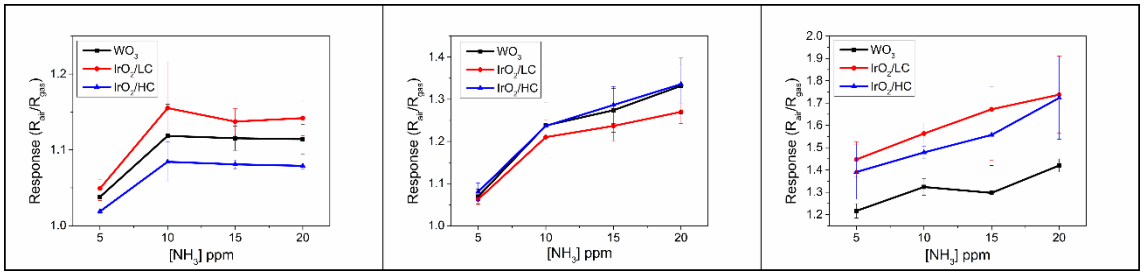

Figure S7. The left panel shows sensor response while operating at 150 ºC; the middle panel shows sensor response while operating at 200 ºC; the right panel shows sensor response while operating at 250 ºC under 30% R.H. conditions.

Table S1. Average response times (t90) for ethanol, hydrogen sulfide and nitrogen dioxide at different operating temperatures in seconds. t90 values appear in bold when they correspond to the operating temperature in which sensor response is the faster for a given gaseous species.

Sensor	Gas	Concentration (ppm)	150 ºC	200 ºC	250 ºC
WO_3	Ethanol	20	832	450	255
IrO_2/LC	Ethanol	20	1125	364	115
IrO_2/HC	Ethanol	20	600	110	**45**
WO_3	H_2S	20	1265	380	40
IrO_2/LC	H_2S	20	925	215	**19**
IrO_2/HC	H_2S	20	1315	390	20
WO_3	NO_2	1	1530	1570	1180
IrO_2/LC	NO_2	1	1500	1600	1170
IrO_2/HC	NO_2	1	**765**	870	1340

Baseline resistance measurements performed under nearly dry and humid conditions

We have measured the resistance of the sensors employing different materials under dry (R.H. <3%) and wet (35% R.H.) conditions at the different operating temperatures.

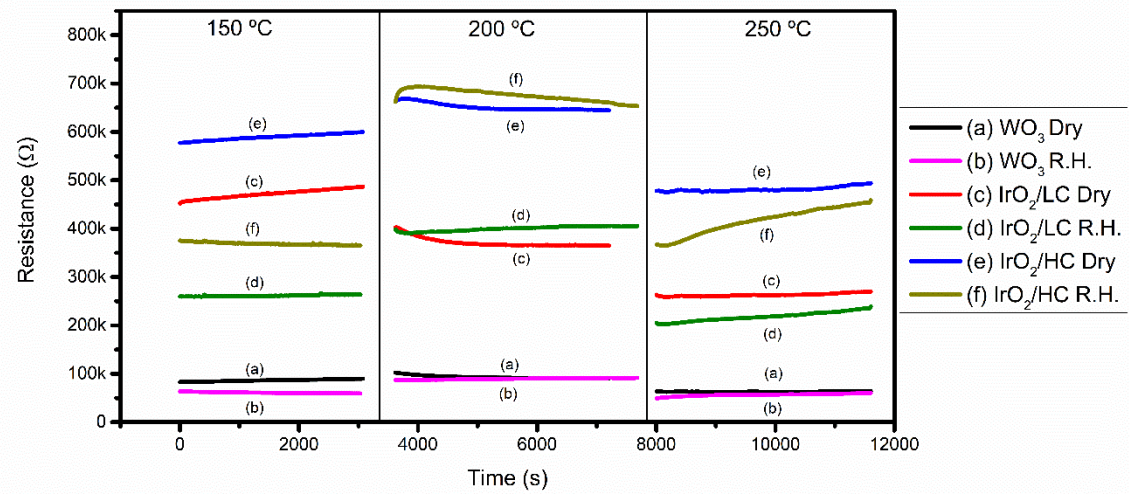

Figure S8. Resistance comparison for all sensors under synthetic air flow for dry and R.H. conditions tested at 150 ºC, 200 ºC and 250 ºC.

The effect of ambient moisture on the baseline resistance of the different nanomaterials studied is summarized in Figure S8. For the temperature range tested, the presence of iridium oxide in tungsten oxide nanowires results in increased baseline resistance. When under dry conditions, the resistance of the films increases when the amount of iridium oxide is increased. This supports our assumption that the presence of IrO_2 helps increasing the amount of oxygen species adsorbed on tungsten oxide nanowires (oxygen adsorbates trap electrons via the conduction band of tungsten oxide, which results in an increased baseline resistance).

The baseline resistance of iridium oxide loaded tungsten oxide films operated at 150 ºC is heavily affected by changes in ambient moisture. Baseline resistance decreases if water content is increased. In comparison, the baseline of pure tungsten oxide films is little affected by such changes. These results support the mechanism in which water molecules are split generating iridium oxyhydroxide (IrO_2OH) and releasing electrons towards the conduction band of tungsten oxide nanowires.

Furthermore, the optimal working temperature is found experimentally at 200 ºC, suggesting a trade of between the water molecule adsorption and subsequently iridium hydroxylation and the desorption of byproducts leading to an equilibrium were the electron transfer and the material response are maximized. The baseline resistance of iridium oxide loaded tungsten oxide nanowires is less affected by moisture conditions when these materials are operated at 200 ºC and 250 ºC. This is because the adsorption of water molecules on IrO_2 is less favored at high temperature in comparison to 150 ºC. In addition, 250 ºC is the temperature tested at which water adsorption is less favored and sensor response is decreased dramatically as the iridium hydroxylation (derived from its interaction with water molecules), a key step, is also reduced.

Additional XPS results

In the XPS spectrum recorded after an IrO_2-WO_3 sensor had been exposed to NO_2 we observed a low intensity peak centered at 407.3 eV (see Figure S9) that can be associated to nitrogen species adsorbed at the sensor active layer. A closer inspection shows that this peak can be reproduced by two components (Gaussian-Lorentzian) and a background (Shirley). The component at 407, 6 eV is representative of photoelectrons emitted from nitrogen atoms in NO_3^- [S1-S4] while the other component at 405,7 eV has been reported to be due to the presence of physisorbed NO_2 [S2,S4].

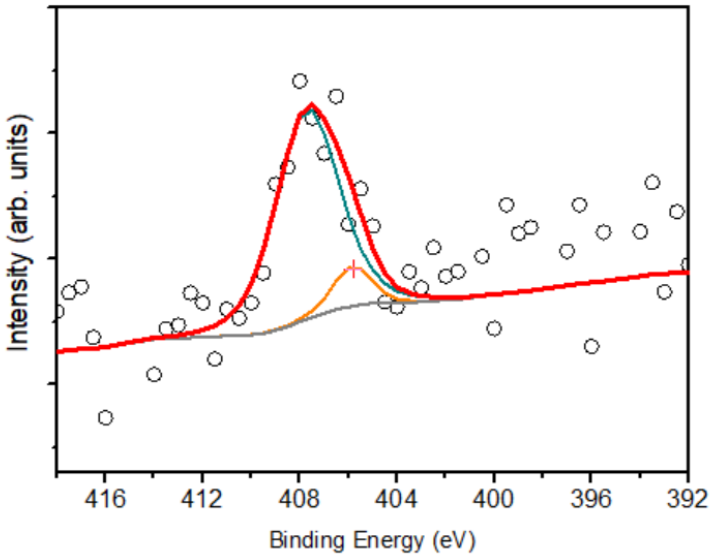

Figure S9. XPS spectrum recorded in the N1s core level region for an IrO_2-WO_3 sensor previously exposed to NO_2. The spectrum was reproduced using two Lorentzian-Gaussians and a Shirley background.

Additional TOF-SIMS studies

TOF-SIMS was used to explore an Ir-IrO_2-WO_3 sensor exposed to humidified air. Figure S10 displays the peaks two isotopes of IrO_2-OH^-. These peaks occur with differences between the theoretical and experimental m/z ratios as low as 0.01. Besides, the experimental isotopic ratio $^{191}IrO_3H^-/IrO_3H^-$ (0.80) is close to the theoretical one (0.59). Hence, these observations demonstrate that IrO_2-OH^- moieties occur at the surface of the material exposed to humidity under operating conditions. It also worth mentioning that, in the same way, the occurrence of IrO_2-H^- isotopes were also confirmed in the negative spectra.

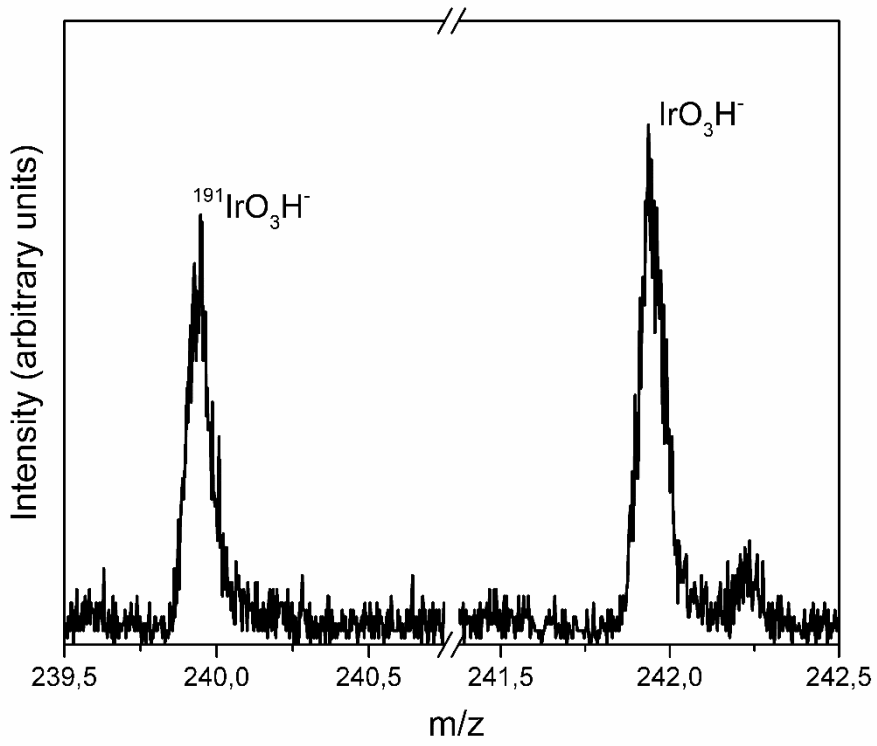

Figure S10. Negative ToF-SIMS spectrum from m/z = 239.5 to 242.5. The Figure displays the IrO_3H^- isotopes."

S1. Haubrich, J.; Quiller, R. G.; Benz, L.; Liu, Z.; Friend, C. M. (2010). In-Situ Ambient Studies of the Chemistry of NO_2 and Water on Rutile TiO_2 (110). *Langmuir*, 26, 2445−2451.

S2. Rodriguez, J. A.; Jirsak, T.; Liu, G.; Hrbek, J.; Dvorak, J.; Maiti, A. (2001). Chemistry of NO_2 on Oxide Surfaces: Formation of NO_3 on TiO_2 (110) and NO_2↔O Vacancy Interactions. *J. Am. Chem. Soc.*, 123, 9597−9605.

S3. Baltrusaitis, J.; Jayaweera, P. M.; Grassian, V. H. (2009). XPS Study of Nitrogen Dioxide Adsorption on Metal Oxide Particle Surfaces Under Different Environmental Conditions. *Phys. Chem. Chem. Phys.*, 11, 8295–8305.

S4. Aduru, S.; Contarini, S.; Rabalais, J. W. (1986). Electron-, X-Ray-, and Ion-Stimulated Decomposition of Nitrate Salts. *J. Phys. Chem.*, 90, 1683–1688.

Supporting information for:

Tungsten oxide – lutetium bisphthalocyanine n-p-n hetero-junction: From nanomaterials to a new transducer for chemosensing

M. Bouvet,[a*] M. Mateos,[a] A. Wannebroucq,[a] E. Navarrete[b] and E. Llobet[b]

[a.] *Institut de Chimie Moléculaire de l'Université de Bourgogne (ICMUB), UMR CNRS 6302, Univ. Bourgogne Franche-Comté, 9 avenue Alain Savary, 21078 Dijon cedex, France. Fax: +33-380-396-098; Tel: +33-380-396-086; E-mail: marcel.bouvet@u-bourgogne.fr*

[b.] *Microsystem Nanotechnology for Chemical Analysis (MINOS-EMaS), Universitat Rovira i Virgili, Avda. Països Catalans, 26, 43007 Tarragona, Spain. E-mail : eduard.llobet@urv.cat*

Figure S1 corresponds to the ESEM image obtained for a sample of tungsten oxide AA-CVD grown at 370 °C and subsequently annealed at 500 °C for 2 hours in dry air. The sample has been grown onto the application substrate that already comprised interdigitated ITO electrodes. The image shows that the tungsten oxide layer uniformly covers the whole electrode area.

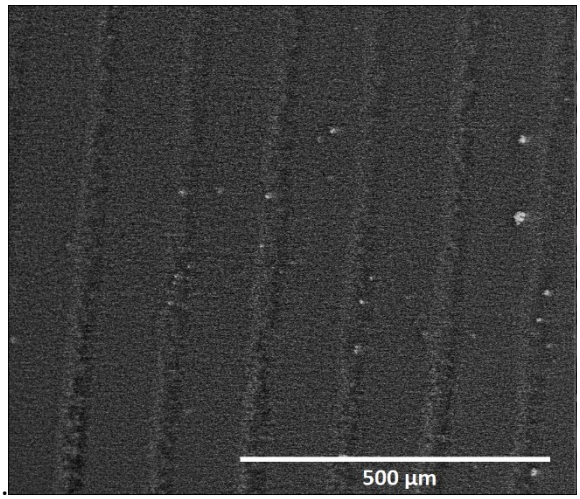

Figure S1. E-SEM micrograph. Interdigitated ITO electrodes are covered with an AA-CVD grown WO_3 layer. The electrode pattern is still visible underneath the 5-micron thick tungsten oxide film.

After the annealing an XRD was carried out to determine the crystalline structure present on the WO_3 film. Figure S2 shows the spectrum obtained. The features in this spectrum match those of the JPDC card 43-1035 for a crystalline tungsten trioxide belonging to the monoclinic system with a space group $P2_1/n$. The cell parameters are a = 9.05 Å, b = 9.07 Å, c = 11.61 Å and the angle β = 90.77°. The peaks indicated by an asterisk correspond to the presence of the ITO electrodes on the substrate where tungsten oxide was grown. Once the tungsten oxide film had ben coated with the thin Pc_2Lu film, further XRD analysis did not reveal changes to the spectrum shown in Figure S2. This is indicative that the organic film was below 100 nm thick.

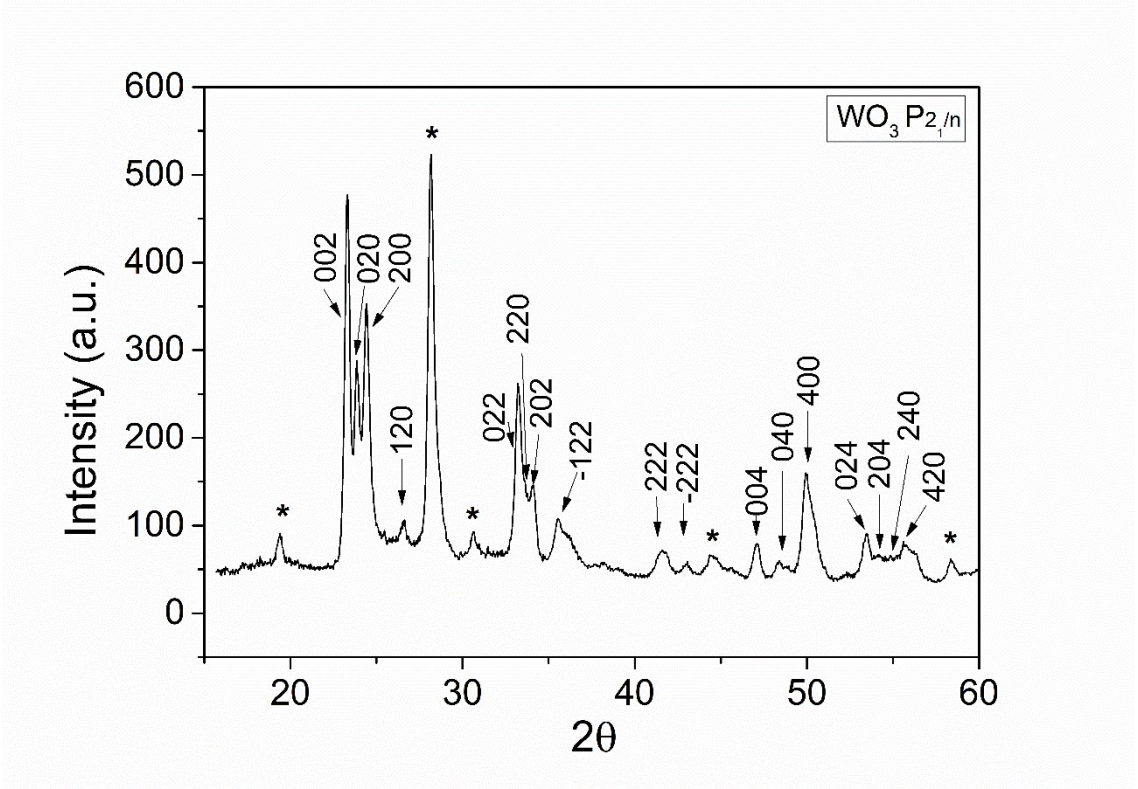

Figure S2. XRD spectrum obtained for the WO_3 nanowire films. Tungsten oxide shows a monoclinic crystalline phase.

Figure S3 shows typical EDX results obtained for an AACVD tungsten oxide film coating a silicate glass substrate in which ITO interdigitated electrodes had been patterned. The Si, Ca and Na peaks correspond to the silicate glass substrate and the In peak can be attributed to the electrodes. The EDX shows clearly the presence of tungsten and, finally, of some carbon contamination, which is often detected in samples exposed to ambient air.

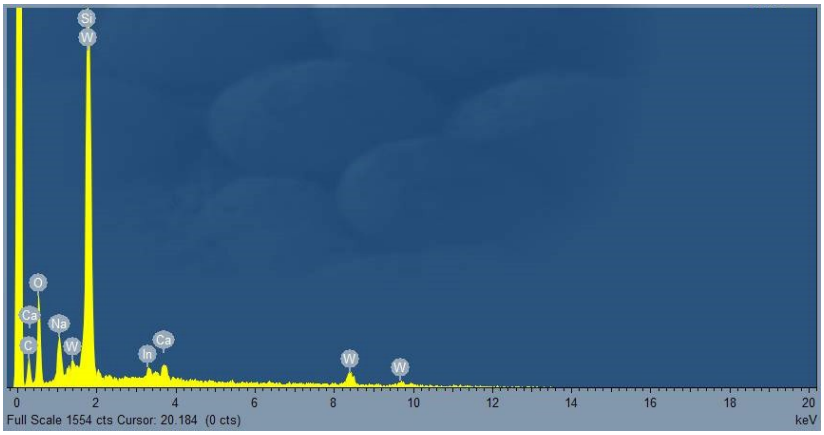

Figure S3. EDX spectrum obtained for an AACVD tungsten oxide film coating a glass substrate having ITO electrodes.

To check the contact between the ITO electrodes and the WO_3 layer a current-voltage curve was measured. A DC voltage sweep was applied to the interdigitated electrodes underneath the tungsten oxide layer. Figure S4 displays these results. The fact that the current-voltage characteristic is almost linear supports the existence of an ohmic contact between the electrodes and the tungsten oxide film.

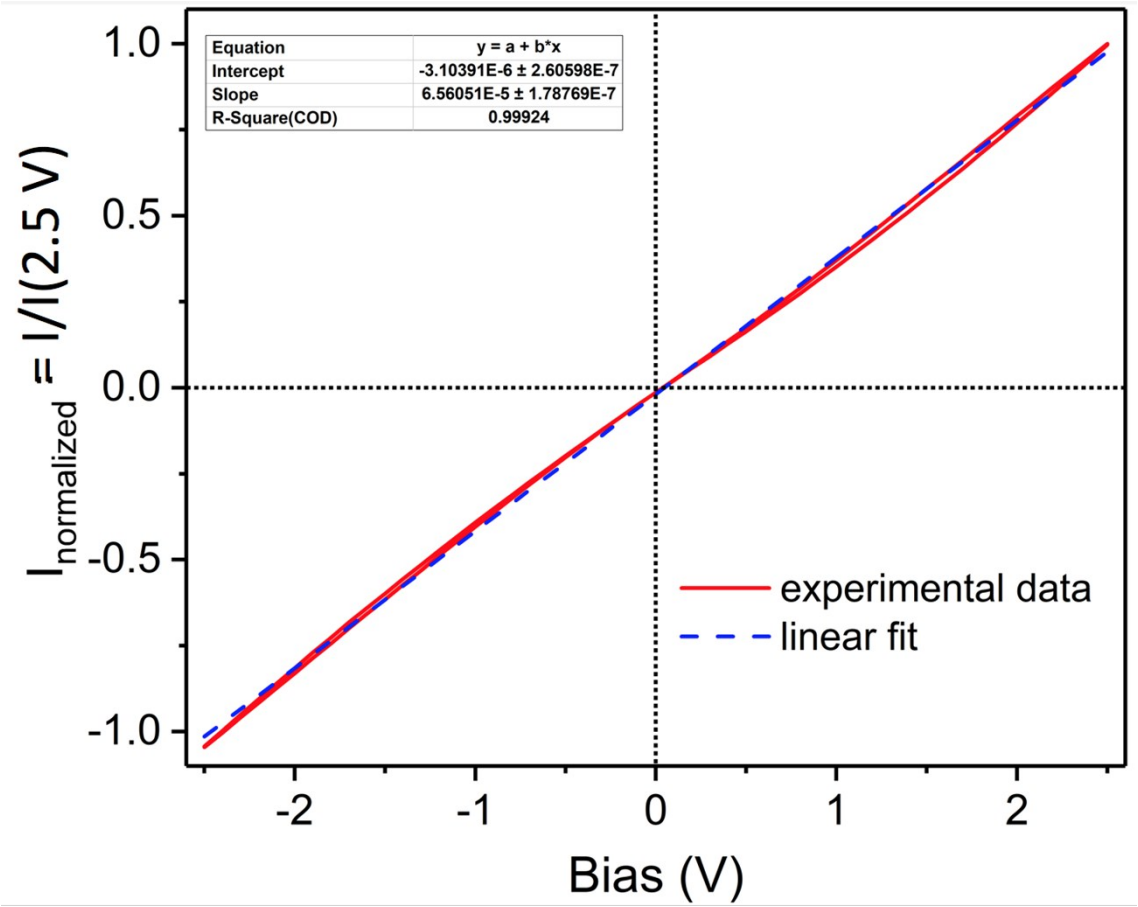

Figure S4. Voltage vs Intensity plot obtained for the WO_3 layer coating interdigitated ITO electrode

To investigate what the limit of detection is for the organic-inorganic MSDI devices discussed here, an experiment was carried out in which low ammonia concentrations were measured repeatedly (1 to 9 ppm). These results are summarized in Figure S5. Response intensity is highly reproducible. The fact that for 1 ppm, the signal is still 6 times higher than the noise level observed, is indicative that the limit of detection for ammonia is clearly below 1 ppm (in the hundreds of ppb range).

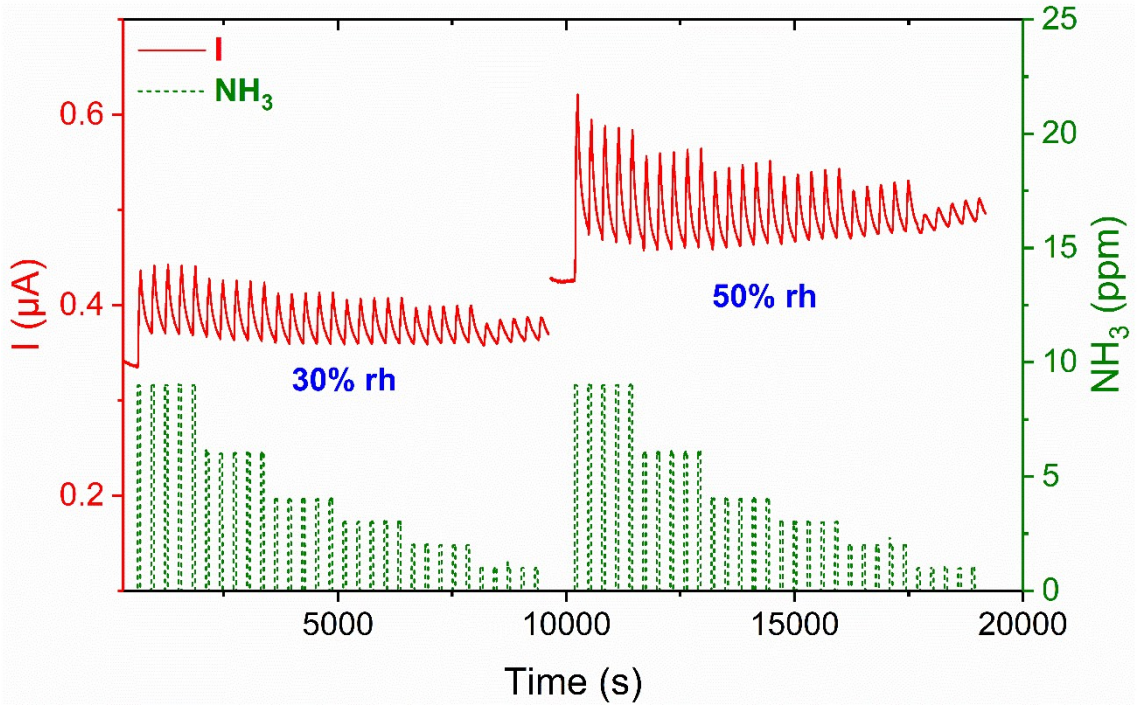

Figure S5. Variation of the current (red line) as a function of time during exposure to NH_3 in the range 1-9 ppm (dotted line), at relative humidity values of 50 % and 30 % (1 min exposure and 4 min recovery); T = 20 °C.

Annex II

Publication List

Publications directly related with the thesis

1) Kowalski, L., Pons-Nin, J., Navarrete, E., Llobet, E., & Domínguez-Pumar, M. (**2018**). Using a Second Order Sigma-Delta Control to Improve the Performance of Metal-Oxide Gas Sensors. Sensors, 18(2), 654. doi: 10.3390/s18020654

2) Alvarado, M., Navarrete, È., Romero, A., Ramírez, J., & Llobet, E. (**2018**). Flexible Gas Sensors Employing Octahedral Indium Oxide Films. Sensors, 18(4), 999. doi: 10.3390/s18040999

3) Navarrete, E., Bittencourt, C., Umek, P., & Llobet, E. (**2018**). AACVD and gas sensing properties of nickel oxide nanoparticle decorated tungsten oxide nanowires. Journal of Materials Chemistry C, 6(19), 5181–5192. doi: 10.1039/c8tc00571k

4) Llobet, E., & Navarrete, E. (**2019**). Nanomaterials for the Selective Detection of Hydrogen at Trace Levels in the Ambient. *Handbook of Ecomaterials*, 1223–1246. doi: 10.1007/978-3-319-68255-6_12

5) Agarwal, S., Rai, P., Navarrete, E., Llobet, E., Güell, F., Kumar, M., & Awasthi, K. (**2019**). Gas sensing properties of ZnO nanostructures (flowers/rods) synthesized by hydrothermal method. Sensors and Actuators B: Chemical, 292, 24–31. doi: 10.1016/j.snb.2019.04.083

6) Bouvet, M., Mateos, M., Wannebroucq, A., Navarrete, E., & Llobet, E. (**2019**). A tungsten oxide–lutetium bisphthalocyanine n–p–n heterojunction: from nanomaterials to a new transducer for chemo-sensing. Journal of Materials Chemistry C, 7(21), 6448–6455. doi: 10.1039/c8tc06309e

7) Navarrete, E., Bittencourt, C., Noirfalise, X., Umek, P., González, E., Güell, F., & Llobet, E. (**2019**). WO_3 nanowires loaded with cobalt oxide nanoparticles, deposited by a two-step AACVD for gas sensing applications. Sensors and Actuators B: Chemical, 298, 126868. doi: 10.1016/j.snb.2019.126868

8) Navarrete, E., Bittencourt, C., Umek, P., Cossement, D., Güell, F., & Llobet, E. (**2020**). Tungsten trioxide nanowires decorated with iridium oxide nanoparticles as gas sensing material. Journal of Alloys and Compounds, 812, 152156. doi: 10.1016/j.jallcom.2019.152156

Publications not included with the thesis

1) Alvarado, M., Navarrete, E., Llobet, E., Ramirez, J., & Romero, A. (**2017**). Comparing performance of flexible and rigid substrates for I_2O_3 based gas sensors. 2017 IEEE Sensors. doi: 10.1109/icsens.2017.8233946

2) Navarrete, E., González, E., Vilic, T., & Llobet, E. (**2017**). Cobalt or Silver Doped WO_3 Nanowires Deposited by a Two-Step AACVD for Gas Sensing Applications. Proceedings, 1(4), 438. doi: 10.3390/proceedings1040438

3) Llobet, E., Navarrete, E., Annanouch, F. E., Alvarado, M., Gonzalez, E., Ramirez, J., Dominguez-Pumar, M., Vallejos, S. and Gracia, I. (**2018**). Single-Crystalline Metal Oxide Resistive Gas Sensors Advances and Perspectives. 2018 Ieee Sensors. doi: 10.1109/icsens.2018.8589734

4) Navarrete, E., Bittencourt, C., & Llobet, E. (**2018**). Gas Sensing Properties of WO_3 Nanowires Decorated with Iridium Oxide Nanoparticles. Proceedings, 2(13), 964. doi: 10.3390/proceedings2130964

5) Casanova-Cháfer, J., Navarrete, E., & Llobet, E. (**2018**). Gas Sensing Properties of Carbon Nanotubes Decorated with Iridium Oxide Nanoparticles. Proceedings, 2(13), 874. doi: 10.3390/proceedings2130874

6) Casanova-Cháfer, J., Navarrete, E., Noirfalise, X., Umek, P., Bittencourt, C., & Llobet, E. (**2018**). Gas Sensing with Iridium Oxide Nanoparticle Decorated Carbon Nanotubes. Sensors, 19(1), 113. doi: 10.3390/s19010113

7) Kowalski, L., Navarrete, E., Llobet, E., & Dominguez-Pumar, M. (**2019**). Control of Surface Potential in WO_3 Gas Sensors Using UV Light. 2019 20th International Conference on Solid-State Sensors, Actuators and Microsystems & Eurosensors XXXIII (TRANSDUCERS & EUROSENSORS XXXIII). doi: 10.1109/transducers.2019.8808408

8) Navarrete, E. & Llobet, E. (**2021**). Synthesis of p-n Heterojunctions via Aerosol Assisted Chemical Vapor Deposition to Enhance the Gas Sensing Properties of Tungsten Trioxide Nanowires: A Mini-Review. Journal of Nanoscience and Nanotechnology, 21(4), 2462–2471. https://doi.org/10.1166/jnn.2021.19105

Publications submitted for publication or in preparation

1) Navarrete, E., Suematsu, K., Llobet, E. & Shimanoe, K. "Differences in gas sensing mechanisms for 1-D WO_3 Nanowires and 2-D lamellar WO_3 nanoparticles"
2) Navarrete, E., Güell, F., Martínez-Alanis, P.R. & Llobet, E. "Chemical Vapor Deposited ZnO Nanowires for Ethanol and NO_2 Gas Detection"

Annex III

Contribution to conferences

EUROSENSORS XXXI 2017
Paris, France

Oral contribution: *"Cobalt or Silver doped WO_3 nanowires deposited by a two-step AACVD for gas sensing applications"*

IBERNAM 9th 2018
Tarragona, Spain

Poster contribution: *"Gas Sensing properties of WO_3 Nanowires Decorated with Iridium Oxide Nanoparticles"*

EUROSENSORS XXXII 2018
Gratz, Austria

Poster contribution: "*WO_3 Nanowires Decorated with Iridium Oxide Nanoparticles for NO_2 Detection"*

Graduated Student Meeting 2018
Tarragona, Spain

Poster contribution: *"WO_3 Nanowires Decorated with Nickel Oxide Nanoparticles for H_2S Detection"*

TRANSDUCERS 20th & EUROSENSORS XXXIII 2019
Berlin, Germany

Poster contribution: "*Control of surface potential in WO_3 gas sensors using UV light"*

ISOEN 18th International Symposium on Olfaction and Electronic Nose 2019
Fukuoka, Japan

Poster contribution & Robot competition participation: *"Minos Mobile Sniffer Robot"*

IBERNAM 20th 2019
San Sebastian, Spain

Poster contribution: *"P-N heterojunctions metal oxide gas sensors"*